UNIVERSITÀ DEGLI STUDI DI PAVIA
DOTTORATO DI RICERCA IN FISICA – XXII CICLO

Study of electroweak effects on W boson production cross-section and decay in the muon channel at the LHC with the ATLAS experiment

Silvia Franchino

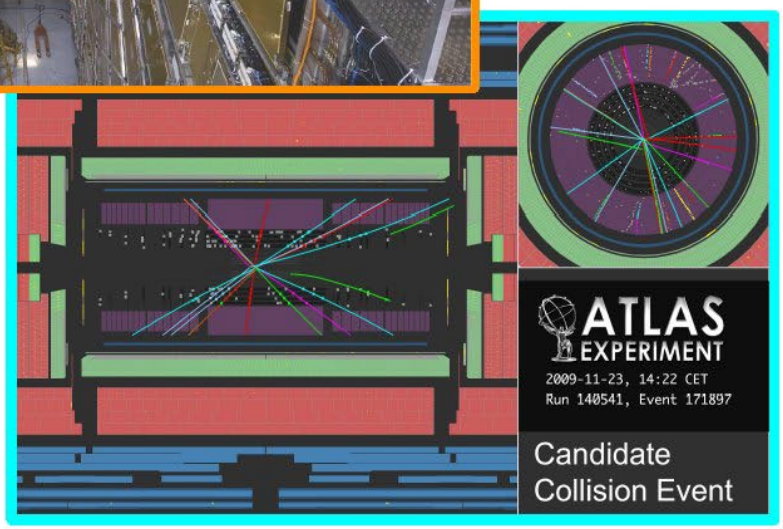

Tesi per il conseguimento del titolo

Università degli Studi di Pavia | Dipartimento di Fisica Nucleare e Teorica | Istituto Nazionale di Fisica Nucleare | Texas Tech University

DOTTORATO DI RICERCA IN FISICA – XXII CICLO

Study of electroweak effects on W boson production cross-section and decay in the muon channel at the LHC with the ATLAS experiment

dissertation submitted by

Silvia Franchino

to obtain the degree of

DOTTORE DI RICERCA IN FISICA

Supervisors: **Prof. Michele Livan (Tutor) (Università di Pavia)**
Dott. Valerio Vercesi (INFN Pavia)
Dott.ssa Gabriella Gaudio (INFN Pavia)
Prof. Richard Wigmans (Texas Tech University)

Referee: **Dott.ssa Sandra Leone (INFN Pisa)**

Cover: The ATLAS experiment during the installation phase (CERN courtesy, described in chapter 1), the W boson production (discussed in Chapter 5), the ATLAS logo, and the event display of the first LHC collisions seen by ATLAS (Chapter 1 and 2).

Study of electroweak effects on W boson production cross-section and decay in the muon channel at the LHC with the ATLAS experiment

Silvia Franchino
PhD thesis – University of Pavia
Printed in Pavia, Italy, December 2009
ISBN: 978-88-95767-29-1

Contents

Table of contents **i**

Introduction **1**

1 The LHC and its detectors **5**
1.1 The Large Hadron Collider (LHC) . . . 5
1.1.1 Overview of the LHC detectors . . . 11
1.1.2 The LHC start-up and plans . . . 14
1.2 The ATLAS detector . . . 18
1.2.1 Coordinate System . . . 20
1.3 Inner Detector . . . 21
1.4 Calorimetry . . . 23
1.4.1 Electromagnetic Calorimeter . . . 24
1.4.2 Hadronic Calorimeters . . . 25
1.5 Muon Spectrometer . . . 27
1.6 Magnetic System . . . 32
1.6.1 Magnetic field characteristics . . . 33
1.7 Forward Detectors . . . 35
1.8 Detector Control System (DCS) . . . 35
1.9 Trigger and Data Acquisition (TDAQ) . . . 36
1.9.1 ATLAS Analysis Model . . . 40
1.10 Installation and Commissioning . . . 42

2 The MDT chambers and their commissioning **47**
2.1 Momentum measurement . . . 48
2.1.1 Momentum resolution . . . 49
2.2 Monitored Drift Tube Chambers . . . 51
2.2.1 Working principles and layout . . . 51
2.2.2 Mechanical structure . . . 53
2.2.3 Naming conventions . . . 54
2.2.4 Readout electronics . . . 55
2.2.5 Power supplies . . . 61

2.3 Track reconstruction . . . 62
2.4 Calibration of MDT chambers . . . 64
2.5 Alignment system . . . 68
2.6 Commissioning of MDT chambers . . . 71
2.6.1 Overview of commissioning procedures . . . 72
2.6.2 Online Monitoring System . . . 73
2.7 Hardware commissioning . . . 75
2.7.1 Data quality . . . 79
2.8 ATLAS combined cosmic runs . . . 86
2.9 Data analysis results . . . 90
2.9.1 Cosmic rays . . . 90
2.9.2 LHC first data . . . 94

3 Dual REAdout Method (DREAM) with crystals 101
3.1 The Dual Readout Method DREAM . . . 102
3.1.1 The fibre dual readout module . . . 103
3.1.2 Advantages of the dual readout method . . . 105
3.2 The Dual Readout Method with crystals . . . 106
3.2.1 Test beam setup and data acquisition . . . 107
3.3 Results of undoped $PbWO_4$ crystals . . . 110
3.3.1 Temperature studies . . . 110
3.4 New Crystals for Dual Readout . . . 118
3.5 Mo- and Pr-doped $PbWO_4$ crystals . . . 119
3.5.1 Emission spectrum . . . 119
3.5.2 2008 test beam setup . . . 121
3.6 Experimental results for $PbWO_4$:Mo . . . 122
3.6.1 The time structure of the signal . . . 122
3.6.2 Cherenkov/Scintillation ratio . . . 123
3.6.3 Experimental results for $PbWO_4$:Mo 5% . . . 125
3.7 Experimental results for $PbWO_4$:Pr . . . 126
3.7.1 The time structure of the signal . . . 126
3.7.2 Cherenkov/Scintillation ratio . . . 127
3.7.3 Changing the doping concentration . . . 129
3.8 Comparison of Mo- and Pr-doping for calorimeter purposes . . . 130
3.8.1 Effects of light attenuation . . . 130
3.8.2 Cherenkov Light Yield . . . 132
3.8.3 Conclusions from Pr and Mo doping tested during 2008 135
3.9 2009 test beam and preliminary results . . . 137
3.9.1 Preliminary results . . . 140

4 The ATLAS physics programme 145
4.1 Search for the Higgs boson . . . 145
4.2 Standard Model physics and precision measurements . . . 149
4.2.1 Minimum bias physics . . . 149
4.2.2 Electroweak bosons studies . . . 151

4.2.3 Bottom physics . . . 153
4.2.4 Top physics . . . 154
4.3 Physics beyond the Standard Model . . . 156
4.3.1 Supersymmetry . . . 156
4.3.2 Other physics beyond the Standard Model . . . 157
4.4 LHC early physics . . . 159
4.5 The ATLAS analysis software . . . 162
4.5.1 Event generation . . . 164
4.5.2 Detector simulation . . . 167
4.5.3 Digitization . . . 172
4.5.4 Event reconstruction and analysis . . . 172

5 W boson cross section measurement 175
5.1 Introduction . . . 175
5.2 W boson production and decay . . . 176
5.2.1 PDFs uncertainty . . . 178
5.2.2 W boson observables . . . 180
5.3 QCD corrections and Monte Carlo tools . . . 182
5.4 Radiative EW corrections . . . 183
5.5 Cross section measurement . . . 187
5.6 EW effects to W boson observables . . . 194
5.7 Evaluation of EW effects . . . 200
5.7.1 Generated events . . . 200
5.7.2 Reconstructed data . . . 204
5.7.3 Analysis of EW corrections on acceptances . . . 206
5.7.4 Analysis of EW corrections on photons observables . . . 210
5.7.5 Tails of kinematic distributions . . . 213

Conclusions 217

A Acronyms and abbreviations 219

Introduction

In November 2009 a new generation of High Energy Physics (HEP) experiments became operative at the Large Hadron Collider (LHC), at CERN, the European Laboratory for Particle Physics in Geneva (Switzerland). LHC is a proton-proton collider with designed centre of mass energy of 14 TeV and 10^{34} cm^{-2}s^{-1} design luminosity, which, exploring the TeV scale of elementary interaction, will open new frontiers for particle searches. One of the major goals would be the discovery of the Higgs boson, necessary to confirm the spontaneous symmetry breaking mechanism in the Standard Model, and supposed to play a fundamental role in the generation of the masses of particles. A large part of the research program is also devoted to verify the predictions of models beyond the Standard Model, through the search, for example, of supersymmetric particles or new gauge bosons. Experiments are also ready to study any unexpected physics beyond the electroweak scale. Furthermore, the high cross sections allow to study many Standard Model processes with high precision. It will be possible, for example, to make accurate measurement of the top quark mass and its decay properties, and to study in detail CP violation and rare B decays.
In order to best exploit the physics research potentiality that will be provided by the collider, four experiments have been installed on the LHC ring: two general purpose detectors (ATLAS and CMS), a beauty physics experiment (LHC-b), designed to make precise measurements of CP violation, and an heavy-ion detector (ALICE), dedicated to the study of physics of strongly interacting matter at high energy density, thanks to the LHC capability of accelerating also ions of masses up to the Pb nucleus.

An overview of the LHC collider, its schedule as known at the moment and a general view of the ATLAS detector is the subject of **Chapter 1**.
More details on the ATLAS physics program and on the software used for the analysis are given on Chapter 4.
Among final state particles, muons play a special role in HEP experiments since they cross the entire detector losing a small amount of energy mainly by ionization, while other particles are generally contained inside the calorimeter

systems. Therefore muons can be detected in the outer part of the experiment in a cleaner environment. This characteristic, combined with the presence of many interesting muonic physics signatures, has driven the choice in the ATLAS experiment of a high resolution Muon Spectrometer with standalone trigger and muon momentum measurement capability. The largest possible discovery reach for new physics requires a momentum measurement accuracy of the order of 1% for p_T = 100 GeV and of 10% for p_T = 1 TeV. This is necessary, for example, for the reconstruction of muons from Higgs and heavy gauge bosons decays. These p_T resolutions translate into a required precision of the position resolution of the muon track of 50 μm for p_T = 1 TeV. The magnetic field, necessary to bend tracks in order to measure the particles momentum, is provided by an air-code toroidal system. This configuration has the main advantage of minimizing the contribution of multiple scattering and energy loss to the momentum measurement precision and of ensuring a stable resolution over a wide pseudorapidity interval. The price to pay, with respect to a magnetic system in iron, like in the CMS experiment, is the limited field strength, which implies large dimensions, in order to be able to obtain the required resolution.
The necessity to cover a huge area with high precision detectors has led to the choice of Monitored Drift Tube (MDT) technology as precision chambers for the ATLAS Muon Spectrometer (except for the very forward region where, due to the high particles flux, Cathode Strip Chambers (CSC) are used). MDTs are characterized by two multilayers of drift tubes that provide a single wire resolution of 80 μm, when operated at high gas pressure (3 absolute bar). The multiple measurement capability inside a single chamber ensure the required station resolution.
In **Chapter 2** the performance requirements of the ATLAS Muon Spectrometer, the muon momentum measurement principles and the main characteristics of the MDT chambers are discussed. This chapter is focused on the commissioning phase with cosmic rays of the ATLAS experiment, in particular of the MDT chambers. The period of commissioning started in 2005 with the installation of the first chambers. During the lasts four years all the ATLAS detector elements have been progressively installed in the cavern and then commissioned, firstly in stand-alone and then in combined cosmic runs with all the sub-detectors available at the moment. This phase of commissioning continued in parallel with the installation the whole of ATLAS until now, in view of the first LHC data. Before LHC start-up, cosmic rays remain the best source of real data physics analysis in ATLAS. They offer the possibility to test the stability of the detector and work out problems, both hardware and software, as early as possible. They also offer the possibility of developing techniques that will be used in real LHC data analysis. In this chapter the commissioning procedures of the MDT chambers are presented in detail.

As the ATLAS experience teaches, most of the detectors used in the modern collider experiments are very complex, and they need many years of design and tests on prototypes before being really used and built at full scale. For this reason, there are now many efforts to conceive and test detectors to use on the next generation of high energy physics experiments. One of these new promising techniques in calorimetry is the Dual REAdout Method (DREAM). This technique is not subject to the limitations of traditional hadronic calorimeters and the DREAM international collaboration is trying different approaches, like the use of different fibres, or homogeneous media, in order to build an high resolution hadronic calorimeter prototype. In **Chapter 3** this technique is described in details, in particular the results of DREAM test beams, using homogeneous media like crystals are shown.
This work has been accomplished in the framework of "*International Certificate of Doctoral Studies*", between the University of Pavia and the Texas Tech University.

The second part of the thesis is focused on the ATLAS data analysis. **Chapter 4** gives an overview of the physics goals of the ATLAS experiment and of most of the tools used for the analysis and for the simulation of data.
Chapter 5 is focused on the measurement of the W boson cross section, in its muon decay channel and on the evaluation of electroweak effects. In order to evaluate the detector sensitivity and hence the uncertainty in the calculation of the cross section, a detailed study of kinematic and geometrical detector acceptances is presented, depending on the physic processes enabled in the event generators for production and decay of the W boson. All the analysis presented is performed assuming a centre of mass energy of 10 TeV, that should be the most probable value of 2009/2010 collisions of LHC. The event generators used for the analysis are `HORACE`, that introduces electroweak NLO effects and `HERWIG` for the QCD parton shower. The effect of adding `PHOTOS`, and enabling initial state radiation, hard and soft matrix elements are also evaluated.
The study of W and Z bosons, that are well known physics objects, can help in understanding the detector during the first period of data taking. The cross section measurement, and the comparison with the theoretical calculations, can be a good test for LHC, which will be followed at higher luminosities by precise measurements of W and Z properties, in order to test the Standard Model down to a few percent.

Chapter 1

The LHC and its detectors

The project and development of accelerators and detectors in exploring the particle physics field is strictly related; in fact, detectors are designed in order to better exploit the physics opportunities given by the specific collider. In this chapter the characteristics of the Large Hadron Collider (LHC) and its four experiments ATLAS, CMS, LHCb and ALICE are briefly described. The second part of the chapter is the focused on the description of the ATLAS detector, the experiment in which I worked.

1.1 The Large Hadron Collider (LHC)

The Large Hadron Collider (LHC) project was approved by CERN's Council in December 1994 and it is now (Autumn 2009) ready to start.
The LHC will provide proton-proton (pp) collisions with centre of mass energy of 14 TeV, at a design luminosity of 10^{34} cm^{-2}s^{-1} and heavy ion collisions (Pb - Pb) with centre of mass energy of 2.76 TeV per nucleon per beam, yielding a total centre of mass energy of 1.15 PeV and a nominal luminosity of 10^{27} cm^{-2}s^{-1}. The high energy and high luminosity of LHC offer a large range of physics opportunities like:

- check the validity of the Higgs mechanism in the SM via the search of the Higgs boson in the whole mass range theoretically allowed;
- perform precision measurements on the known particles and interactions, in order to observe possible deviations from the SM predictions;
- search for new physics such as:
  - the hypothetical supersymmetric particles;
  - new quarks or leptons;
  - verify the possible existence of new physics at the electro-weak scale;
  - hypothetical new gauge bosons Z' and W';

and, of course, discover new physics not foreseen by any model.

Previous accelerators

Among the many accelerators built before LHC, two of them were designed for general purpose studies in high energy physics: the Large Electron Positron (LEP) at CERN and the Tevatron at Fermilab.
LEP was a circular e^+ e^- collider designed to study electroweak physics and to probe possible new physics at the Fermi scale. The e^+e^- LEP collider was switched off, after 11 years of running, on November 2000. At first it operated at $\sqrt{s} \sim 90$ GeV, the Z^0 mass peak; later, in the LEP2 phase, the energy was raised up to $\sqrt{s} \sim 200$ GeV, at a luminosity of 10^{32} cm^{-2}s^{-1}. Unfortunately there was no "new physics" in the accessible energy range, but the extremely clean environment allowed for precision physics, such as the measurement of the one loop correction to electroweak observables, obtaining indirect limits on the top quark mass ($173.1^{+10.4}_{-8.3}$ GeV) and setting an upper limit on the Higgs boson mass (114^{+69}_{-45} GeV, $m_H < 260$ GeV at 95% CL) [2, 3].
Tevatron is a circular $p\bar{p}$ collider operating at $\sqrt{s} \sim 2$ TeV, and luminosity 6×10^{32} cm^{-2} s^{-1}, and is currently working (Run II). It is the highest energy particle collider in the world until collisions begin at LHC and a lot of discoveries and measurements has been done by its two experiments CDF and D0. Among its achievements it worths to recall the discovery of the top quark in 1995 and later, the first observation of single top quark production and measurement of its mass ($m_t = 173.1 \pm 1.3$ GeV) [5]. Tevatron has also observed B_s oscillations [6], and found exclusion limits for many beyond SM scenarios (supersimmetry, extradimensions, ...). The current integrated luminosity is about 6 fb^{-1}.

In order to improve LEP and Tevatron results, it was necessary to increase both energy and luminosity for LHC. The LHC has been designed in order to exploit as much as possible the existing CERN accelerator resources. It is located in the tunnel that has housed the LEP, and it uses the present CERN's accelerator complex (Figure 1.1 left) in order to achieve the required collision energy. The LINAC, the Booster, the Proton Synchrotron (PS) and the Super Proton Synchotron (SPS) are used to gradually accelerate the collision particles and finally inject them into LHC[1].
The impossibility to obtain the required luminosity with a $p\bar{p}$ collider, because of the difficulty to produce a sufficiently intense antiproton beam, leads to the choice of a pp collider. On the other hand, in order to collide two beams of equally charged particles they must circulate in separate and opposite magnetic lines. In the LEP tunnel there was hardly room for two separate magnetic

[1]The LHC injector scheme is the following: the protons are produced and accelerated to 50 MeV by the proton Linac, before being injected into the 1.4 GeV Proton Synchrotron (PS) booster (PSB). The PS itself accelerates the protons to 26 GeV and finally the Super Proton Syncrotron (SPS) injects protons at 450 GeV into the LHC.

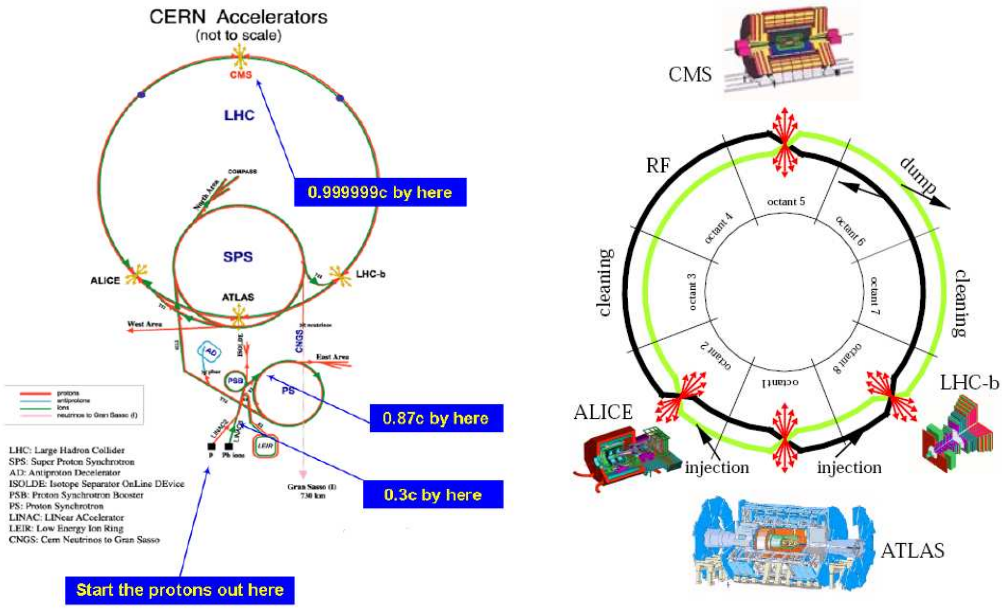

Figure 1.1: *The CERN accelerator complex (left), and the basic layout of the LHC with the four experiments (right).*

rings. A solution to this problem was found using a twin-aperture magnet with two coils and beam channels using the same mechanical structure and cryostat (Figure 1.2).

Figure 1.2: *Superconducting magnets of LHC.*

The aim of LHC, is to provide centre of mass energy greater than 1 TeV at parton level. Being LHC an hadron collider, when a collision occurs, quark and gluon constituents are actually colliding with each others, and the effective centre-of-mass energy ($\sqrt{s}$), unlike in the case of e^+e^- colliders, is smaller than the centre-of-mass energy of the machine ($\sqrt{\hat{s}}$) and is given by:

$$\sqrt{\hat{s}} = \sqrt{x_a x_b}\sqrt{s} \tag{1.1}$$

where x_a and x_b are the fractions of the proton momentum carried by the two colliding partons.
The centre of mass energy achievable is limited by the bending power needed to keep the beams circulating in the 27 km circumference ring of the LEP tunnel. From the approximate relation:

$$p(TeV) = 0.3 \cdot B(Tesla) \cdot R(km) \tag{1.2}$$

where p is the momentum, B the magnetic field provided by the magnets of the machine and R the radius of the collider ring ($R \sim 4.3$ km), one can deduce that the bending power needed to achieve a beam momentum $p = 7$ TeV, is about 4.5 Tesla. In order to achieve such bending power, the LHC relies on superconducting magnets[2] that are at the edge of present technology. Other large superconducting accelerators (Tevatron, HERA and RHIC) all use classical NbTi superconductors, cooled by supercritical Helium at temperatures slightly above 4.2 K, with fields below or around 5 T. The LHC magnet system, while still making use of the well-proven technology based on NbTi Rutherford cables, cools the magnets to a temperature below 2 K, using superfluid Helium, and operates at fields above 8 T. One detrimental effect of reducing the temperature by more than a factor of two is the reduction of the heat capacity of the cable by almost an order of magnitude. As a result, for a given temperature margin (difference between the critical temperature of the superconductor and the operating temperature), the energy deposition that can trigger a quench is substantially reduced. This means that the temperature margin must be significantly larger than that used in previous projects and that a tighter control of movements and heat dissipation inside cables is needed. Since the electromagnetic forces increase with the square of the field, the structures retaining the conductor motion must be mechanically much stronger than in earlier designs.
Another complication arises from the adoption of the "two-in-one" superconducting magnets, that accommodates the windings for the two beam channels in a common cold mass and cryostat, with magnetic flux circulating in the opposite sense through the two channels. In fact, this design, makes the magnet structure complicated, especially for the dipoles, for which the separation of the two beam channels is small enough that they are coupled both magnetically and mechanically.
A total amount of about 100 tonnes of superfluid Helium must flow constantly and be cooled permanently. Among many remarkable properties, superfluid Helium has a very high thermal conductivity, which makes it the coolant of choice for the refrigeration and stabilization of large superconducting systems.
Table 1.1 summarizes the main LHC parameters, while a more detailed description can be found in [1].

[2]Due to magnetic saturation of iron, the magnetic field in conventional magnets reaches a maximum of 2 T, which is the upper limit of the magnetic field for traditional magnets. Another reason to choose superconducting magnets is that for conventional magnets the heat dissipation is excessive.

Parameter LHC	**Value**
Circumference	26.659 km
Injection energy	450 GeV
Initial beam energy	3.5 - 5 TeV
Design beam energy	7 TeV
Dipole field	8.3 T
Bunch spacing	25 ns
Bunch length	75 mm
Bunches per ring	2808
Particles per bunch	10^{11}
Initial luminosity	10^{29} cm^{-2} s^{-1}
Design luminosity	10^{34} cm^{-2} s^{-1}
Mean lifetime per beam	22h

Table 1.1: *Main parameters of the LHC.*

Physics at a *pp* collider provides different features with respect to LEP. When elementary particles like e^+e^- collide, the interaction energy is fixed, providing clean experimental conditions. For LHC, proton beams have been chosen instead of electrons because charged light particles are limited by the energy loss of the synchrotron radiation emission which at LEP amounted to E_{loss}=2.8 GeV per turn. Hadron colliders are not limited by the same energy loss; in fact, given a fixed radius of the ring in which particles have to circulate, the energy loss ΔE^p_{loss} for protons is smaller than the one of electrons by 13 orders of magnitude:

$$\frac{\Delta E^p_{loss}}{\Delta E^e_{loss}} \propto \left(\frac{m^e_0}{m^p_0}\right)^4 \sim 10^{-13} \tag{1.3}$$

However, the experimental conditions are worse in the case of hadron collisions because the centre of mass energy at the parton level is not known (Equation: 1.1) and also beacuse there are much more background events due to QCD, as will be better explained later.
At the nominal luminosity of LHC (L =10^{34} cm^{-2}s^{-1}), the total event rate (R), defined as the number of events produced per second by the *pp* interactions, is expected to be:

$$R = \sigma \cdot L = 100mb \cdot 10^{34} cm^{-2} s^{-1} \approx 10^9 events/s \tag{1.4}$$

where 100 mb is the total inelastic cross section that is estimated to be at the LHC energies. However, the event rate for the production of interesting events is many order of magnitude smaller. In fact, as is possible to see from Figure 1.3, the cross sections of some "interesting" processes are $\sigma_b \sim 0.63$ mb, $\sigma_W \sim 150$ nb, $\sigma_t \sim 0.9$ nb, σ_H (m_H = 150GeV) $\sim$ 24pb, σ_H (m_H = 500GeV) $\sim$ 9pb.
The hadron collisions at high energy are dominated by large-distance interac-

tions. In this case the momentum transfer is small (*soft collisions*) and therefore particle scattering at large angle is suppressed; the produced hadrons tend to be concentrated along the incident beam direction. The particles produced in the final state of such interactions have large longitudinal momentum, but small transverse momentum (p_T) relative to the beam line ($<p_T> \approx 500$ MeV). These events are called "minimum bias" events.

Occasionally, head-on collisions occur between two partons (quarks or gluons) of the primary protons. These interactions, characterized by large momentum transfers (*hard scattering*), are the interesting physics events. In hard collisions, particles in the final state can be produced at large angles with respect to the beam line (high p_T) and massive particles can be created. These events are, however, very rare in comparison to the soft interactions.

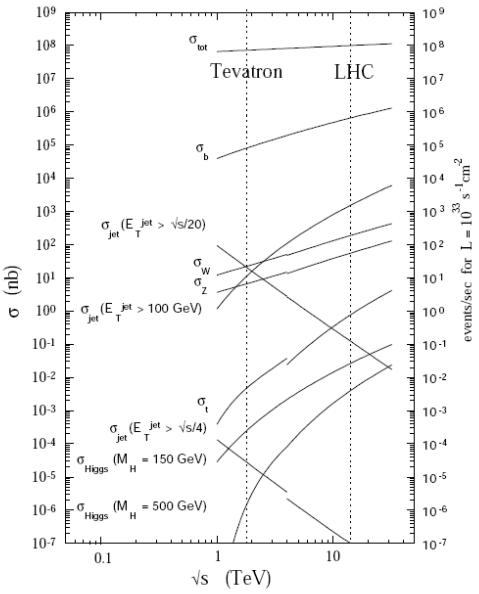

Figure 1.3: *Cross section for hard scattering versus the centre of mass energy. The right scale represents the expected event rate at a luminosity of 10^{33} $cm^{-2}s^{-1}$.*

In order to reach the design luminosity, protons are grouped in bunches of about 10^{11}, colliding at a given interaction point every 25 ns, a bunch spacing 100 times shorter than LEP (21 μs) and more than factor of 10 shorter than Tevatron RunII (396 ns). Given such high rate of interactions, the LHC detector must have a fast response time to avoid the integration of the detectors signals over many bunch crossing. This requires sophisticated and highly performing readout electronics and triggering tools. Furthermore, at the design luminosity, the inelastic cross section leads to an average of 23 soft interactions occurring simultaneously (pile-up) at each bunch crossing and overlapping interesting high-p_T events. This gives rise, every 25 ns, to about 1100 charged particles that pass through the detector and hide "interesting" events. Such particles can be removed with appropriate cuts, like selecting only signatures with p_T higher than a proper threshold, as is shown in Figure 1.4.
In order to discriminate the different tracks and efficiently reconstruct the interesting events, the LHC detectors must have a fine read-out granularity, limited by the cost and the complexity of so large a number of electronic channels. An experimental challenge is due to the huge QCD background expected at LHC. As is shown in Figure 1.3, the rate of high p_T events at a hadron collider is indeed dominated by QCD jet production from the fragmentation

of quarks and gluons.
Another important issue for LHC detectors is that they must be radiation resistant, in order to survive at high flux of particles coming from pp collisions. In fact, has been calculated that in 10 years of LHC running there will be up to 10^{17}n/cm^2, that correspond to a dose of about 10^7 Gy.

The effects are much bigger near the beam pipe and in the forward regions. In the inner parts of each detector, charged hadrons from inelastic proton-proton interactions dominate the radiation backgrounds at small radii, while the effects of other backgrounds, such as neutrons, become more important further out. A thorough understanding of the impact of background radiation has been a critical element in the design phase of most of the components of the detectors and a number of deleterious effects have been considered. Among these effects there are the increasing of detector occupancy, that can lead to inefficiencies in tracking detectors and energy resolution degrade in calorimeters, the radiation damages in silicon detectors or ageing effects in wire detectors. Nuclear interaction in dense materials will lead also the creation of radio-nuclides and then radio-activation of materials, that is a radiological hazard which impacts access and detector maintaining.

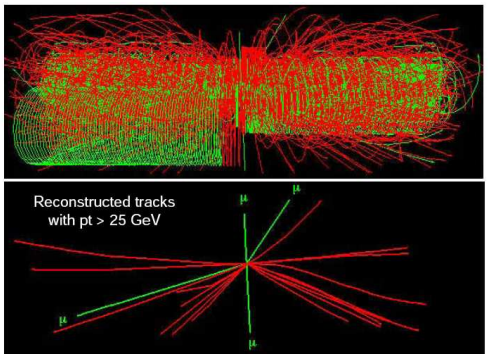

Figure 1.4: *Simulation of an event of $H \rightarrow ZZ \rightarrow 4\mu$ overlapped with 23 minimum bias events in the ATLAS inner tracker (longitudinal view). In the upper figure all the charged particles are shown, while in the lower one a cut $p_T > 25$ GeV was applied and the final state muons of the Higgs decay are visible.*

1.1.1 Overview of the LHC detectors

As is shown in Figure 1.1, the LHC's beams will cross in four interaction points; in order to exploit the full discovery potential of the collider, two general purpose experiments (ATLAS "A Toroidal Lhc ApparatuS" [7] and CMS "Compact Muon Solenoid" [9]), and two specialized experiments (LHCb "LHC beauty" [10]) and (ALICE "A Large Ion Collider Experiment" [11]) has been planned and built. The ATLAS detector is described in details in Section 1.2.

- **ALICE** will study the collisions between ionized lead ions. The goal is to investigate the behaviour of the nuclear matter at very high energy and density, and in particular will explore the formation of the quark-gluon plasma[3] that is expected to be produced in the heavy-ion collisions.

[3] A new state of the matter that was present in the first universe, and that is characterized by so high density and temperature to avoid bounded states of quarks.

- **LHCb** is optimized for B-physics studies; it will study the CP violation, using B-mesons coming from pp collisions. These mesons are expected to be produced at high η, near the incoming beam. The experiment is built in the LEP's DELPHI experimental cavern, and it is an one-arm open-geometry forward collider detector, covering high pseudorapidity regions.

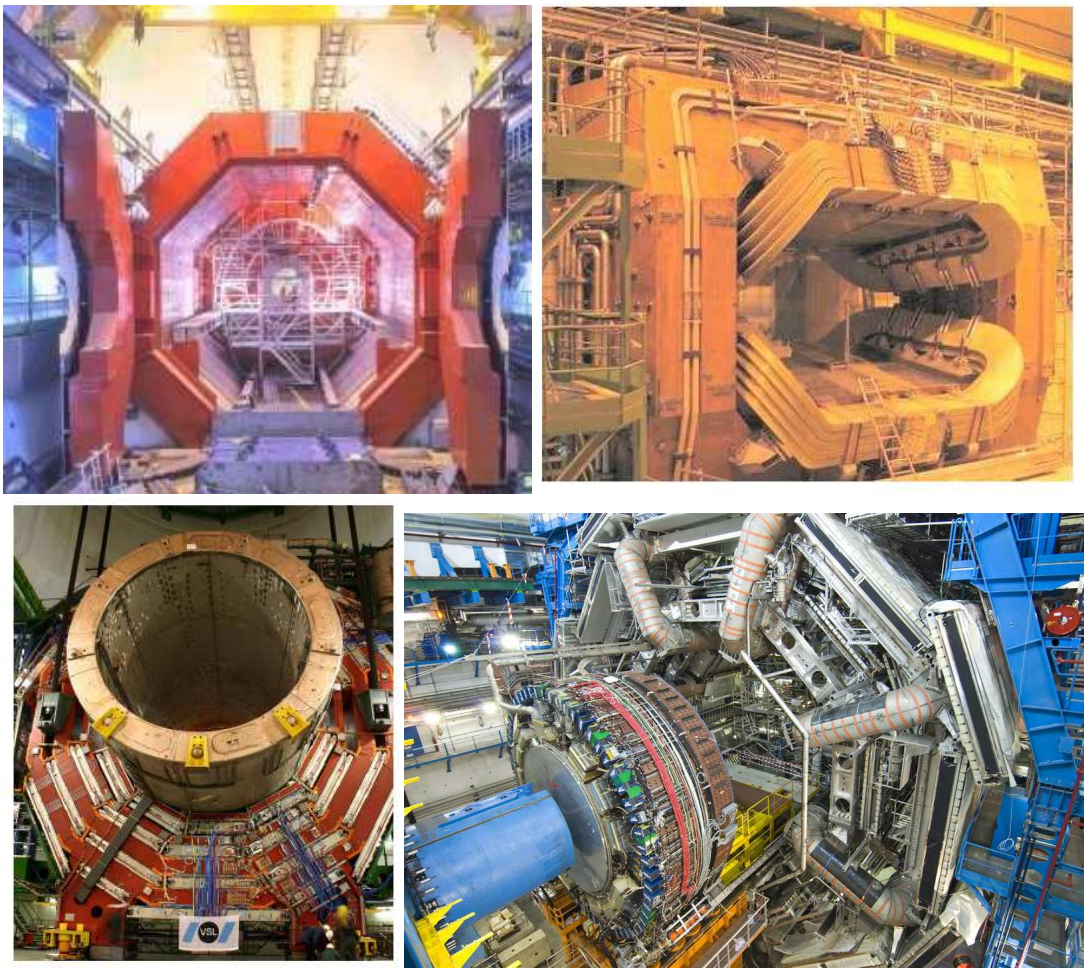

Figure 1.5: *Pictures of the four LHC experiments: ALICE (top left), LHCb (top right), CMS (bottom left) and ATLAS (bottom right) [14].*

- **CMS** has, like ATLAS, the "onion like" structure characteristic of a general purpose experiment. The main difference, with respect to ATLAS, is in the muon spectrometer. They use complementary techniques. In ATLAS, the magnetic field is toroidal and in air in order to achieve a really good muon spectrometer performance, due to the small Coulomb scattering; CMS has a single superconducting solenoidal magnet generating an uniform magnetic field of 4T, and the return joke of the B field

is done in iron. In this way CMS has a better tracking performance in the inner detector, due to the higher magnetic field, but a worse muon spectrometer.

All of these experiments have been installed and commissioned with cosmic rays (for ATLAS see Chapter 2), and they are ready to record the firsts LHC collision data in Autumn 2009.
Given the physics programme, described in details in Chapter 4, that the two general purpose experiments has been projected to achieve, the main physics performance requirements of ATLAS and CMS can be summarized as follows:

- Leptons should be identified and measured over the p_T range from a few GeV (soft leptons produced in the decays of B-hadrons) to a few TeV (heavy particles decaying into leptons, *e.g.,* additional gauge bosons W' and Z').

- Very good electromagnetic calorimeter for electron and photon identification and measurements; the granularity must be high enough to allow the reconstruction of the $H \rightarrow \gamma\gamma$ decay.

- Calorimetry should hermetically cover the full azimuthal angle and as much as possible of the pseudorapidity region (see Section 1.2.1). This is required mainly for a reliable measurement of the missing transverse energy, which is in turn needed to obtain information about weakly interacting particles as neutrinos, LSPs, etc. A large calorimetric coverage is also needed to detect the forward jets produced in association with heavy Higgs boson.

- Efficient vertex tagging, in order to provide secondary vertex information necessary for the reconstruction of B-hadron decay, for the tagging of b - jets, for the recognition of events containing the τ lepton ($H^{\pm} \rightarrow \tau\nu_{\tau}$, $A \rightarrow \tau\tau$) and for the study of $t\bar{t}$ events.

- Excellent electron-jet and photon-jet separation capabilities. In order to observe a possible $H \rightarrow \gamma\gamma$ signal over the background jets faking electrons should be rejected by a factor of 10^6.

- Triggering at LHC will be much more difficult than at the present machines. The interaction rate of 10^9 events/s must be reduced to about 100 recorded events per second, which is an affordable rate of events for permanent storage and further analysis. Therefore, a very selective and at the same time efficient trigger, providing a rejection of $\sim 10^7$, is needed. Excellent particle identification capabilities are needed already at the trigger stage, in order to extract efficiently the interesting physics signal while reducing the large QCD backgrounds down to acceptable rates.

1.1.2 The LHC start-up and plans

The LHC rings were fully cold by mid August 2008; from that period the final commissioning phase started: continued powering tests and injection tests, consolidation and machine checkout were done, in preparation for beam. The beam commissioning was done for one of the eight sectors per time, until the 10th of September 2008, when the two protons beams were circulating to the entire LHC rings and passed through all the four experiments for the first time. The main steps of beam commissioning are shown in Figure 1.6 with a picture of the LHC beam, as seen from beam monitors during the start-up.

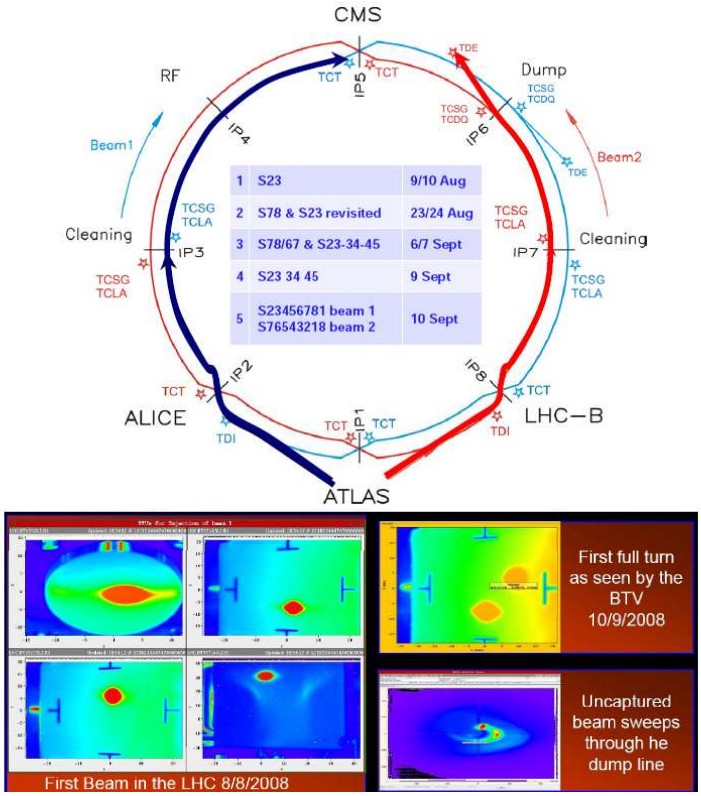

Figure 1.6: *Injection tests of the two beams in the LHC sectors during 2008 and screen shots of the LHC beam monitors during the start-up day.*

Initial beam commissioning progressed extremely well; however, on the 19th September 2008, during the commissioning of the last bend circuit, an accident occurred in sector 3-4, provoking a destructive release of a large volume of Helium from the magnet cold mass into the insulation vacuum of the sector. After a period in which the temperature in the zone of the accident rose close to room temperature, inspections started and was possible to establish the cause of the accident. Investigations [12] have shown that a faulty electrical connection between two magnets was the cause of the accident (Figure 1.7). This provoked the melting of the material surrounding the splice, and

subsequently an electric arc developed between the two exposed cable ends. This arc melted through the Helium line in which the cable travels, releasing Helium into the insulation vacuum of the interconnect. The rapid and voluminous expansion of the Helium caused a pressure wave that propagated along the insulation vacuum, causing physical displacement and extensive damage to about 50 magnets, for a total length of about 700 m.

Besides the mechanical damages itself, soot and debris of superinsulation were spread inside the beam and insulation vacuum. Such a scenario was never considered as realistic in the past. Fortunately, compared to the damage to the magnets there was very limited damage to the infrastructure after the accident (tunnel concrete, cables, etc.) and to other equipment (electronics, instrumentation). This accident lead to a sudden long shut-down of the machine, during which LHC has necessitated a full-scale repair. Among them there was the removal, repair and re-installation of 53 magnets, the repair of the cryogenic line and the cleaning of the beam vacuum etc. New systems, like new quench detectors, have also been installed to monitor the LHC closely and to ensure that similar accidents cannot happen again. Finally, extra pressure relief valves have been installed[4] to release Helium in a safe and controlled manner if there will be any leaks inside the LHC cryostat at any time.

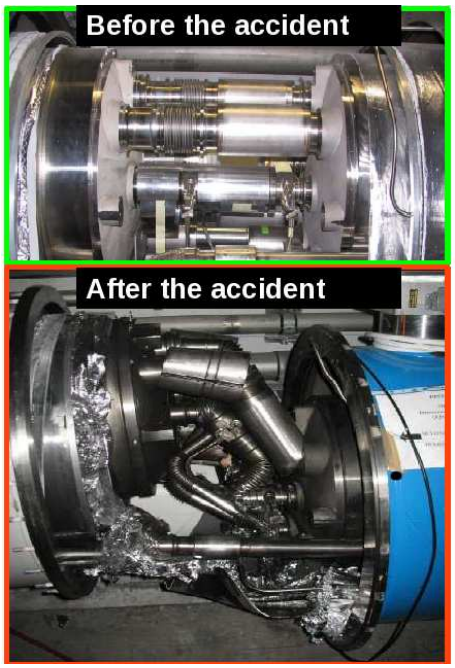

Figure 1.7: *Picture of the magnet connection that caused the accident, before and after it.*

According to simulations, a splice developing a resistance of 50-100 nΩ is regarded as potentially dangerous at high currents such the ones delivered by superconducting magnets; different techniques to detect splices with potentially dangerous resistance have hence been developed.
All these operations lasted until the Summer 2009; the last replaced magnet was lowered into the tunnel the 30th of April 2009, and at the beginning of September 2009 the cool-down of the last repaired sector started.
At the time of writing, the procedure for the 2009 start-up will be to inject and capture beams in each direction, to take collision data for a few shifts at the injection energy (450 GeV), and then commission the ramp to higher

[4]These valves have been installed only on the four sectors that have been warmed up during the 2009 shut-down, the remaining sectors will be equipped with them in the long 2010 shut-down.

energy. The first high-energy data should be collected a few weeks after the first beam of 2009 is injected. The LHC will run at 3.5 TeV per beam until a significant data sample has been collected and the operations team has gained experience in running the machine. In fact, detailed analysis of the resistance data from the entire ring determined that this energy should be safe for the beginning. Thereafter, with the benefit of that experience, the energy will be taken towards 5 TeV per beam. At the end of 2010, the LHC will be run with lead ions for the first time. After that, the LHC will shut-down and work will begin on moving the machine towards 7 TeV per beam.
Finally, on the 20th of November 2009, the LHC managed to be operational again, after the long shutdown, with circulating beams on the machine.

Figure 1.8: *The monitor in the ATLAS control room announcing the 2009 LHC start-up in ATLAS.*

A couple of days after, on the 23th, with great excitement of all the CERN community, the first 900 GeV collisions were recorded by the four LHC experiments, as is shown on the event displays of Figure 1.9.

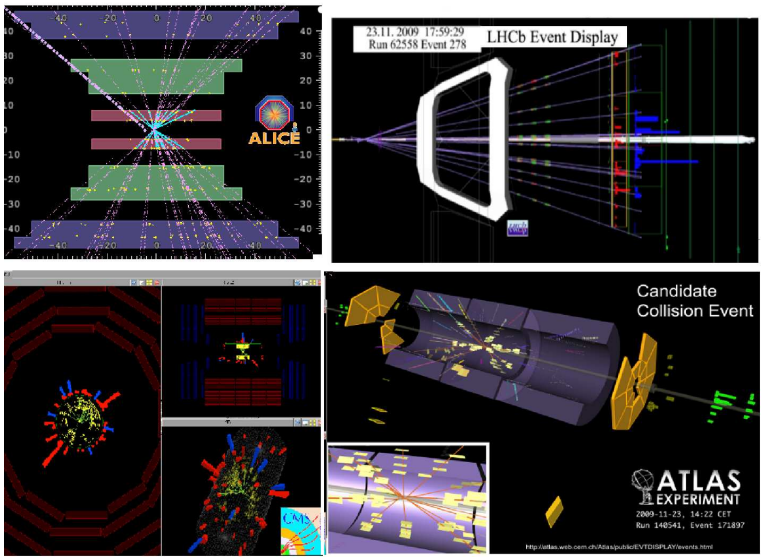

Figure 1.9: *Event displays of the first LHC collisions in the four experiments.*

Other important milestones on the road to first physics at the LHC in 2010 have been set the 30th of November 2009, and the 8th of December 2009. In

these dates LHC has become the world's highest energy particle accelerator, having accelerated its twin beams of protons to an energy of 1.18 TeV and having colliding them a week later. During the time of writing the LHC is going through its commissioning procedure with circulating beams, it has run with solenoid magnets in the ALICE, ATLAS and CMS detectors turned up to full field. A couple of weeks of collisions at 900 GeV have been taken with stable beam conditions and four proton bunches per beam, and also a couple of days with collisions at 2.36 TeV.

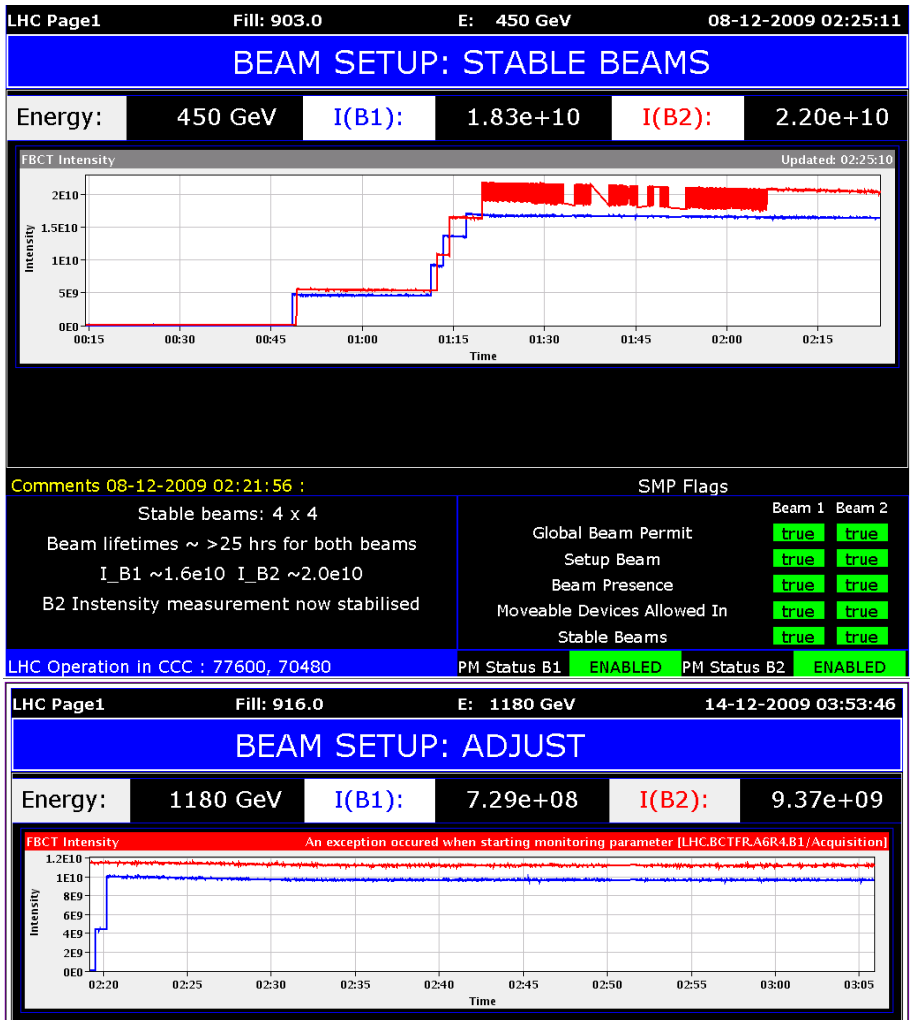

Figure 1.10: *The LHC operational page that gives informations about beam conditions. In this page the beam energy and intensity are shown. On the top: stable beams conditions with 4×4 bunches at 450 GeV, on the bottom: "adjusting" beam conditions at 1180 GeV.*

In Figure 1.10 two screen-shots of the LHC operational page that gives informations about beam conditions are shown, both for the beam stable condition at 450 GeV per beam, that for 1180 GeV energy. The beam stable condition for this energy has, however, not yet been reached.

1.2 The ATLAS detector

As described in the section above, the high interaction rates, radiation doses, particle multiplicities and energies, as well as the requirements for precision measurements have set new standards for the design of particle detectors at LHC. The overall ATLAS detector layout [7, 69] is shown in Figure 1.11 and its main performance goals are listed in Table 3.1.

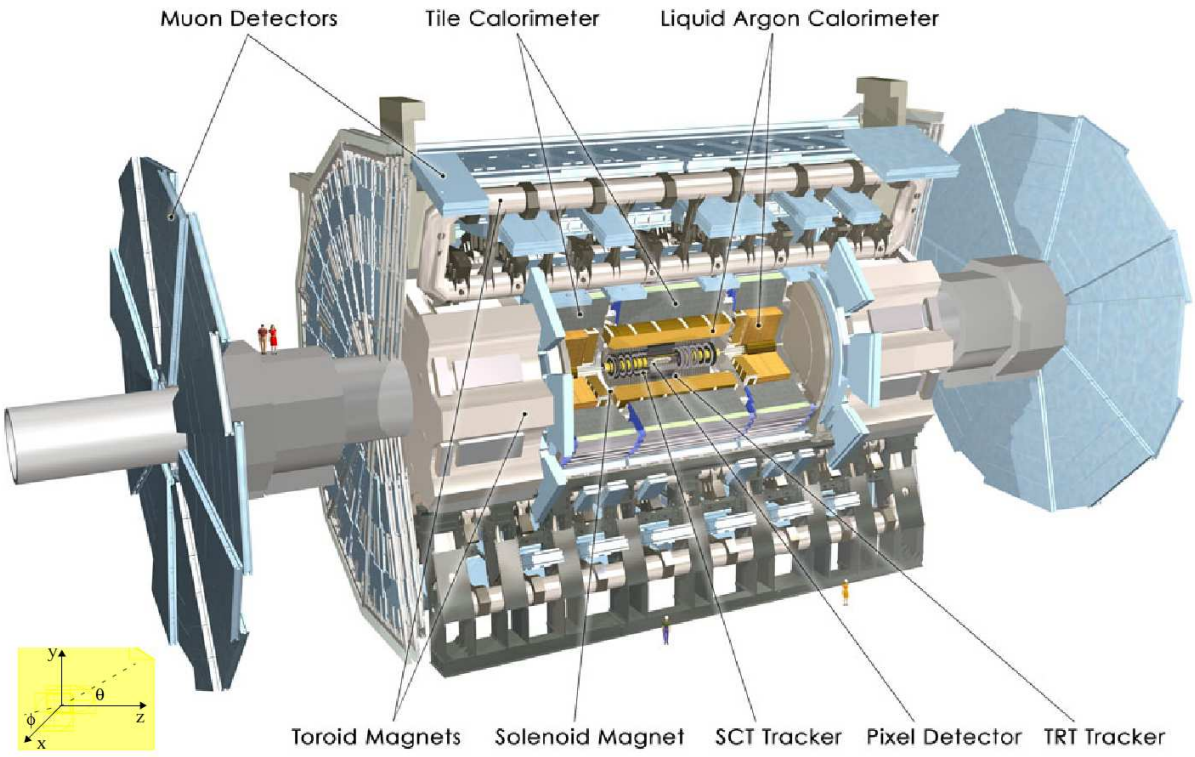

Figure 1.11: *The ATLAS experiment.*

Detector component	**Required resolution**	**η coverage**	**Trigger coverage**
Tracking	$\sigma_{p_T}/p_T = 0.05\%\ \mathrm{p}_T \oplus 1\%$	± 2.5	
EM calo	$\sigma_E/E = 10\%/\sqrt{E} \oplus 0.7\%$	± 3.2	± 2.5
HAD calo			
barrel, end-cap	$\sigma_E/E = 50\%/\sqrt{E} \oplus 3\%$	± 3.2	± 3.2
forward	$\sigma_E/E = 100\%/\sqrt{E} \oplus 10\%$	$\lvert\eta\rvert \in [3.1, 4.9]$	$\lvert\eta\rvert \in [3.1, 4.9]$
Muon spectr	$\sigma_{p_T}/p_T = 10\%$ at 1TeV	± 2.7	± 2.4

Table 1.2: *General performance goals of the ATLAS detector. Units for E and p_T are in GeV.*

The magnet configuration, described in details in Section 1.6, includes a thin superconducting solenoid surrounding the inner detector cavity, and three large superconducting air-core toroids arranged with an eight-fold azimuthal symmetry in the muon spectrometer, around the calorimeters. This fundamental choice drove the design of the rest of the detector. The air-core toroid system is characteristic of the ATLAS experiment, with a long barrel and two inserted end-cap magnets, and generates strong bending power in a large volume within a light and open structure. Multiple-scattering effects are therefore minimised, and excellent muon momentum resolution is achieved with three layers of high precision tracking chambers (Section 1.5). The muon instrumentation includes also, trigger chambers with timing resolution of few ns. The muon spectrometer defines the overall dimensions of the ATLAS detector ($\sim 44 \times 25$ m). The inner detector is described in Section 1.3; pattern recognition, momentum and vertex measurements, and electron identification are achieved with a combination of discrete, high-resolution semiconductor pixel and strip detectors in the inner part of the tracking volume, as well as straw-tube tracking detectors with the capability to generate and detect transition radiation in its outer part. The calorimetry system, described in Section 1.4, is composed by high granularity liquid-argon (LAr) electromagnetic sampling calorimeters, with excellent performance in terms of energy and position resolution. The hadronic calorimetry is provided by a scintillator-tile calorimeter, which is separated into a barrel part and two extended barrel cylinders, one on either side of the central barrel. In the end-caps LAr technology is also used for the hadronic calorimeters.
The proton-proton interaction rate at the design luminosity of 10^{34} cm^{2}s^{-1} is approximately 1 GHz, while the event data recording, based on technology and resource limitations, is limited to about 200 Hz. This requires an overall rejection factor of $5{\times}10^6$ against minimum-bias processes while maintaining maximum efficiency for the new physics and Standard Model precision measurements. A three-level trigger system (Section 1.9) has been designed to reduce this rate down to the level at which only interesting events are fully reconstructed.

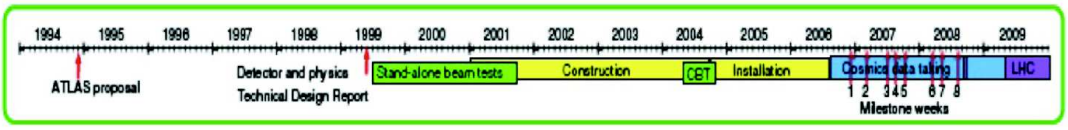

Figure 1.12: *The ATLAS experiment history.*

The ATLAS experiment is a very complex mixing of different detector technologies, and it took a very long period (almost 15 years) for their design and construction. As is shown in Figure 1.12 the official proposal of the ATLAS experiment was on 1994; then there were many years of construction of pro-

totypes and test beam for specific subdetectors until the 2004 when there was the combined test beam that involved almost all the detector technologies. From the year 2000 many institutes from all over the world were involved on the production of all the detectors, and also Pavia has contributed with the construction of 56 muon drift chambers. At the end of 2004 it started the long and complex phase of the installation of the experiment and related services (Section 1.10), that was concluded in 2008, in view of the first LHC beam. From 2005 the commissioning phase of all the installed detectors started, and was done in parallel with the installation of the remaining parts. In Chapter 2 is described the commissioning phase of the MDT chambers both with cosmic rays and with the first LHC beam data.

1.2.1 Coordinate System

The coordinate system and nomenclature used for describing the ATLAS detector and the particles emerging from the *pp* collisions are briefly summarised here.

The beam direction defines the z-axis and the x-y plane is transverse to the beam direction. The positive x-axis is defined as pointing from the interaction point to the centre of the LHC ring and the positive y-axis is defined as pointing upwards. The side-A of the detector is defined as the one with positive z and side-C is the one with negative z. The azimuthal angle ϕ is measured around the beam axis, and the polar angle θ is the angle from the beam axis. The pseudorapidity is defined as:

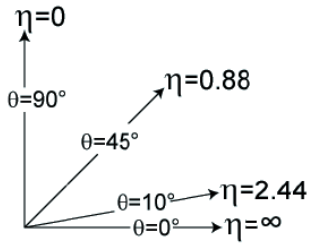

Figure 1.13: *Psudorapidity η as a function of the angle θ.*

$$\eta = -ln[tan(\theta/2)] \tag{1.5}$$

The transverse momentum p_T, the transverse energy E_T, and the missing transverse energy E_T^{miss} are defined in the x-y plane unless stated otherwise. The distance ΔR in the pseudorapidity-azimuthal angle space is defined as

$$\Delta R = \sqrt{\Delta\eta^2 + \Delta\phi^2} \tag{1.6}$$

1.3 Inner Detector

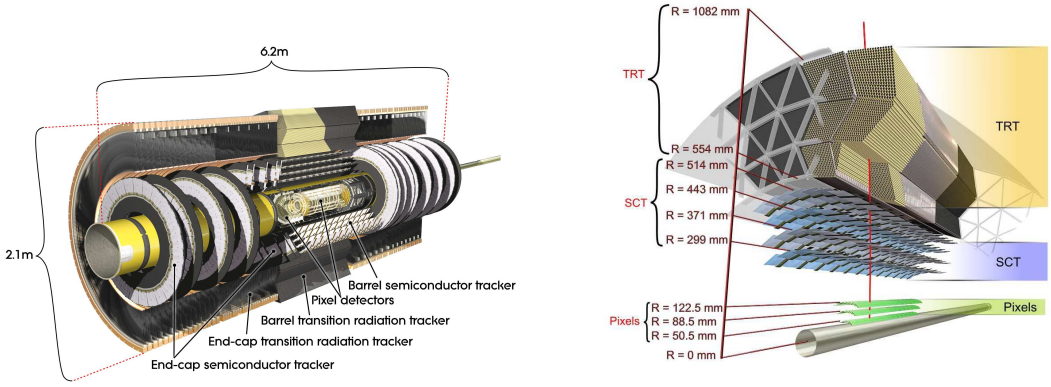

Figure 1.14: *Three dimensional views of the ATLAS Inner Detector.*

The ATLAS Inner Detector (ID) is designed to provide hermetic and robust pattern recognition, excellent momentum resolution and both primary and secondary vertex measurements for charged tracks above a given p_T threshold (nominally 0.5 GeV), and within the pseudorapidity range $|\eta| < 2.5$. It also provides electron identification over $|\eta| < 2.0$

The Inner Detector, whose three dimensional view is shown in Fig. 1.14, is 7 m long, has a radius of 115 cm and is contained inside the superconducting solenoid magnet (2T). It consists of three parts: the barrel region, covering the central pseudorapidity region ($|\eta| \leq 1$, ± 80 cm from the collision point), in which the sensors are arranged in concentric cylinders around the beam axis, and two end-cap regions, covering the gap $1 \leq |\eta| \leq 2.5$, with disks perpendicular to the beam axis.

The momentum and vertex resolutions, needed in the high track density environment expected at LHC, require high precision measurement to be made by fine granularity detectors. This leads to the choice of the silicon semiconductor technology: pixel detectors close to the interaction region and silicon strips in the outer part. Due to the significant amount of material introduced by the silicon trackers and because of their cost, to obtain a large number of tracking points required for the pattern recognition, straw tube trackers are used at higher radii. This allows continuous track following with much less material and a lower cost.

These three detectors are independent and complementary; the combination of the three techniques offers very robust pattern recognition and high precision in both ϕ and z coordinates. High p_T tracks emerging from the interaction point cross (see Fig.1.14) first of all the beam pipe (1 mm of beryllium with a radius of 2.5 cm), then at least three pixel layers, four double silicon strips planes (SCT, Semi-Conductor Tracker) and about 36 straw tubes of the Tran-

sition Radiation Tracker (TRT). The TRT allows also electron identification complementary to that of the calorimeter.

Pixel Detector

The system consists of three barrels at average radii of 4, 10, 13 cm and five disks on each side between radii 11 and 20 cm along the beam line, to complete the angular coverage.
The pixel detector is designed to provide a very high granularity, high precision set of measurements as close to the interaction point as possible. The system provides three precision measurements over all its pseudorapidity range, and determines the impact parameter resolution and the ability of the Inner Detector to find short lived particles such as B hadrons and τ leptons.
The two dimensional segmentation of the sensors gives space points without any of the ambiguities associated with crossed strip geometry, but requires the use of advanced electronic techniques for the readout.
All pixel sensors are identical and have a minimum pixel size of 50×400 μm^2. The pixel layers are segmented in R-ϕ and z. The intrinsic accuracies are 10 μm ($R\phi$) and 115 μm (z for the barrel and R for the end-cap disks). The pixel detector has approximately 80 million readout channels, which are invaluable for the pattern recognition in the crowded environment of the LHC.
The first detector layer (called B-layer) is placed as close as possible to the beam line (about 4 cm from the interaction point), and is very important for impact parameter measurements and vertexing for heavy-flavour and τ lepton tagging. It was originally intended for the low luminosity phase only, now, however, in order to maintain adequate tracking performances, has been proposed to replace it after approximately three years of operation at design luminosity.

Semi-Conductor-Tracker (SCT)

The SCT detector is placed at intermediate radii range and is planned to provide eight precision position measures per track in the intermediate radial range, contributing to the measurement of momentum, impact parameter and vertex position, as well as providing good pattern recognition thanks to the high granularity.
It consists of four concentric barrel layers positioned between radii 30 and 52 cm and 9 disks on either side covering the required pseudorapidity range. The basic element is composed by two detectors bonded together edge-to-edge. The innermost detector is given a relative rotation (stereo angle) of 40 mrad which respect to the outermost, which lies with its long axis parallel to the beam pipe. They consist of two 6.4 cm long daisy-chained sensors with a strip pitch of 80 μm. In the end-cap region, the detectors have a set of trapezoidal strips running radially and a set of stereo strips at an angle of 40 mrad. The mean pitch of the strips is also approximately 80 μm. The intrinsic accuracies per module in the barrel are 17 μm ($R\phi$) and 580 μm (z), and in the disks

are 17 μm ($R\phi$) and 580 μm (R). The total number of readout channels in the SCT is approximately 6.3 million.

Transition Radiation Tracker (TRT)

The TRT is composed by straw tube detector (drift chambers), interleaved with material which provides transition radiation for electron identification. The tubes are filled with a mixture containing Xenon to detect these photons. The straws are 65 μm thick Kapton tubes and have an internal diameter of only 4 mm to limit the occupancy. The detector consists of a central section which has a barrel geometry for $|\eta| \leq 0.8$ and two end-cap sections consisting of multi-plane wheels at higher $|\eta|$. The barrel region has a total of 73 layers of axial straw tubes (parallel to the beam axis) and extends from an inner radius of 56 cm to an outer radius of 107 cm.
The two end-caps have 18 wheels of radially oriented straw tubes, the first 14 nearest the interaction point cover a radius of 64 to 102 cm and the last four wheels extend down to a radius of 48 cm to provide coverage of the full pseudorapidity range.
The total number of TRT readout channels is approximately 351000.
The TRT detector provides typically 36 measurements per track for nearly all pseudorapidity with spatial resolution of 170 μm. This contribute significantly to the momentum measurement, since the lower precision per point, compared to the silicon, is compensated by the large number of measurements and the higher average radius.

1.4 Calorimetry

The ATLAS calorimeters consist of sampling detectors with full ϕ-symmetry and coverage around the beam axis. The calorimeters closest to the beam-line are housed in three cryostats, one barrel and two end-caps. The barrel cryostat contains the electromagnetic barrel calorimeter, other than the solenoid magnet, whereas the two end-cap cryostats each contain an electromagnetic end-cap calorimeter (EMEC), a hadronic end-cap calorimeter (HEC), ($1.5< |\eta| < 3.2$) located behind the EMEC, and a forward calorimeter (FCal) to cover the region closest to the beam ($3.1< |\eta| < 4.9$). All these calorimeters use liquid argon as the active detector medium; liquid argon has been chosen for its in-

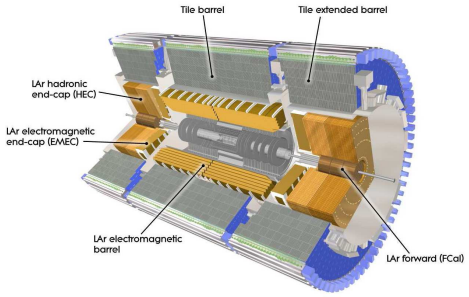

Figure 1.15: *The calorimeter system.*

trinsic linear behaviour, its stability of response over time and its intrinsic radiation-hardness.
Fig. 1.15 gives an overview of the ATLAS calorimeter system.
These calorimeters cover the range $|\eta|<4.9$, using different techniques suited to the widely varying requirements of the physics processes of interest and of the radiation environment over this large $|\eta|$-range. Over the η region matched to the inner detector, the fine granularity of the EM calorimeter is ideally suited for precision measurements of electrons and photons. The coarser granularity of the rest of the calorimeter is sufficient to satisfy the physics requirements for jet reconstruction and E_T^{miss} measurements.
The total thickness of the EM calorimeter is greater than 22 radiation lengths (X_0) in the barrel and than 24 X_0 in the end-caps. The approximate 9.7 interaction lengths (λ) of active calorimeter in the barrel (10 λ in the end-caps) are adequate to provide good resolution for high-energy jets. Together with the large η-coverage, this thickness will also ensure a good E_T^{miss} measurement, which is important for many physics signatures and in particular for SUSY particle searches.
The designed energetic resolution of each part of the calorimeter system is given in Table 3.1.

1.4.1 Electromagnetic Calorimeter

The electromagnetic (EM) calorimeter is a LAr detector with accordion-shaped kapton electrodes and lead absorber plates over its full coverage. It is divided into a barrel part ($|\eta|<1.475$) and two end-cap components ($1.375< |\eta| <3.2$).

The accordion geometry provides complete ϕ-symmetry without azimuthal cracks, and a fast extraction of the signal at the rear or at the front of the electrodes. The electrodes are positioned in the middle of the gap by honeycomb spacers. The lead thickness in the absorber plates has been optimised as a function of η in terms of EM calorimeter performance in energy resolution. The accordion waves are perpendicular to the incident particles; in the barrel, they are axial and run in ϕ, and the folding angles of the waves vary with radius to keep the liquid-argon gap constant. In the end-caps, the waves are parallel to the radial direction and run axially. Since the liquid-argon gap increases with radius in the end-caps, the wave amplitude and the folding angle of the absorbers and electrodes vary with radius. All these features of the accordion geometry lead to a very uniform performance in terms of linearity and resolution as a

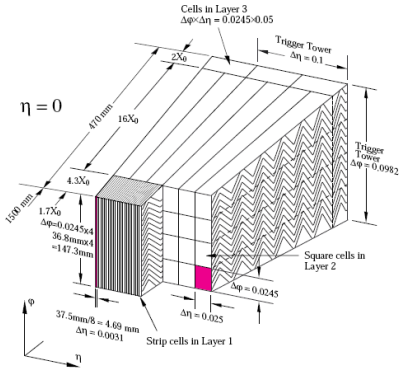

Figure 1.16: *Design of a module of an accordion LAr calorimeter.*

function of ϕ .
Over the region devoted to precision physics ($|\eta| < 2.5$), the EM calorimeter is segmented into three longitudinal sections. For the end-cap inner wheel, the calorimeter is segmented in two longitudinal sections and has a coarser lateral granularity than for the rest of the acceptance.
In the region of $|\eta| < 1.8$, a presampler detector is used to correct for the energy lost by electrons and photons upstream of the calorimeter. The presampler consists of an active LAr layer of thickness 1.1 cm (0.5 cm) in the barrel (end-cap) region.

1.4.2 Hadronic Calorimeters

Tile Calorimeter

The tile calorimeter is placed directly outside the EM calorimeter envelope. Its barrel covers the region $|\eta| < 1.0$, and its two extended barrels the range $0.8 < |\eta| < 1.7$. It is a sampling calorimeter using steel as absorber and scintillating tiles as active material. The barrel and extended barrels are divided azimuthally into 64 modules (Fig. 1.17).

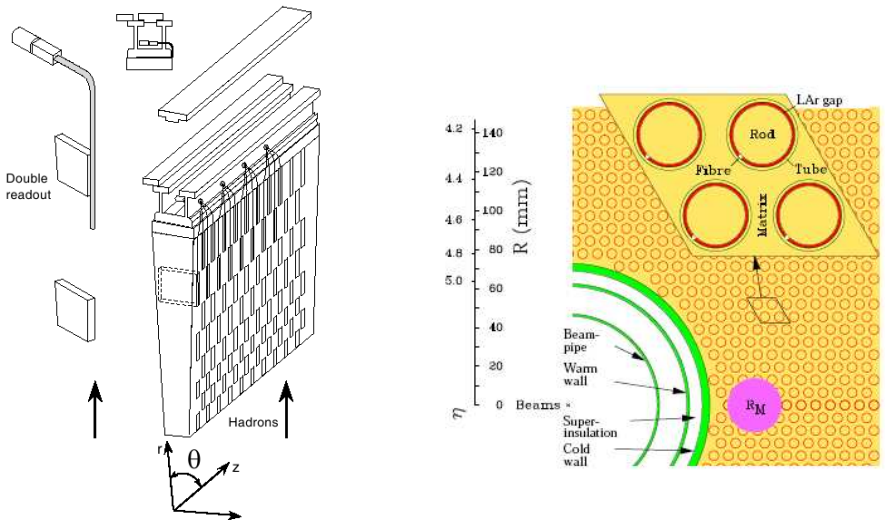

Figure 1.17: *Design of a module of the tile calorimeter (left), and of FCal with the matrix of copper plates and the copper tubes and rods with the LAr gap for the electrodes (right).*

Radially, the tile calorimeter extends from an inner radius of 2.28 m to an outer radius of 4.25 m. It is longitudinally segmented in three layers approximately 1.5, 4.1 and 1.8 interaction lengths thick for the barrel and 1.5, 2.6, and 3.3 λ for the extended barrel. The total detector thickness at the outer edge of the tile-instrumented region is 9.7 λ at $\eta = 0$. The tiles are 3 mm thick and the

total thickness of the steel plates in one period is 14 mm. Two sides of the scintillating tiles are read out by wavelength shifting fibres into two separate photomultiplier tubes. In η, the readout cells built by grouping fibres into the photomultipliers are pseudo-projective towards the interaction point. The resulting granularity is $|\Delta\ \eta\ \times\ \Delta\ \phi| \sim 0.1 \times 0.1$.

LAr hadronic end-cap calorimeter (HEC)

The hadronic end-cap calorimeter (HEC) is a copper/liquid-argon sampling calorimeter with a flat plate design, which covers the range $1.5 < |\eta| < 3.2$ and is integrated in the same cryostat that contains the EM and FCal. The HEC consists of two cylindrical wheels, with a radius of 203 cm, in each end-cap cryostat, each wheel containing two longitudinal sections. Each of the four HEC wheels is constructed by 32 identical wedge-shaped modules. The modules of the front wheels are made of 24 copper plates, 25 mm thick each, plus a 12.5 mm thick front plate. In the rear wheels, the sampling fraction is coarser with modules made of 16 copper plates, 50 mm thick each, plus a 25 mm thick front plate. The copper plates are interleaved with 8.5 mm LAr gaps, providing the active medium for this sampling calorimeter. The resulting sampling fractions for the two wheels are 4.4% and 2.2% respectively. Three electrodes divide the 8.5 mm gaps into four separate LAr drift zones, 1.8 mm width each, individually supplied with high voltage. The readout cells are defined by pads etched on the central foil in each gap. The arrangement of these pads provides a semi-pointing geometry. The size of the readout cells is $\Delta\eta \times \Delta\phi \sim 0.1 \times 0.1.$ in the region $|\eta| < 2.5$ and 0.2×0.2 for larger values of pseudorapidity.

LAr forward calorimeter (FCal)

The FCal is a particularly challenging detector due to the high level of radiation it has to cope with. It is integrated into the end-cap cryostats, and provides coverage in pseudorapidity of $3.1<|\eta|<4.9$. In order to reduce the amount of neutron albedo in the inner detector cavity, the front face of the FCal is recessed by about 1.2 m with respect to the EM calorimeter front face. The FCal is approximately 10 interaction lengths deep, and consists of three modules in each end-cap: the first, made of copper, is optimised for electromagnetic measurements, while the other two, made of tungsten, measure predominantly the energy of hadronic interactions. Each module consists of a metal matrix, with regularly spaced longitudinal channels, with the electrode structure consisting of concentric rods and tubes parallel to the beam axis. The LAr in the gap between the rod and the tube is the sensitive medium. This geometry allows for excellent control of the gaps, which are as small as 0.25 mm in the first section, in order to avoid problems due to ion buildup.

1.5 Muon Spectrometer

The muon spectrometer (MS) forms the outer part of the ATLAS detector and it is designed to detect muons exiting the barrel and end-cap calorimeters and to measure their momentum in the pseudorapidity range $|\eta| < 2.7$. It is also designed to trigger on these particles in the region $|\eta| < 2.4$. The driving performance goal is a stand-alone transverse momentum resolution of approximately 10% for 1 TeV tracks, which translates into a sagitta along the z (beam) axis of about 500 μm, to be measured with a resolution of less then 50 μm. Muon momenta from few GeV ($\sim$ 5-6 GeV), even to the high end of the accessible range ($\sim$ 3 TeV), may be measured by the spectrometer in stand-alone, that provide adequate momentum resolution and excellent charge identification. The lower limit in momentum of muons entering in the muon spectrometer is about 3 GeV; muons with lower momentum are in fact absorbed by the calorimeter.

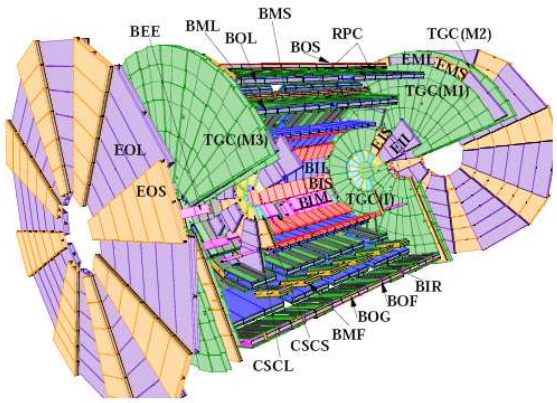

Figure 1.18: *Schematic view of the ATLAS muon spectrometer with all the chamber typologies: the precision measurement tracking chambers (MDT and CSC) and the trigger chambers (RPC and TGC). The first letter (B and E) of the MDT naming scheme refers to barrel and end-cap chambers, respectively. The second and third letters refer to layer (inner, middle, and outer) and sector (large and small) types, respectively.*

Precision-tracking chambers in the barrel region are located between and on the eight coils of the superconducting barrel toroid magnet, while the end-cap chambers are in front and behind the two end-cap toroid magnets. The ϕ symmetry of the toroids is reflected in the symmetric structure of the muon chamber system, consisting of eight octants.
Barrel chambers are of rectangular shape and arranged cylindrically around the beam pipe; end-cap chambers are trapezoidal and arranged in planes orthogonal to the beam pipe. The chambers in the barrel are arranged in three concentric cylindrical shells around the beam axis at radii of approximately 5 m, 7.5 m and 10 m. The end-cap chambers are arranged in four disks on

each side of the interaction point perpendicular to the beam axis, located at distances of |z| ∼ 7.4 m, 10.8 m, 14 m, and 21.5 m from the interaction point. Figure 1.18 shows the overall layout of the muon system[5], while the table shown in Figure 1.19 gives an overview of the main parameters of the sub-systems of the muon detector.

		Chamber resolution (RMS) in			Measurements/track		Number of	
Type	**Function**	z/R	ϕ	time	barrel	end-cap	chambers	channels
MDT	tracking	35 μm (z)	–	–	20	20	1088 (1150)	339k (354k)
CSC	tracking	40 μm (R)	5 mm	7 ns	–	4	32	30.7k
RPC	trigger	10 mm (z)	10 mm	1.5 ns	6	–	544 (606)	359k (373k)
TGC	trigger	2–6 mm (R)	3–7 mm	4 ns	–	9	3588	318k

Figure 1.19: *Parameters of the four sub-systems of the muon detector. Numbers on brackets refer to the complete detector configuration.*

Four chamber technologies are employed in the ATLAS muon spectrometer. The precision momentum measurement is performed by the **Monitored Drift Tube chambers (MDT)**; they cover the pseudorapidity range $|\eta|<2.7$ (except in the inner most end-cap layer where their coverage is limited to $|\eta|<2.0$). In the forward region ($2<|\eta|<2.7$) **Cathode-Strip Chambers (CSC)** are used in the innermost tracking layer due to their higher rate capability and time resolution.
The precision-tracking chambers have been complemented by a system of fast trigger chambers with an excellent time resolution, lower than few tens of nanoseconds. In the barrel region ($|\eta|<1.05$), three layer of **Resistive Plate Chambers (RPC)** were adopted for this purpose, while in the end-cap ($1.05<|\eta|<2.4$) four layers of **Thin Gap Chambers (TGC)** were chosen.
The purpose of the precision-tracking chambers is to determine the coordinate of the track in the bending plane. After matching of the MDT and trigger chamber hits in the bending plane, the trigger chamber coordinate in the non-bending plane is adopted as the second coordinate of the MDT measurement[6].

[5]In the centre of the detector ($|\eta| \sim 0$), a gap in chamber coverage has been left open to allow for services to the solenoid magnet, the calorimeters and the inner detector. The size of the gap varies from sector to sector depending on the service necessities, the biggest gaps of 1-2 m being located in the large sectors. The angular range, seen from the interaction point, where a high momentum (straight) track is not recorded in all three muon layers due to the gaps is about $\pm 4.8^\circ$ ($|\eta| \leq 0.08$) in the large and $\pm\ 2.3^\circ$($|\eta| \leq 0.04$) in the small sectors. Additional gaps in the acceptance occur in sectors 12 and 14 due to the detector support structure (feet).

[6]This method assumes that in any MDT/trigger chamber pair a maximum of one track per event be present, since with two or more tracks the η and ϕ hits cannot be combined in

To achieve an high sagitta resolution, the locations of MDT wires and CSC strips along a muon trajectory must be known to better than 30 μm. To this effect, a high-precision optical alignment system, monitors the positions and internal deformations of the MDT chambers, as described in Chapter 2; it is also complemented by track-based alignment algorithms.
In the following, each of the four muon spectrometer technologies is briefly reviewed, a part from the MDTs to which the next chapter is fully dedicated.

Cathode-Strip Chambers (CSC)

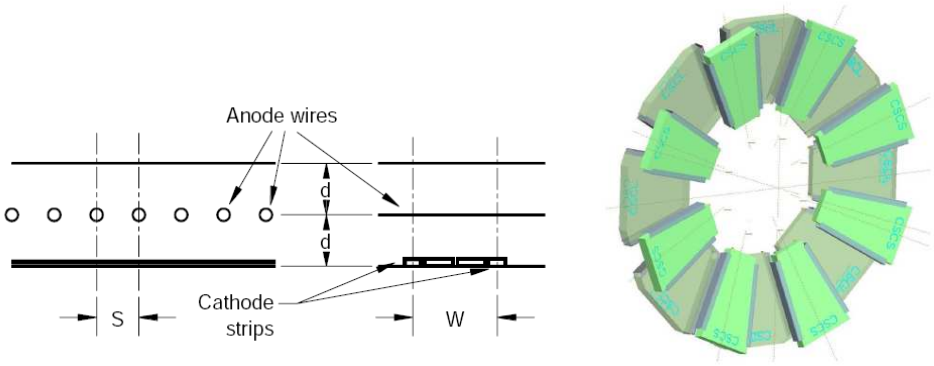

Figure 1.20: *Cross section of a CSC and layout of an end-cap CSC wheel with 8 small and 8 large chambers.*

As already seen, cathode strip chambers (CSC) are employed in the ATLAS Muon Spectrometer in the very forward pseudorapidiy range (η = 2.0-2.7) in the first end-cap layer. There are 32 CSCs in total, 16 chambers on either detector side. As in the case of the MDTs, the CSCs are segmented into large and small chambers in ϕ. The whole CSC system consists of two disks with eight chambers each (eight small and eight large) as shown in Fig. 1.20. Each chamber contains four CSC planes resulting in four independent measurements in η and ϕ along each track.
The CSC are multiwire proportional chambers with both cathode planes segmented into strips in orthogonal directions; one with the strips perpendicular to the wires (providing the precision coordinate) and the other parallel to the wires, providing the transverse coordinate. The position of the track is obtained by interpolation between the charges induced on neighbouring cathode strips. With a readout pitch of 5.08 mm in the bending direction, the CSC

an unambiguous way. Simulations have shown that the probability of a track in the muon spectrometer with $p_T > 6$ GeV is about 6×10^{-3} per beam-crossing, corresponding to about 1.5×10^{-5} per chamber. Assuming uncorrelated tracks, this leads to a negligible probability to find more than one track in any MDT/trigger chamber pair. When correlated close-by muon tracks do occur, caused for example by two-body-decays of low-mass particles, the ambiguity in η and ϕ assignment will be resolved by matching the muon track candidates with tracks from the inner detector.

reaches a resolution of 60 μm per CSC plane; in the non-bending direction the cathode segmentation is coarser leading to a resolution of 5 mm. The difference in resolution between the bending and non-bending planes is due to the different readout pitch, and to the fact that the azimuthal readout runs parallel to the anode wires.
Operation is considered safe up to counting rates of about 1000 Hz/cm^2, which is sufficient up to the forward boundary of the muon system at $|\eta| = 2.7$ (this rate is much more high than the allowed counting rates of the MDT chambers: about 150 Hz/cm^2).

Resistive Plate Chambers (RPC)

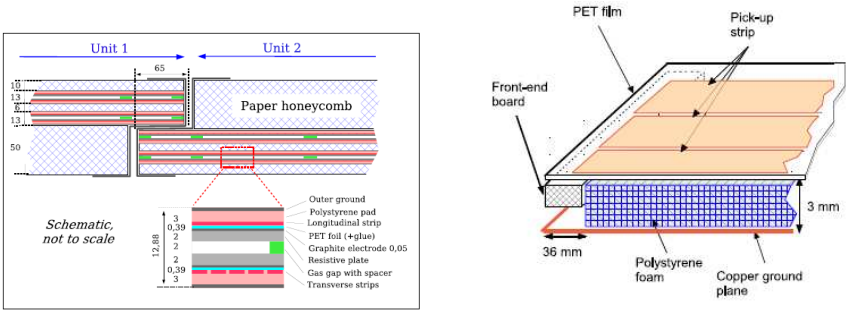

Figure 1.21: *Cross section of an RPC.*

Resistive Plate Chambers (RPC) are employed in the ATLAS Muon Spectrometer as trigger chambers in the barrel. They cover the pseudorapidiy range $|\eta|$ <1.0 and are arranged in three concentric cylindric layers around the beam axis, as shown in Fig.2.6. RPC1 and RPC2 are located directly in front and behind the middle barrel chamber MDTs, RPC3 chambers are located on the outer MDT layer[7].
Each station consists of two independent detector layers, each measuring η and ϕ . A track going through all three stations thus delivers six measurements in η and ϕ. This redundancy in the track measurement allows the use of a 3-out-of-4 coincidence in both projections for the low-p$_T$ trigger (RPC1 and RPC2 stations, see Section 1.9) and a 1-out-of-2 for the high-p$_T$ trigger (RPC3 station). This coincidence scheme rejects fake tracks from noise hits and greatly improves the trigger efficiency in the presence of small chamber inefficiencies.
The RPC is a gaseous parallel electrode-plate (*i.e.,* no wire) detector, and has a typical space-time resolution of 1cm $\times$ 1 ns. Two resistive plates, made of phenolic-melaminic plastic laminate, are kept parallel to each other at a distance of 2 mm by insulating spacers. The electric field between the plates of

[7]In addition to the RPCs that are assembled together with the MDTs into stations, there are some RPCs that are not attached to any MDT.

about 4.9 kV/mm allows avalanches to form along the ionising tracks towards the anode. The signal is read out via capacitive coupling to metallic strips, which are mounted on the outer faces of the resistive plates. The gas used is a mixture of $C_2H_2F_4$:Iso-C_4H_{10}:SF_6 (94.7:5:0.3) and combines relatively low operating voltage (due to the low SF_6 concentration), non-flammability and low cost, while providing a plateau for safe avalanche operation.
The RPC chambers are composed, for the majority of the cases, of two rectangular detectors, contiguous to each other, called units. Figure 1.21 shows the mechanical structure of the RPC units and the way how two RPC units are assembled together to form a chamber, minimising acceptance losses. Each RPC unit is thus made of two detector layers (*i.e.,* gas volumes) and four readout strip panels.

Thin Gap Chambers (TGC)

As the RPCs, Thin Gap Chambers (TGC) provide two functions in the end-cap muon spectrometer: the muon trigger capability and the determination of the second, azimuthal coordinate to complement the measurement of the MDTs in the bending direction. The middle layer of the MDTs in the end-cap is complemented by seven layers of TGCs, arranged in one triplet and two doublets, while the inner layer is complemented by only two layers. End-cap inner TGCs are mounted on support structures of the barrel toroid coils. The TGC chambers, forming circular disks, are mounted in two concentric rings (Fig 1.22), an outer or end-cap one covering the rapidity range $1.05 < |\eta| < 1.92$ and an inner or forward one covering the rapidity range $1.92 < |\eta| < 2.4$.

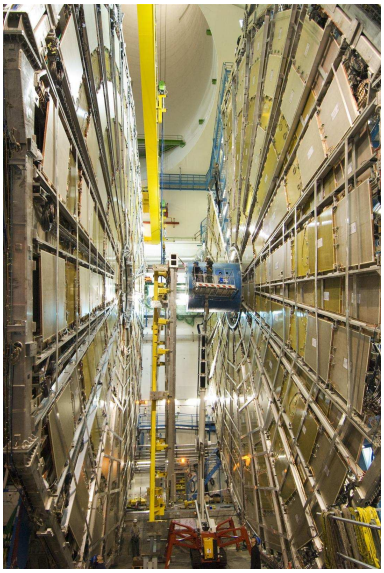

Figure 1.22: *TGC end-cap wheels during the installation phase [14].*

TGCs are Multi Wire Proportional Chambers with the characteristic that the wire-to-cathode distance (1.4 mm) is smaller than the wire-to-wire distance (1.8 mm), see Fig. 1.23. With an highly quenching gas mixture of CO_2 and n - C_5H_{12} (n-pentane), this cell geometry allows for operation in a quasi-saturated mode, *i.e.,* with a gas gain of $\sim 3 \times 10^5$. The high electric field (2900 V) around the TGC wires and the small wire-to-wire distance lead to very good time resolution for the large majority of the tracks; in fact, including the variation of the propagation time on wires and strips, signals arrive with 99% probability inside a time window of 25 ns.
Figure 1.23 shows the cross-section of a TGC triplet and doublet. The structure consists of wire planes (anode), cathode planes, strip planes, shields and

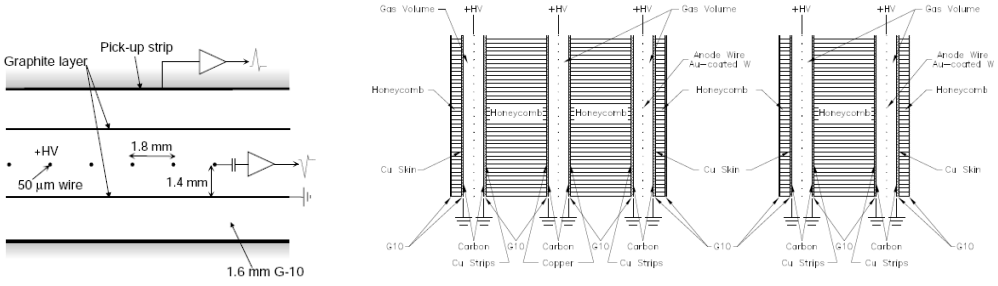

Figure 1.23: *Cross section of an TGC (triple and double modules).*

honeycomb support structures. The cathode planes consist of 1.6 mm thick FR4 (Flame Resistant 4) plates, graphite coated on the inside, *i.e.,* facing the wires, and with copper cladding on the other side. Two of the copper layers in the triplet and doublets are segmented into readout strips to read the azimuthal coordinate ϕ, while anode wires are arranged in the azimuthal direction and provide signals for radius information. The solid copper layers serve as DC grounds, while the segmented ones, being connected to amplifiers, are virtual grounds for the wire signals. All TGC units[8] are enclosed on their periphery by a gas-tight envelope which is continuously flushed by CO_2. This is done to keep a dry atmosphere in the region where the HV elements are located as well as to dilute any potential leak of the operating gas (n-pentane).

1.6 Magnetic System

ATLAS has a unique hybrid system of four large superconducting magnets: a solenoid and a toroid system. The spatial arrangement of the coil windings is shown in Figure 1.24.

Central solenoid

The central solenoid is coaxial with the beam axis and provides a 2 T axial magnetic field for the inner detector. To achieve the desired calorimeter performance, the layout was carefully optimised to keep the material thickness in front of the calorimeter as low as possible, resulting in the solenoid assembly contributing a total of ~ 0.66 radiation lengths. This required, in particular, that the solenoid windings and LAr calorimeter share a common vacuum vessel, thereby eliminating two vacuum walls. The inner and outer diameters of the solenoid are 2.46 m and 2.56 m and its axial length is 5.8 m.

[8] A gas volume containing a wire plane and two cathodes is called a chamber, while the entirety of three or two chambers in a triplet or doublet arrangement is called a unit.

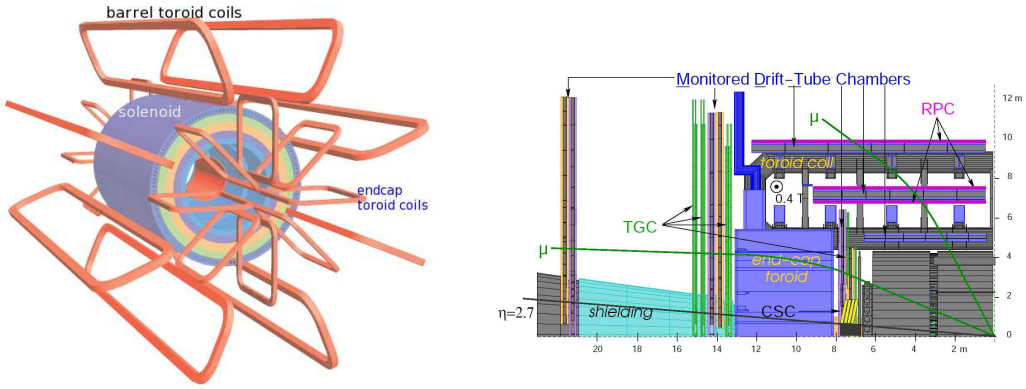

Figure 1.24: *Left: geometry of the ATLAS magnetic system. Right: effects of the magnetic field on the trajectory of the muons passing through the barrel and the end-cap of the muon system [7].*

Toroid

The toroid system consists of three large air-core toroids: two in the end-cap, that provide 1T magnetic field, are inserted at each end of the barrel one that provides 0.5 T. Each of the three toroids consists of eight coils assembled radially and symmetrically around the beam axis. The barrel toroid coils are housed in eight individual cryostats (Fig.1.30), with the linking elements between them providing the overall mechanical stability. The overall size of the barrel toroid system as installed is 25.3 m in length, with inner and outer diameters of 9.4 m and 20.1 m, respectively.
Each end-cap toroid consists of eight racetrack-like coils in an aluminium alloy housing; each of them consists in a single cold mass (Fig 1.29 top). They are supported off and can slide along the central rails, which facilitates the opening of the detector for access and maintenance.

1.6.1 Magnetic field characteristics

The determination of the magnetic field strength is rather different in the inner detector (ID) and the muon spectrometer.
In the inner detector, the systematic error affecting the momentum measurement of charged tracks is dominated by the relative alignment of detector components and by bending-power uncertainties, the former being the more demanding. For example a high-precision measurement of the W-boson mass is a challenging goal for such measurements; a lepton from W decay carries typically a transverse momentum of 40 GeV, resulting in a sagitta of approximately 1 mm as the lepton traverses the ID cavity. The systematic alignment uncertainties in the ID are unlikely to improve beyond the 1 μm level or 0.1% of the sagitta. This suggests setting a target of $\sim 5\times\ 10^{-4}$ for the fractional

bending power uncertainty, so that it remains negligible in the determination of the absolute momentum scale. Such stringent requirements can only be achieved reliably by in-situ mapping, using dedicated instrumentation inside the ID cavity; the inner detector is the equipped with four NMR probes fixed to the wall of the inner warm vessel. These probes measure the field strength with an accuracy of around 0.01 mT. In Figure 1.25, on the left, the modelled magnetic field strength in the inner detector cavity is shown. At nominal current, the total magnetic field is 1.998 T at the interaction point, and drops steeply from $\sim$ 1.8 T at z=1.7 m to $\sim$ 0.9 T at the end of the inner detector cavity.

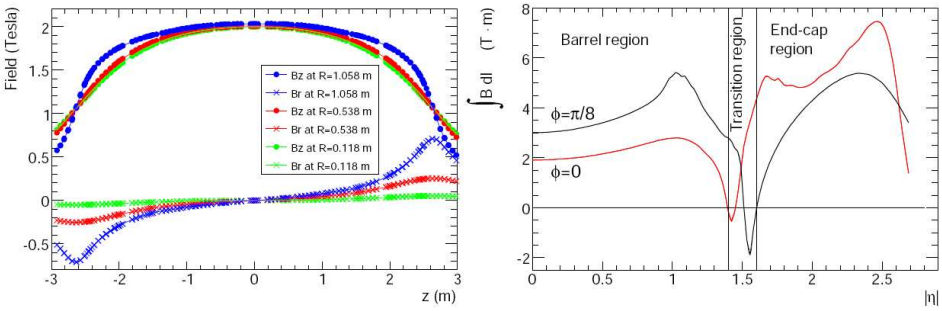

Figure 1.25: *Left: longitudinal and radial dependence of the magnetic field in the inner detector cavity. Right: predicted field integral as a function of* $|\eta|$ *from the innermost to the outermost MDT layer in one toroid octant.*

For the muon spectrometer the modelling and measurement of the magnetic field is much more complicated. In fact, the field is highly non-uniform, and residual bending-power uncertainties, if large enough, would translate primarily into degraded muon momentum resolution. In the muon spectrometer, the expected sagitta is approximately 0.5 mm for a muon with a momentum of 1 TeV. The extraction of the momentum from the Monitored Drift Tube chamber measurements requires a precise knowledge of the field integral between consecutive chambers along the muon trajectory. Because the field gradient can reach 1 mT/mm, local bending power uncertainties translate into fluctuations of the momentum scale from one region in space to another, adding in quadrature to the overall momentum resolution. In addition, as better explained in Chapter 2, the interpretation, in terms of spatial coordinates, of the drift time measured in the MDTs is sensitive to the local electric and magnetic fields experienced by the ionisation electrons in each tube. For a given muon trajectory, three sources of uncertainty affect the measured curvature: field measurement errors, accuracy on the relative position of muon chambers and magnet coils, and trajectory measurement errors, in particular along the direction of MDT wires. The magnetic field has then to be calculated in situ and with high granularity. To this end, the muon spectrometer is equipped with an

array of approximately 1730 Hall cards, which remain mounted permanently and precisely on the MDT chambers and continuously measure all three field components; an additional 64 cards are mounted on the inner and outermost faces of the end-cap toroid cryostats to complement the MDT sensor system in the forward region, and two NMR probes, installed at low-gradient locations in the barrel toroid, complement the system. The 3-D sensor readings are compared with field calculations and are used for reconstructing the position and the shape of the toroid conductors with respect to the muon chambers. Once the geometry of the coils is known, the field can be calculated anywhere in the muon spectrometer. Simulation studies using a simplified coil deformation model have shown that the magnetic field can be reconstructed to a relative accuracy of 0.2%. In Figure 1.25, on the right, the bending power as a function of the pseudorapidity in the muon spectrometer is shown. It shows good magnetic field coverage up to $|\eta| \sim 2.6$. The regions with low field integral, between $|\eta| = 1.4$ and $|\eta| = 1.6$, correspond to trajectories in the plane of an end-cap coil or of a barrel coil, where the field of one magnet largely cancels the bending power of the other. The circulating current on the toroid coils is around 20000 A.

1.7 Forward Detectors

Three smaller detector systems cover the ATLAS forward region. The main functionality of these systems is to determine the luminosity delivered to ATLAS.
At $\pm$ 17 m from the interaction point lies **LUCID** (LUminosity measurement using Cerenkov Integrating Detector). It detects inelastic p-p scattering in the forward direction, and is the main online relative-luminosity monitor for ATLAS.
The second detector is **ALFA** (Absolute Luminosity For ATLAS). Located at $\pm$ 240 m, it consists of scintillating fibre trackers located inside Roman pots which are designed to approach as close as 1 mm to the beam.
The third system is the Zero-Degree Calorimeter (**ZDC**), which plays a key role in determining the centrality of heavy-ion collisions. It is located at 140 m from the interaction point, in both sides, just beyond the point where the common straight-section vacuum-pipe divides back into two independent beam-pipes. The ZDC modules consist of layers of alternating quartz rods and tungsten plates which will measure neutral particles at pseudorapidities $|\eta| > 8.2$.

1.8 Detector Control System (DCS)

In order to enable coherent and safe operation of the ATLAS detector, a Detector Control System (DCS) has been defined and implemented. DCS serves also as a homogeneous interface to all sub-detectors and to the technical in-

frastructure of the experiment. It controls, continuously monitors and archives the operational parameters, signals any abnormal behaviour to the operator, and allows automatic or manual corrective actions to be taken. Typical examples are high- and low-voltage systems for detector and electronics (as is better explained on Chapter 2 concerning MDT chambers), gas and cooling systems, magnetic field, temperatures, and humidity. The DCS also enables bidirectional communication with the data acquisition system in order to synchronise the state of the detector with data taking. It also handles the communication between the subdetectors and other systems which are controlled independently, such as the LHC accelerator, the CERN technical services, the ATLAS magnets, and the detector safety system.
The software applications chosen to manage the control system of all the LHC experiments is PVSS[9].

1.9 Trigger and Data Acquisition (TDAQ)

The Trigger and Data Acquisition system (TDAQ) of the experiment is designed to select interesting events at a manageable rate for permanent storage and further analysis.

Given a target data flux of about 300 MB/s and an expected event size of $\sim$ 1.6 MB, the design output rate is $\sim$ 200 Hz. The required five order of magnitude online event selection is achieved via a three levels trigger architecture: a fast first level trigger (LVL1), implemented on custom hardware, is followed by two software based High Level Trigger systems (HLT): the second level trigger (LVL2) and the Event Filter (EF). An overview of the three levels TDAQ architecture is shown in Fig.1.26 [13].

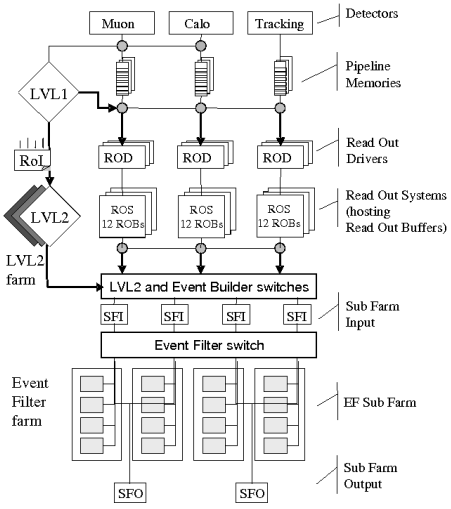

Figure 1.26: *Schema of the ATLAS TDAQ system.*

Each trigger level refines the decisions made at the previous level and, where necessary, applies additional selection criteria. The LVL1 trigger searches for high transverse momentum muons, electrons, photons, jets, and τ leptons decaying into hadrons, as well as large missing and total transverse energy. Its selection is based on informations from a subset of detectors. For example, high transverse-momentum muons are identified using trigger chambers: RPC in the barrel, and TGC in the end-cap region of the spectrometer. Calorimeter selections are based on reduced-granularity information from all the calorimeters. The LVL1 selects events with a maximum rate of 75kHz and a latency of less than 2.5 μs (about 100 bunch crossings). During this time, the

[9]PVSS is the German abbreviation for "*Process visualization and control system*".

front-end electronics of the various sub-detectors keep the complete event data in pipeline memory buffers. Data for rejected events are discarded, while the data for selected ones (about 160 GB/s) are passed via the Readout Drivers (RODs) into 1600 Readout Buffers (ROBs). Event data remain there and are pulled by LVL2 and by the Event Builder (EB) nodes on demand[10].
In each event, the LVL1 trigger also defines one or more Regions-of-Interest (RoIs), *i.e.,* the geographical coordinates in η and ϕ , of those regions within the detector where its selection process has identified interesting features. The RoI data include information on the type of feature identified and the criteria passed, *e.g.,* a threshold. This information is subsequently used by the high-level trigger.
For each event accepted by LVL1, a list of the Regions of Interest (RoIs) is given to LVL2, which provides a rejection factor of 20-30, bringing the rate to 3 kHz with an average latency of 40 ms. Its selections use, at full granularity and precision, all the available detector data within the RoIs.
The final stage of the event selection is carried out by the Event Filter, which reduces the event rate to roughly 200 Hz. Its selections are implemented using offline analysis procedures within an average event processing time of the order of four seconds. The HLT algorithms use the full granularity and precision of calorimeter and muon chamber data, as well as the data from the inner detector and offline software, to refine the trigger selections. Better information on energy deposition improves the threshold cuts, while track reconstruction in the inner detector significantly enhances the particle identification.
Events selected by the EF are then moved to permanent event storage at CERN computer centre.

LVL1 Muon Trigger The LVL1 muon trigger in both the barrel and the end-cap regions is based on three trigger stations each. The basic principle of the algorithm is to require a coincidence of hits in the different trigger stations within a road, which tracks the path of a muon from the interaction point through the detector. The width of the road is related to the p_T threshold to be applied.
For the barrel, the trigger algorithm operates in the following way: if a track hit is generated in the second RPC doublet (the pivot plane), a search for a corresponding hit is made in the first RPC doublet, within a road whose centre is defined by the line of conjunction of the hit in the pivot plane with the interaction point. The width of the road is a function of the desired cut on p_T: the smaller the road, the higher the cut on p_T. The algorithm is performed in both the η and the ϕ projections to reduce accidental triggers from low-energy particles in the cavern. A 3-out-of-4 coincidence of the four layers of the two doublets is required, which ensures excellent rejection of fake tracks from noise hits and greatly improves the stability of the trigger performance

[10]The ROBs are implemented in custom made PCI cards (ROBINs), each hosting three ROBs. The ROBINs are hosted in about 150 Readout system PCs (ROSs).

in the presence of small chamber inefficiencies. The high-p_T algorithm makes use of the low-p_T trigger built from hits in RPC1 and RPC2, and of the information generated in the RPC3 station. The algorithm operates in a similar way to the low-p_T one.
For the end-cap TGC trigger, the algorithm extrapolates pivot-plane hits to the interaction point, to construct roads following the apparent infinite-momentum path of the track. Deviations from this path of hits in the trigger planes closer to the interaction point are related to the momentum of the track. Coincidence signals are generated independently for R and ϕ. A 3-out-of-4 coincidence is required for the doublet pair planes, for both wires and strips, a 2-out-of-3 coincidence for the triplet wire planes, and 1-out-of-2 possible hits for the triplet strip planes. Six sets of windows are constructed around the infinite-momentum path, corresponding to three different high-p_T and three different low-p_T thresholds. Trigger signals from both doublets and the triplet are involved in identifying the high-p_T candidates, while in case of the low-p_T candidates the triplet station may be omitted to retain high efficiency, given the geometry and magnetic field configuration of a specific region.
The two muon trigger schema are shown in Figure 1.27

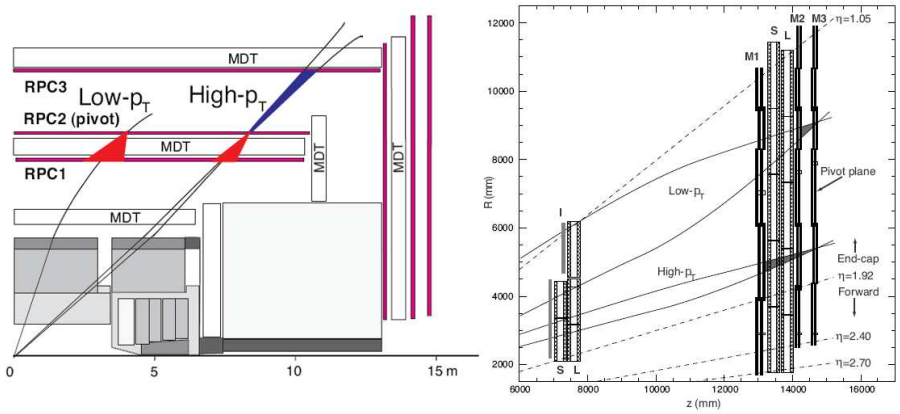

Figure 1.27: *Schema for LVL1 muon RPC barrel (left) and TGC end-cap trigger [7].*

The results from the muon barrel and end-cap trigger processors which form the input to the Muon to Central Trigger Processor Interface (MUCTPI) provide information on up to two muon-track candidates per muon trigger sector. The information includes the position and p_T threshold passed by the track candidates. The MUCTPI combines the information from all the sectors and calculates total multiplicity values for each of the six p_T thresholds. These multiplicity values are sent to the Central Trigger Processor (CTP) for each bunch-crossing.

LVL1 Calo trigger The LVL1 calorimeter trigger is composed by two subsystems: the Cluster Processor (CP) and Jet/Energy-sum Processor (JEP). The CP identifies electron/photon and τ-lepton candidates with transverse energy, E_T, above the corresponding programmable threshold and satisfying, if required, certain isolation criteria. The JEP receives jet trigger elements, which are 0.2×0.2 sums in $\Delta\eta \times \Delta\phi$, and uses these to identify jets and to produce global sums of scalar and missing transverse energy. Both processors count the multiplicities of the different types of trigger objects. The CP and JEP send these feature multiplicities, as well as transverse-energy threshold information, to the CTP for every bunch-crossing.

Central Trigger Processor (CTP) The Central Trigger Processor (CTP) receives trigger information from the calorimeter and muon trigger processors, which consists of multiplicities for electrons/photons, τ-leptons, jets, and muons, and of flags indicating which thresholds were passed for total and missing transverse energy, and for total jet transverse energy. Additional inputs are provided for special triggers such as a filled-bunch trigger based on beam-pickup monitors, and a minimum-bias trigger based on scintillation counters. In the next step the CTP uses look-up tables to form trigger conditions from the input signals. The trigger conditions are combined to form up to 256 trigger items, where every trigger condition may contribute to every trigger item. An example for a trigger item would be that the following conditions have been fulfilled: at least two muons have passed a particular threshold, and at least one jet has passed a particular threshold. Furthermore each trigger item has a mask, a priority (for the dead-time generated by the CTP), and a pre-scaling factor (between 1 and 2^{24}). The CTP then sends information about the trigger decision for all trigger items to the LVL2 trigger (RoI builder) and the data acquisition (ROS). Part of the readout data of the CTP is the number of the current luminosity block. A luminosity block is the shortest time interval for which the integrated luminosity, corrected for dead-time and pre-scale effects, can be determined. In case of detector failures, data can be rejected from the boundary of the last luminosity block known to be unaffected, and the interval should therefore be as small as possible to avoid unnecessary data loss.

High Level Trigger event selection The HLT starts from the RoIs delivered by the LVL1 trigger and applies trigger decisions in a several steps, each refining existing information by acquiring additional data from increasingly more detectors. A list of physics signatures (trigger chains), implemented event reconstruction (feature extraction) and selection algorithms are used to build signature and sequence tables for all HLT steps. Feature extraction algorithms typically request detector data from within the RoI and attempt to identify features, *e.g.,* a track or a calorimeter cluster. Subsequently, a hypothesis algorithm determines whether the identified feature meets the criteria (such as a shower shape, track-cluster match or E_T threshold) necessary to

continue. Each signature is tested in this way. The decision to reject the event or continue is based on the validity of signatures, taking into account pre-scale and pass-through factors. Thus events can be rejected early after an intermediate step if no signatures remain viable. In this manner the full data set associated with the RoI is transferred only for those events which fulfil the complete LVL2 trigger selection criteria, *i.e.,* the amount of data transferred between the ROS and the LVL2 trigger is minimised for those events which are rejected.
The Event Filter is a processing farm; on each processing node a configurable number of independent processing tasks receive and process events. For those events passing the selection criteria, a subset of the data generated during the event analysis is appended to the event data structure, enabling subsequent offline analysis to be seeded by the results from the Event Filter. An integral part of the selection process is the classification of the events according to the ATLAS physics streams. To this end, for those events which fulfil the selection criteria, a tag is added to the event data structure identifying into which physics stream the event has been classified.
The event-filter output nodes (SFO) receive events which have passed the Event Filter selection criteria, interface the DAQ/HLT to CERN central data-recording facility, and de-couple the data-taking process from possible variations in the central data-recording service.

1.9.1 ATLAS Analysis Model

Event produced by the ATLAS detector, as well as the ones from the other three LHC experiments, will then be elaborated, reconstructed and distributed around the globe through the Worldwide LHC Computing Grid (WLCG) that connects computers that are scattered over a wide geographic area, allowing their computing power to be shared. Thanks to this system, all members of the ATLAS collaboration will be enabled to speedy access to all reconstructed data for analysis during the data-taking period, and to raw data for monitoring or calibrations.

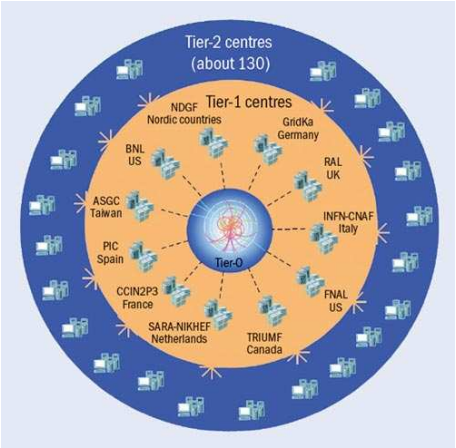

Figure 1.28: *The LHC computing grid.*

The WLCG is based on four-tiered model. A primary backup and event processing will occur at CERN, in the Tier-0 centre of LCG. After initial processing, this data will be distributed to a series of Tier-1 centres around the world (11 centres). These facilities archive the RAW data, provide the reprocessing capability and allow scheduled analysis of the processed data by physics anal-

ysis groups.
The Tier-1 centres will make data available to the 130 Tier-2 centres, each consisting of one or several collaborating computing facilities, which can store sufficient data and provide adequate computing power for specific analysis tasks. The Tier-2 facilities also provide the simulation capacity for the experiment.
Individual scientists will access these facilities through Tier-3 computing resources, which can consist of local clusters or even individual PCs, and which may be allocated to LCG on a regular basis.
The calibration centres, which include some Tier-2 Grid centres as well as the CAF (CERN Analysis Facility), perform a first pass calibration and alignment within 24 hours after the data has been taken. The obtained constants are then used for the bulk processing of the data, once they have been validated by a second re-processing of the express stream. Data are then distributed to the Tier-1 and Tier-2 centres for data analysis. Further data re-processings with improved reconstruction software and calibration constants can then take place at the Tier-1 centres. The reconstruction and monitoring chain also runs continuously online to provide an online event display and histograms monitoring the data quality during detector operations.
In Figure 1.28 a cartoon of the hierarchy of the computing grid is displayed, and in Table 1.3 it is a summary of the main tasks of each Tier centre in ATLAS[68].

Computing centre	**location**	**task**
Tier-0	CERN	Data recording; initial data reconstruction; data distribution.
Tier-1	11 centres	Permanent storage; re-processing; analysis.
Tier-2	$\sim$ 130 centres	Simulation; end-user data analysis.
Tier-3	$\sim n$ centres	User's analysis

Table 1.3: *Distribution of the tasks of the LHC computing grid system.*

1.10 Installation and Commissioning

The ATLAS detector has been installed underground in a cavern, situated in Switzerland at Point 1 on the LHC ring. The main cavern is 92.5 metres underground and the detector is almost as large as the cavern in which it is housed.
The construction of the ATLAS subdetectors was distributed over many institutions around the world[11]. The components then had to be brought to CERN in a timely manner, a considerable challenge itself in terms of their size, complexity and fragile nature. In most cases, final assembly and testing were made at CERN on the surface, prior to installation underground.

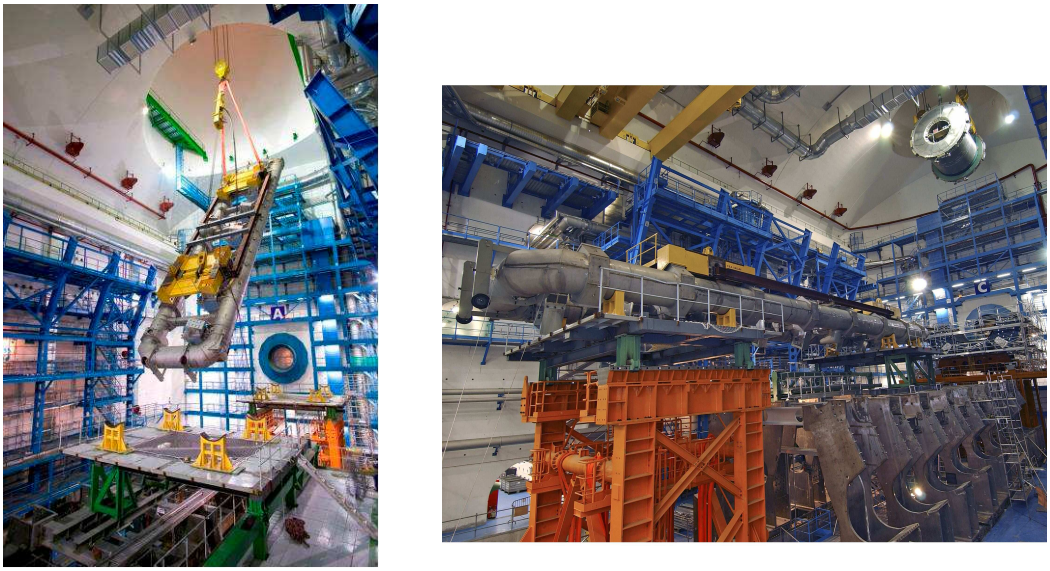

Figure 1.29: *Lowering of the first barrel toroid coil, and of the barrel LAr calorimeter down to the cavern in October 2004 [14].*

Ensuring that all the pieces of the puzzle fitted together turned out to be a particularly difficult challenge, since the physics goals and the geometry of the detector require minimal clearances between neighbouring parts. One of the most stringent requirements of the ATLAS detector is to ensure hermetic coverage over most of the solid angle: installation of the detector had therefore to be performed to great accuracy, in order to guarantee optimal coverage.

The detector had to be assembled and tested in the main cavern mostly because of the nature of the barrel toroid magnet structure; some sub-systems, like the Inner Detector, were assembled on the surface, while others were directly installed, piece by piece, in the main cavern.

[11]The INFN and the physics department of the University of Pavia have contributed with the construction of 56 MDT chambers.

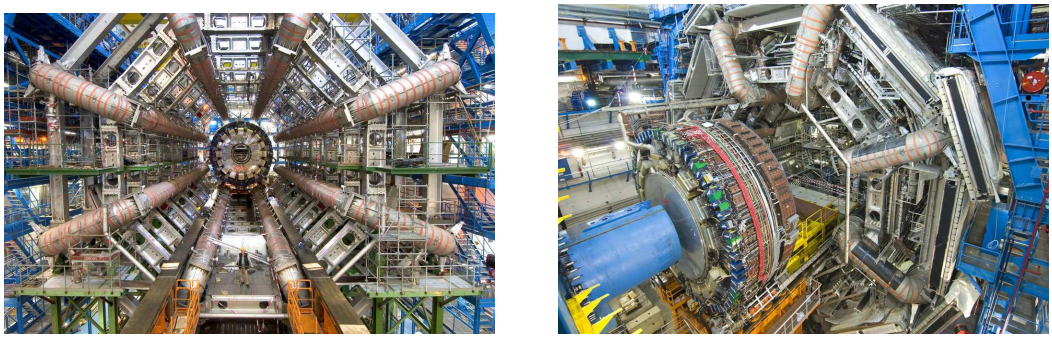

Figure 1.30: *The ATLAS barrel toroid, as in July 2005 (left) with the eight coils installed, and in January 2006 (right) with muon chambers and end-cap calorimeter [14].*

The civil engineering work for the ATLAS experimental area started in November 1997 whilst the previous accelerator (LEP) was still in operation and the situation remained so until the end of 1999. The work included the excavation and concreting of two 60 m long shafts (the widest shaft with a 18m diameter), two new large caverns along with the linking galleries, and the erection at the surface of six new buildings.
The cavern was made available empty in June 2003. The first operation was to install the general infrastructure (metallic structures around the cavern walls, temporary electricity and lighting, ventilation ducts, and the overhead travelling cranes). With the steel structures installed, the first elements of the ATLAS detector installed were the stainless steel support feet, 18 in total, in order to provide the mechanical support for most of the ATLAS sub-systems[12]. The detector elements were then lowered inside the cavern via the two shafts, and then assembled.
The barrel toroid was the first to be installed (from October 2004), and then completed with the last coil put in place in July 2005 (Figures 1.29, 1.30) . In Figure 1.30 the eight magnetic coils and the aluminium support structure for the muon chambers are well visible.
In parallel with the barrel toroid assembly, the first 100 muon barrel chambers were installed in between the struts/girders and the ATLAS feet, the LAr calorimeter was lowered (Figure 1.29), and the tile calorimeter modules were assembled together (Figure 1.30 right).
The LAr cryostats were also lowered in the cavern and the Tilecal modules were mounted around to form the barrels.
By May 2006, the central and both extended barrel calorimeters were completed and had been moved to their location inside the toroid. At the same time, the barrel toroid structure and the big end-cap wheels were progressively equipped with muon chambers. The last pieces of the muon spectrometer, the

[12]The barrel toroid magnet, the calorimeters, the barrel muon chambers, the end-cap toroid magnets, the services and the access structures, amounting to about 6000 tonnes.

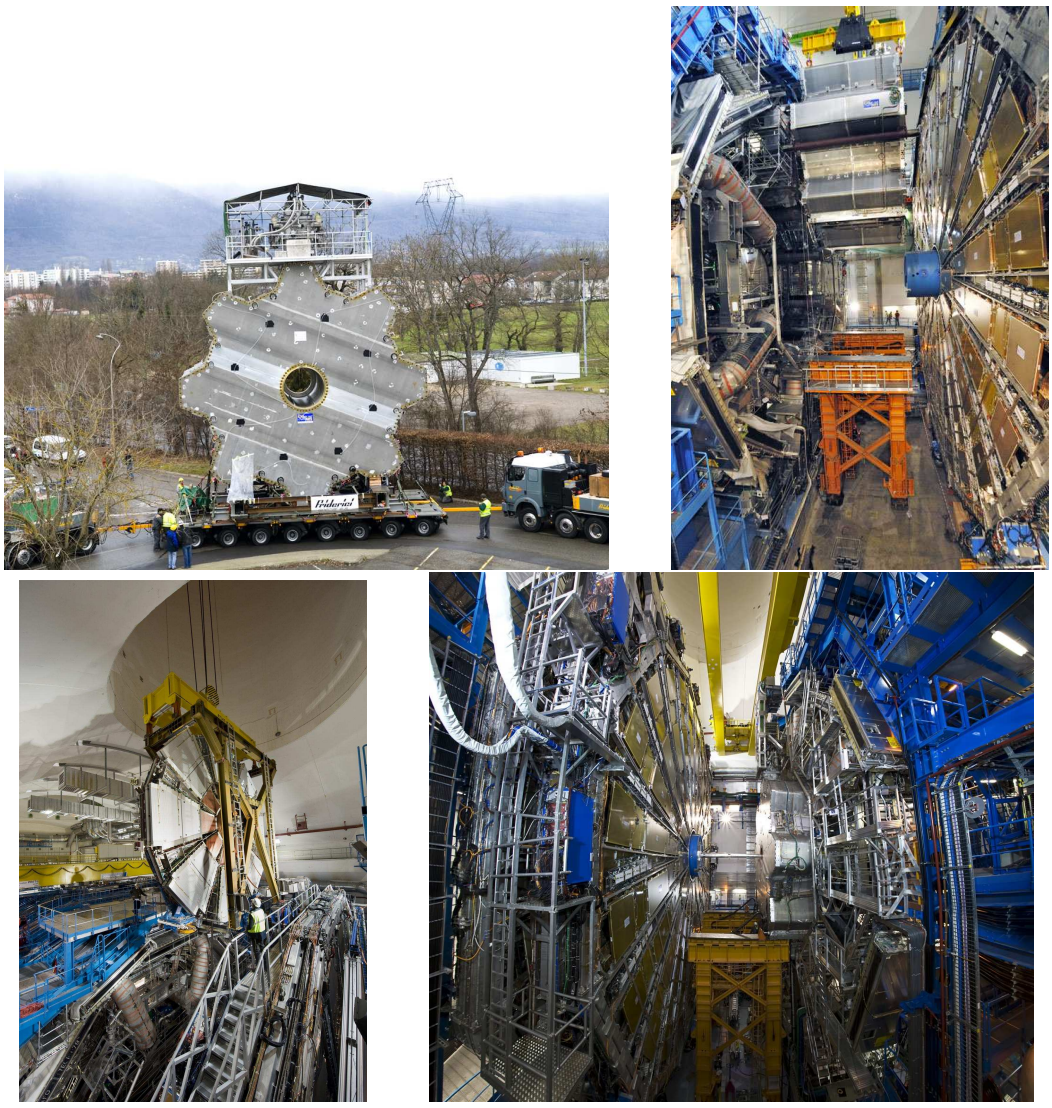

Figure 1.31: *Transportation (top left) and installation (top right) of an end-cap toroid magnet, on June 2007. One of the TGC big wheels can be seen on the right of the picture. (Bottom) Lowering of the last piece of ATLAS, the small wheel of the muon chambers, on February 2008 (left), and a view of the final configuration of the barrel (right), with also beampipe installed, before closing the end-cap wheels [14].*

small muon end-cap wheels were mounted on surface and lowered through the shafts (February 2008), as well as the toroid end-cap cryostats (June 2007), as is shown in Figure 1.31.
The inner detector was installed in two phases: TRT and SCT in August 2006 and Pixel in June 2007 (see Figure 1.32).

Each component that has been installed, in parallel with all the other installation operations, has been connected to its readout electronics, operated with its respective cooling, gas or other specific hardware, and integrated in

Figure 1.32: *Left: the TRT and SCT being installed in August 2006; Middle: the Pixel detector being inserted in June 2007; right: the ID volume sealed with the complex end-plate with 1000 feed-through in April 2008 [14].*

the global ATLAS Trigger and Data Acquisition System (TDAQ). The full chain was then commissioned (as is explained in the next chapter for the case of MDT chambers).
On 16th June 2008 the whole ATLAS experiment, with also the beam pipe, was closed for the first time, in view of the LHC operation in September 2008. After the LHC accident and hence its shut-down, all the ATLAS experiment was open again, after a period of a couple of months of cosmic run data taking with all the detector online.

Subsetector	**Number of channels**	**Operational fraction**
Pixels	80 M	98.5 %
SCT	6.3 M	99.5 %
TRT	350 k	98.2 %
LAr	170 k	99.1 %
Tile	9800	99.5 %
HEC	5600	99.9 %
FCal	3500	100 %
MDT	350 k	99.3 %
CSC	31 k	98.4 %
RPC	370 k	95.5 %
TGC	320 k	99.8 %

Table 1.4: *Readiness of the full ATLAS experiment as during the combined cosmic ray acquisition in July 2009.*

After the opening of the detector, more than 250 consolidation activities have

been done, amongst the most crucial there were the repair of the inner detector cooling system, and to the the exchange of the front-end electronic cards for the electromagnetic calorimeters. The extra shutdown period has also allowed some schedules to jump forwards, for instance the very forward muon chambers (EE chambers) have already been partially installed, even though this was not planned until the 2009/2010 shut-down.
The ATLAS detector has been closed again on the 9th May 2009, and during July experienced a second long cosmic ray data taking with all the system working, in order to be ready for the LHC re-start.
In Table 1.4 there is an overview of the readiness of the full ATLAS experiment as during the combined cosmic ray acquisition in July 2009. It is then possible to conclude that all the ATLAS system is in a good shape, being all the detectors operational at almost 100%, and ready for LHC collisions.

Chapter 2

The MDT chambers and their commissioning

The ATLAS Muon Spectrometer (MS) has been built to provide a fast trigger on high transverse momentum muons (p_T>6 GeV) and a precise measurement of muon momentum up to the TeV scale (momentum resolution dp_T/p_T of 10% for 1 TeV muons).

Monitored Drift Tubes (MDT) chambers are employed for the precision measurement in the bending plane, both in the barrel and in the end-caps. This precision measurement of muon tracks is made on the $r-z$ projection, in a direction parallel to the bending plane of the magnetic field; the axial coordinate (z) is measured on the barrel and the radial coordinate (r) in the end-cap region (Fig. 1.22).

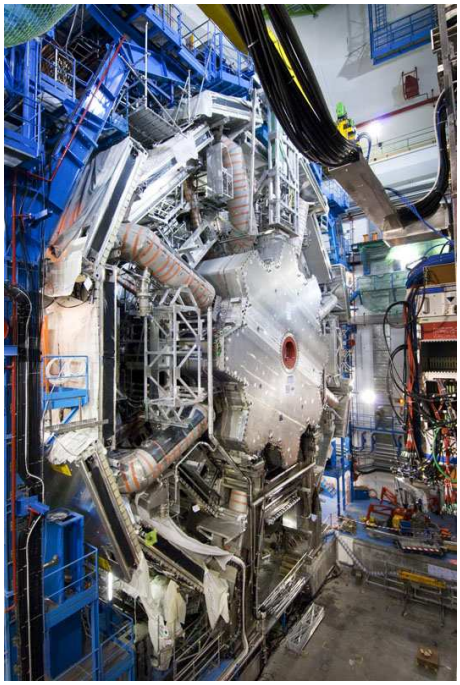

Figure 2.1: *Picture of ATLAS. The MDT chambers are well visible over the coils of the toroid.*

In this chapter the procedure of measuring the muon momentum is reported. This is followed by detailed description of the MDT chambers, from their mechanical structure (Sections 2.2.1, 2.2.2) to the readout electronics (Section 2.2.4), calibration (Section 2.4) and alignment procedures (Section 2.5). Tracking performance is then explained in Section 2.3. The second part of the chapter is focused on the commissioning procedures of the MDTs, both in stand-alone (Section 2.6.1) and in combined cosmic runs, together with all the ATLAS detectors (Section 2.9.1). In Section 2.9.2 the performances of some ATLAS detector using the first LHC splash events are also shown.

2.1 Momentum measurement

The muon momentum estimation is based on the measurement of three points along the track of the particle, that is deflected by the magnetic field. The trajectory curvature is a measure of the muon momentum. It is convenient to express the curvature in terms of a "sagitta", which is the distance from the point measured in the middle station to the straight line connecting the points in the inner and outer stations (Figure 2.2).

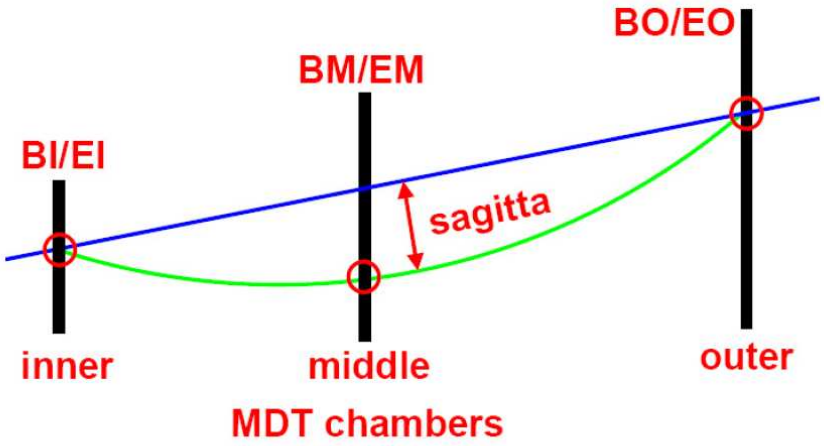

Figure 2.2: *Definition of sagitta as measured in the ATLAS muon spectrometer.*

The precision in the measurement of the muon momentum is hence correlated to the sagitta measurement. Referring to Figure 2.3, that shows the magnetic field direction of the ATLAS toroid, if the magnetic field B is present in a region of length L, and it is perpendicular to the particle trajectory, the sagitta s can be expressed as:

$$s = \rho(1 - cos\frac{\alpha}{2}) \approx \rho\frac{\alpha^2}{8} \tag{2.1}$$

and the bending angle α, as long as $\alpha \ll 1$, can be expressed as a function of the momentum p:

$$\frac{L/2}{\rho} = sin\frac{\alpha}{2} \approx \frac{\alpha}{2} \qquad \Rightarrow \qquad \alpha \approx 0.3\frac{B \cdot L}{p}$$

In this way the value of the momentum p can be extracted from the measurement of the sagitta s.
In the ATLAS muon spectrometer, the three measurement points are the three

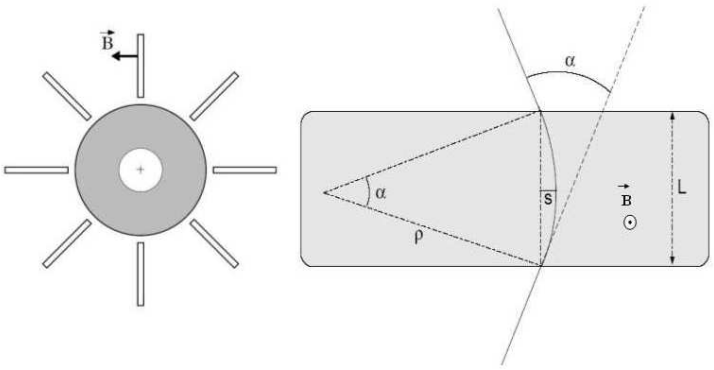

Figure 2.3: *Geometrical sketch for calculation of the track sagitta.*

MDT stations (see Section 2.2.3). A muon with a momentum of 1 TeV has a sagitta of about 500 μm, and the target momentum measurement precision of 10% translates into a sagitta precision of 50 μm. The actual resolution depends not only on the local precision of the points measured in the muon chambers, but also on the relative positions of the three stations. Therefore, particular care on the alignment and on the monitoring of chamber position as a function of time[1] has to be given.

2.1.1 Momentum resolution

Figure 2.4 shows how contributions to the muon spectrometer momentum resolution vary as a function of p_T. Three resolution regimes are clearly visible:

- Low momentum (p_T<30 GeV) the resolution is dominated by fluctuations in the energy loss of the muons traversing the material in front of the spectrometer, which influence the extrapolation from the muon spectrometer to the interaction point. In this momentum range the inner detector, which does not suffer from the calorimeters, provides the more precise momentum measurement.

- Moderate momentum (30 GeV<p_T<300 GeV) multiple scattering in the spectrometer plays an important role in this region. The multiple scattering depends on the amount of material traversed and on the distribution of the material along the track[2].

- High momentum (p_T>300 GeV) the resolution is dominated by the precision with which the track deflection is measured; single hit resolution, limited by detector characteristics, alignment and calibration, dominates.

[1] From the continuous monitoring of their positions come the the name "monitored" of the MDT chambers.

[2] As already explained in Chapter 1, the ATLAS choice to have an air core toroidal magnet has been taken in order to keep the multiple scattering as low as possible.

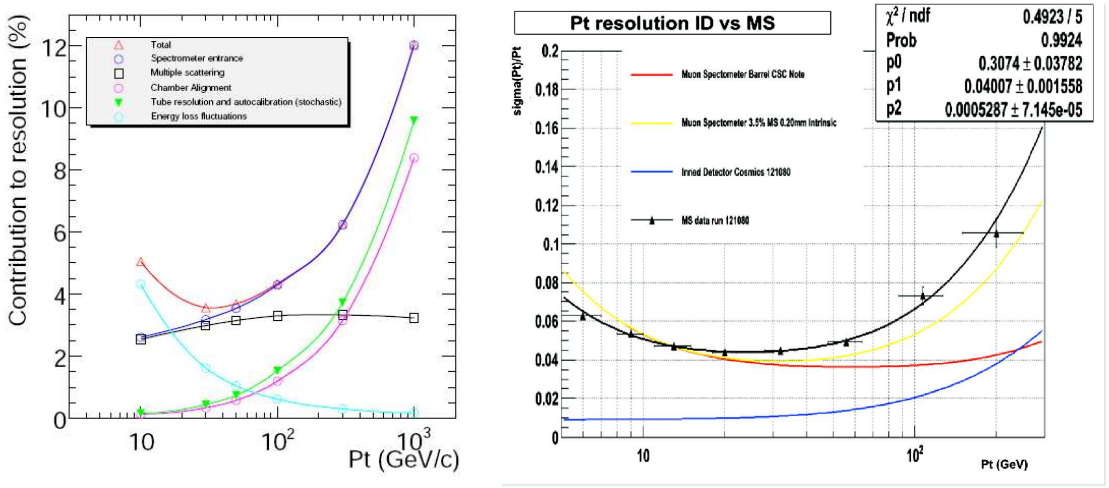

Figure 2.4: *Contributions to the momentum resolution for muons reconstructed in the Muon Spectrometer as a function of transverse momentum in the barrel as calculated (left) and measured with 2008 cosmic runs (right). [7, 18]*

The limited knowledge of the magnetic field in the muon spectrometer and of the material distribution along the muon trajectory give also a contribution.

As already seen in Section 1.6.1, the magnetic field will be known with an accuracy better than 2×10^{-3}, using measurements from the 1730 magnetic field sensors which are mounted on the muon chambers. As a consequence, the relative impact on the momentum resolution is less than 3%. It has been studied [7] that the space drift-time relationship of the MDT chambers must be determined with 20 μm accuracy in order to give a negligible contribution to the momentum resolution up to $p_T = 1$ TeV. A strategy to calibrate the spatial resolution of MDTs with muon tracks with the required accuracy is described in detail in Section 2.4.
The initial misalignment will be the dominant source of performance degradation. The muon chambers are installed with a positioning accuracy of about 1 mm in the muon spectrometer with respect to the nominal value. In order to reach the design momentum resolution, however, muon chambers alignment has to be known with an accuracy better than 30 μm in the bending plane. A bias of 30 μm on the sagitta of a 1 TeV muon, in fact, corresponds to a systematic shift in the measured momentum of 60 GeV. It will be possible to measure the muon performance of a misaligned muon spectrometer with events like $Z \rightarrow \mu^+\mu^-$ that will lead to a clearly visible resonance peak in the dimuon mass distribution even in the case of the initial misalignment. The description of the alignment procedure is written in Section 2.5.

2.2 Monitored Drift Tube Chambers

2.2.1 Working principles and layout

The basic detection elements of the MDT chambers are pressurized cylindrical aluminum drift tubes with a diameter of 30 mm, operating with Ar:CO_2 gas mixture (93:7) at 3 bar. Inside each tube there is a tungsten-rhenium anode wire with a diameter of 50 μm, at a potential of 3080 V.

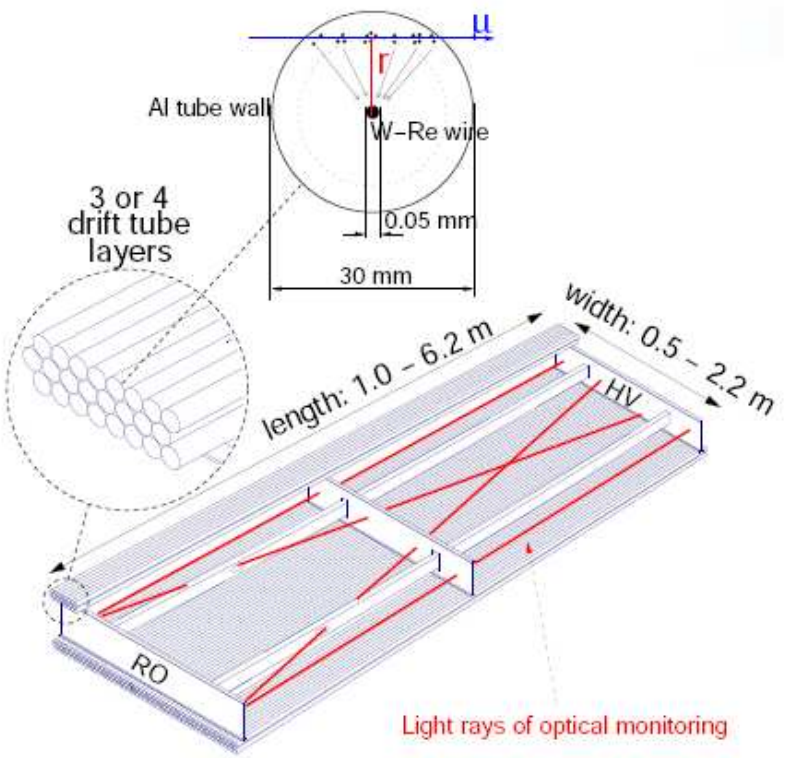

Figure 2.5: *Schematic view of an MDT chamber with its structural components, and operation principles. Red lines show the in-plane alignment system.*

The wire is held in position at the tube ends by a cylindrical end-plug which guarantees the concentricity of the wire with respect to the tube with an accuracy of σ<10μm RMS. The central conductor holding the wire also serves for the gas transfer in and out of the tube. Signal transmission to the electronics and connection to the HV supply system are at opposite ends of the tube. The main MDT parameters are summarized in Table 2.1, and in Figure 2.5 the structure of a barrel MDT chamber is shown.
A muon crossing a drift tube ionizes the detector gas. The interactions of the muon with gas particles are independent between each others, and the number of ionization clusters per unit length is governed by a Poisson distribution. In

Argon at 3 bar the mean number of clusters per cm of track is about 100, each of them having $\sim$ 3 electrons [15]. The clusters of ionization electrons drift towards the anode wire, guided by the radial electric field:

$$E(r) = \frac{V}{r \cdot ln\frac{b}{a}} \tag{2.2}$$

where a is the wire radius, b the inner tube radius and V the high voltage applied to the anode. In the high-field region near the central wire the charge is multiplied in an avalanche process, creating new electron-ion pairs. The anode voltage is chosen such that the avalanche amplification factor (gas gain) is 2×10^4. The positive ion cloud moves from the avalanche zone towards the cathode, inducing a current signal on the anode wire. A contribution due to the signal induced by the drifting electrons is also present. However, since the drift distance of the electron avalanche is only as large as the amplification zone near the wire (*i.e.,* about 150 μm) the electron signal is a sharp spike of only about 100 ps width containing very little charge. Therefore, this electron pulse is negligible compared to the ion signal.

Parameter	**Design value**
Tube material	Aluminum
Outer tube diameter	29.97 mm
Tube wall thickness	0.4 $\pm$ 0.020 mm
Wire material	W-Re (97%:3%); 3% gold plating
Wire diameter	50 μm
Wire pitch	30.035 mm
Gas mixture	Ar:CO_2 (93%:7%)
Gas pressure	3 bar (absolute)
Gas gain	2×10^4
Wire potential	3080 V
Maximum drift time	$\sim$ 750 ns
Average tube resolution	$\sim$ 75 μm

Table 2.1: *Main MDT tube parameters.*

The tube concept lends itself to high-pressure operation, thereby reducing the deleterious effect of longitudinal diffusion and the fluctuations of the number of primary electrons on the single-wire resolution. One of the advantages of the cylindrical geometry is the radial electric field (Eq: 2.2): the measurement accuracy, therefore, depends only weakly on the angle of incidence of the track onto the chamber plane, as the coordinate of the track is determined by the radius of the circle around the wire to which the track is tangential (see Fig. 2.17).
On the other end, the long pulse train caused by the track segments far from

the tangential point, may produce several threshold crossings (hits) per track. The maximum drift time from the wall to the wire is about 700 ns. A muon passing through a drift tube thus generates a pulse train with a duration of this order, while only the arrival time of the central track part, closest to the wire, is relevant for the track coordinate.
The operating gas mixture ($Ar:CO_2$, 93:7), was selected because of the good ageing properties[3], that are crucial for the high background radiation and the long term working of these chambers.
However, there are two main disadvantages using this gas mixture with respect to typical gas mixtures: an highly non-linear dependence of the drift velocity on the electric field and a greater drift time (700 ns drift time is about 50% longer than, for example, $Ar:CH_4$). A large drift time results in a high tube occupancy. The non-linearity of the $Ar:CO_2$ gas leads to a reduction of spatial resolution at high counting rates due to the distortion of the electric field created by the positive ions. At full LHC luminosity, counting rates up to 10 kHz per tube will be expected due to the conversion of background photons and neutrons. An additional complication for tracking comes from the fact that the detailed shape of the space drift-time relation in $Ar:CO_2$ depends on environmental parameters like temperature and pressure as well as on the local magnetic field due to the Lorentz force. In order to maintain the high spatial resolution under varying environmental conditions, an online and recursive calibration system based on measured tracks is foreseen (Section 2.4).

2.2.2 Mechanical structure

An MDT chamber consists of two close-packed multilayers of drift tubes with a support structure between them, as shown in Figure 2.5. Depending on the position in the muon spectrometer, a multilayer may have three or four layers. Four-layer chambers are located in the inner stations where the gamma and neutron radiation rates are highest and thus the background hits are more frequent. By adding another layer of tubes, in fact, the difficult pattern recognition in these regions is made more reliable.
Building the precision-tracking chambers out of individual tubes offers several advantages, among which the possibility to reach an high level of operational reliability, because the failure of a single tube does not affect the operation of most of the others.
In order to cover the whole spectrometer area of 5500 m^2, 1150 MDT chambers with 354000 tubes have been required. The shapes and dimensions of the MDT chambers were chosen to optimize solid coverage, while respecting the envelopes of the magnet coils, support structures and access points. In fact, in order to keep the acceptance losses due to the ATLAS support structure

[3]Studies of ageing behavior of different gases [19, 20], have shown that $Ar:CO_2$ gas mixtures are much less sensitive to ageing effects than mixtures containing hydrocarbons.

to a minimum, many "special" chambers were designed, especially in the lower sectors of the barrel. MDT chambers are rectangular in the barrel, and trapezoidal in the end-cap.

2.2.3 Naming conventions

In order to distinguish the different MDT chambers inside the muon spectrometer, the following naming conventions have been introduced, as it is shown in Figure 2.6:

- **Region**: there are two regions: barrel (B) and end-cap (E).
- **Station**: it is related with the distance from the nominal interaction point. In the barrel there are three MDT Stations, located at a radii of approximately 5 m, 7.5 m and 10 m, that are named *Barrel Inner* (BI), *Barrel Middle* (BM) and *Barrel Outer* (BO). In the end-cap the chambers are arranged in four stations, named *End-Cap Inner* (EI), *End-Cap Extra* (EE), *End-Cap Middle* (EM), and *End-Cap Outer* (EO), located at distances of $|z| \sim 7.4$ m, 10.8 m, 14 m, and 21.5 m from the interaction point.
- **Sector**: the MS, due to the octagonal geometry of the toroidal magnet, is divided in the xy-plane (azimuthal ϕ-plane) in 16 sectors. In both barrel and end-cap regions the precision chamber sectors are divided into 6 *Large* (L) sectors, that cover the solid angle between the eight superconducting coils and correspond to the odd sectors, and 6 *Small* (S) sectors, in the region of the coils, corresponding to even sectors.
- **Side**: along the beam (z) axis with respect to the interaction point the MS is divided into 2 regions called *side A* (towards the positive side of the z axis) and *side C*.
- **Projective tower**: it is the ensemble of all the chambers located in a solid angle, centered on the interaction point.

Each chamber has a name like $Y_1Y_2Y_3.Z_1Z_2Z_3$, where: YYY uniquely identify its position in the MS:

- Y_1: Region (B=barrel, F=Forward, E=End-cap);
- Y_2: Station (I=Inner, E=Extra, M=Middle, O=Outer);
- Y_3: chamber type (L=Large, S=Small);

ZZZ describes in detail the position of the chamber:

- Z_1: Number of the chamber in the sector. For most of the chambers there are 12 chambers of the same type for each sector, 6 in side A, and 6 in side C. The number increases following the z axis, the chamber 1 being closer to the interaction point;

- Z_2: Side (A or C);

- Z_3: Sector number (from 1 to 16).

Following this convention, for example, the chamber BOS2A12 is located in the barrel (B), outer station (O) and small sector (S). On the z axis direction, it is the second chamber of this type in side A (2A) and it is located in sector 12.

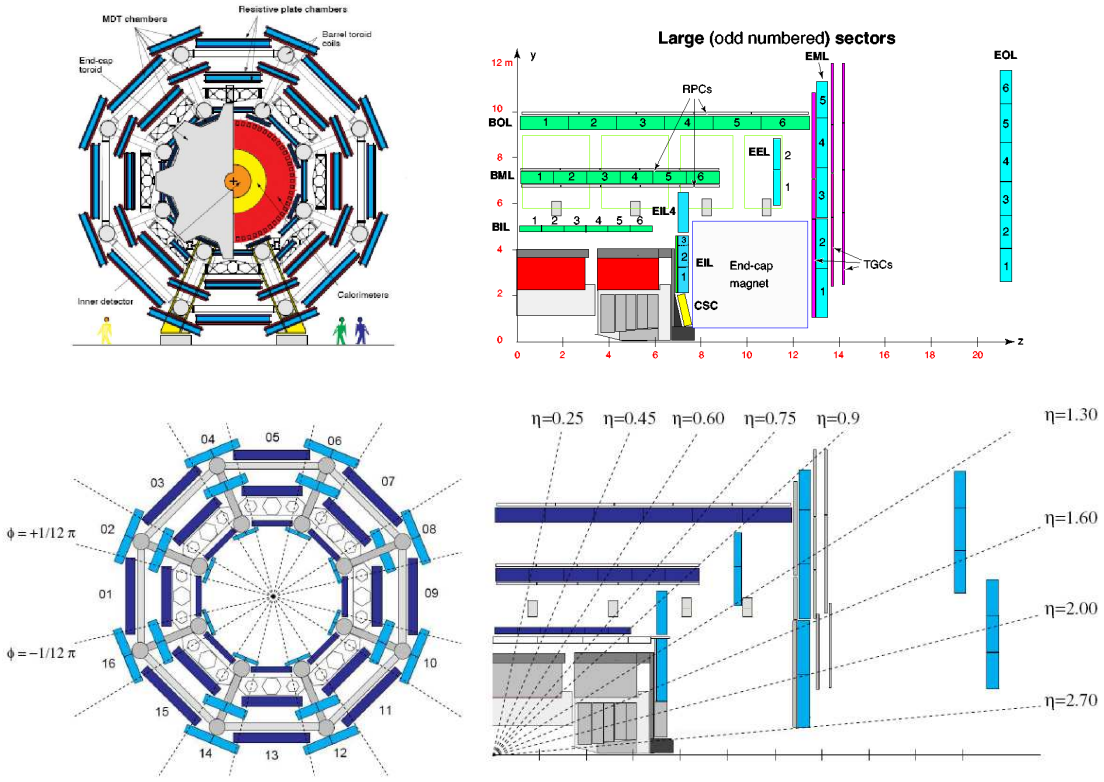

(a) ϕ-binning (b) η-binning

Figure 2.6: *Top: cross section view of the ATLAS muon spectrometer (left) perpendicular to the beam axis (non bending plane), (right) view along a plane containing the beam axis. Bottom: ϕ and η binning of the muon spectrometer.*

2.2.4 Readout electronics

The MDT readout electronics chain is partially located on each chambers (front-end electronics), and partially (off-chamber electronics) in the service cavern. The front-end electronics is designed to optimize the performances of the MDT drift properties in the radiation environment foreseen at LHC, while the off-chamber is shielded from radiation by the concrete walls of the cavern. A detailed description can be found here [16].

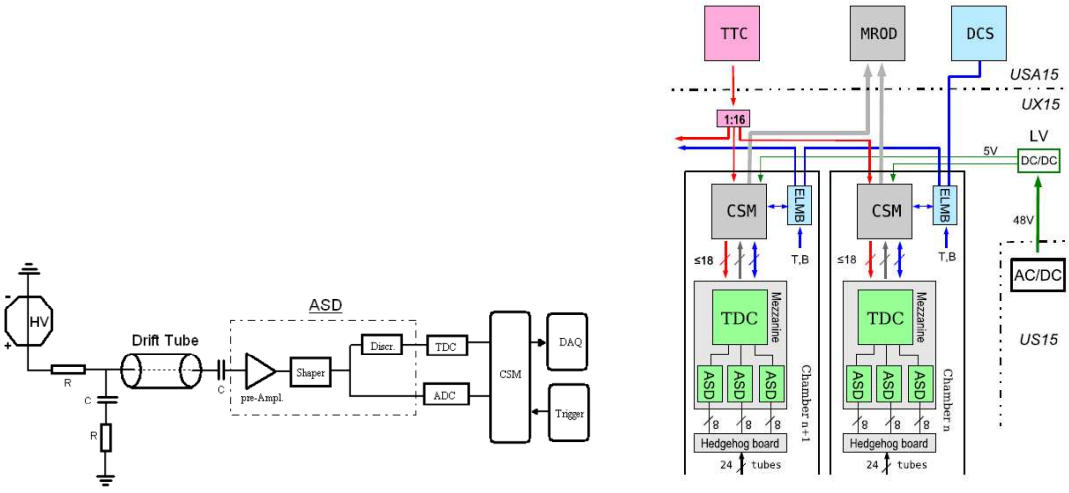

Figure 2.7: *Front-end electronics schema for each MDT tube (left) and for each MDT chamber (right).*

On-chamber electronics

The MDT on-chamber readout electronics chain consists of (see Figures 2.7):

- **ASD (Amplifier-Shaper-Discriminator) chip** is at the first stage of the readout, and serves eight tubes. Its tasks, as its name suggests, are to amplify, shape and discriminate the analogical signal of the anode wire. For a gas gain of 2×10^4, the response function of the ASD is ~ 3 mV per primary electron. An additional feature of the ASD is the measurement of the pulse height of the signal, which allows the monitoring of the gas gain as well as pulse height dependent corrections (slewing corrections). The pulse height is measured by an **Analogue-to-Digital Converter (ADC)**.
- **TDC (Time-to-Digital Converter) chip** uses the binary differential signals produced by the ASD; the arrival times of the signals are stored in a large buffer memory together with an identifier of the corresponding

tube. The time is measured in units of the **TTC (Timing, Trigger and Control)** clock of 40.08 MHz, which is the bunch crossing (BC) frequency of the LHC machine. In the TDC the BC interval of 1/40.08 MHz = 24.95 ns is subdivided in 32 bits, resulting in "fine time" period of 0.78 ns. Each TDC serves three ASDs and hence 24 tubes.

- **Mezzanine card** is a 9 ×11 cm^2 printed circuit-board where both a TDC and three ASD chips are implemented (Fig. 2.8, left). It is mounted on the readout side of the chamber and serves 24 tubes. The mezzanine card is the basic readout element of the MDTs and is connected to the tubes via a signal distribution card (hedgehog board).

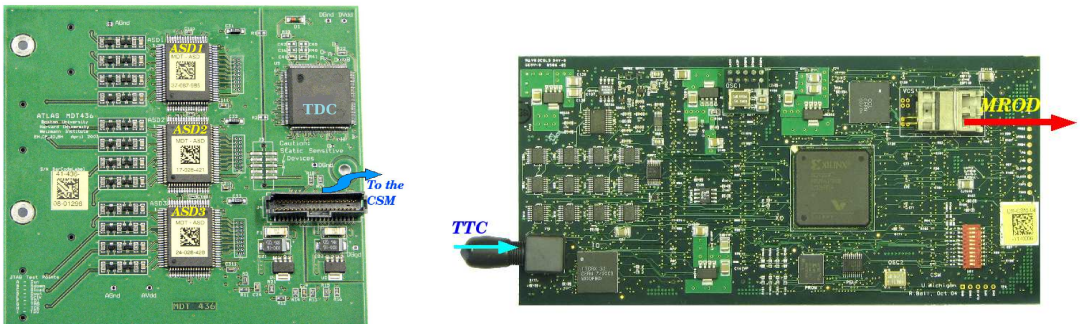

Figure 2.8: *Left: a mezzanine board for a three tube layer MDT chamber. The three ASD and the TDC chips, plus the CSM cable connector are shown. Right: a CSM board, showing the connections to the TTC and the MROD fibres.*

- **Motherboard** is a passive interconnect printed circuit board which ensemble all the informations coming from the mezzanines and it is connected to another board, the CSM (see below). It also receives the low voltage power necessary for all the chamber front-end electronics, and routes temperature readout to the ELMB.

- **CSM (Chamber Service Module)** is a printed circuit board, one for each chamber, that collects signals coming from up to the 18 mezzanine boards. It communicates with the off-chamber electronics via two fibres, one coming from the TTC distribution box and the other going to the to the ReadOut Driver (ROD). A picture of a CSM board is shown shown in Figure 2.8 right.

- **ELMB (Embedded Local Monitor Board)**, also known as **MDM (MDT DCS Module)**, is a CANbus node, one for each chambers, that reads the temperature and magnetic field values from sensors distributed over the chamber. In addition to supplying the JTAG string to the CSM (see next paragraph), the ELMB is also used to load configuration code

into the CSM and to monitor temperature sensors and supply voltages on the mezzanine boards.

ASD and TDC chips are programmed following the **JTAG protocol** (Joint Test Action Group) via a shift register. In this way, many parameters and functions can be controlled, like the setting of discriminator threshold and dead time as well as triggering of test pulses for calibration or deactivation of noisy channels. The JTAG information is distributed by the Detector Control System (DCS) through serial lines, using CANbus protocol.

An overview which depicts the on-chamber electronics on the readout side of a chamber at different stages of the assembly is shown in Figure 2.9. In particular the CSM, the mezzanine cards (before and after being covered by a Faraday cage), the MDM, and the RO hedgehog (a board which passively terminate the drift tube wires with capacitors and resistors) are well visible.

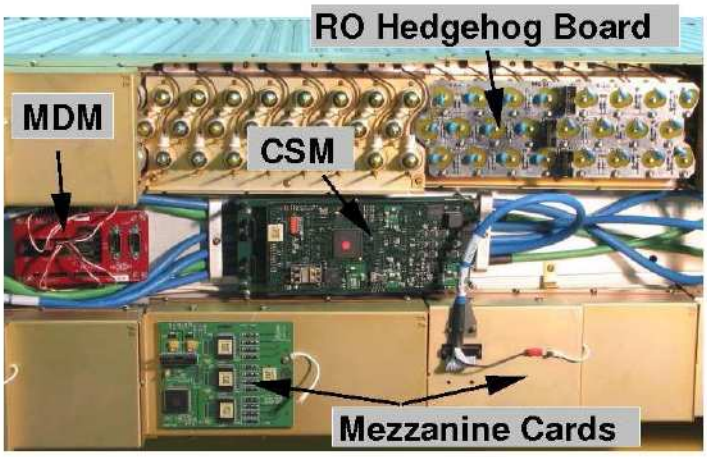

Figure 2.9: *Photograph of the read-out side of an MDT chamber at different stages of the assembly. The MDM, CSM, mezzanines and hedgehog board are visible.*

Off-chamber electronics

The CSM broadcasts the TTC signals to the TDCs and collects the hits they sent back for each LVL1 trigger (see Section 1.9). Subsequently, the data are formatted, stored in a large derandomising buffer, and sent via optical link to the **MROD (MDT Readout Driver)** in the USA15 service cavern.

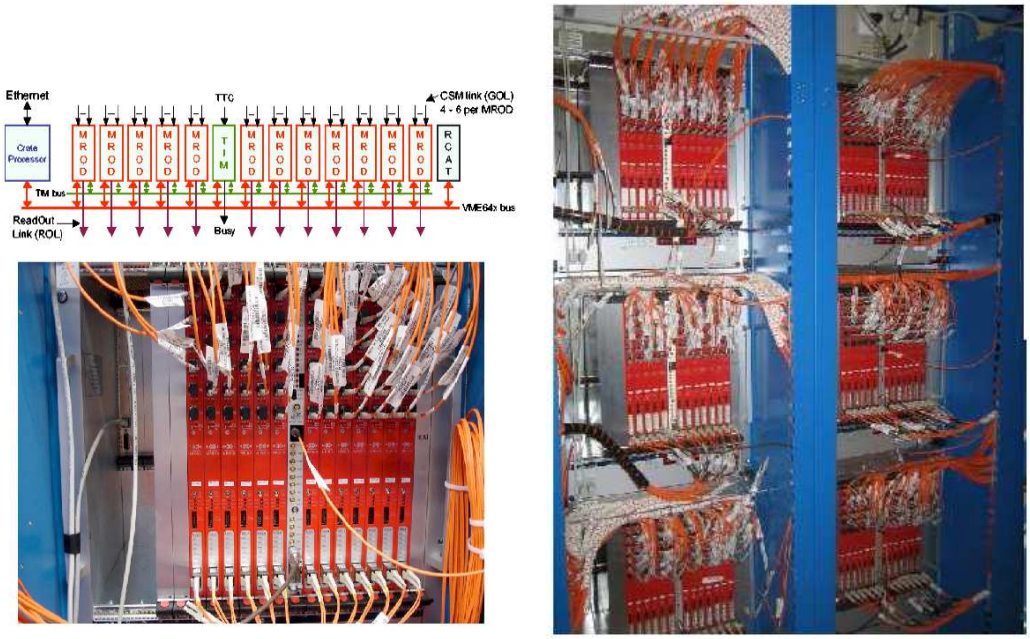

Figure 2.10: *Left: overview of connectivity of MROD modules. Twelve modules reside in a VME crate, together with a crate processor, a module for receiving TTC system information and outputting the Busy signal (TIM) and a module for reloading the flash memories in the MRODs (RCAT). The CSMs are connected via the optical fibres at the top, the fibres at the bottom are the ReadOut Links connecting to the ROBs. The fibre connecting to the middle of the TIM module is the TTC fibre, the coaxial cable connected at the bottom transports the BUSY signal. Sixteen crates house in total 204 MROD modules. Right: picture of the MROD crates located in USA15 during the cabling phase.*

The main task of the MROD is to receive the data streams from the CSMs. Being the hits associated with the track of a single muon, in most of the cases, coming from a single "projective tower", the MROD have been designed in a way to read six CSM of the same tower. In this way, for each track, only one MROD should be interested to the particular event, and the number of requests for MDT data generated by the second-level trigger for a muon "Region of Interest" (ROI) is kept low. Information from the TTC system is also received. Figure 2.10 shows an overview of the connectivity of the MRODs.

The MROD builds event fragments from the incoming time division sequences sent by the CSMs, detects and reports errors and inconsistencies in the data, where possible initiates corrective action, collects statistics and allows to sampling and analyzing the data (Data Quality). Event fragments are output via the Read-Out Link (ROL), which is an optical link using S-Link protocol and connecting to a Read-Out Buffer (ROB), from where the data can be retrieved by the Trigger/DAQ system (see Section 1.9). The length of the optical fibres connecting CSMs and MRODs is of the order of 100 m. The Muon Spectrometer is read out by 204 MROD modules, housed in 16 VME crates with 12 or 13 modules each.

Threshold scans

At the beginning of operation of MDT chambers installed into the ATLAS cavern, in particular the chambers of sector 13, we studied the behaviour of the noise level, changing the discriminator threshold.
MDT chamber electronic tests were done both with high voltage (HV) on, at standard 3080 V, and high voltage off. When HV is off, no multiplication processes can occur in the gas volume, since no electric field can accelerate ionization electrons towards the anode wire. If hits are registered when HV is off, this means that it is only electronics that generate them. As explained in [21], in order to operate the ASD chip at 5σ above the thermal noise level (75 Hz), the nominal threshold must be set[4] to Vthr = -40 mV.
For any particular threshold settings, in fact, we expect to get random noise hits which are Poisson distributed in time and a Gaussian function of threshold:

$$R(x) = R_0 \cdot e^{-} \frac{(x - V_{off}^2)}{2 \cdot \sigma^2} \tag{2.3}$$

where R_0 is the maximum rate of hits, V_{off} is the measured offset voltage of the channel, σ is the Gaussian width of ASD noise distribution and x is the threshold setting. The parameters R_0, V_{off} and σ are extracted during production chip testing for each channel and placed in the production database. Both tests at production sites and simulation studies with GARFIELD [24], suggest that the noise level decreases with an exponential law with the increasing threshold, in particular, it is found that noise rate is reduced by a factor 1/e every 2-2.5 mV. The threshold scan was performed starting from -34 mV up to -48 mV, in steps of 2 mV, both with HV on and off. For each run, the noise level per tube was calculated as described in Equation 2.4. Figure 2.11 shows the exponential trend as a function of the threshold, for a sample tube in BIL2A13. No major differences are observed between the HV on and HV off distributions.

[4]During the cosmic ray data taking a mean threshold value of -38 mV has been chosen, but with an hysteresis value of -8.75 mV. This is only an average value, in fact, each ASD, depending from its characteristics and noise level, has its proper value that is written in a database.

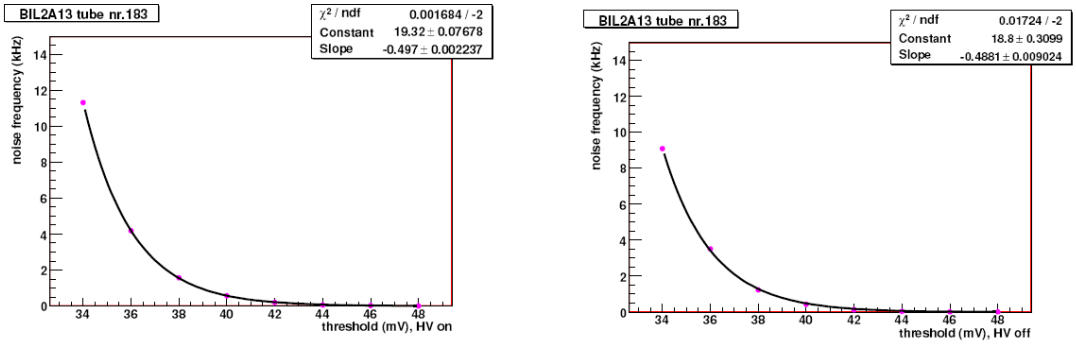

Figure 2.11: *Noise frequency as a function of the disciminator threshold for the BIL2A13, tube 183. The noise is decreasing exponentially both with HV on (left) and HV off (right).*

2.2.5 Power supplies

Low voltage (LV) power supply for the on-chamber readout electronics comes from 5 V sources being routed via shielded cables to the motherboards from where power is distributed to the mezzanine boards, separately for the analog and digital circuitry. Each mezzanine board draws about 270 mA for the analog part and 140 mA for the digital part at about 4 V.

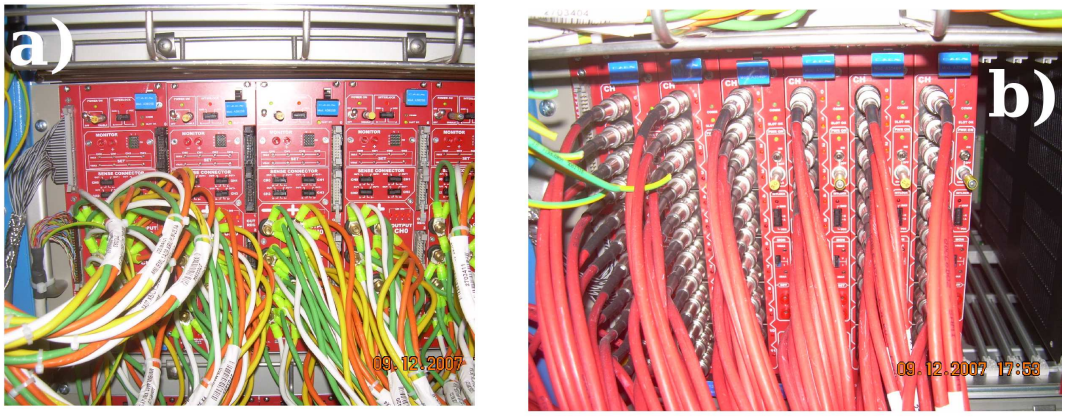

Figure 2.12: *Photograph of the crate with Low Voltage CAEN DC/DC Modules connected to the chambers (a) and high voltage modules (b).*

Low-voltage power muon system distributors are located in electronics racks on the outside of the muon system. One low-voltage channel supplies two MDT chambers in parallel, consequently connecting their grounds. The low voltage system chain consists of DC/DC distributors (2-8 V, 25A per channel), hosted in crates inside the collision hall (Fig. 2.12 a) that are remotely controlled and monitored by computers outside the hall, and AC/DC converters (48V), lo-

cated in rack on the service hall PX, which is adjacent to the ATLAS collision cavern. For safety reasons, and to avoid ground loops that can increase the chamber noise, all the system is properly grounded.
High voltage power is generated in the same racks as the low voltage (Fig. 2.12 b), and is distributed via coaxial cables to the chamber end opposite the RO. For the high-voltage DC/DC distributors the nominal output is 3080 V with a maximum current of 1 mA per channel. One high-voltage distribution channel supplies one MDT multilayer and is split at the detector into separate lines for the individual tube layers. This is done via a passive splitter circuit containing a low-pass filter to reject high frequency noise.
A PVSS interface integrated into the general ATLAS DCS controls and monitors the power supply remotely, recording the history of changes in voltage and current.

2.3 Track reconstruction

ATLAS employs a variety of strategies for identifying and reconstructing muons, in particular there are three strategies: reconstruction in stand-alone, combined and tagged.

Standalone tracking algorithms These algorithms reconstruct standalone muons by finding tracks in the muon spectrometer and then extrapolating these to the beam line. There are two main stand-alone algorithms, called Muonboy [25] and MOORE [27]. Both of them use three step in order to find tracks:

- The first pattern recognition is performed at a level of single multilayer, starting from a "Region of Activity" derived from the LVL1 trigger chambers. Patterns are defined by a collection of hits (circles in the drift tubes derived from the time-radius relation) consistent with a trail left by a passing muon. These patterns are called "segments".
- The second step is a track fit to each pattern at a level of single chambers. If the best χ^2 of the fits to the patterns is below the χ^2 cut, the corresponding pattern is accepted as belonging to a valid track. Otherwise the procedure is repeated for sub-patterns with one hits less and so on. If no track is found that satisfies all cuts, the pattern is rejected;
- The last step is the combination of track segments of individual chambers into a "global" track, taking into account also effects due to magnetic field and passive material.

At this point tracks are extrapolated to the interaction point[5], taking in account the energy loss in the calorimeters. Muonboy treats the energy loss

[5]In the case of cosmic ray reconstruction, this constraint is released.

by parameterization and MOORE uses calorimeter measurements when available. The trajectory is parametrized by five parameters: the charged inverse momentum (q/p), track angles (θ and ϕ) and coordinates of the perigee (d_0 and z_0). The covariance matrix of the parameters is also provided.
Standalone algorithms have the advantage of a slightly greater $|\eta|$ coverage, out to 2.7 compared to 2.5 for the inner detector, but there are holes in the coverage at $|\eta|$ near 0 and 1.2. Very low momentum muons (around a few GeV) may be difficult to reconstruct because they do not penetrate to the outermost stations. Muons produced in the calorimeter, *e.g.,* from π and K decays, are likely to be found in the standalone reconstruction and constitute a background for most physics analysis.

Combined tracking algorithms Combined muons are found by matching standalone muons to nearby inner detector tracks and then combining the measurements from the two systems in a single track. There are two combined tracking algorithms: STACO [25], and MuID [26]. STACO associates Muonboy and ID tracks statistically using those covariant matrices. MuID combines the MOORE and ID tracks by global fitting using the original measurements in MS and ID. Combined tracks have better p_T resolution than the ones in standalone over the full p_T and η range.

Tagged tracking algorithms The third strategy is the one implemented by tagging algorithms, that are used to extend the acceptance to lower p_T and fill the efficiency gap in the transition region between barrel and endcap. They extrapolate inner detector tracks to the spectrometer detectors and search nearby hits. There are two algorithms of this type: MuTag [25] and MuGirl [28]. MuTag defines a tag chi-square using the difference between any nearby segment and its prediction from the extrapolated track. MuGirl uses an artificial neural network and creates MS segments by fitting and refits the ID track with the hits from the segments.

The muon finding efficiency (and fake rate) may be increased by including muons found by multiple algorithms but care must be taken to remove overlaps, *i.e.,* cases where the same muon is identified by two or more algorithms.

2.4 Calibration of MDT chambers

The muon precision chambers require an accurate calibration procedure in order to convert the measured drift times (t) into drift distances (r) from the anode wire (drift radius) that are subsequently used into patter recognition and track fit procedures.

The space-time relation is not constant, but depends on gas properties (composition, pressure, temperature) and on the magnetic field. Gas conditions have dramatic effects on segment residuals of the track fit; it has been studied [29] that even a 12-hour difference can change the gas conditions and hence can cause as effect up to 10-20 μm upon the segment residuals. In Figure 2.13 two r-t relations for MDTs in the end-cap, taken in different period of cosmic data taking, are shown[6]. The black/dashed curve is taken during the fall 2008, the red/solid curve corresponds to the detector conditions on January 2009. In the Figure is also possible to see that this relation is highly not-linear, and this shape is a characteristics of the Ar:CO_2 gas mixture.

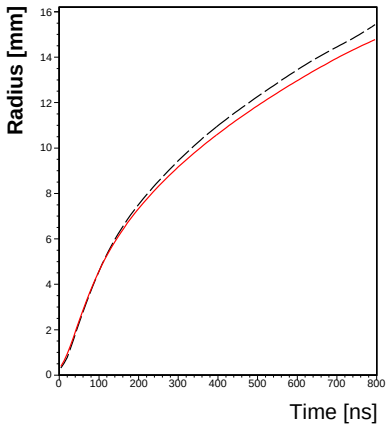

Figure 2.13: *r-t relation for end-cap MDT chambers extracted in two different period of cosmic data taking.[29]*

We also know that chamber gas temperature can vary by $\mathcal{O}(6°C)$ between the top and the bottom of the ATLAS detector, as is clearly visible from Figure 2.14 that shows the DCS report from the temperature probes upon MDT chambers.

Being the r-t relation dependent from the local conditions of the gas, the calibration should be done for each tube of each chamber. However, the model adopted for the calibration of the MDT spectrometer divides the whole spectrometer into a number of calibration regions, each region corresponding to a chamber, and each using a unique calibration parametrization. In order to limit the number of calibration regions and to keep the corresponding data collection and analysis to a manageable size, the data inside a region are corrected for local differences in environmental parameters (mainly B field) and reduced to the same nominal drift conditions.

Then, the space-time functions are computed with an iterative method, using the data themselves, and the procedure is applied until the quality of the track fit is satisfactory. This procedure is called "auto-calibration", and gives the possibility to derive the space-time relation for each MDT chamber in situ, in

[6]In the end-cap, given the low cosmic ray illumination, these calibration functions are made using a special gas monitoring MDT chamber on the surface, through which the gas supply flows.

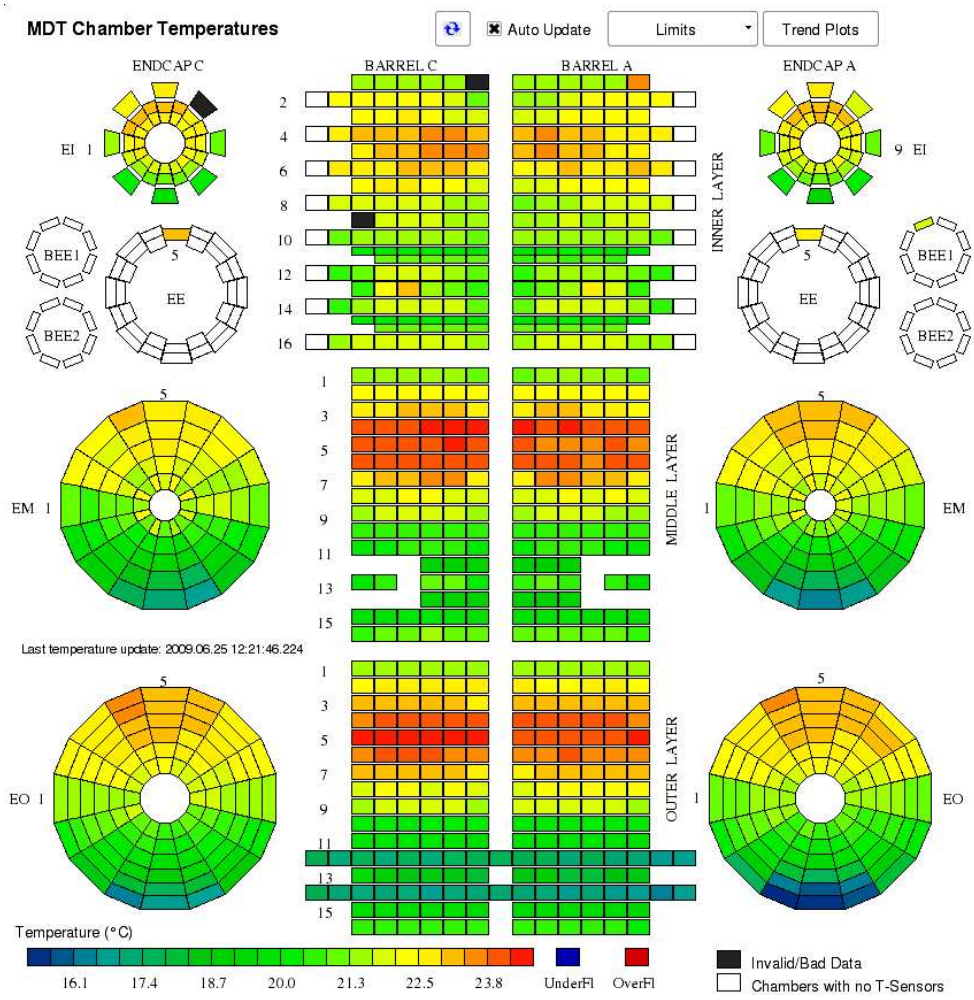

Figure 2.14: *Temperature scan of all the MDT chambers as seen from the DCS panel. A difference of 5-6° C between upper and lower sector is visible.*

a self-consistent way in any operating condition, and eliminating the need of a priori knowledge of the r-t relations for any operating condition[7].

The TDC spectrum The starting point of the MDT calibration is the TDC spectrum (the distribution of drift times as measured by the TDC), that is characterized by two parameters: the "start" time t_0 and the "maximum drift time" t_{max}.
Due to different time delays caused by different read-out cable lengths, FE electronics response, LVL1 trigger latency or time of flight of the muons, the

[7]Ideally, if all parameters were correctly measured and their influence on the r-t function were completely known: r-t(B, T, etc..), only one r-t function would be sufficient for the entire MDT system, independent of time. In reality, however, the corrections and environmental conditions are not known with sufficient precision.

drift time measurements of different muon chambers are in fact not synchronized. In order to determine the effective drift time of the hits produced in the drift tubes, the t_0 (the "start" time), has to be determined for each detector element. Qualitatively, tracks with drift time $\sim t_0$ pass near the wire, while drift times $\sim (t_0 + t_{max})$ are caused by tracks passing near the tube.

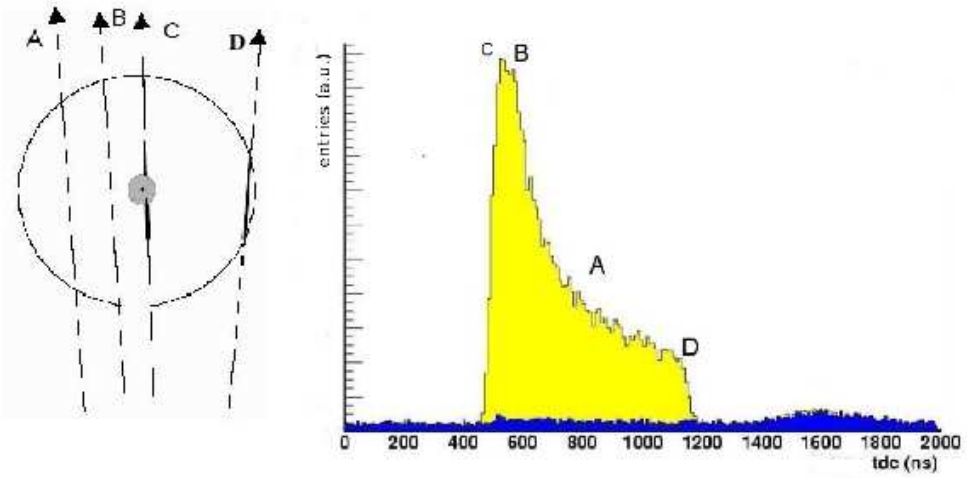

Figure 2.15: *Right: an example of TDC spectrum (yellow) with flat superimposed noise counts (blue); each part of the spectrum is due to muons passing in different points of the tube with respect to the wire (left).*

In Figure 2.15 on the right it is shown a typical TDC spectrum; the blue baseline represents the noise that is randomly distributed on the time windows, the yellow spectrum is associated to muons tracks passing thought the drift tube. The spectrum can be divided in four different zones, each of them correspond to a different distance from the wire of the muon. Muons passing near the wire (C) cause a sharp peak on the TDC spectrum, that corresponds to the t_0; muon passing near the tube wall (D) cause the tail trailing edge of the spectrum (t_{max}). The peak after the trailing edge is due to the shape of the radial electric field; cluster created in the avalanche region are, in fact, suddenly collected. A more detailed analysis of TDC spectra from cosmic rays during the commissioning phase is reported in Section 2.7.1.
The TDC distribution, in particular the length of the drift time, is also influenced by the presence of the magnetic field, that lengthen the path of electrons and slows down their velocity, as is shown in Figure 2.16 that displays how the TDC spectrum of the same MDT chamber is influenced by the presence of the magnetic field.
The calibration of the MDT chambers is performed in three steps using the acquired data: in the first step the drift-time measurements of the individual chambers are synchronized (t_0 determination), in the second step the space drift-time relationships (r-t relations) are determined, in the third step the spatial resolutions of the drift tubes are measured.

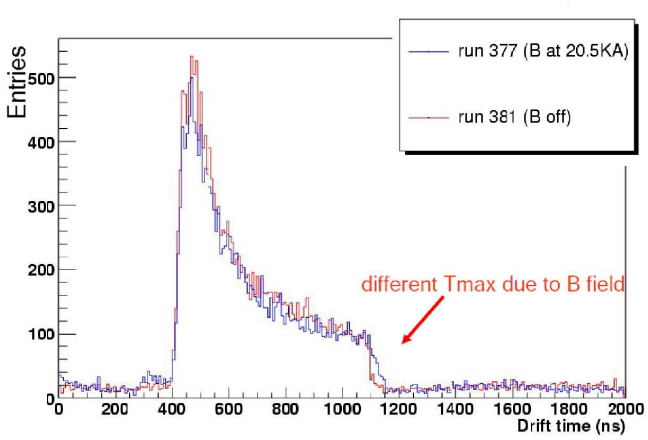

Figure 2.16: *TDC distribution of the same chamber with (blue line) and without (red line) the toroid magnetic field.*

An initial rough estimate of r-t is obtained with an accuracy of 0.5 mm by integrating the drift-time spectrum of a chamber by approximating the spatial hit distribution dn/dr by the number of hits divided by the inner tube radius in the equation relating the drift-time spectrum dn/dt with the drift velocity dr/dt:

$$\frac{dn}{dt} = \frac{dn}{dr}\frac{dr}{dt} \approx \frac{N_{hits}}{r_{max}}\frac{dr}{dt} \Rightarrow r(t) \approx \frac{r_{max}}{N_{hits}} \int_0^t \frac{dn}{dt'}\, dt'.$$

An r-t relationship with significantly higher accuracy of about 20 μm is obtained from the initial estimate by applying iterative corrections $\delta r(t)$ which minimize the residuals of track segments fitted to the hits of chambers. The adopted minimization procedure, takes into account the dependence of the parameters of the fitted segment on the applied corrections $\delta r(t)$ and is based on geometrical constraints coming from the precise knowledge of the wire positions.

The spatial resolution of the drift tubes can be deduced from the width of the residual distribution. In Figure 2.17 a segment of muon track crossing a multilayer of an MDT chamber and the drift radii with which the track has been built are shown; on the right of the figure an example of residual distribution obtained from firsts cosmic data is shown, it shows an RMS value of 160 μm, that is a first step of resolution towards the goal of 50 μm precision on the muon sagitta measurements. In cosmic ray events in addition to the constant time offset several variable delays, time jitters, are spoiling the t_0 determination procedure: the FE electronics clock is not synchronous with the muon crossing time, and the time of flight between trigger chambers and precision chambers can vary depending on cosmic trajectories.

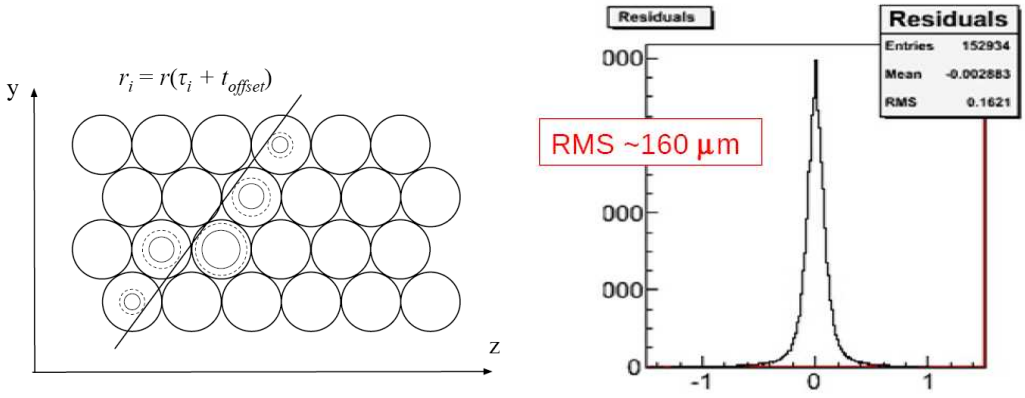

Figure 2.17: *Left: a cosmic ray crossing the MDT tubes and the radii with which the track has been built. Right: the residual distribution with RMS of 160 μm.*

2.5 Alignment system

As explained above, the ATLAS muon spectrometer employs an air-core toroid magnetic field, which has the advantage of causing only minimal multiple scattering due to the small amount of material present between chambers. As a consequence of this design, however, a relatively low and inhomogeneous magnetic field strength can be achieved, causing the bending of a 1 TeV muon track is such that the track sagitta varies between 0.5 mm at pseudorapidity $\eta = 0$ and 1 mm at $\eta = 2$. Consequently, in order to measure the momentum of a 1 TeV muon to 10% at all angles, the resolution on the sagitta measurement must be better than 50μm in the bending direction of the magnetic field, transverse to the MDT tubes, and the additional contribution to resolution coming from the chamber alignment should not exceed that value.
Given the large scale of the spectrometer and the number of chambers, it would be extremely difficult or even impossible to keep the geometry of the chambers and their positions stable on the scale of the required accuracy of 50 μm. Therefore a different approach was chosen for alignment: the chambers have been positioned with a precision of about 1 mm and 2 mrad with respect to their nominal position. In order to achieve more than two orders of magnitude tighter in positioning accuracy, an alignment system was built which relates the position of each chamber to that of its neighbors, both within an MDT layer and along r-z trajectories within MDT towers. In this way, the chamber movements and deformations will be continuously monitored, and the measured deviations from the ideal geometry are used as corrections in the offline track reconstruction. A schematic representation of the alignment system in a large sector is shown in Fig.2.18.

Due to different geometrical constraints, the alignment strategies are somewhat different in the barrel and end-cap regions and several specialized optical

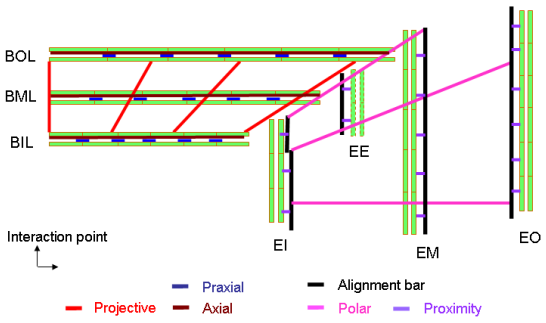

Figure 2.18: *Schema of the alignment of the ATLAS Muon Spectrometer.*

alignment sensors have been developed.
In the barrel, the chambers inside an MDT row are referenced to each other by chamber-to-chamber alignment sensors (praxial and axial systems, see Fig 2.18), while the projective system connects the inner, middle, and outer MDT layers, simulating the trajectories of an infinite-momentum track originating from the interaction point[8]. This optical network is able to reliably detect relative changes in chamber position at the 20 μm level. However, because of its essentially projective configuration, it remains insensitive to some specific geometrical distortions, and therefore unable to provide absolute chamber positions on its own. Additional optical lines link MDT chambers to the barrel toroid cryostat, or relate adjacent chambers in large and small sectors.
In the end-caps, the light path between the inner and the middle layer is obstructed by the cryostat vessels of the toroid magnets. The polar alignment therefore proceeds in two steps using high precision rulers (alignment bars), as an intermediate reference. The polar (quasi-projective) optical lines connect the alignment bars installed in each EI, EM and EO layer; the chambers, in turn, are optically connected to their neighboring bars by proximity sensors.

Three different optical systems are used in the ATLAS alignment; all three systems are based on the principle of a three point straightness monitor: an optoelectronic image sensor (CCD or CMOS) monitors the position of an illuminated coded mask through a lens. The sensor image is analyzed online and converted into parameters characterizing the deviation from the nominal geometry: two translations perpendicular to the optical axis, and the rotation around and the longitudinal position along the axis, the latter is derived from the optical magnification.
An internal chamber alignment system (in-plane alignment) was also imple-

[8]In the barrel, the projective system works in this way: BIL chambers hold the mask, BMLs the lenses and BOLs the image sensor. Chambers in the small sectors (BIS, BMS and BOS) are not equipped with projective lines and are referenced to the adjacent large chambers by Chamber-Chamber Connection sensor (CCC).

Figure 2.19: *View from an in-plane alignment lens within an MDT chamber [30].*

mented, which continuously monitors potential deformations of the frame of each cambers. The alignment system consists of a set of four optical alignment rays, two running parallel to the tube direction and two in the diagonal direction (red lines in Figure 2.5). The lenses for the light rays are housed in the middle, while LEDs and CCD sensors are located in the outer spacers. This system can record deformations of a few μm and was designed to operate during production, installation, and operation of ATLAS.
It is worth to notice that the optical alignment techniques are insufficient to reconstruct, on their own, the absolute positions of the MDT barrel chambers: only variations in relative position can be determined with the required precision. Track-based alignment algorithms must therefore be used[9] in combination with the optical system to achieve the desired sagitta accuracy, and also to determine the global positions of the barrel and end-cap muon-chamber systems with respect to each other and to the inner detector, in the overall ATLAS reference frame. Some results of alignment with cosmic rays during the commissioning phase are reported in Section 2.9.1.

[9]The useful runs for the alignment with tracks are the one taken with no magnetic field.

2.6 Commissioning of MDT chambers

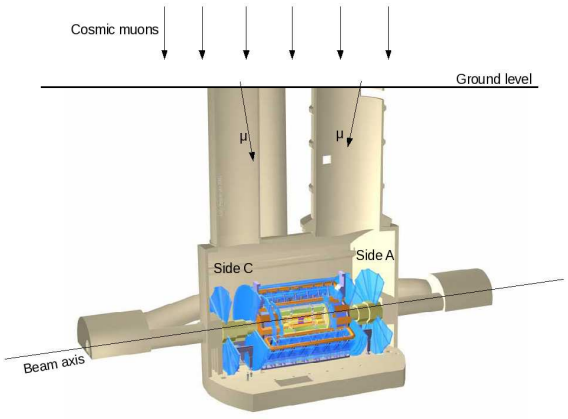

Figure 2.20: *Cartoon of the ATLAS experiment and its cavern. The two shafts, through which cosmic rays can reach the detector, are shown.*

The commissioning activity of MDTs, as all the other ATLAS detectors, is organized in a series of tests, first at the level of single chambers, and then on the ATLAS system as a whole. The goal of the commissioning phase is to understand the behaviour of the detector in situ, in order to be ready to register first LHC data. MDT commissioning is divided in three levels of tests, whose goal is to check the integrity of single chambers also after providing final services, to integrate them in the ATLAS data acquisition system, and to study their performances in combined runs with cosmic rays first, and with Standard Model processes, once collisions will be delivered.
The early in-situ cosmic studies started during the summer 2005, and involved just few chambers of the lower sectors of the spectrometer. As more and more chambers were installed in the spectrometer and have passed a preliminary integrity test, they were included in cosmic data taking. These cosmic runs were performed both in stand-alone mode, with detectors of the muons spectrometer involved, and in combined mode among all the ATLAS detectors ready for data taking. Cosmic runs have been valuable to develop and commission beside the detectors, also trigger and data acquisition chain, together with the online and offline data quality monitoring tools. Moreover reconstruction software took advantage of combined runs. Such cosmic runs have provided vital input into the readiness of the detector prior to first collisions by identifying dead or inefficient channels, verifying the timing, alignment, and signal reconstruction of the various subdetector; and providing the initial calibration constants of the experiment.
In September 2008 almost all the ATLAS subdetectors were ready to register the first collisions from LHC that delivered the first particles through ATLAS on the September 10th. The first events (splash events against collimators)

were recorded. Unfortunately the LHC accident forced a long (more than 1 year) shut down of the collider (see Section 1.1.2), but the ATLAS detector kept running for almost three months with cosmic rays, in order to going on with the commissioning phase, and acquire as much data as possible for calibration and alignment purposes. In this way the detector should be much more understood and ready for early collisions.

2.6.1 Overview of commissioning procedures

The high reliability of the MDT chambers was assured by a series tests, from the 11 production sites all over the world to their final position in the ATLAS cavern. At the production sites, each chamber was certified at a level of single tube and also after the assembly (gas tightness, dark currents, mechanical tension and wire centering were measured). Once at CERN, all the chambers have been equipped with their full read-out electronic chain, and middle and outer chambers have also been integrated with their own RPC detectors. Once chambers were provided with their final cabling, cosmic rays have been acquired to look again at the single tube response and noise level. Then the chambers have been moved to the SX1 experimental area, that is the surface site above the ATLAS cavern. Further noise and pulse tests have been performed to ensure that chambers suffered no damage during the transport to SX1. At this point, chambers were installed, one by one, on the ATLAS muon spectrometer support.
After that, they were required to pass the final three level commissioning certification:

- **Level 1**. Just after installation, quick integrity tests were performed on individual chambers, such as gas tightness. High voltage was provided to each tube layer in order to exclude presence of shorts. Once chambers were slided to their final position, low voltage, front-end electronics initialization, temperature and B-field sensors were also checked.

- **Level 2**. Chambers were connected to their final services: high voltage supply lines were connected from MDT layers to power supplies; readout data fibres were connected from CSMs to their respective MROD channels; low voltage supply lines were powered up; gas connections were secured and the chambers were flushed with fresh gas from the MDT gas circulation system; temperature monitoring and optical alignment data were read out.

- **Level 3**. Chamber passing Level 2 tests were integrated in stand-alone run first, using random triggers (both HV on and off), and in combined runs in a second stage. High rate tests, up to 100 kHz, has also been performed. The main goal of a stand-alone run is a low-level analysis of MDT performance, like checking the readout of every mezzanine and

to find noisy or dead tubes. These runs are intended to provide high statistics datasets, very useful to spot several type of problems on the chambers quickly during the period of commissioning, in order to allow some opportunity for remediation.
The Level 3, high-level analysis extends beyond specific measurements of individual tube and electronic channels and includes measurements of overall chamber performance.

2.6.2 Online Monitoring System

The challenging experimental environment and the extreme detector complexity impose the necessity of a common, scalable, distributed monitoring framework [32, 33], which can be tuned for optimal use by different ATLAS subdetectors at the various levels of the ATLAS data flow.
The monitoring tools used for the commissioning of MDTs, that are also used for the others detectors, are the following:

- **GNAM** (GNAM is Not AtlMon[10]) is an Online Monitoring framework developed to monitoring ATLAS detectors. This application has been designed mainly to monitor the detector status and to quickly access run conditions, and to check the hardware conditions (*i.e.,* dead/noisy channels, electronic mappings) as well as the data quality (*e.g.,* synchronizations among different detectors). A schema of GNAM is reported in Figure 2.21. The GNAM framework samples physics events at all DataFlow levels (ROD - ROS - SFI - SFO) and build histograms out of the event data. It also allows to publish those histograms via the Online Histogramming Service.

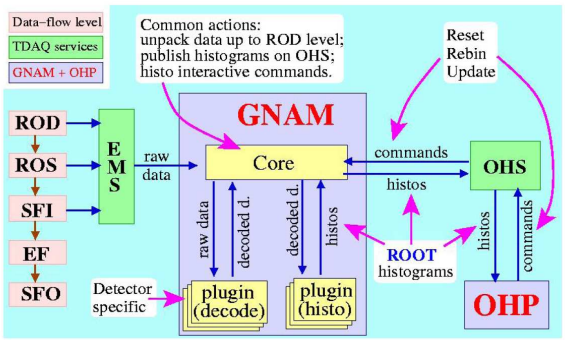

Figure 2.21: *Schema of the GNAM monitoring framework and its interaction with the other DAQ tools.*

[10]When this project was started, the most natural name was AtlMon; as it was already used by a completely different application, it was turned to this recursive acronym, in pure GNU-like style.

- **OHP** (Online Histogram Presenter) is a stand-alone application that displays and organizes the GNAM histograms, with predefined configuration and allows for browsing the full number of histograms.

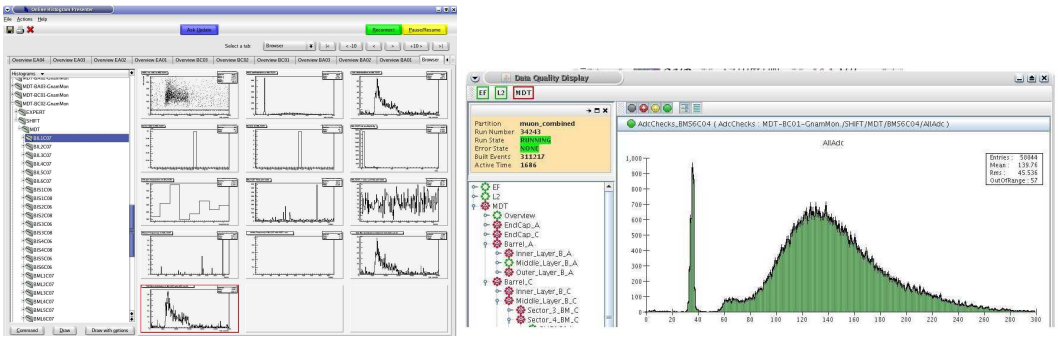

Figure 2.22: *Screen-shots of the OHP panel (left) and DQMF panel (right).*

- **DQMF** (Data Quality Monitoring Framework) allows shifters to browse through a subset of GNAM histograms, which are automatically tested and flagged for problems. With a rate of million of histogram updates per minute during the global ATLAS running, in fact, it is practically impossible for a shifter to check by eye the status of all histograms during the run. DQMF perform automatic checks of histograms, providing analysis algorithms to them, according to a user defined configuration. The output of DQMF are histograms presented with a color code, depending from the results of the algorithms. In this way is much more easy to identify problems in the chambers marked with red color.

- **gnaMon** is a graphical interface to display monitoring histograms produced by GNAM for the MDT chambers. This has been used to spot main problems on the chambers both online that offline, during the commissioning phase. In particular algorithms for identifying dead and noisy elements have been implemented.

2.7 Hardware commissioning

The problems that we encountered during the commissioning of installed chambers were different, but they can be classified in six groups, each of them was treated with different priority:

- **Low voltage problem**: this problem can be spotted from the DCS panel. This is the most important problem because without power supply to the front-end electronics it is not possible to do any other test to the chamber. This can be due to problems with the power supply module, or in the communication between the mainframe and the LV module, or with any connectors in the chain from the power supply to the motherboard and CSM.

- **Initialization problem**: not being able to initialize the chamber electronics though the JTAG interface may be caused by an interrupted or bad connection between the TTC clock signal transmitted through optical fibre from USA15 to the CSM, or to a broken CSM board.

- **Readout problem**: this problem can be spotted from both noise standalone or cosmic runs looking at the monitoring histograms. Some failure in the readout chain from the CSM to the MROD results in empty monitoring plots for the chamber under test. In many cases this problem is due to broken optical fibres[11]. It may also be caused by the swapping of fibres between different chambers, both on the chamber side, and in the MROD modules. Or again, from the CSM board that could be broken or with the firmware not up to dated.

- **Gas problem**: this can be caused by a leak on either the chamber or on connections. In the latter it may affect all the chambers connected to the same line. Gas problems are related both to the leak of gas and the contamination with water. When these problems occur it is not possible to switch on the HV, to avoid chamber damage due to sparks.

- **High voltage problem**: as the LV problem it can be due both to the power supply, or to a bad connection to the chamber[12]. In many cases metallic dust that went through the faraday cage, due to installation works, can cause a short.

- **DCS/ELMB problem**: these problems can cause the not correct initialization of the front-end electronics, they are often caused by a wrong or broken connection of the CANbus chain between adjacent chambers or between the motherboard and the ELMB box on the chamber.

[11] During commissioning tests, in fact, work on the chamber side was still going on, in particular for the installation of other detector component. Optical fibres are very fragile, and many of them have been damaged.

[12] In order to avoid sparks that can damage the drift tubes, every HV cable from the power supply to the chambers have been tested before being connected.

- **Minor problem**: many other minor problems could occur, they are classified as "minor" because do not interfere with the chamber commissioning tests, and could be solved later. Problems of this kind can be a single mezzanine not working, or some temperature or magnetic field probes broken etc....

During the commissioning a database containing informations of the status of the chambers and accessible via web was particularly useful. Figure 2.24 shows a screen-shot, displaying all the MDT chambers of each station with different colors depending from their status (OK, HV problems, LV problem, Gas Leak, DCS problems, Readout problems, Minor problems). In this particular screen-shot many chambers with different problems are visible. In the same database, clicking on a particular chamber, it is possible to see all the thread of interventions that has been done in order to fix each problem. An example is reported on the lower part of Figure 2.24 (that particular list has been chosen because report a wide spectrum of problems relative the hardware commissioning).

Problem type	
HV Bad cable/connector	2
HV broken wire	4
HV broken channel	2
LV short or bad/short cable	10
TTC/RO broken PC	16
TTC/RO bad connection	4
RO long fiber splice	3
DCS ELMB exchange	3
DCS B-sensor short	1
Broken DCS chain	3
GAS broken tubes	4
Broken mezzanine	6
CSM Exchange	7
Motherboard exchange	1
Other cabling interventions	18
Not understood	5
TOTAL	89

Figure 2.23: *Statistic of problems encountered during a 6-months period of continuous commissioning.*

Usually, problems are spotted by the MDT shifter during stand-alone, or cosmic runs, and are reported in the database. Experts will work on those issues after the run period, when they can access the experimental cavern, and use the data acquisition in stand-alone mode in order to debug the problematic chambers in a more efficient way, thus avoiding interference with the data taking.
During the commissioning phase for the first time every chamber was active for long periods, allowing also to check the stability of the system. A number of new problems not encountered in previous short tests occurred, like loosing front-end electronics initialization, or setting busy in data acquisition. This required a lot of software optimization work, especially from the data acquisition point of view and also on CSM firmware programming.
In Figure 2.23 a table showing a statistics of different problems encountered from the beginning of the commissioning phase up to December 2007, after almost six months of regular commissioning is reported. The number of chambers that needed any kind of interventions was 89, about 25% of the total chambers commissioned at that time.

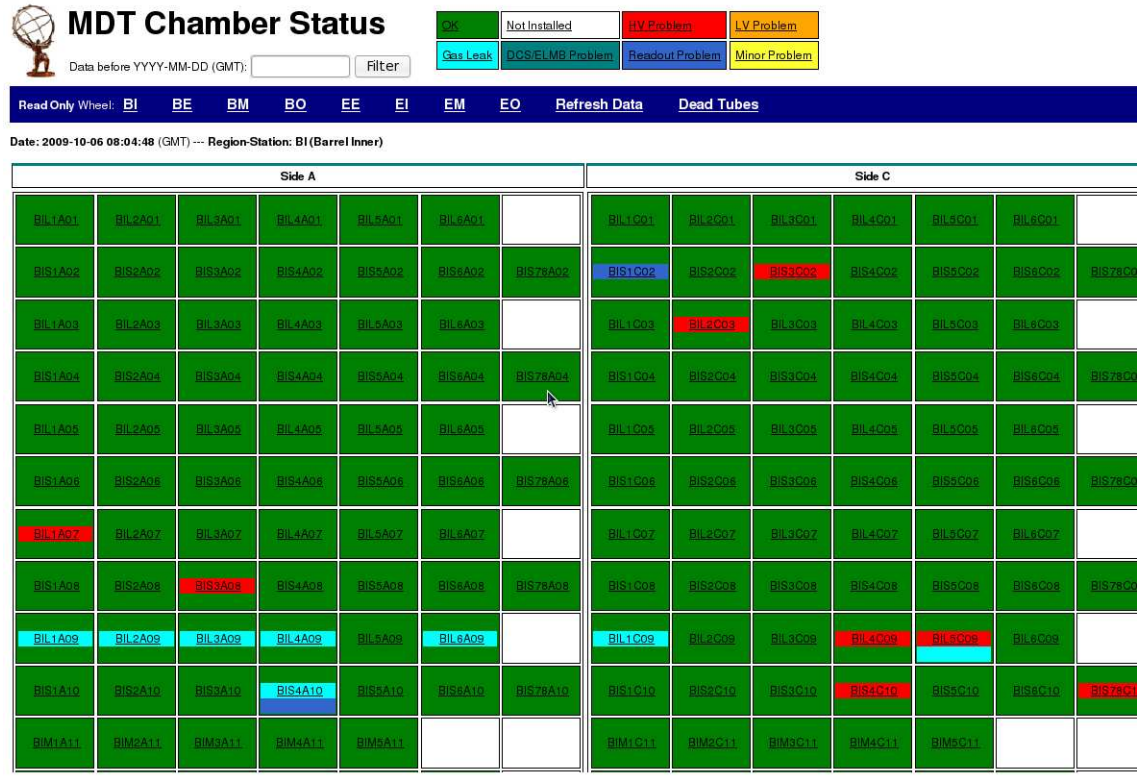

OK Readout Problem	2009-01-24 14:49:59	jdubb		Mezzanine card #3 dead in run 100918
OK	2009-01-19 13:06:02	jdubb		ML1 was drawing ~30 uA current in last month. Measured again, current is down to acceptable values, but still high. Probably related to lower humidity in UX15 (currently only 25%, was 40-50%). DCS HV interlock lifted. Should be further monitored. Cables from HV splitter box to hedgehog cards labeled wrong: 2 labeled ML1/2, ML1/1 does not exist. HV mapping of tube layers might therefore be wrong and has to be verified.
HV Problem	2008-11-08 17:55:40	jdubb@CERN.CH		HV problem persists, ML1 still draws ~25 uA
HV Problem	2008-08-08 13:52:56	vonloeb@CERN.CH		After discussions: not clear if chamber should be operated until its clear weather short is external or internal to the tubes (but looks external since it's on 3 of 4 layers)
OK HV Problem	2008-08-07 16:44:38	vonloeb@CERN.CH		ML1 draws 27 uA in total, ramp up possible with higher trip limit
HV Problem	2008-08-07 15:57:25	jdubb@CERN.CH		ML1: 27 uA @ 3080V | layer1: 10 uA | layer2: 10 uA | layer3: 6 uA | layer4: 160 nA
OK	2008-07-30 16:59:56	ventura@CERN.CH		mezz 3 reads out OK rn:)
Readout Problem	2008-07-11 10:18:48	tsarouch@CERN.CH		BIS4C14 mezz num 3 (starting frmo 0) excluded from run
OK Readout Problem	2008-07-10 18:57:54	franchin@CERN.CH		replaced CSM. To investigated if it's ok now
Readout Problem	2008-07-03 17:12:07	franchin@CERN.CH		ok fibers
Readout Problem	2008-06-23 21:13:21	emountri@CERN.CH		HV plugged
HV Problem Readout Problem	2008-06-19 13:56:58	emountri@CERN.CH		TDC L1ID error -> setting MDTs busy
HV Problem	2008-05-15 19:37:20	iodice@CERN.CH		HV UNPLUGGED

Figure 2.24: *Top: screen-shot of the MDT chamber status database used for the commissioning of the MDT chambers. Each box represent an MDT chamber, and colors represent the status: green = ok, blue= readout problems, light blue = gas leak, red = HV problem etc... Bottom: the thread of interventions on a specific chamber in order to solve each problem and make it working.*

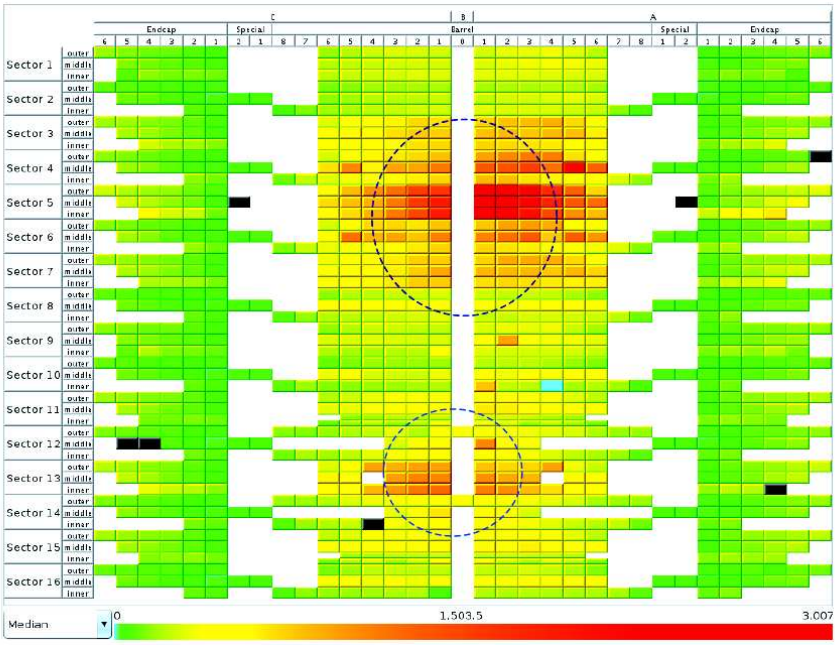

Figure 2.25: *Screen-shot of gnaMon monitoring application displaying the MDT hit occupancy for all ATLAS MDT chambers. Each chamber is represented by a small box.*

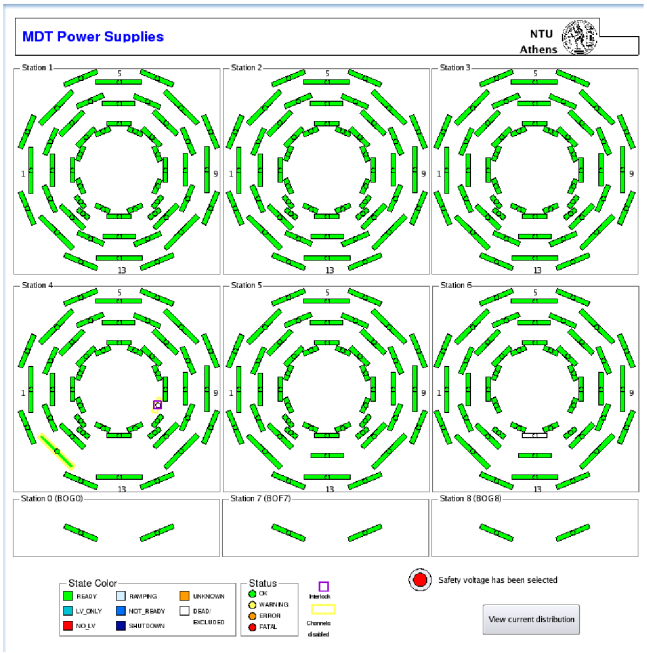

Figure 2.26: *Screen-shots of the DCS panel showing the situation of the LV and HV for each chamber of the barrel, side A.*

The hardware commissioning phase, at least for the more serious problems, was concluded in August 2008, in preparation for the first LHC collisions. When the cavern was re-opened during winter 2009, a lot of hardware work was completed and many secondary problems have been solved. Overall the MDT system is now in a very good shape, with a 99.3% of channels working, as observed during the combined cosmic ray acquisition in July 2009 (Table 1.4). A screenshot of the gnaMon application, taken during that data taking period, is shown in Figure 2.25. The colour of the box is related to the median number of raw hits per tube in that MDT chamber using a logarithmic scaling. Two regions much more illuminated by cosmics are well visible; they corresponds to sector 5, and 13, in which chambers are horizontal and hence have the mayor acceptance for cosmic muons. The seven chambers not included in the data taking are marked by dark grey boxes.
In Figure 2.26 a screen-shot of the DCS panel, taken during the combined run in July 2009, is shown; it summarizes the situation of HV/LV for all the chambers of the barrel, side A. Being almost all the chambers marked as green this means no power supplies problems occurred.

2.7.1 Data quality

As already said, the online monitoring tools were very useful during the commissioning phase, in order to spot problems related to the output signals of the chambers. Looking at online monitoring histograms it is possible to focus on the fundamental and most critical aspects of MDT functioning, such as:

- determination of isolated faulty tubes and electronics channels;
- identification of the morphology of electronics related faults at various levels of chamber granularity. The morphology of a fault helps determine if the source is an isolated electronics channel, an high voltage problem, a gas problem, or related to an ASD chip, a CSM module or MROD channel;
- visual determination of the integrity of the TDC spectra;
- chamber electronic noise frequency and hit occupancy.

Hit profiles

Particularly useful in order to identify dead channels are the hit profiles; the correct relation between electronics channels, coded in the databases, and the geometric tube position is obtained from mapping file, which is read by the analysis program. Figure 2.27 shows a hit profile of all the chambers of sector 10. It is possible to see that the chamber BIS5A10 has a readout problem, in fact, it does not have any hit. The chamber BMS5A10 has low number of

entries, and this can be due to a faulty connection between the CSM and the MROD, and BIS1A10 is very noisy.

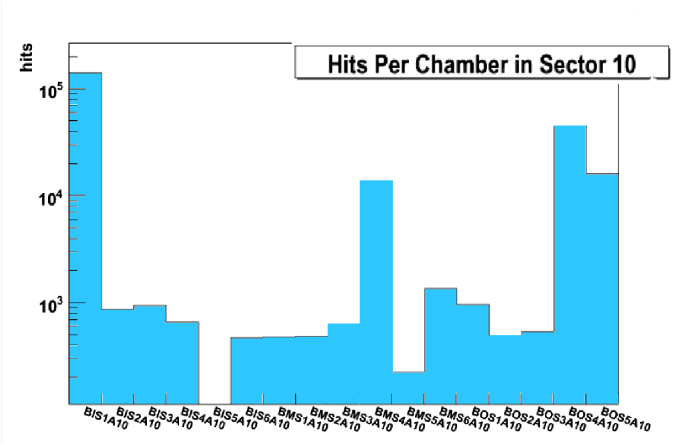

Figure 2.27: *An example of a GNAM plot for the monitoring online. In this case the hit multeplicity per chamber for all the chambers of sector 10 is shown. From the plot we can see that chambers BIS5A10 and BMS5A10 have some readout problems.*

In Figure 2.28a a two dimensional hit profile showing the number of entries per mezzanine card per chamber is reported. In this way, if a mezzanine card is faulty it is immediately visible. In Figure 2.28b the number of hits per tube for a chamber is shown; this plot it is useful for the identification of dead tubes. If a dead tube is found, nothing can be done in order to fix it, but the information needs to be propagated to the offline reconstruction software.

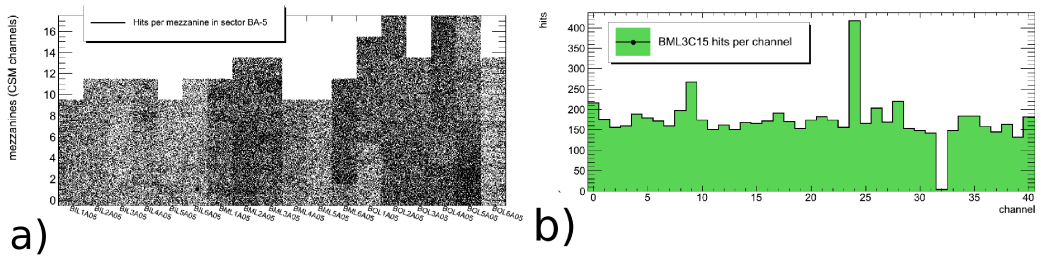

Figure 2.28: *Hit profile histograms showing the numbers of hits per tube (a) and the hit entries per mezzanine for each chamber of a sector.*

In Figure 2.29 a typical high voltage problem , spotted with the hit profile, is shown. The hit occupancy per tube of a BOL chamber is displayed, and it is clearly visible a gap in half of histogram, it indicates that HV is off for

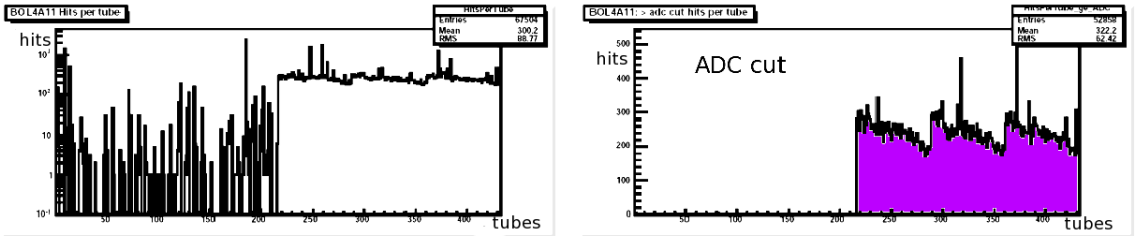

Figure 2.29: *Occupancy plot per tube of a chamber with an high voltage problem in the first multilayer; on the right it is the same plot, but with a cut on the ADC spectrum.*

one multilayers. The occupancy before ADC cut is shown on the left; some hits due to electronics noise are still present. Selecting hits with ADC counts[13] greater than a defined threshold (Fig. 2.29 right) only physical hits are shown and the absence of HV is more evident.
The hits per tube plot shown in Figures 2.28b and 2.29 are analyzed by gnaMon which translates the information in chamber geometry. In this way the source of the spotted problems is more easily recognized, *e.g.,* missing mezzanine in Figure 2.30a, or missing HV on a tube layer as in Figure 2.30 b.

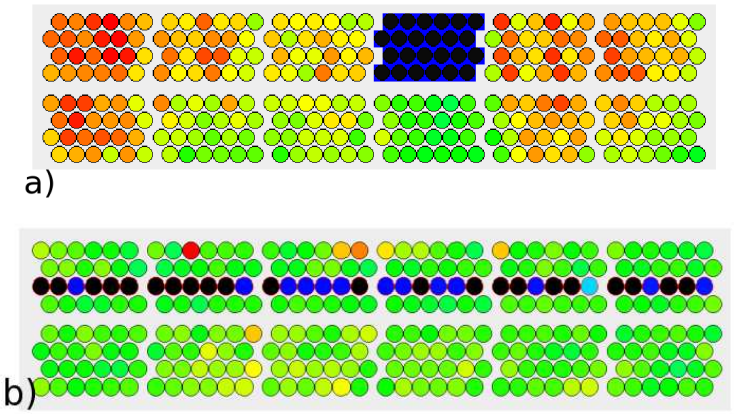

Figure 2.30: *gnaMon screen-shots showing the occupancy per tube of two BIL chambers. (a) A black box that represents an entire mezzanine that is not working is visible, b) an entire layer with no HV can be seen.*

Another useful plot is the hit multiplicity for each chamber. The inner chambers, having 8 layer of tubes, should have 8 hits per event, while medium and outer chamber should have 6 hits per events. Figure 2.31 shows the hit multiplicity for an inner and a medium chamber. The peak at one hit is the noise that occurs scorrelated with the triggered events, and hence has a mean

[13]ADC counts are related to the charge deposit in the drift tube.

number of hits per event of one. Chambers with no high voltage, have a peak at one hit and not higher multiplicities.

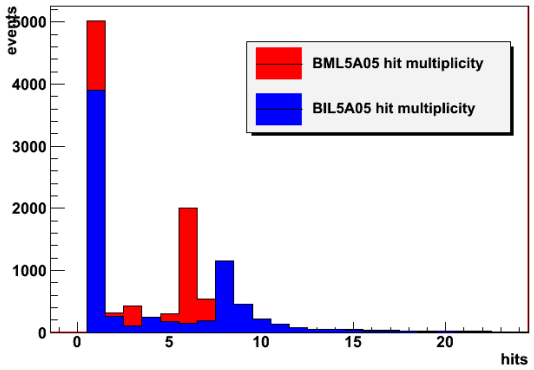

Figure 2.31: *Hit multiplicity for an inner and a medium chamber.*

TDC and ADC distributions

Beside finding dead tubes, the aim of stand-alone tests is also to measure the quality of the single drift tubes and the related electronics, by calculating the noise frequency of each single channel. Noise frequencies are calculated also in cosmic runs, but two slightly different definitions are given. In a noise test a software random trigger is used to open the matching window, uncorrelated with cosmics crossing the tube. The TDC spectrum is therefore expected to be flat (*i.e.,* hits occur with equiprobable drift times), as is shown in Figure 2.32.

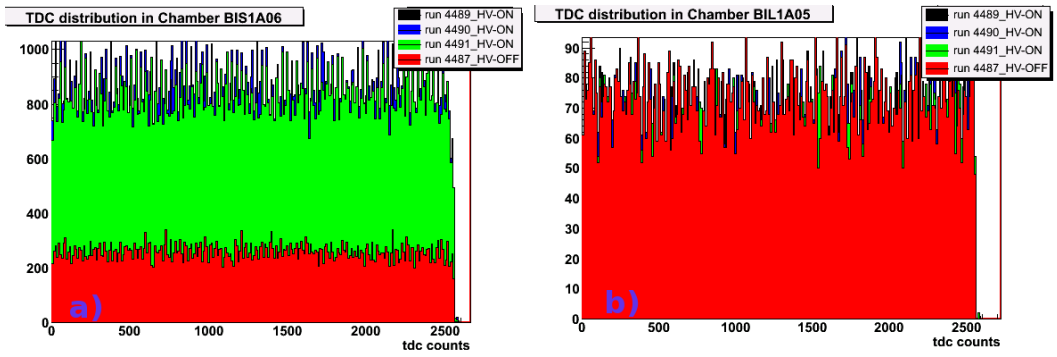

Figure 2.32: *Noise-run TDC flat spectra. a) Usual behavior of a chamber: when HV is on the noise is higher; b) noise level is the same with and without HV; this highlights an high voltage problem.*

The tube noise frequency is calculated by normalizing the number of entries

per bin (*i.e.,* tube) in the TDC spectrum histogram at the total number of recorded events, according to the following:

$$f(kHz) = \frac{entries}{events} \cdot \frac{10^6}{time\ window\ (ns)} \tag{2.4}$$

In cosmic run spectra it is used the same formula for the calculation of noise frequencies, but the time window in this case is reduced to the "non physical time windows". Noise hits, in fact, occurring at random times, are spread out all over the integration time window, and are not correlated to a physical particle (muon) crossing the tube (blue spectrum of Figure 2.15). In particular, since physical hits occur only in the region between t_0 and t_{max}, noise hits can be easily identified, by counting hits preceding the leading edge and following the trailing edge[14]. Such noise counts must be normalized to the total number of events and to the non-physical time window that is, in principle, different from tube to tube. Figure 2.33 shows on the left a typical cosmic ray TDC spectra.

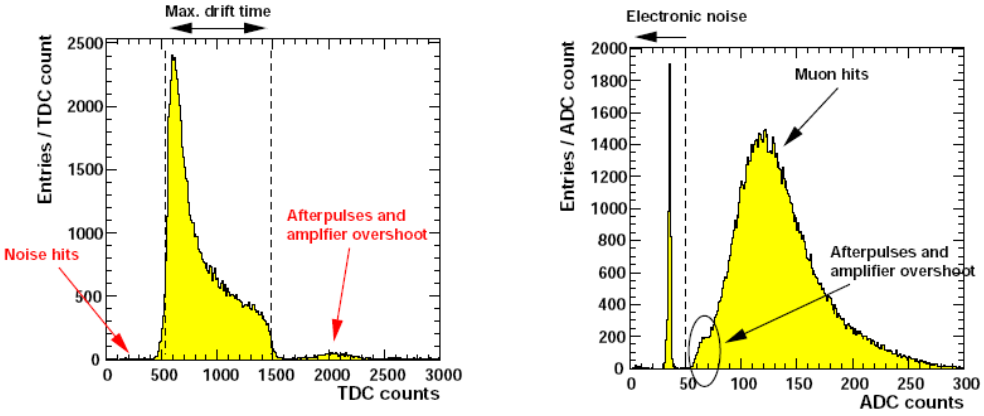

Figure 2.33: *TDC spectrum (left) and ADC spectrum (right) from cosmic rays.*

Noisy channels are then reported in an apposite database and then masked into the track reconstruction procedure. A single tube is tagged "noisy" if noise level is higher than 10 kHz. This limit is fixed from the simulation of ATLAS cavern background, consisting mainly of thermalised slow neutrons, long-lived K_0 and low-energy photons escaping the calorimeters and the forward beam and shielding elements. This 10 kHz threshold also fixes the limit for a mezzanine ($\sqrt{24} \times 10$ kHz=50 kHz) and for a full chamber ($\sqrt{N\ tubes} \times 10$ kHz). In particular "hot tubes" are defined as the ones with frequency higher than 50 kHz.

Two different sources of noise must be taken into account. Noise can be due to some defects of the tube itself, which modify the electric field and cause spourious discharges in the gas volume, or to the ASD channel it is connected to.

[14]The noise frequency is calculated using only the window preceding the t_0 because in the region after the t_{max} some after-pulse are present.

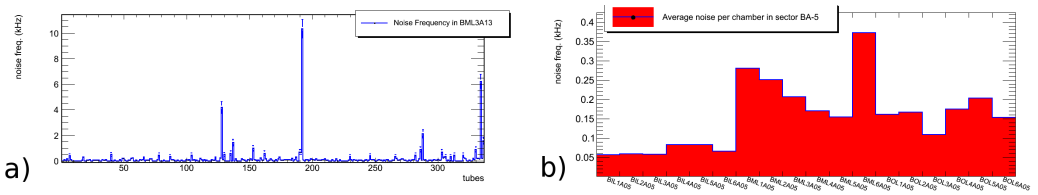

Figure 2.34: *Noise plot per tube (a) and average noise per chamber (b).*

This can be easily identified in a cosmic run by selecting hits over a prefixed ADC threshold. A typical ADC spectrum (see Figure 2.33 right), is a two peak distribution. The former, that is the one at lowest value, is the so-called pedestal; hits belonging to the pedestal are noise hits, not correlated with a muon crossing the tube. The second peak represents the muon signal, but is mixed to after-pulses and amplifier overshoot, usually with lower ADC values. Pure electronic noise is characterized by a peak on the pedestal distribution of the ADC spectrum, but can be easily eliminated before track reconstruction by a cut on the ADC value. Noise signals due to high voltage discharges, on the other end, normally have a non-zero pulse charge.
The discrimination between physical and noise hits is also visible through the ADC versus TDC distribution, as shown in Fig. 2.35

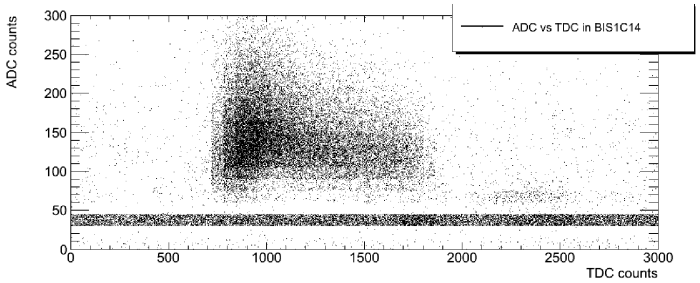

Figure 2.35: *ADC versus TDC distribution of cosmic spectra of a "good" chamber.*

If hits with drift times lower than t_0 and higher than t_{max} are noise hits, they are associated with ADC values on the pedestal (<45 ADC counts in this example). Indeed, since there is not any time correlation, noise hits are spread out all over the time window (flat horizontal line in the picture). Hits from real tracks, instead, arrive within the physical time window, and they are associated with ADC value higher than the pedestal. The ADC spectrum for a noisy chamber and the corresponding correlation with drift time distribution are, on the other end, much more crowded on the region before and after the leading and trailing edge of the TDC distribution; an example is shown in Fig.2.36
Many other problems can also be spotted, looking at the TDC spectra. MDT drift time spectra are very sensitive to the operation gas mixture; they are

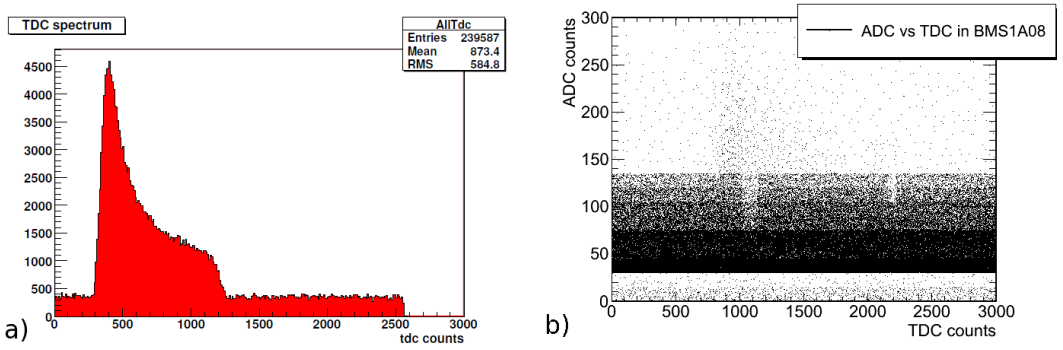

Figure 2.36: *a) TDC distribution of a very noisy chamber; b) ADC versus TDC distribution for another noisy chamber; in this case the noise level hide almost completely the muon signals.*

particularly useful during the commissioning phase to detect anomalies in the gas system of a chamber. A deviation of the drift time spectra of a chamber from the regular shape may be caused by high water concentrations in the operating gas mixture. Drift time, in this case, are longer, since the electron velocity in the drift field is reduced. A second reason is a CO_2 content above than normal (7%). This second case can be distinguished from the case of excessive humidity by analysing also the pulse height spectra: water has a very small effect on the gas gain, while additional values of CO_2 reduce the gain and thus shift the ADC spectra towards smaller values. In Figure 2.37 there is an example of how the TDC distribution can be changed by a gas problem; it is clearly too much short and there is no a real plateau. The ADC vs TDC scatter plot (Fig 2.37 b) has the clear drop-off in the region with triggered muons. Gain is going down with distance from the wire.

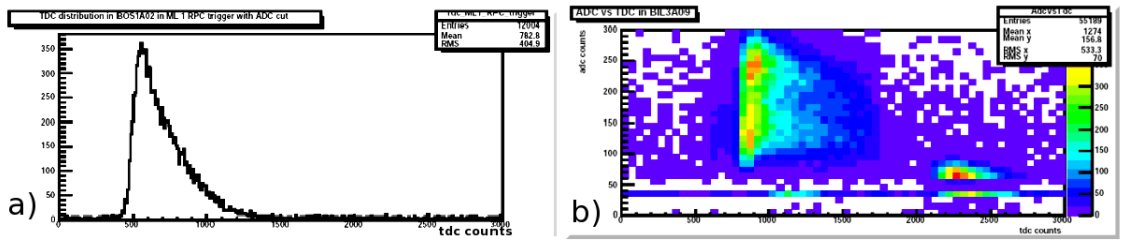

Figure 2.37: *TDC spectrum and ADC versus TDC distributions for a chamber with a gas problem.*

2.8 ATLAS combined cosmic runs

In 2008, waiting for the LHC collisions, the ATLAS detector has been operated for several months. In addition to a few days in which the LHC beam has been circulated in the machine, but without beam-beam collisions, extensive running periods with cosmic ray acquisition has been performed.
The main goal of these week-long runs was to operate the experiment as wolly as possible at that time, and to mantain stable running for the period, thereby exercising the data flow, run control and configuration aspects of the TDAQ system, and using ATLAS control room as if in data taking mode. In 2008 ATLAS registered millions of events, corresponding to a raw data volume greater than 1.2 PB and to about 700 TB of derived data, allowing for a relevant test of the computing model as well. A great amount of data was also taken during the July 2009 cosmic run. During these periods, data were collected with different magnet configurations to allow for some specific studies such as the determination of alignment constants. Figure 2.38 shows the accumulated statistics in the global cosmic run of autumn 2008 (left), and the one taken during the July 2009 cosmic run (right).

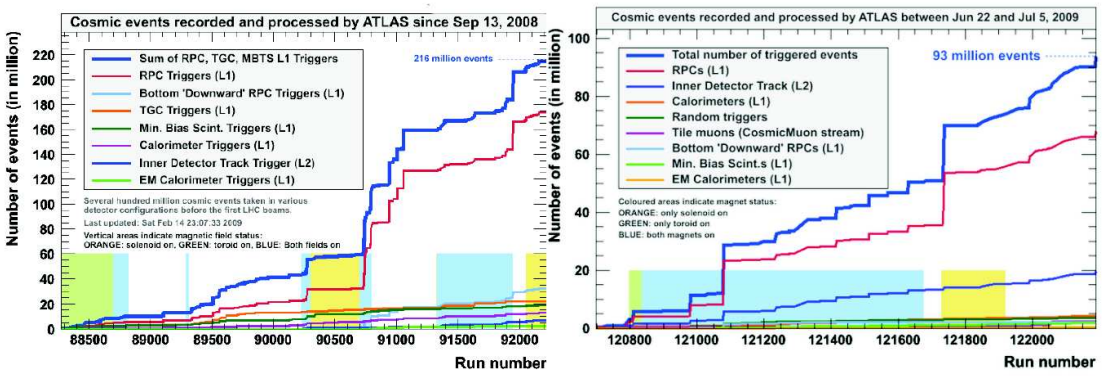

Figure 2.38: *Number of cosmic ray events collected in ATLAS versus time on Autumn 2008 (left) and Summer 2009 (right).*

As already mentioned, before these long run periods and starting from December 2006, eight week-long periods of combined runs, including all the available and commissioned detectors were performed, called "mileston weeks". In Table 2.2 the detectors included in each milestone week, and the goals are reported.
The reconstruction algorithms used during this first data period are in some cases exactly those that will run for collision data. However, specific adaptations to deal with particles not coming from the interaction point and, for the case of cosmic rays, not synchronized with the readout clock were needed in some algorithms. Given the differences between LHC collision data and the data recorded by ATLAS so far from cosmic rays and LHC single beam operations, LHC collisions are of course needed to make the final test of the

Time	**detectors added**	**goals**
M1-Dec 06	Barrel calorimeters, calorimeter trigger, upper barrel MDT	Muon reconstruction with magnetic field
M2-Mar 07	More sectors of MDTs endcap calorimeters,	Stable combined runs, calo and RPC trigger
M3-Jun 07	Barrel SCT, TRT, Muon big weel side C final DAQ, EB farms	Combined runs; event-display; first data streaming Tier-0 → Tier-1 centers
M4-Aug 07	More chambers of muon big wheel side C	Data quality monitoring, external calibration centers, DAQ to DCS (slow control) communication, HLT algs
M5-Oct 07	ID end-cap, Pixel	As M4
M6-Dec 07	Endcap magnets	Combined run with full toroidal magnetic field
M7-May 08	Full system (no CSC)	Use the full trigger chain
M8-July 08	Full system (no CSC)	Immediate DQ all systems, high rate runs with LVL2 filter, identify reasons for run stops, exercise data flow
M9-Autumn 08	Full system (no CSC)	Collect enough data (B field on/off) to calculate efficiencies, alignments, cross-detector studies and stability.

Table 2.2: *Overview of the milestone weeks of combined ATLAS runs. The detectors that were ready to be added to the combined runs and the main goals af each run are shown.*

operation chain described above. However, a very significant part of this chain has already been exercised with real data. Thanks to the cosmic ray commissioning phase, the Tier-0 processing has reached a very stable and robust level of operation, the data quality is continuously monitored both online and offline, data are being analyzed in detail and alignment and calibration corrections leading to very significant improvements have been provided. A large scale re-processing of about 300 million events with improved software and detector calibration constants has also taken place successfully at the Tier-1 centers.
Other than exercise all the ATLAS system as a whole, these combined period have been useful also to train a great number of shifters for each detector.

During the normal LHC running, in fact, ATLAS will need about three shifter per day per task, and that means about 45 persons per day in the main control room[15].

MDT shifter has the task to keep running every MDT chamber that does not have main problems; before the combined run starts, he has to verify the behaviour of the MDT system, checking that every chamber have:

- Low voltage power;
- Initialization of front-end electronics;
- Flushing gas at the nominal pressure;
- High voltage;
- Temperature electronics, power supplies modules, MROD racks, etc.. below a safety threshold.

These tasks can be done with the help of many monitoring panels of the DCS, like the one shown in Figure 2.40 in the case of HV monitoring, or in Figure 2.14 and 2.26.
The shifter can exclude from the combined run chambers with problems through the MDT control panel (Fig: 2.39); all the chambers included in the run should have stable running conditions, in order to don't interfere with the combined run.

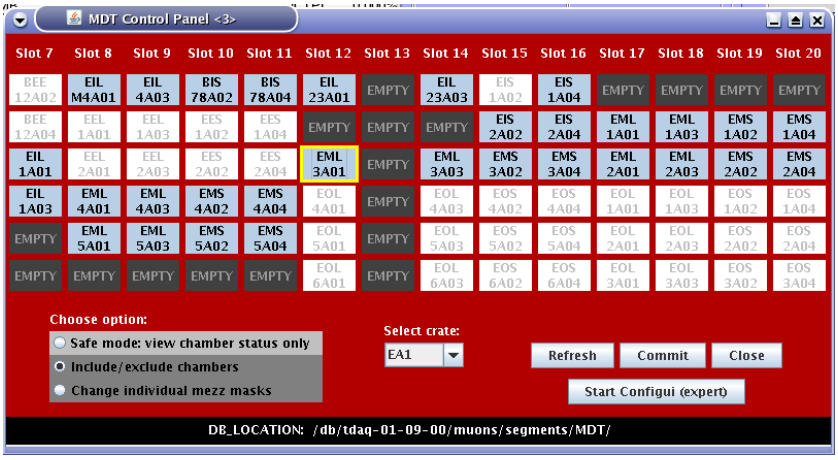

Figure 2.39: *The MDT control panel that enable/disable chambers in the data acquisition. Blue boxes represents enabled chambers, while the white ones represents chambers not included in the current data acquisition.*

[15]Other than shifters in the main control room will also be the necessity to have, expecially in the first period in which all the system will be not yet stable, a great number of experts available.

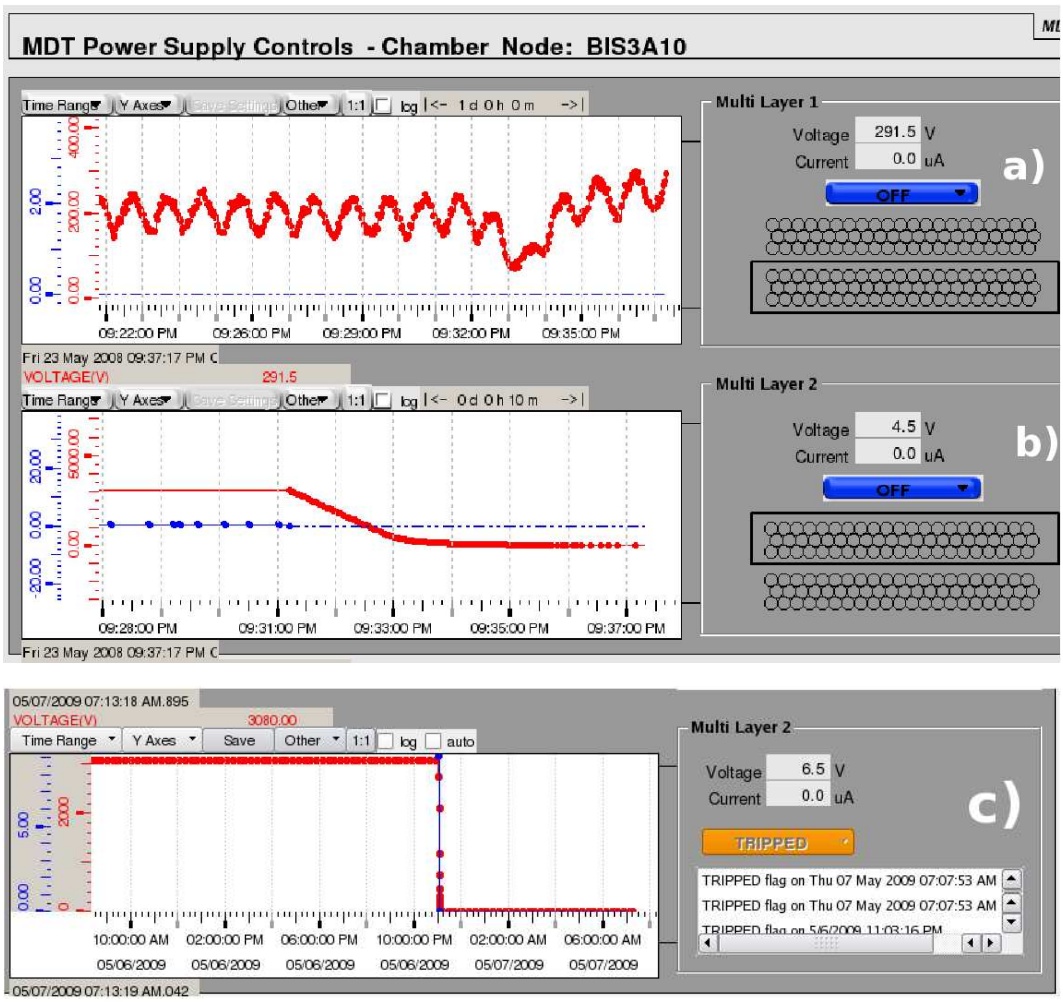

Figure 2.40: *Screen-shots from the DCS panel showing the HV behaviour in function of time for three different cases. a) this multilayer has some problem because the HV value is oscillating; b) "normal" behaviour, HV is stable until the switching off; c) the multilayer is tripped and the HV has been switched off by the security system.*

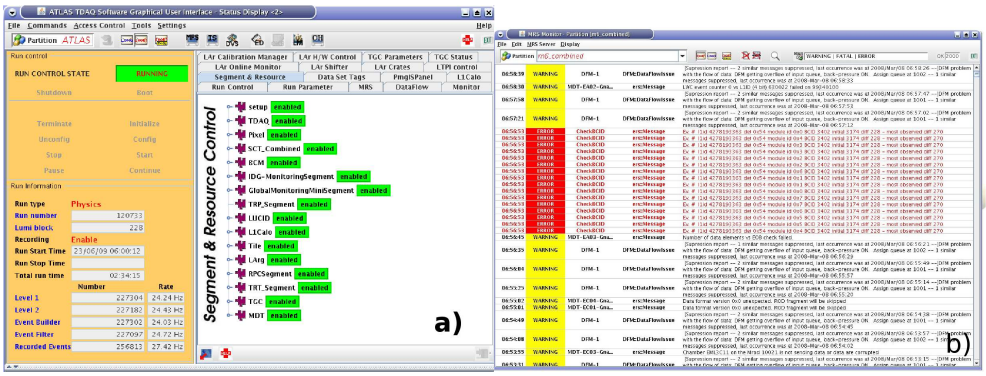

Figure 2.41: *a) Main DAQ run control panel that is used to start/stop runs, include all the necessary partitions and monitor the current number of events; b) MRS panel which shows the error messages from the DAQ during the run.*

When all the ATLAS detectors are ready to start, the shift leader gives the OK to start a combined run, and the run control shifter has the task to manage the run, and include all the partitions of the DAQ; in Figure 2.41 a) the main DAQ run control panel is shown.
During the run the MDT shifter has the task to keep running the detector and controlling its status with the help of DCS panels and from the Message erroR Service (MRS) that is a list of errors or warnings that are encountered during the run (Fig 2.41 b). When the acquired statistics of the current run is enough, shifters have also to check online histograms in order to ensure the correct behaviour of the sub-system they have to control.

2.9 Data analysis results

2.9.1 Cosmic rays

The large statistics of comic runs allowed to perform detailed detector studies although it is still not enough to reach the precision required in the alignment of the all the detectors. The end-cap is in fact not well illuminated by cosmics, and cosmics are randomly distributed over the time, and not synchronized with the LHC clock. Some examples of these studies will be given below for each sub-system: inner detector, calorimeters and muon spectrometer. In addition to real data, a simulation of cosmic rays going through the ATLAS detector has also been provided for different magnet and detector configurations to allow for data/Monte Carlo comparisons. In Figure 2.42 an event display showing a cosmic ray event recorded by the whole ATLAS system is shown. Cosmic ray data have also allowed detailed studies in the calorimeters, for example validating the timing and energy calibrations.
Progress in the understanding of the whole muon spectrometer performance

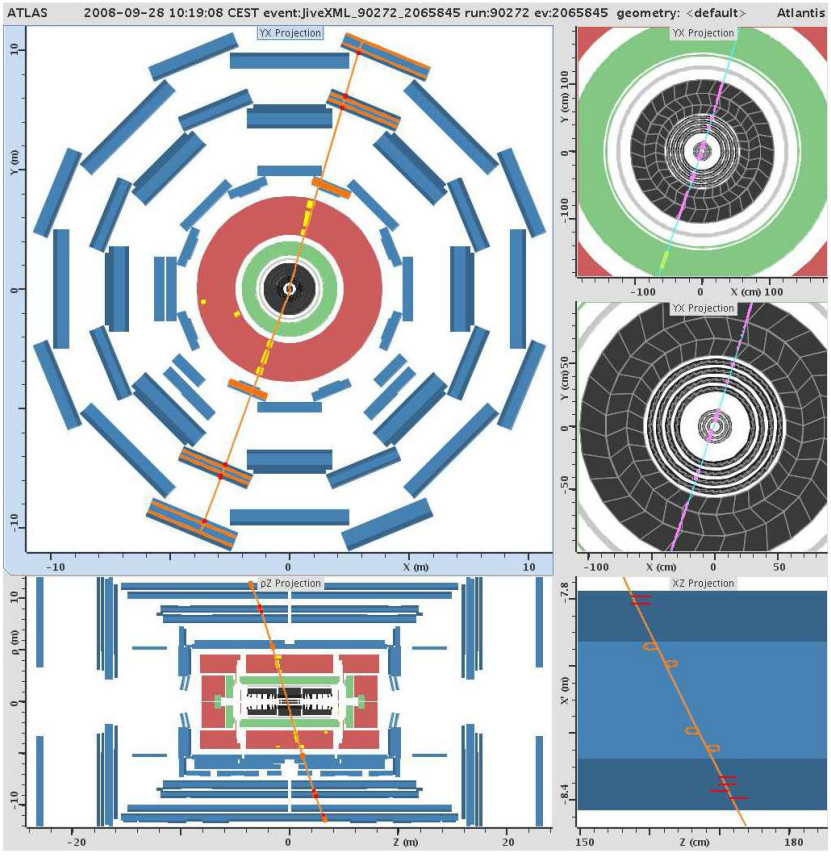

Figure 2.42: *An ATLAS online event display showing a cosmic muon going through the whole ATLAS, with magnetic field.*

has been achieved in terms of both tracking and triggering, providing first alignment and calibration corrections as well as lists of problematic channels. An example of the alignment status is shown in Figure 2.43 where the improvement of the residual distributions in one of the muon chambers thanks to the optical and track based alignment is clearly visible. The performance of combined tracking algorithms using measurements from both inner detector and the muon spectrometer can be verified with cosmic rays.
Figure 2.44 shows the difference in the azimuthal angle ϕ_0 and momentum obtained for tracks reconstructed in the inner detector and muon system for both real and simulated data. The value of momentum measured in the MS is lower than the one measured by the ID because of the energy loss in the calorimeters. In the same figure is also visible a very good correlation between the angles ϕ_0 and θ_0 of the tracks reconstructed with the muon spectrometer and whith the inner detector. In spite of the fact that no alignment corrections were used, the data/MC agreement is fairly good, and indeed combined tracks are well reconstructed for cosmic rays, as can be seen from an event-display shown in Figure 2.42.

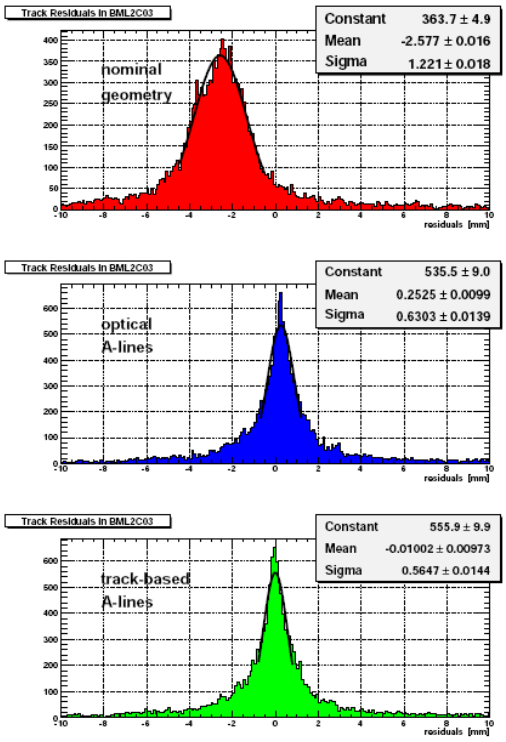

Figure 2.43: *Measured residual for cosmic tracks passing in a middle muon chamber before alignment (top) and after applying the alignment corrections obtained by the optical system (middle) and those obtained using tracks (bottom) [34].*

A good correlation between the MDT and RPC hits position of the tracks recontructed is visible from the Figure 2.45b. In Fig. 2.45a the coordinate of coming cosmic muons is shown. The two circular regions are corresponding to the two shafts of the ATLAS pit.

In Figure 2.4 (right) a preliminary measurement of the Muon Spectrometer momentum resolution, using cosmic rays, is shown (black dots). The red curve corresponds to the calculated resolution, as the convolution of each effect contributing to the total resolution (Figure 2.4 left). The agreement is quite good at low momenta, while for $p_T \gtrsim 70$ GeV the resolution from cosmics become worst.

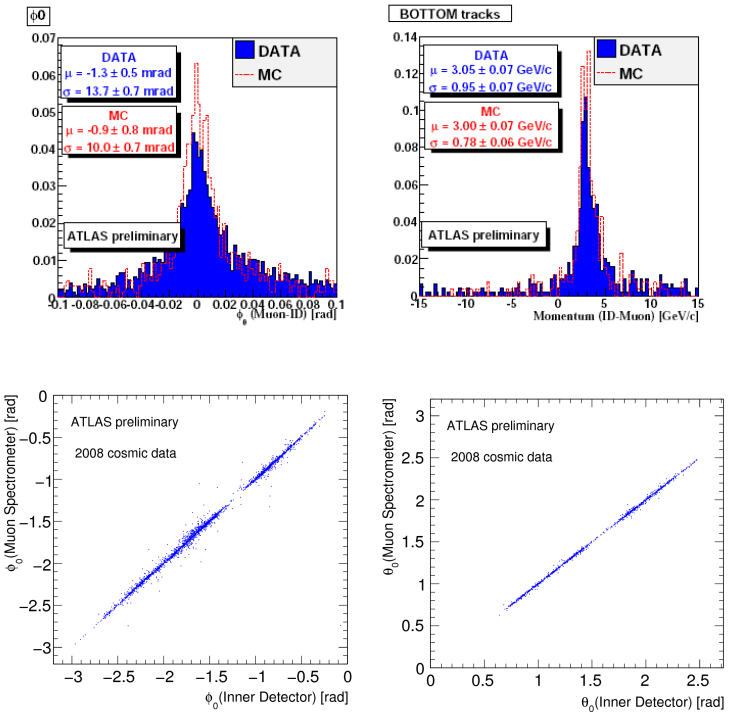

Figure 2.44: *Top: difference on the ϕ_0 (left) and momentum (right) track parameters reconstructed in the inner detector and muon spectrometer for both real and simulated data [34]. Bottom: correlation plots on the ϕ_0 and θ_0 angles between the MS and ID recontructed tracks. [18]*

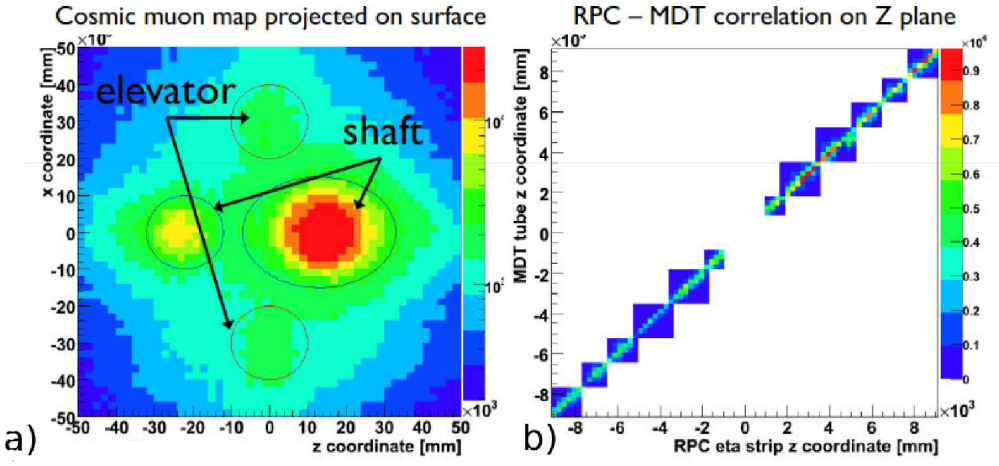

Figure 2.45: *a): x-z plot of the illumination of the whole RPC system from cosmic rays that shows that cosmics arrive in particular form four points that are the shaft of the ATLAS pit and the elevators. b): Correlation plot between RPC and MDT hits. [18]*

2.9.2 LHC first data

As explained in Chapter 1, single-LHC beam started to run into the collider in the summer 2008, one sector per time, and on the 10th of September 2008, the LHC managed to have the first bunch of protons at the injection energy of 450 GeV circulating around the ring and therefore going through the ATLAS detector. Previously, for safety reasons, the tertiary collimators 140 meters away from the ATLAS detector were closed and therefore for each beam injection a shower of particles was expected to go through the detector, producing the so-called splash events (Figure 2.46).

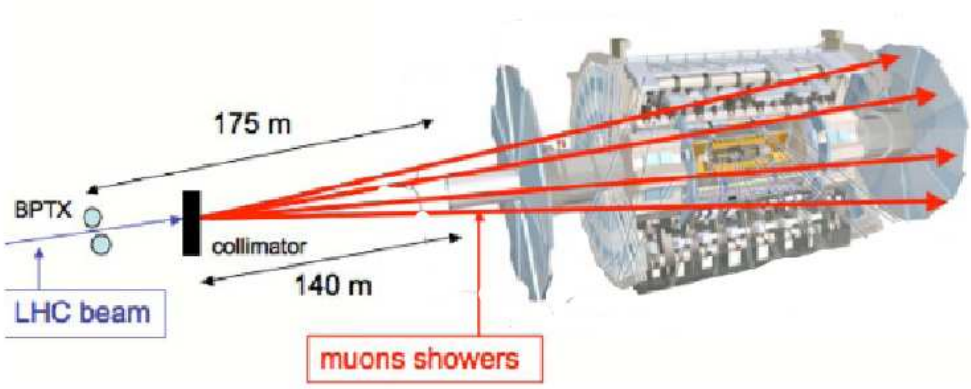

Figure 2.46: *Cartoon of a splash event against the collimator.*

Once the collimators were opened and beam was circulating through ATLAS, physics events were expected to be beam halo events containing mainly muons or the outcome of the interactions of the beam protons with the pipe walls or residual gas in the pipe.
Thanks to the previous commissioning period with cosmic rays, the ATLAS detector was ready to take data and reconstruct it successfully at the start-up of the LHC. For safety reasons, the Pixel detector was turned off and the SCT, muon chambers and the forward calorimeter were working at reduced high voltage. The first level trigger and the data acquisition were fully operational. The High Level Trigger (HLT) was available, however, since the plan was to store all events, it was decided to only use the HLT for streaming the data based on the first level trigger results, not applying any selection algorithm.
As Level-1 trigger for these events were used both the Beam Timing Pickup (BPTX), the LUCID detector and the Minimum Bias Trigger Scintillators (MBTS).

One of the first splash events seen by the ATLAS detector is shown in Figure 2.47. As expected, these events are characterized by a huge number of

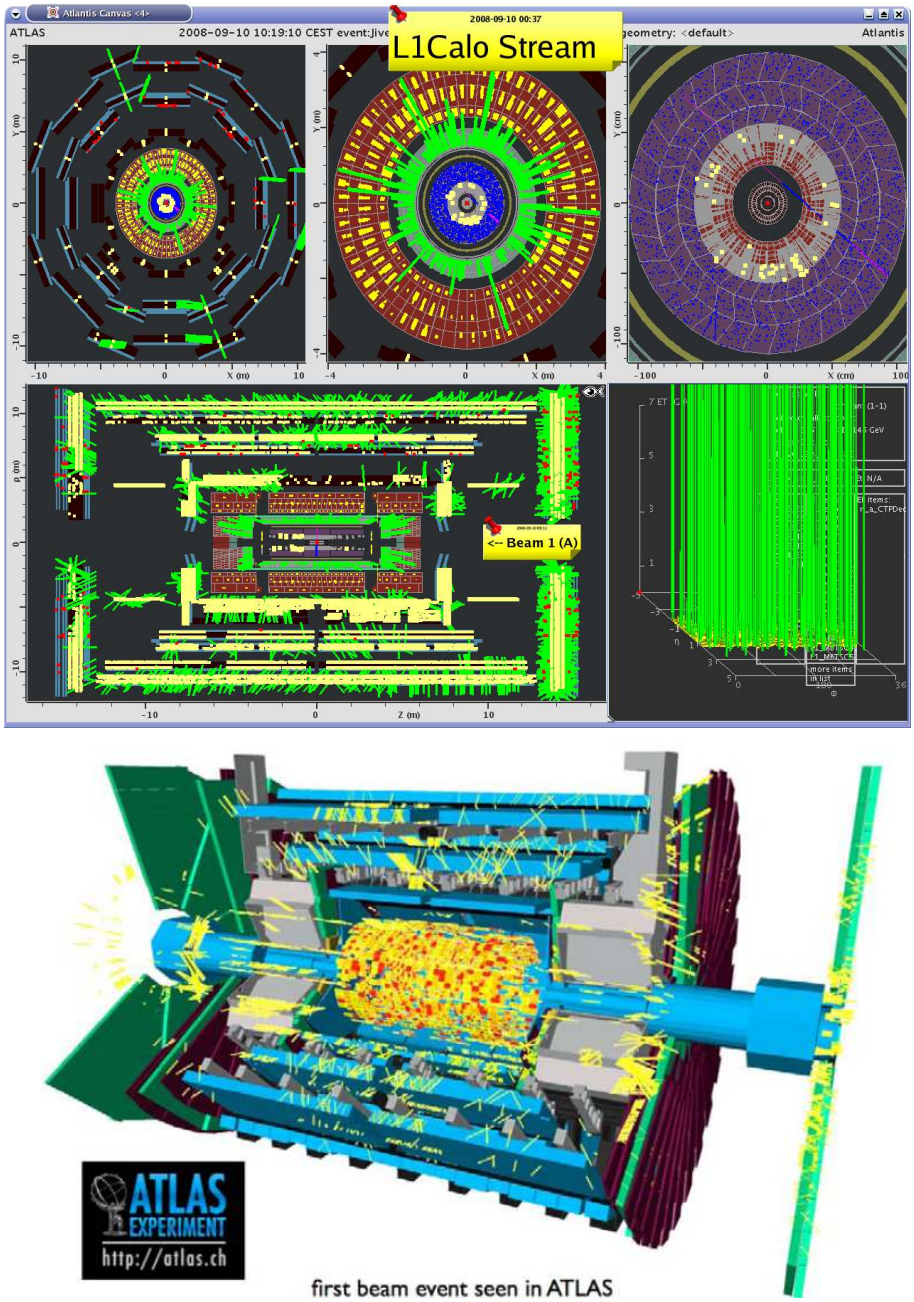

Figure 2.47: *First LHC splash-event seen by the ATLAS detector [35].*

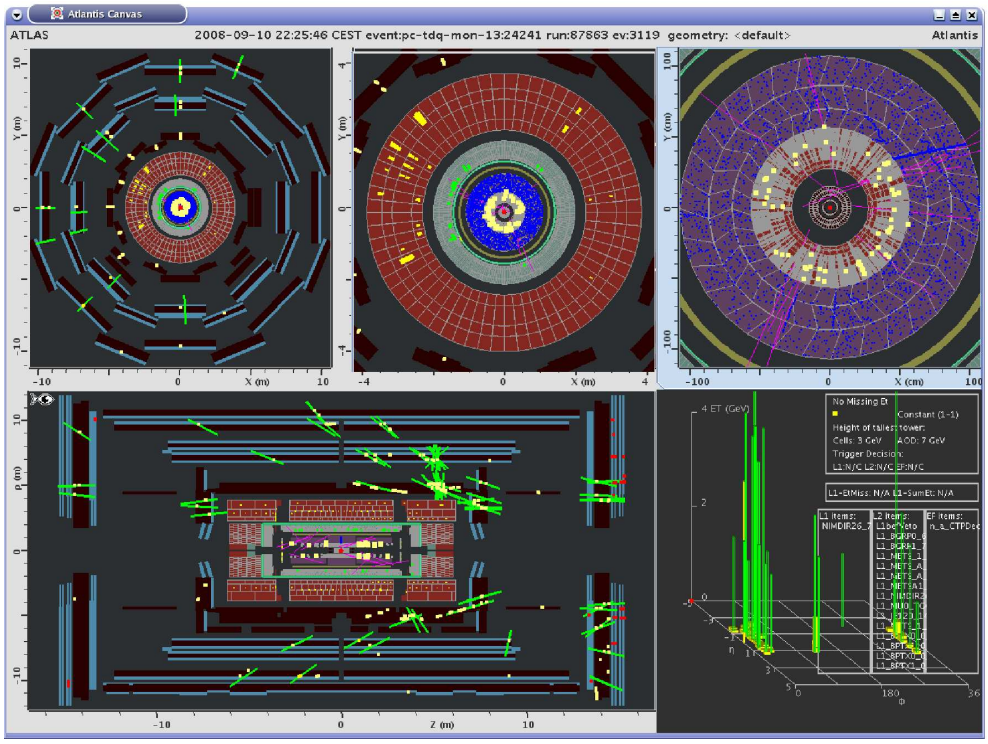

Figure 2.48: *Online event display of one of the beam halo event seen by ATLAS. [35]*

Figure 2.49: *Webcam view of the ATLAS control room, 10th September 2008.*

signals in the detectors, *e.g.,* more than 10^5 hits in the muon chambers, and a huge energy deposit in the calorimeters, more than 10^3 TeV in the hadronic calorimeter and several TeV in the electromagnetic one. Such an activity were caused by up to 2×10^9 protons at the energy of 450 GeV, colliding with the collimator.
In Figure 2.48 an event display of one of the splash events but less crowded is shown. It is possible to see the effect of the magnetic field on charged particles through the endcap of the muon spectrometer. Since these events produce a signal in almost all channels of the detector, they turned out to be very useful to find dead channels (expecially for the end-cap MDT chambers that are not well illuminated by cosmic rays). The beam events were useful in particular for timing studies for sub-detectors and triggers, which are difficult with cosmic-ray muons that are randomly distributed.
The energy deposition in the LAr EM Calorimeter is shown in Figure 2.50, where energy vs ϕ is displayed. The 8-fold structure of the magnetic system is visible, together with lower response for $\phi = \pi/2$ due to passive material (mainly support structure).

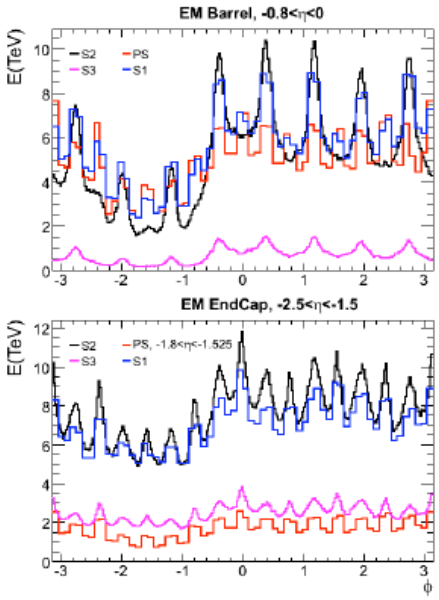

Figure 2.50: *Energy deposition in the LAr.*

Figure 2.9.2a displays beam halo events as detected by the TRT. Figure 2.9.2b shows a comparison of the angle θ with respect to the beam axis of the tracks reconstructed in the muon spectrometer for cosmic rays and single beam data. One can see that cosmic muons are mostly vertical (the two peaks correspond to the two shafts) while those recorded during LHC single beam operations

were horizontal as expected for beam halo muons.

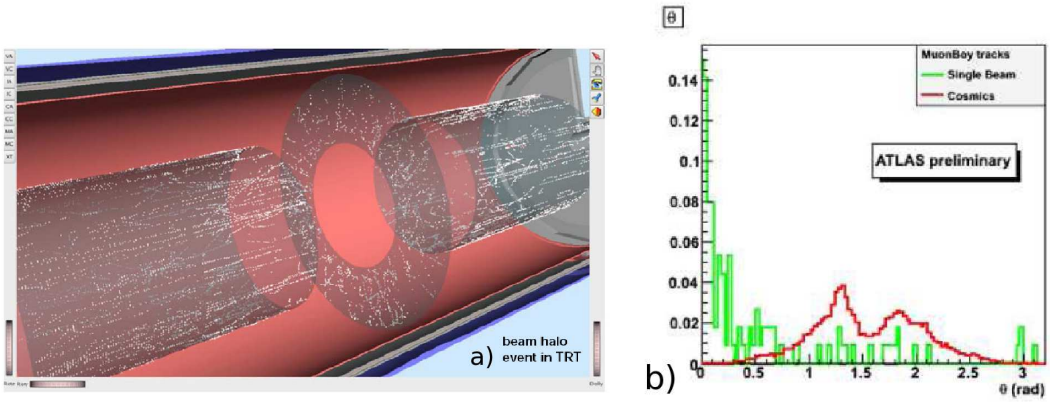

Figure 2.51: *a) Beam halo events viewed by the TRT. b) Distribution of the θ of the tracks reconstructed in the muon spectrometer for cosmic rays and LHC single beam data. [35]*

Concerning beam-gas interactions, none of these events have been observed in the ATLAS recorded data, probably because of the excellent vacuum reached in the pipe. Some candidates for beam hitting the beam pipe were observed. Anyway, due to the fact that the inner detector was not fully working during this period, the identification of this kind of events is difficult.
In conclusion, the first 2008 beam provided valuable operations experience to all the detector communities, and was exciting despite the later disappointment (see Figure 2.49, showing the ATLAS control room in the first day of LHC beam).

Finally, at the end of November 2009, the ATLAS experiment started again to record data from LHC activities. Other splash events have been delivered, and on the 23th November, during the early commissioning of the LHC, two proton bunches were circulating for the first time concurrently on the machine with the injection energy of 450 GeV. The bunches used were the so-called "pilot-bunches": low intensity bunches used during machine commissioning, with a few 10^9 protons per bunch. Although the proton intensity was very low, with only one pilot bunch per beam, and no specific attempt was made to maximize the interaction rate and collision optics, all the LHC experiments reported a number of collision candidates (Figure 1.9). In Figure 2.52 two event-displays of the first candidate collisions seen by ATLAS are shown. At the time of writing, the LHC commissioning is still going on and the ATLAS experiment is recording data with two LHC beams circulating, but not colliding. Beam halo events are seen at a rate of about 25 Hz. These events are useful mainly for timing studies between the detectors. A couple of week of 900 GeV collisions data have just been taken. For security reasons, the pixel detector have been switched off for the first days of LHC running, until the beams have reached

stable conditions. Also in all the others detectors the gain have been taken as low as possible[16]. In Figures 2.52 and 2.53 the online event displays of some of the first collisions data seen by ATLAS (with also the pixel detector) are shown, both at 900 GeV and at 2.36 TeV.

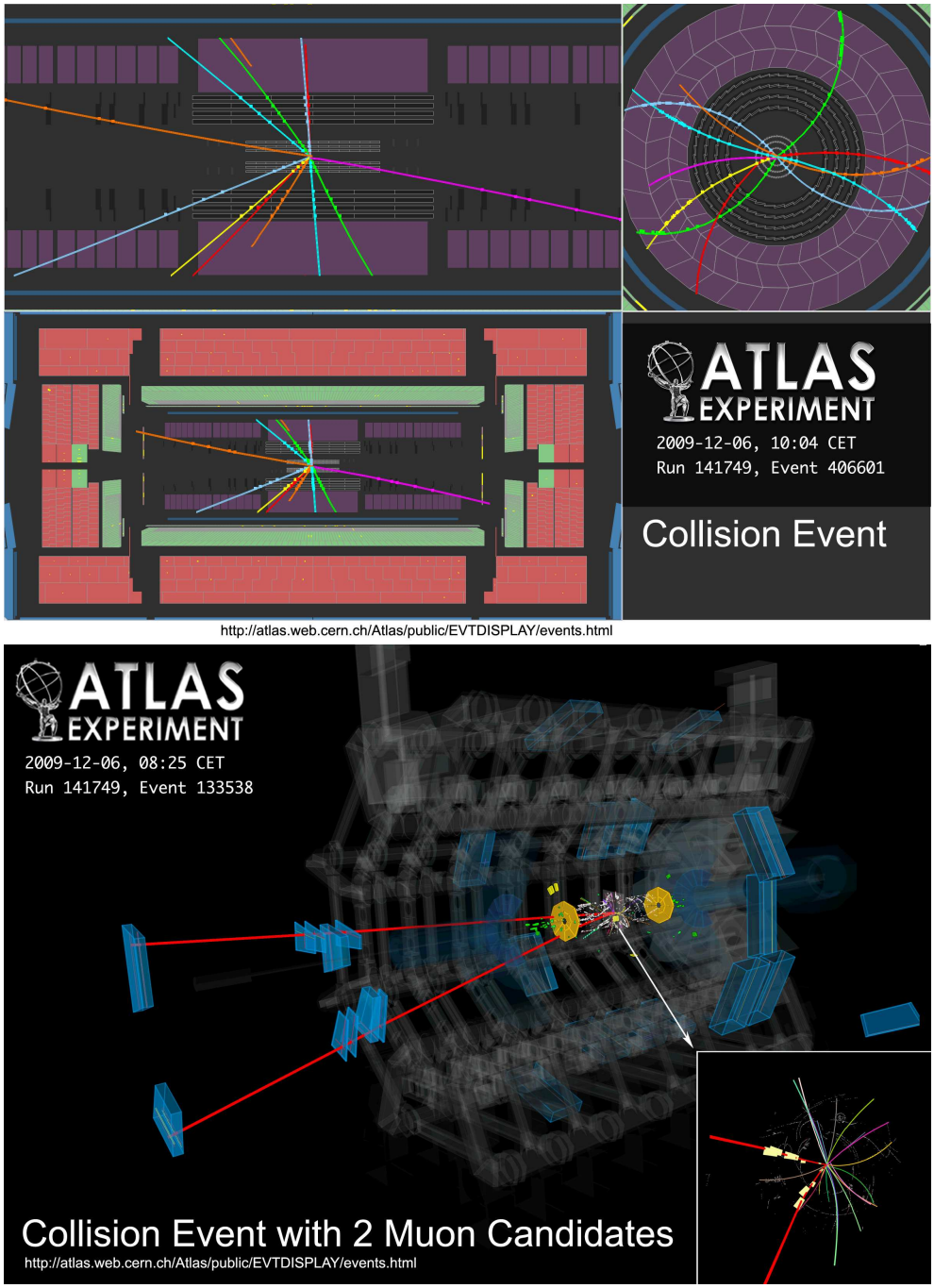

Figure 2.52: *Event display of two collision events at $\sqrt{s}$ of 900 GeV. [35]*

[16]For the MDTs the HV value has been set to 3000V for every chambers but the inner ring of the end-cap that is closer to the beam, for which the value of 2760 V has been chosen

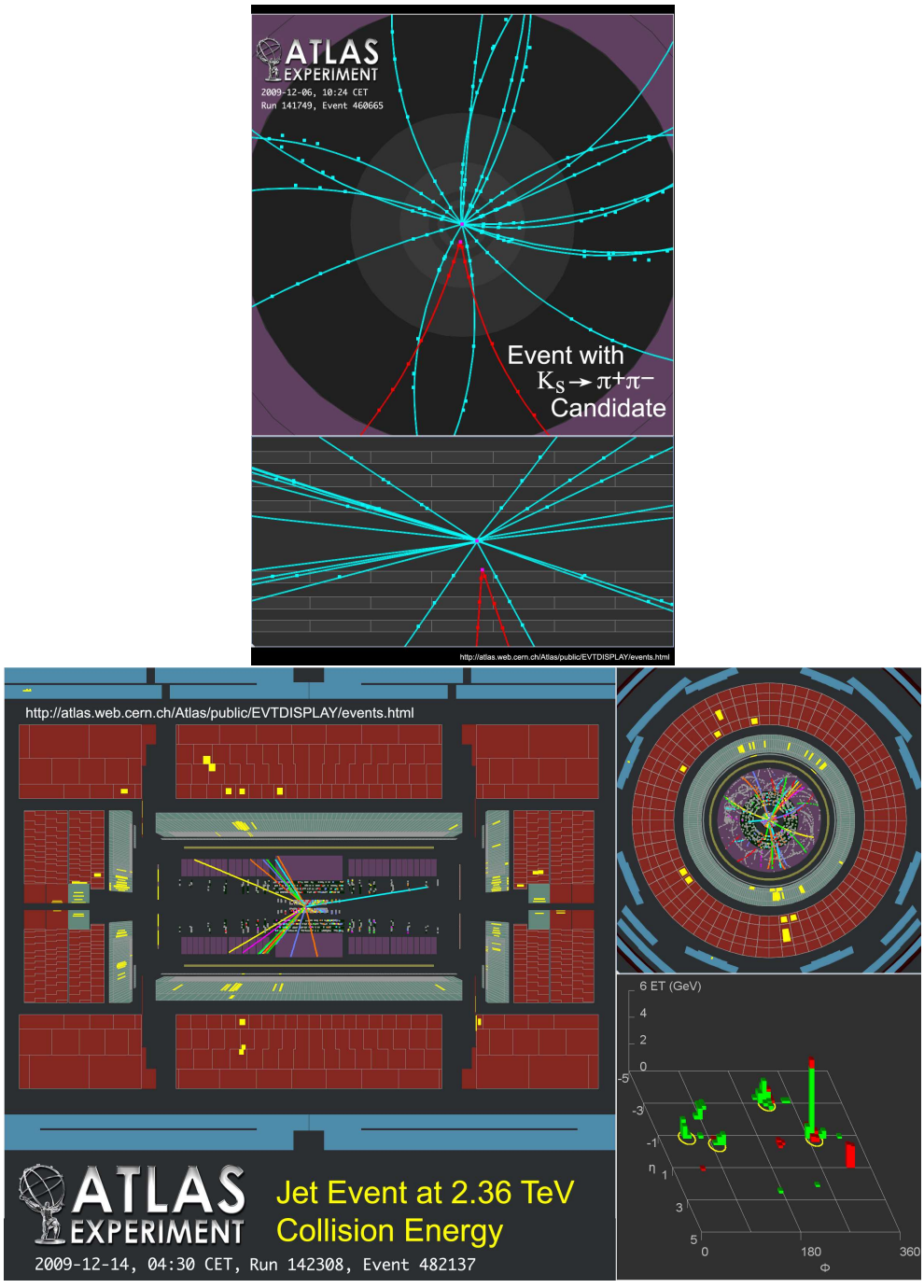

Figure 2.53: *Event display of a $K_s \rightarrow \pi\pi$ candidate at $\sqrt{s}$ of 900 GeV and multiple jet event at 2.36 TeV. [35]*

Chapter 3

Dual REAdout Method (DREAM) with crystals

As we have seen on the Chapter 1, most of the detectors used in the modern collider experiments are very complicated, and they need many years of design and tests on prototypes before being really used and built in a full scale. This is the reason why, in these years, there are so many efforts to conceive and test detectors to use on the next generation of high energy physics experiments. The Dual REAdout Method (DREAM) is one of these new promising techniques about calorimetry, which is not subject to the limitations of traditional hadronic calorimeters.
In this chapter some results from the R&D of the DREAM project are reported. Some of the data analysis work was carried out during the period spent at the Texas Tech University - Lubbock- Texas, under the supervision of the DREAM project leader: prof. Richard Wigmans, and within the program for the International Certificate of Doctoral Studies of the University of Pavia.

This chapter is organized as follows. In Section 3.1 are shortly described the principles and the advantages of the Dual Readout technique for calorimetric purpose. This technique was first demonstrated with a fibre calorimeter (Section 3.1.1) , and then was extended to homogeneous calorimeters (Section 3.2). This chapter is focused on studies on $PbWO_4$ crystals that represented the main subject of the analysis performed for the thesis. First, a study of the Cherenkov and scintillation signal dependence on the temperature of a $PbWO_4$ crystal is described (Section 3.3.1); after that, in Section 3.5, are reported some results obtained on Molybdenum and Praseodymium-doped $PbWO_4$ crystals, and conclusions on the feasibility of such crystals for use in Dual Readout calorimetry.

3.1 The Dual Readout Method DREAM

The goal of the DREAM project is to develop an hadronic calorimeter with improved performances with respect to those built in the past. The resolution of a calorimeter is affected by fluctuations, therefore, in order to improve the resolution it is necessary to eliminate or reduce the effects of the dominant ones.
In non-compensating calorimeters, the hadronic energy resolution is dominated by fluctuations in the electromagnetic fraction (f_{em}). In fact, a shower developed by hadrons has an electromagnetic (em) component, due to the decay in 2 γs of neutral pions, and a non electromagnetic ($non-em$) one, that is populated mostly by spallation protons, neutrons and charged pions produced in nuclear reactions. The electromagnetic shower develops in the same way as those initiated by high-energy electrons or photons, and the calorimeter, if is not compensating, generates a signal per unit deposited energy for the the electromagnetic shower component which is larger (e/h>1) or smaller (e/h<1) than for the non electromagnetic one. The e/h ratio, *i.e.,* the ratio of the detector response to em and $non-em$ shower components respectively, depends on the choice of the passive and active calorimeter media and on the sampling fraction, *i.e.,* on the ratio between the amount of active and passive materials. The fraction of the initial hadron energy converted into π^os, and therefore producing the electromagnetic fraction, varies strongly from event to event, depending on the detailed processes occurring in the early phase of the shower development, *i.e.* the phase during which production of these particles is energetically possible. The Dual Readout Method (DREAM) proposed to reduce the effects of these fluctuations by measuring the f_{em}value on event-by-event basis. This goal is reached measuring simultaneously different types of signals which provide complementary information about details of the shower development. In particular it is possible to compare the scintillation light (S) and Cherenkov signal (C) produced in the same detector. S is produced by all particle passing though the detector, but C is created almost exclusively by the em shower. In fact, electrons and positrons through which the energy of the em shower component is deposited are relativistic down to a fraction of 1 MeV and thus dominate the production of Cherenkov light in hadron showers [36]. The large majority of particles in the hadronic component are non relativistic (*e.g.,* spallation protons has typically energies of 100 MeV).
The amount of scintillation light is, in first approximation, proportional to the energy deposited by the shower particles in these fibres. On the other hand, the Cherenkov quartz fibres only produce light when they are traversed by charged particles traveling faster than c/n; the speed of light in the fibre. By measuring the signals from both types of fibres simultaneously, one therefore measures how much energy was deposited in the calorimeter and what fraction of that energy was carried by the em shower component. As we have seen above, with this method, the dominant source of fluctuations contributing to the hadronic energy resolution can thus be eliminated, since it allows a mea-

surement f_{em}event by event.

This technique was first applied to a **fibre calorimeter**, the DREAM module, in 2003 [38] and later, in 2006, it was extended also to **homogeneous calorimeters** such as $PbWO_4$ and BGO crystals [41], [42] in order to eliminate sampling fluctuations and to increase the amount of Cherenkov photoelectrons.

3.1.1 The fibre dual readout module

The fibre module was built at Texas Tech University in 2001, and the performance was studied in testbeams at CERN starting from 2003. As we can see from figure 3.1, it is constituted by a copper absorber structure, equipped with fibres of two types: scintillating plastic, and quartz. The basic element is a 200 cm long extruded copper tube (cross section 4×4 mm^2, with a central hole of 2.5 mm diameter). Three scintillating fibres (S) and four quartz Cherenkov fibres (Q) are inserted in the hole. The calorimeter consists of about 6000 of such tubes. The fibres are split as they exit at the rear into bunches of two types of fibres, and are read with different photomultipliers.

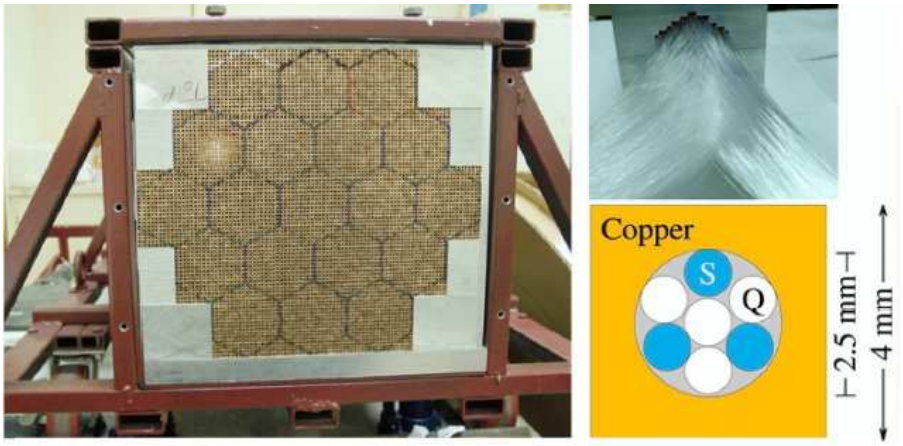

Figure 3.1: *Layout of the DREAM fibre calorimeter.*

Measuring f_{em}event by event

The response to hadrons (R), either for scintillation or the Cherenkov light, can be expressed in terms of the electromagnetic shower fraction f_{em} and the e/h ratio:

$$R(f_{\mathrm{em}}) = f_{\mathrm{em}} + \frac{1}{e/h}(1 - f_{\mathrm{em}}) \tag{3.1}$$

Defined in this way, R = 1 for *em* showers. This relationship holds separately for both sampling media. The e/h value of a copper/quartz-fibre calorimeter

was measured to be ~ 5, while for the copper/plastic-scintillator structure is estimated to be 1.4 [39].
Based on Eq. 3.1, we can write the ratio between the Cherenkov (C) and the scintillation (S) signals as:

$$\frac{C}{S} = \frac{f_{\mathrm{em}} + 0.21(1 - f_{\mathrm{em}})}{f_{\mathrm{em}} + 0.77(1 - f_{\mathrm{em}})} \tag{3.2}$$

where 0.21 and 0.77 represent (in the case of the DREAM fibre module) the h/e ratios of the Cherenkov and scintillator calorimeter structures, respectively. From Eq. 3.2 it's easy to see that measuring the C/S ratio, event by event, one can easily extract the electromagnetic fraction f_{em}.

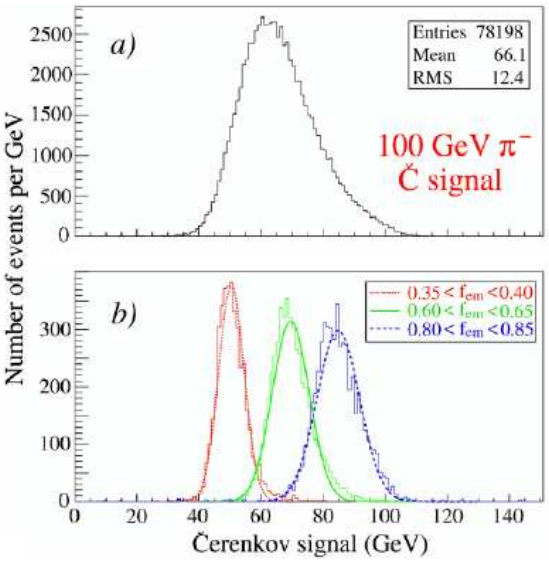

Figure 3.2: *Cherenkov signal distribution for 100 GeV π^- (a) and distributions for subsamples of events selected on the basis of the measured f_{em}value, using the C/S method (b).*

The merits of this method are clearly illustrated in Figure 3.2 , which shows the overall Cherenkov signal distribution for 100 GeV π^- (a), as well as distributions for subsamples selected on the basis of their f_{em} value (b), determined by equation (3.2). Each f_{em} bin probes a certain region of the overall signal distribution, and the average value of the subsample distribution increases with f_{em}. Moreover the plot shows that the skewed C signal distribution is the sum of many gaussian distributions, each characterized by a certain value of f_{em}. Once the value of f_{em} is determined for a shower, the signals can be corrected in a straightforward way for the effects of non-compensation.

3.1.2 Advantages of the dual readout method

The fact that $<f_{\mathrm{em}}>$ increases with energy causes also a non linearity in the response, that can be again eliminated by the event-by-event correction.
In conclusion, as a result of the DREAM method:

- the effects of **fluctuations in the electromagnetic component**, which are responsible for all traditional problems in non-compensating calorimeters, can be eliminated;
- the **hadronic shower energy** is correctly reconstructed, based on electron calibration;
- the **signal distribution** becomes much more Gaussian in shape.

The elimination of the effects of the dominant source of fluctuations means that other types of fluctuations now dominate the detector performance. Further improvements may be obtained by concentrating on these.In the DREAM fibre detector these fluctuations include, apart from fluctuations on *side leakage* which can be eliminated by making the detector larger, *sampling fluctuations* and *fluctuations in the Cherenkov light yield*. The latter effect played a prominent role (contributing $35\%/\sqrt{E}$ to the measured resolution) and was caused by the small number of Cherenkov photoelectrons constituting the signals (8 p.e./GeV).
As described in Section 3.2, these effects may be effectively reduced by using a homogeneous calorimeter that produces a separable mixture of scintillation and Cherenkov light.
Once the mentioned effects have been eliminated, the performance of this type of detector may approach the theoretical hadronic energy resolution limit. This limit is determined by the so-called **fluctuations in visible energy**, which result from the fact that some (variable) fraction of the energy carried by the showering particle is used to provide the nuclear binding energy needed to release nucleons and nucleon aggregates in nuclear reactions. This energy does not contribute in any way to the signal. However, it has been shown that efficient detection of the neutrons abundantly produced in these processes may be an effective tool for reducing the (effects of) fluctuations in visible energy, and that hadronic energy resolutions of 15-20% $/\sqrt{E}$ might be achieved this way [36].
As is explained in [48], [49], the contributions of neutrons to hadronic signals from the DREAM calorimeter are measured by analyzing the time structure of these signals. The neutrons, which mainly originate from the evaporation stage of nuclear breakup in the hadronic shower development process, contribute to the signal through elastic scattering off protons in the plastic scintillating fibres. This contribution is characterized by an exponential tail in the pulse shape, with a time constant of $\sim$20 ns. This complementary information makes it possible to further improve the hadronic performance of dual-readout calorimeters.

3.2 The Dual Readout Method with crystals

There is no reason why the DREAM principle would only work in fibre calorimeters, or even in sampling calorimeters. One could in principle use a homogeneous (fully sensitive) detector, like dense high-Z crystals (*e.g.,* $PbWO_4$, BGO), in which both Cherenkov and scintillation light are produced, provided that the signal due to different components can be separated. In this way both effects which limit the resolution of the fibre detector can be eliminated.
The improvement of the calorimeter performance is, in that case, determined by the precision with which the relative contributions to the total signal of these two types of light can be determined.

Since 2006, every year, the DREAM collaboration has done a beam test in order to apply the dual readout principles to homogeneous media. So far, we have tested $PbWO_4$ (undoped and doped with Molybdenum and Praseodymium) and BGO crystals.
In order to separate the scintillation and Cherenkov components, we have used different characteristics of the two types of light, summarized in Table 3.1.

	Cherenkov	*Scintillation*
Time structure	Prompt	Exponential decay
Light spectrum	$1/\lambda^2$	Characteristic peaks
Directionality	Cone: $\cos\theta_C = 1/\beta n$	Isotropic

Table 3.1: *Different properties of Cherenkov and scintillation light*

1. **Time Structure**
   Cherenkov light is prompt, while the scintillation mechanism is characterized by one or several time constants, which determine the pulse shape. Detailed measurements of the time structure were performed, with the help of an high sampling frequency scope, to study the properties of the prompt component in the signals from the crystals.

2. **Spectral properties**
   Cherenkov light exhibits a $1/\lambda^2$ spectrum, while the scintillation spectrum is a specific characteristic of the crystal, because depends on its energy band structure (Fig 3.11). Of course, the extent to which these differences may be observed in the measured signals depends also on filters, if any are used, and on the wavelength dependence of the quantum efficiency of the light detector.

3. **Directionality**
   Contrary to scintillation light, which is emitted isotropically, Cherenkov light is emitted at a characteristic angle ($\cos\theta_C = 1/\beta n$) by the relativistic (shower) particles that traverse the detector. We measured the signals

for different orientations (*i.e.,* angles θ) of the crystal with respect to the beam, as is shown in Fig 3.3. Although this feature is very useful for quantitative evaluation of the Cherenkov contribution, it cannot be used in a realistic 4π experiment.

Another difference is that the Cherenkov light is **polarized**, but we haven't exploited this characteristic.

3.2.1 Test beam setup and data acquisition

All the measurements described in this chapter were performed in the H4 beam line of the Super Proton Synchrotron at CERN with a 50 GeV electron beam. In the case of the 2007 tests, we used a pure $PbWO_4$ crystal[1], with cross section of 2.2 × 2.2 cm^2, corresponding to 2.5 radiation lengths and length 18 cm; the doped crystals, tested in 2008, had a length of 20 cm and a cross section of 2.0 × 2.0 cm^2 (2.25 X_0). In 2007 we tested also a $Bi_4Ge_3O_{12}$ (BGO) semiconical crystal (from the electromagnetic calorimeter of the L3 experiment at LEP) with length of 24 cm and cross section of 2.4×2.4 cm^2 on one side and 3.2× 3.2 cm^2 on the other end. The light produced by particles traversing the crystal under test was read out by two photomultiplier tubes (PMTs) located at opposite ends: one on the left (as seen by particles), called PMTL, and one on the right, called PMTR. Both PMTs are of the same type: they have 10 multiplication stages and are equipped with a borosilicate window.
In order to reduce the light trapping effects of the large refractive index of $PbWO_4$ (n = 2.2), the PMTs were coupled to the crystal by means of silicone "cookies" (n = 1.4)[2].
In the case of doped crystals we have used also different types of filters, as is shown in Figure 3.3 on the left, and better explained in Section 3.5. The crystal under study was mounted on a platform able to rotate around a vertical axis. The crystal was oriented in the horizontal plane and the rotation axis went through its geometrical centre. The particle beam was also steered through this centre, as illustrated in Figure 3.3 right. The angle θ, which is frequently used in the following, represents the angle between the crystal axis and a plane perpendicular to the beam line. The angle increases when the crystal is rotated such that the crystal axis Left-Right (L-R) approaches the direction of the traveling beam particles. We call as Cherenkov angle the angle at which the Cherenkov light has a maximum in one of the two PMTs: $\theta = 30°$for the Right PMT and θ = -30 for the Left one. We also call as "anti-Cherenkov" the opposite angle: the angle at which every PMTs have only scintillation light, but not Cherenkov. The crystal orientation shown in Fig 3.3 right corresponds

[1]The measurements were done with the crystal (courtesy of the ALICE experiment) covered with a foil of aluminized Mylar to avoid dispersions of light produced by particles passing through it.

[2]Adding cookies, in fact, the change of refraction index that the light have exiting from the crystal is much smooth that with air, and total refractions are avoided.

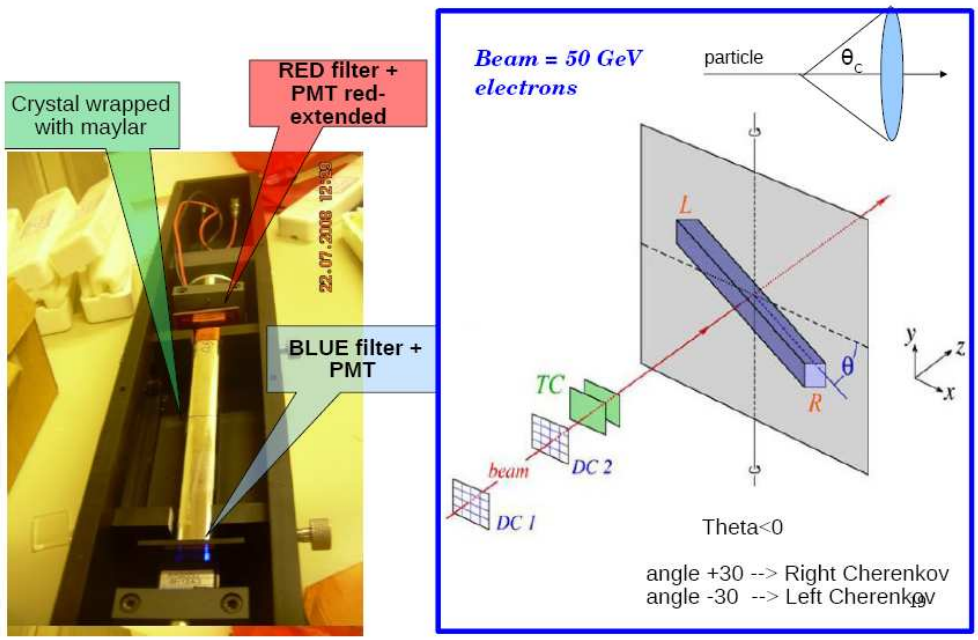

Figure 3.3: *Left Picture of the single crystal. It's possible to see the crystal covered with the Mylar, the two PMT with red and blue filters (used only for doped crystals).Right Schema of the experimental setup with the beam hitting the crystal in the centre, the beam position chambers (DC1, DC2), the trigger counters (TC). The coordinate system and the rotation angle θ between the beam and the crystal axis are also indicated.*

to $\theta = -30°$that is Cherenkov angle for the Left PMT and anti-Cherenkov of the Right one.
Two small scintillation counters (TC) provided the signals that were used to trigger the data acquisition system. These trigger counters were 2.5 mm thick, and the area of overlap was 6×6 cm^2. A coincidence between the logic signals from these counters provided the trigger. The trajectories of individual beam particles could be reconstructed with the information given by two small drift chambers (DC1, DC2) which were installed upstream of the trigger counters. About 10 m downstream of the crystal, placed behind about 20 interaction lengths of concrete blocks, a 50×50 cm^2 scintillator paddle served as a muon counter. The first 10 interaction lengths consisted of the DREAM fibre calorimeter, which in studies about single crystal, only served to recognize and eliminate hadron contamination from the beam.
For the temperature studies, the temperature of the crystal was controlled by means of a thermoelectric system, based on the Peltier effect. A thermal conductive paste was used to increase the coupling efficiency between the crystal and the thermoelectric plate. With a computer-controlled system, it was possible to achieve temperature scan between 13 and 43°C for this setup.

Measurement of the time structure of the crystal signals were a very important part of the tests described here. In order to limit distortion of this structure as much as possible, we used special, 15 mm diameter cables to transport the detector signals to the counting room. Such cables were also used for the signals from the TC, and these were routed such as to minimize delays in the DAQ system. The crystal signals were sent into a unity-gain Linear Fan-out unit, output signals of which were used to measure the time structure and the total charge. The time structure was measured with an oscilloscope[3], with sampling rate of 2.5 GHz. The charge measurements were performed with 12-bit Caen ADCs. These had a sensitivity of 100 fC/count and a conversion time of 5.7 μs. The data acquisition system used VME electronics; the trigger logic was implemented through NIM modules and the signals were sent to a VME I/O register, which also collected the spill and the global busy information.

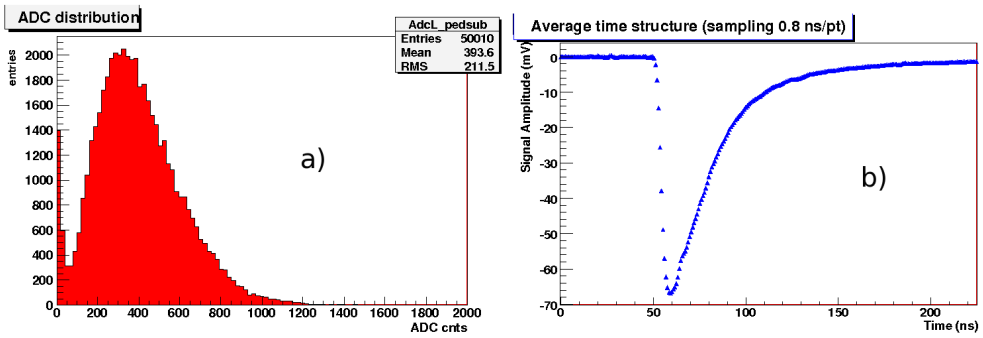

Figure 3.4: *The signal of a beam of 50 GeV electrons traversing the $PbWO_4$ crystal is read from both sides of the crystal with an ADC counter and an oscilloscope. Fig (a) shows the ADC spectrum, that is proportional to the mean energy released by particles traversing the crystal, and Fig (b) shows the average time structure of the signals.*

The quality of the information obtained in this way is illustrated in Fig. 3.4, which shows a typical ADC signal distribution (a) and the average time structure of the signals (b) from one PMT, generated by 50 GeV electrons traversing the crystal.

[3]In order to study the time structure of doped crystals, we have performed different measurements, changing the sampling rate of the scope.

3.3 Results of undoped $PbWO_4$ crystals

Lead tungstate crystals ($PbWO_4$) are attractive as detectors for electromagnetic showers because of their high density, which implies a short radiation length and Moliere radius, their fast signals and their relative insensitivity to the effects of radiation damage.
Already after the first test-beam studies (in 2006) it was demonstrated that a significant fraction of the signals from scintillating lead tungstate ($PbWO_4$) crystals is due to Cherenkov radiation [41]. This was concluded from the measurements of the time structure of the signals and the non-isotropic nature of the light generated by high-energy electrons and muons traversing a $PbWO_4$ crystal. In the crystal used for these studies, Cherenkov light contributed up to 15% of the signals measured by a photomultiplier tube (PMT). This was very promising and further tests were done about the feasibility to use $PbWO_4$ for the Dual Readout technique.
We also have studied the dependence of the signal as a function of the temperature to further study the Cherenkov presence and to evaluate the fraction of C/S dependence from the temperature.

3.3.1 Temperature studies

It is well known that $PbWO_4$ crystals, which are the detectors of choice in several modern large-scale experiments in high-energy and medium-energy physics, are very delicate. Mechanically, they are very fragile and their scintillation properties are significantly affected by small changes in temperature. In the studies we have carried out, we have examined the temperature dependence of the scintillation properties, including the total light output, the contribution of Cherenkov light to the signals and the decay time of the signals in a temperature range of about ± 15°C around room temperature.

Response anisotropy and time structure

All crucial aspects of the experimental results obtained in this study and discussed below are illustrated in Fig.3.5. This figure shows the average time structure of the signals from one of the PMTs reading out the crystal, for the lowest and highest temperatures at which these measurements were performed: T=13°C (left) and T=45°C (right), respectively. Each of the top graphs depicts the average time structures of the signals measured at both $\theta = 30°$and $\theta = -30°$. The difference between the signals recorded at these two angles is shown in the bottom graphs, separately for each of the two temperatures. At $\theta = 30°$, Cherenkov light produced in the showers initiated in the crystals by the high-energy electrons is preferentially detected in PMTR, since this light is emitted at an angle of $arccos(1/n) = 63°$ by the charged relativistic shower particles traversing the $PbWO_4$ crystal (which has a refractive index n = 2.2). This Cherenkov light manifests itself as an additional prompt com-

ponent, superimposed on the scintillation light that constitutes practically the entire signal measured at $\theta = -30°$. As a result, the signals measured at $\theta = 30°$are larger, and rise steeper than those measured with the same PMT at $\theta = -30°$[4]. The Figure 3.5 also exhibits several other interesting features:

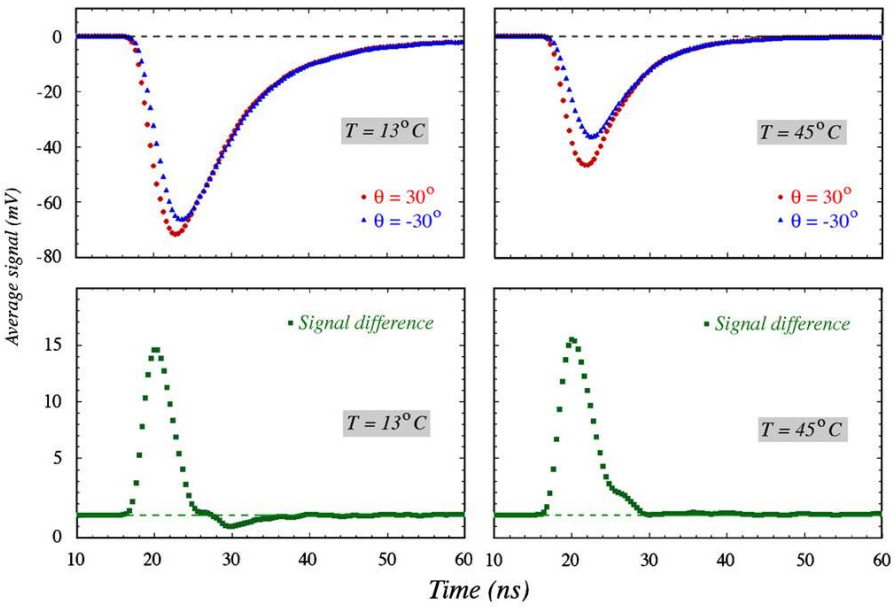

Figure 3.5: *Average time structure of the signals from PMTR measured for 50 GeV electrons traversing the $PbWO_4$ crystal at $\theta = 30°$and $\theta = -30°$(top plots), as well as the difference between these two signals (bottom plots), measured for two different temperatures: 13°C (left) and 45°C (right).*

- the total, time-integrated signals are considerably smaller at the higher temperature;
- this decrease in total signal seems to be entirely due to a reduction of the amount of scintillation light, since the total Cherenkov signal is not significantly different at these two temperatures;
- as a result, Cherenkov light represents a much larger fraction of the total signal at the higher temperature;
- less clear, but nevertheless very significant is the fact that the signal decreases much faster beyond its maximum at the higher temperature.

[4]For PMT L, the opposite effect was observed. As expected, here the signals at $\theta = -30°$were measured to be larger and steeper than those at $\theta = 30°$.

Response anisotropy and the Cherenkov fraction

As we have seen on section 1.2, one of the methods used to distinguish the Cherenkov from scintillation light, is the directionality. By varying the detector orientation with respect to the direction of the incoming particles, a contribution of Cherenkov light would then manifest itself as an angle-dependent asymmetry. By tilting the crystal over an angle θ comparable to θ_C, Cherenkov light produced by the particle shower would be preferably detected in either the L or R PMT. By measuring the *response asymmetry* $(R-L)/(R+L)$ as a function of the tilt angle θ, the contribution of Cerenkov light to the detector signals could be determined[5].
However, a better way to find a non-isotropic component in the light generated on the crystal, *i.e.,* Cherenkov light, is the *response anisotropy*, defined as:

$$\xi(\theta) = \frac{(R_\theta - L_\theta) + (L_{-\theta} - R_{-\theta})}{(R_\theta + L_\theta) + (L_{-\theta} + R_{-\theta})} \tag{3.3}$$

where R_θ and L_θ represent the average signals measured in the PMTs R and L, for the same events respectively, when the crystal is oriented at an angle θ. Since these signals were equalized for $\theta = 0$, as for the asymmetry, a non-zero value of ξ is indicative for a non-isotropic component in the light generated in the crystals, *i.e.,* , Cherenkov light.

The relationship between ξ and the relative contribution of Cherenkov light to the PMT signals can be seen as follows. Let's call the relative contributions of Cherenkov light to the R and L signals ϵ_R and ϵ_L, respectively (with ϵ_R and ϵ_L normalized to the scintillation signals). Because of symmetry considerations, $\epsilon_R(\theta) = \epsilon_L(-\theta)$ and $\epsilon_L(\theta) = \epsilon_R(-\theta)$. Therefore,

$$\xi(\theta) = |\frac{\epsilon_R(\theta) - \epsilon_L(\theta)}{2 + \epsilon_R(\theta) + \epsilon_L(\theta)}| \tag{3.4}$$

The fraction of Cherenkov light, f_c, in the sum of the two PMT signals R and L is:

$$f_c(\theta) = \frac{\epsilon_R(\theta) + \epsilon_L(\theta)}{2 + \epsilon_R(\theta) + \epsilon_L(\theta)} \tag{3.5}$$

Let's consider a single relativistic charge particle traversing the crystal, and ignore the Fresnel reflections. This fraction is zero for $\theta = 0°$and reaches its maximum possible value when Cherenkov light is emitted parallel to the crystal axis. This happens when $\theta = 90°$- θ_C (C light detected on PMTR), or $\theta = \theta_C$ -90°(C light detected in PMTL). At these angles, the ratio of the contributions of Cherenkov and scintillation light to the signals from the PMT that detects the Cherenkov light also reaches its maximum value.
Fig 3.6 shows the measured value of the response anisotropy (a) and the

[5]This method was used at the beginning of our studies on $PbWO_4$ to demonstrate the existence of Cherenkov on the signal generated by beam electrons.

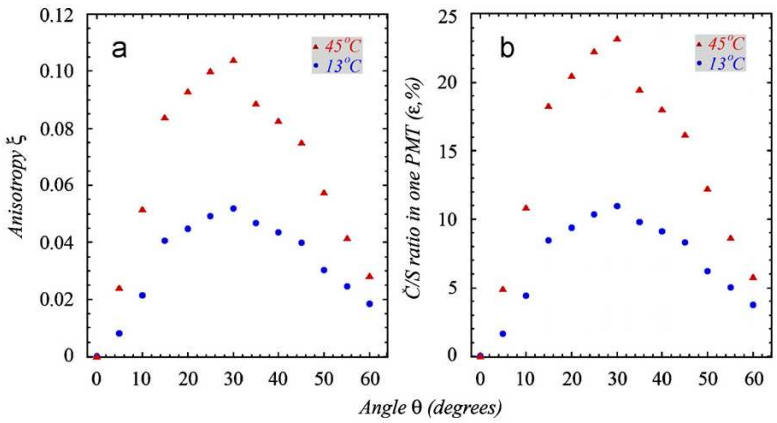

Figure 3.6: *The response anisotropy ξ, (a), and the Cherenkov/scintillation signal ratio in PMTR, ϵ_R, (b), as a function of the angle of incidence (θ) of the electron beam, measured at the temperatures of 13°C and 45°C. Both variables reach their maximum value near the complement of the Cherenkov angle ($90° - \theta_C = 27°$).*

Cherenkov/scintillation ratio in the signals from one PMT, evaluated as described before, (b), as a function of angle, for 50 GeV electrons traversing the $PbWO_4$ crystal. Results are given for the highest (45°C) and the lowest (13°C) temperatures at which complete angular scans were performed. As expected, the anisotropy reaches its maximum value near the angle $|\theta| = 90°$- θ_C at which Cherenkov light emitted by the incoming particles impinges perpendicularly onto the photocathode of one of the PMTs.

Time structure and the Cherenkov fraction

As illustrated in Fig.3.5, the time structure of the PMT signals can also be used to determine the relative contributions of the prompt Cherenkov light. We have chosen as reference for the signals from PMTs the time structure measured for each anti-Cherenkov angle. Then we normalized[6] the trailing edge of the time structure measured at angle θ to that of the reference signal, in order to take into account that the effective thickness of the crystal depends on its orientation with respect to the particle beam. The contribution of Cherenkov light (bottom plot in Fig 3.5) was determined from the excess charge measured in the normalized signal with respect to the reference signal[7].

[6]In practice, we equalized the integrated charge measured from $t = 26 - 50$ ns, assuming that this part of the time spectra contains only contributions from scintillation light.

[7]This procedure was followed separately for both PMTs.

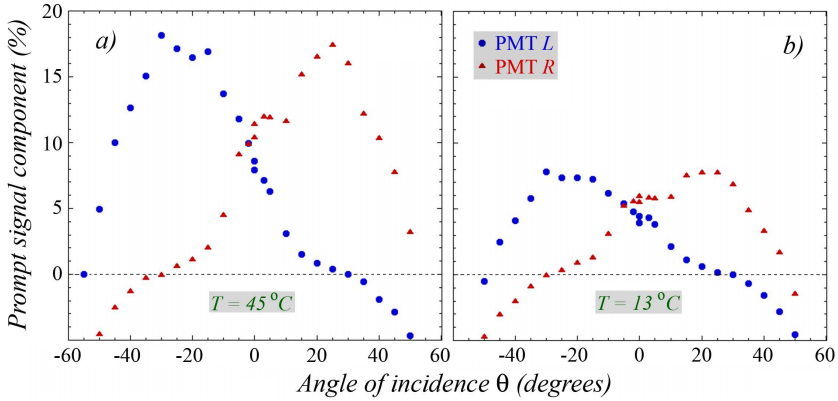

Figure 3.7: *Fraction of the total signal represented by the prompt component, as a function of the angle of incidence (θ) of the electron beam, measured at temperatures of 45° C (a) and 13° C (b). Results are shown separately for PMTL (where the fraction is normalized to zero for θ =30°) and PMTR (normalized to zero for $\theta = -30°$).*

In Fig 3.7 is shown the average fraction of the total signal represented by the prompt component found in this way, as a function of the angle θ. Results are given for the highest (45°C) and the lowest (13°C) temperatures at which measurements were performed, separately for both PMTs. The symmetry between the results for both PMTs is excellent, *i.e.,* , the results for PMT L are, within experimental uncertainties, the same as for PMTR if the sign of θ is inverted. As in the case of the response anisotropy, the largest fraction represented by the prompt signal component was found at $|\theta| \sim 90° - \theta_C$. And as before, this maximum (and thus the relative fraction of Cherenkov light in the signals) increased by more than a factor of two over the temperature range considered here. However, the Figure also exhibits some features that were not revealed by the measurements of the anisotropy. For example, it turns out that at θ =0°, the signals from both PMTs contain a substantial Cherenkov component. The amplitude of this component is about half of that observed at the angle where the prompt component is largest. It also appears that the signals at the anti-Cherenkov angle, *i.e.,* , the signals that were used for "pure" scintillation reference purposes, were not so pure after all. In fact, the prompt component seems to reach a local, secondary maximum precisely at that angle. The factors that may contribute to this effect are Fresnel reflections, contributions from the optical properties of the crystal surfaces, and the quality of polishing and wrapping material.

Temperature dependencies of the C fraction and Light Yield

We have studied the dependence of the Cerenkov fraction on the temperature, both with the anisotropy and the time structure. The results are summarized in Figure 3.8 which gives the ratio of the Cherenkov and scintillation contributions (ϵ) to the signals from a single PMT, derived from the response anisotropy (Eq3.4) ξ (blue dots) and from the time structure of the signals (from the relative contribution of the prompt component to the signals, averaged over the two PMTs) (red triangles), at the angle for which this ratio reaches its maximum value ($|\theta|$ =30°), as a function of the temperature of the crystal[8].

In both analysis ϵ increases by about a factor of two over the temperature range considered here (13-45°C).
Apart from the fact that the measurement of this C/S ratio from the time structure data leads to a systematically underestimated value[9], the results from these two methods are in good agreement with each other. Both methods indicate a substantial and gradual increase in the fraction of Cherenkov light, as the temperature increases; ϵ increases by about a factor of two over the temperature range considered (13-45°C).
This is due to the decrease in the amount of scintillation light produced by the crystal. This may already be concluded from Fig. 3.5, which shows that the prompt component is the same for both temperatures, but that the overall signal is considerably smaller at the higher temperature, causing the scintillation component to be much less pronounced in that case.

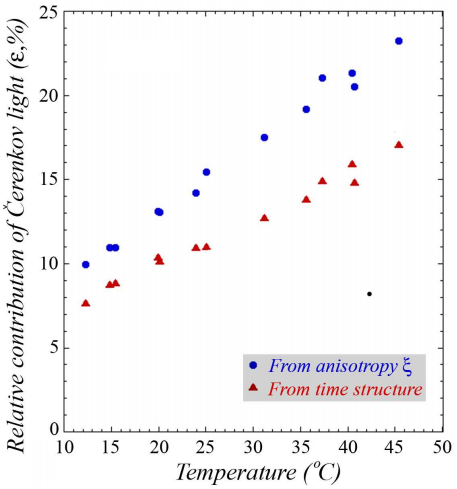

Figure 3.8: *Temperature dependence of the C/S ratio, ϵ, measured in one of the PMTs. ϵ is derived from both the response anisotropy (blue dots), and from the time structure (red triangles).*

We have confirmed this conclusion with a detailed study of the temperature dependence of the light yield of the individual PMTs for different orientations of the crystal. Results of this study are displayed in Figure.3.9; in Fig.3.9a is shown the average signals measured in PMTL for $\theta = -30°$, 0°and 30°as a function of the temperature, over the range from 13°C to 45°C. The same is shown for PMTR in Fig.3.9b. The smaller light yield at θ =0°is a consequence of the increased (apparent) thickness of the rotated crystal; the difference observed between the light yields measured at $\theta = \pm 30°$is the result of different contributions of Cherenkov light to the signals. The data are reasonably well

[8]The time structure data were averaged over both PMTs for this purpose.
[9]This is due to the fact that the reference signal used contains some of the Cherenkov component, as previously described.

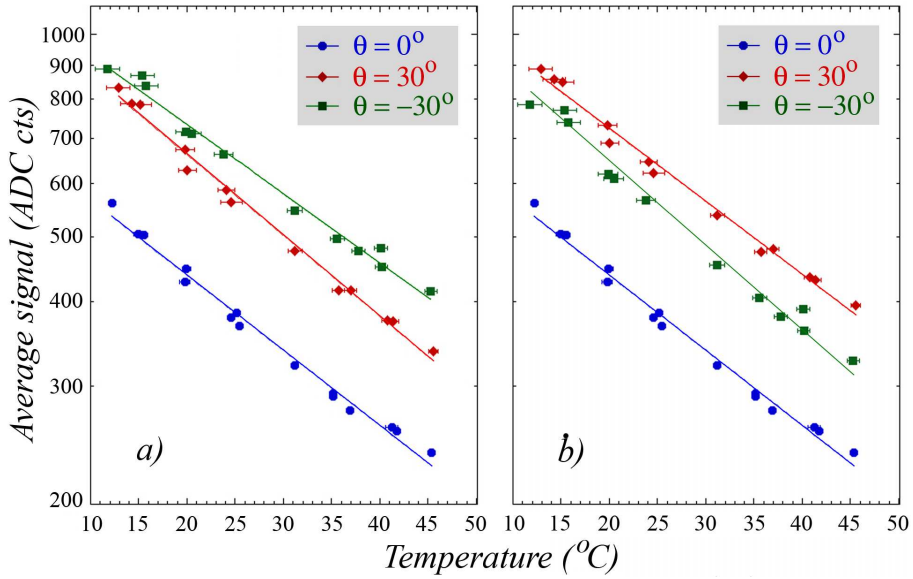

Figure 3.9: *Signals from the $PbWO_4$ crystal as a function of the temperature, measured with PMTL (a) and PMTR (b), for three different angles. The lines represent the results of least-squares exponential fits to the experimental data. The error bars represent only statistical uncertainties.*

described by straight lines in these logarithmic plots: and this indicates, in all the cases, an exponential decrease of the light yield as a function of temperature. However, the slope of the fitted exponential clearly depends on the angle. The temperature dependence of the light yield, expressed in terms of these coefficients, is summarized in Table 3.2.

Angle θ	*Slope PMTL (%/°C)*	*Slope PMTR (%/°C)*
-30°	2.61 ± 0.02	2.99 ± 0.02
0°	2.81 ± 0.02	2.80 ± 0.02
30°	2.95 ± 0.02	2.66 ± 0.02

Table 3.2: *Temperature dependence of the light yield measured in the two PMTs reading out the $PbWO_4$ crystal, for three different orientations. (The errors include only statistical uncertainties).*

Temperature dependencies of the decay constant

When the time structure of the PMT signals is displayed logarithmically, yet another temperature dependent effect of the scintillation process becomes visible. Fig. 3.10 (a) shows the time structure of the (inverted) signals measured with PMTL at $\theta = 30°$, for both the highest (45°C) and the lowest (13°C)

temperatures at which measurements were performed. The trailing edges of the curves are reasonably well described by a single exponential, and is considerably steeper at the higher temperature. The straight lines drawn in this Figure correspond to a decay time[10] of 5.6 ns at 45°C vs. 8.8 ns at 13°C.

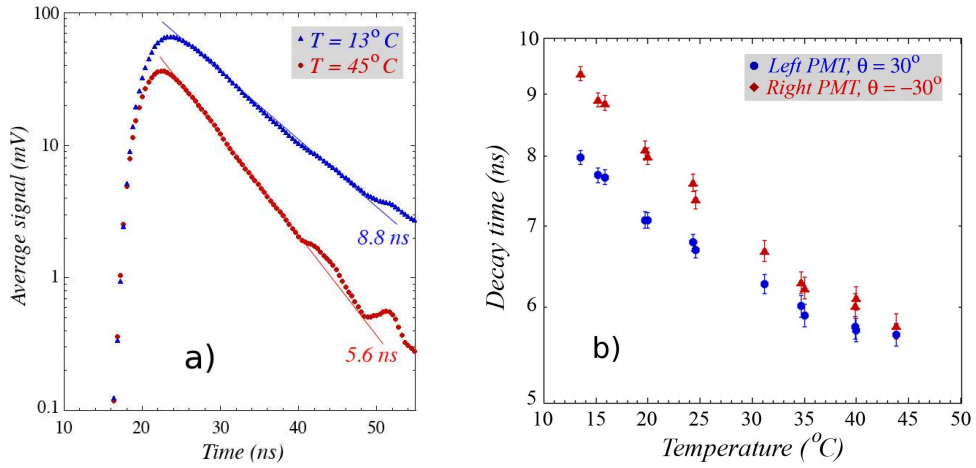

Figure 3.10: *Average time structure of the $PbWO_4$ signals (inverted and in logarithmic scale) from PMTL for $\theta = 30°$, measured at two different temperatures. The trailing edge is well described by a single exponential. (Fig a). Decay constant of the scintillation light is also displayed (Fig b), (from the exponential fit, as shown in Fig a) as a function of temperature for both PMTs. The angle was chosen such as the signals are almost exclusively generated by scintillation light (30° for Left and -30° for Right) (Fig b).*

We have studied the temperature dependence of the decay time of this particular crystal in a systematic way. Since the decay concerns the scintillation process, we concentrated on signals in which the Cherenkov contribution was minimal, *i.e.,* , the anti-Cherenkov angles.
The trailing edge of the average time structure profile was fit to an exponential function over a range starting 2 ns after the maximum amplitude was reached and extending to the point where the signal had dropped to 13.5% (e^{-2}) of the amplitude value. The results are summarized in Table 3.3 and graphically displayed in Fig. 3.10 b for the two PMTs.
These data show that the decay time of the scintillation light produced in $PbWO_4$ crystal gradually decreases by $30 - 40$ % over the temperature range from 13°C to 45°C.

[10]These results concern one particular crystal; the decay time of other similar crystals is not necessarily the same.

Temperature °C	*Decay time (ns)* $PMTL$, $\theta = 30°$	*Decay time (ns)* $PMTR$, $\theta = -30°$
13	7.97 ± 0.11	9.35 ± 0.13
15	7.70 ± 0.11	8.86 ± 0.12
20	7.07 ± 0.11	8.04 ± 0.12
25	6.73 ± 0.11	7.48 ± 0.12
30	6.27 ± 0.11	6.68 ± 0.12
35	5.96 ± 0.11	6.25 ± 0.12
40	5.76 ± 0.11	6.05 ± 0.12
45	5.70 ± 0.11	5.78 ± 0.14

Table 3.3: *Decay time of the scintillation signals from the $PbWO_4$ crystal for different temperatures. (The errors include only statistical uncertainties).*

3.4 New Crystals for Dual Readout

In order to use crystals in dual-readout calorimeters, and to have a better separation between the Cherenkov and the scintillation components, (using the methods described on section 1.2), a "perfect" crystal should have an emission wavelength far from the bulk of Cherenkov radiation, a scintillation decay time of tenths of nanoseconds, and it shouldn't be too much bright for scintillation, otherwise the Cherenkov/scintillation signal ratio would be too low.

Comparison between $PbWO_4$ and BGO crystals

On the Tab 3.4 the main characteristics of both crystals used for our test beam studies, BGO and $PbWO_4$, are summarized.
If we compare the BGO crystal to the $PbWO_4$, we can see that the main disadvantage is that it's too bright; this cause the ratio C/S to be smaller. The advanteges of BGO are that the scintillation spectrum peaks is at 480 nm, (and this allows to use filters to separate the short Cherenkov wavelength to the scintillation light), and that the decay time is around 300 ns. This time is good for separations between prompt peak from Cherenkov to the scintillation emission, and is still good to be used in a detector for high energy physics.

Crystal	*LightYield* % $NaI(Tl)$	*Decay Time(ns)*	*Peak* λ (nm)	*Cutoff* λ (nm)	*Refr. index*	*Density* (g/cm^3)
BGO	20	300	480	320	2.15	7.13
$PbWO_4$	0.3	10	420	350	2.30	8.28

Table 3.4: *Characteristics of crystals used for the Dual Readout Technique*

These behavours of the two different crystals have been confirmed by our measurements during the 2007 test beam [42]. In the case of BGO, we obtained a

good separation between Cherenkov and scintillatin light only from the time structure of the signal[11]. We measured in fact, the C/S ratio in individual events with a relatively accuracy of $\sim$ 20-30% for energy deposit of 1GeV. For the $PbWO_4$, instead, we have seen that it has less favorable properties that BGO. Altough the Cherenkov fraction of the total signal was considerably larger for this crystal, the absence of the two main advantages of the BGO made it harder to extract precise informations on the Cherenkov content of individual event signals. We could manage to obtain good results only with the help of the directionality information, that is not applicable for "real" detectors. Both types of crystals generated Cherenkov signals of at least 30 photoelectrons per GeV per deposited energy. This is sufficient for reducing photoelectrons statistics to a non-dominant source of fluctuations in hadronic dual-readout calorimeters.
Based on the studies on $PbWO_4$ and BGO crystals, we decided to explore the possibility to combine these advantages of BGO with the intrinsically much higher Cherenkov fraction of $PbWO_4$.
We have found on the literature many studies, done with the goal of an "ideal" crystal for the ECal of the CMS experiment, about $PbWO_4$ crystals [44, 45, 50]. We have seen that some doping elements, if added to the $PbWO_4$ crystals, can achieve a shift of the scintillation spectrum to longer wavelengths, and a longer decay time, that is what we wanted for the Dual Readout.

3.5 Mo- and Pr-doped $PbWO_4$ crystals

We have tested these new crystals in a test beam carried on July 2008, in particular lead tungstate doped with small percentage[12] of Molibdenum and Praseodymium. More details can be found here [46, 47].
In this section the characteristics of these two kinds of doped crystals are explained, and the results that we have obtained from the test beam are reported. In particular, for both dopings, the time structure of the signals, the C/S ratio, the effect of light attenuation, and the Cherenkov light yield are described.

3.5.1 Emission spectrum

In Fig: 3.11 is possible to see what are the effects of these two dopings (a) for Molybdenum, (b) for Praseodymium on the emission spectrum of the crystals.

- **$PbWO_4$ crystals doped with Molybdenum**
  We have tested crystals doped with 1%-Mo (pink spectrum) and 5%-Mo

[11] We have analyzed only the signal coming out from the PMT equipped with the UV filter, and we have chosen two time windows in which to integrate the prompt Cherenkov signal and the scintillation tail.
[12] 0.5%, 1%, 1.5% for Pr-doped and 1%, 5% for Mo-doped crystals

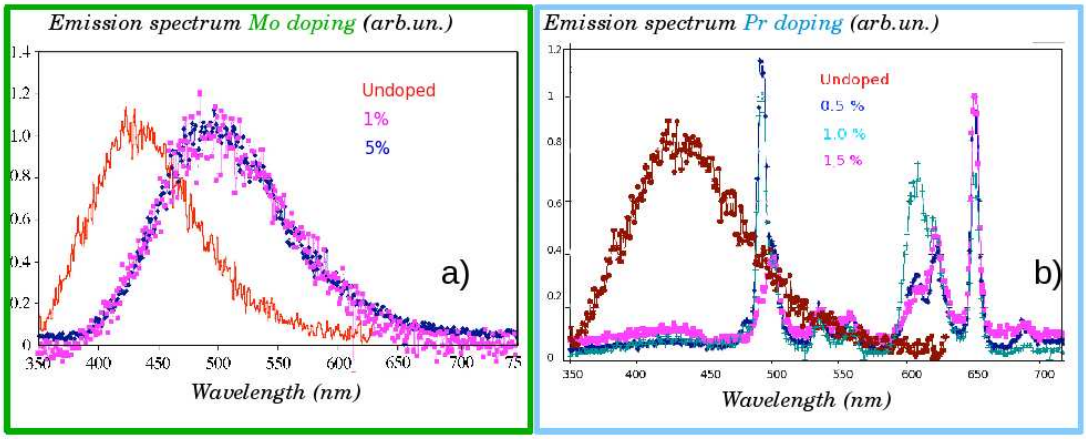

Figure 3.11: *Comparison between radioluminescence spectra of small lead tungstate samples, doped with different percentages of Molybdenum (a)[44] and Praseodymium (b) [45].*

(blue spectrum). The Molybdenum inpurity substitutes the tungsten ion in the matrix and forms a Mo-O_4 complex, which has a large cross section for electron capture, and acts as a wavelength shifter. This effect is illustrated in Fig 3.11(a) which shows the radioluminescence emission spectra measured on small samples of doped and undoped $PbWO_4$ [44]. The maximum of the emission is shifted from $\sim$ 420 nm to $\sim$ 500 nm. There is very little difference between the effects of the 1% and 5% Mo concentration in this measurement, as far as it concerns the emission wavelength. The three curves shown here are normalized to each other; but increasing the doping concentration the intensity of the emission spectrum is also increasing [50].

- **$PbWO_4$ crystals doped with Praseodymium**
  Based on the studies published in [45], we chosed three Pr-dopant concentrations to be used for our crystals: 0.5%, 1%, 1.5%. Similar to other trivalent dopants, Pr^{+3} suppresses scintillation in the host crystal altogether. On the other hand, it introduces new scintillation components with long time constants (in the μs range), based on Pr^{3+} 4f$-$4f transitions in the green-red part of the spectra. This is illustrated in Fig3.11(b), which shows radioluminescence spectra of small $PbWO_4$ doped samples (0.5%, 1% and 1.5% Pr), compared to the one of undoped crystal.

3.5.2 2008 test beam setup

The setup used for the test of doped crystals, is almost the same as all the others DREAM test beams, as explained in Section 3.2.1. We tested, under a beam of 50 GeV electrons, one crystals per time over a rotating platform, with a PMT at each end. As we can see from the Figure 3.11, in both cases the emission spectrum of the doped crystals is red-shifted. This is very convenient for the dual-readout purpose, in fact it gives us the possibility to use different filters to separate the low-wavelength Cherenkov component from the scintillation one. In order to select the wavelength region that contributed to the signal, and to study the C/S signal for each of them, we chose different long-pass filters. We have used a short-pass filter, ultraviolet (UV) or blue (B), to detect the Cherenkov light, whereas the other PMT was used with a long-pass filter: yellow (Y), orange (O) or red (R) for the scintillation light Table 3.5 lists the properties of the filters that we used in our studies.

Filter type	*Filter color*	$> 90\%$ *transm.*
UG11	UV	$\lambda < 400$ nm
BG3	Blue	$\lambda < 500$ nm
OG495	Yellow	$\lambda > 495$ nm
OG570	Orange	$\lambda > 570$ nm
RG610	Red	$\lambda > 610$ nm

Table 3.5: *Wavelength cut of filters used to separate the Cherenkov and scintillation components.*

The filters were sandwiched between the PMT and the crystal, and coupled by means of silicon cookies. We have used two different kinds of PMTs: one type, to be called PMTS (standard), had a bi-alkali photocathode, and was used in conjunction with a blue or ultraviolet filter, in order to detect mainly the Cherenkov component; the other type had a multi-alkali photocathode (red extended), and was used only in the case of Pr-doped crystals, to detect scintillation light. The latter substantially increases the quantum efficiency for longer-wavelength light.

3.6 Experimental results for $PbWO_4$:Mo

In this section, results obtained with the $PbWO_4$ crystal doped with 1% of Molybdenum are described. The effects observed as a result of increased doping levels: from 1% to 5% are also shown.

3.6.1 The time structure of the signal

As suggested from the radioluminescence measurements (Fig: 3.11), almost all light at wavelength shorter than 400 nm (selected with the UV filter) should be due to pure Cherenkov radiation, while the region above 500 nm (yellow filter) is strongly dominated by scintillation light. This has been confirmed by our measurements of the time structure of the signal produced by 50 GeV electrons traversing out 1% Mo-doped $PbWO_4$ crystal (Fig 3.12).
In Fig 3.12a the solid (blue) line represents the time structure measured on one side of the crystal, where a UV filter was mounted between the crystal and the PMT. The dotted (red) line represents the time structure measured on the other end of the crystal, where the light was filtered by the yellow one. These two time structures, which were measured for the same sample of events, are spectacularly different. The UV light produces signals that are very fast, more than 90% of the integrated signal is contained in a time interval of only 7 ns. These characteristics strongly indicate that the light passing the UV filter produced an almost pure Cherenkov signal, while the light passing the yellow filter generated a signal that had all the characteristics of a scintillation signal. The yellow light produces a signal with a rise time (10-90% of maximum amplitude) of 5 ns, and this signal decays to 10% of its maximum value in 64 ns.

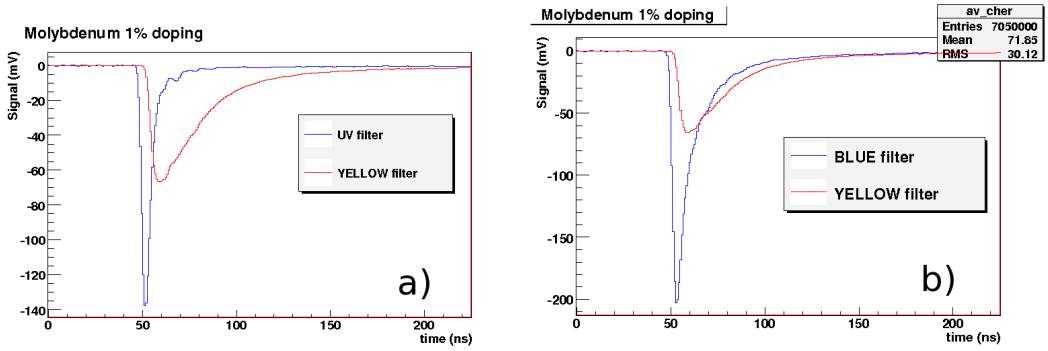

Figure 3.12: *Average time structure of the signals from a $PbWO_4$ crystal doped with 1% Mo, generated by 50 GeV electrons. The angle θ was 30° in these measurements. Shown are the results obtained with yellow filters (red line) and UV (blue line) (Fig a) and Blue filter (Fig b).*

In Fig: 3.13, the yellow signal is inverted and plotted on a logarithmic scale.

The decay exhibits at least two different components.

A fit by eye, represented by the two exponential curves, gives time constants of 26 and 59 ns, respectively, for these components. It is interesting to note that the decay time of 26 ns is in excellent agreement with results reported by Nikl *et al.*[50], who characterized the properties of small samples of $PbWO_4$ crystals doped with various concentrations of molybdenum excited by radioluminescence, photoluminescence and thermoluminescence. For a concentration of 1%, they measured a decay time of 26.3 ns.

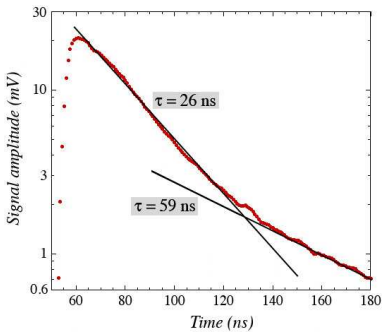

Figure 3.13: *Average time structure of the Yellow signal from the 1% Mo crystal. The straight lines, correspond to exponential decay times of 26 and 59 ns, respectively.*

We repeated these measurements after replacing the UV filter by the blue one (Fig 3.12b), and we observed that, as we expected, the effect of shifting the filter cutoff from 400 to 500 nm is that the blue light will contain a significant fraction of scintillation light, in addition to the Cherenkov light. The tail of the two distributions are almost identical.

Due to these results, we have decided to continue our analysis only with data taken with the UV filter on the Cherenkov side.

3.6.2 Cherenkov/Scintillation ratio

Since the signal passing through the UV filter is completely dominated by Cherenkov radiation, its dependence on the angle of incidence of the beam particles (θ, see Fig 3.3) should be completely different for that of the yellow filter with scintillation light. Figure 3.14 shows the ratio of the signals generated by the light transmitted by the UV and the yellow filters, as a function of the angle of incidence of the beam particles. The UV filter was mounted on the right hand side (R) of the crystal, the yellow filter on the left hand side (L) in these measurements, so that one would expect Cherenkov light to be mainly detected for positive values of the angle θ. C light is emitted at the characteristic angle, $\theta_C = arccos\ 1/n \sim 63°$(in our case). That means that we have a maximum on the PMTR when the crystal is rotated, with respect to the beam, of an angle: $\theta = 90° - \theta_C \sim 27°$. The distributions shown in Figure 3.12 reach indeed their maximum value near that angle.

The signals, and thus their ratio, were determined in two different ways for this analysis. In the first method, we simply integrated the signals over the entire time structure, *i.e.,* , over the entire 224 ns interval covered by the oscilloscope. These results are shown in Figure 3.14a. In the second method, we attempted to optimize the Cherenkov content of the UV signals and the scintillation content of the signals from the light transmitted by the yellow fil-

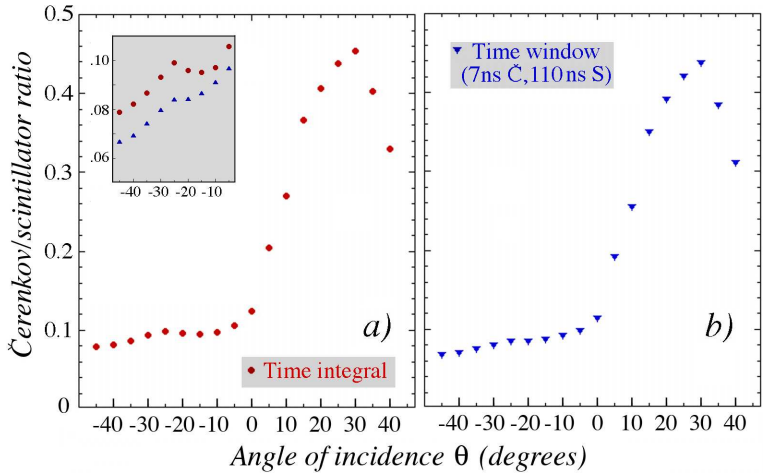

Figure 3.14: *Ratio of the signals from the light transmitted by the UV and the Y filters, as a function of the angle of incidence of the beam particles. The signals are obtained either by integrating over the entire time structure (a), or over limited time intervals chosen in a suitable way in order to have as pure as possible C and S signals respectively (b). The insert shows a blown-up version of the data at* $\theta < 0$.

ter. The UV signals were integrated over a 7 ns time interval (t = 48 - 55 ns), which contained more than 90% of the prompt peak seen in Figure 3.13. The yellow signals were integrated over the time interval $t = 70 - 180$ ns. The ratio of the signals obtained in this way is displayed as a function of θ in Figure 3.14b.

From the similarity of the distributions in Figures 3.14a and 3.14b one can conclude that there is no significant contamination of scintillation light in the signals produced by the light transmitted by the UV filter, since any such contamination would reduce the difference observed between positive and negative values of θ[13].

Upon closer inspection, one may notice a very small bump near the anti-Cherenkov angle ($\theta = -27°$), which is somewhat more pronounced in Figure 3.14a. This is illustrated by the insert in Figure 3.14a. This bump is the result of Cherenkov light that was reflected from the side where the yellow filter was mounted, and detected at the opposite side of the crystal. The efficiency for detecting such light is largest for $\theta = -27°$. However, since this light has to make a roundtrip in the crystal before being detected, it arrives somewhat later at the PMT than the direct Cherenkov light seen for $\theta > 0$. Therefore, the effect is less pronounced in Figure 3.14b, where a very narrow time interval was used to define the Cherenkov signals. The reflected light arrived too late in that case.

[13]Note that the distributions shown in Figure 3.14 should be flat in θ if only scintillation light played a role.

3.6.3 Experimental results for $PbWO_4$:Mo 5%

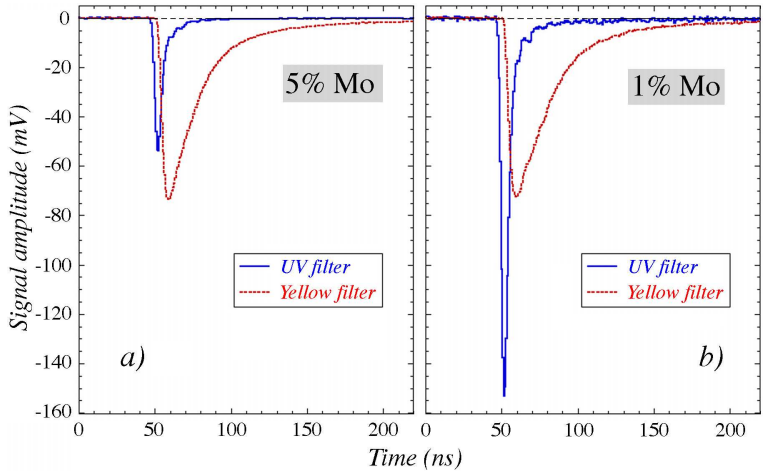

Figure 3.15: *Comparison between the average time structure of the signals from a $PbWO_4$ crystal doped with 5% Mo (a) and 1% Mo (b). Shown are the results obtained with UV and yellow filters, respectively.*

Already after a first look, the doping with 5% of Molybdenum seemed less promising than the one with 1% of Molybdenum, and we decided to dedicate only a little bit of beam time to these measurements. The only data that make possible a comparison between these two crystals concerns measurements with the electron beam at angles of incidence θ= 0, 30 and -30°, in which the filters, PMTs and high-voltage settings were the same (yellow and UV). The Fig 3.15 shows the comparison of the average time structure of the two doping concentrations, for both filters; the angle was θ=30°. As for the 1%-Mo crystal, the light transmitted through the UV filter seems to be pure Cherenkov radiation, while the light passing through the yellow filter appears to be completely dominated by scintillation processes. However, the ratio between these two signals is quite different from that in the 1%-Mo crystal. Whereas the scintillation signals are barely affected by the difference in the doping fraction, the signal produced by the light traversing the UV filter is smaller by about a factor of three. In Fig 3.22(b) the absorption spectrum of the Mo-doped crystals is shown, as measured from the radioluminescence technique. The shaded area represents the bandwidths of the light transmitted through the UV optical filter. We can see that, increasing the concentration of doping, the absorbance of the crystal is changing. In particular the wavelength gap between the trasmission of the UV filter and the absorbance is reducing; hence the amount of Cherenkov light that is detected by the PMT becomed smaller.

3.7 Experimental results for $PbWO_4$:Pr

In this section, I'll describe the results obtained with the $PbWO_4$ crystals doped with praseodymium. In the first subsection, detailed results are given for the measurements performed on the crystal doped with 0.5% Pr with a specific set of filters. In following subsections, I present the effects observed with different filters and different Pr concentrations.
All measurements on these crystals were carried out with the blue filter mounted on the right hand side of the crystal (PMTR). This side of the crystal, intended for detecting the Cherenkov component of the signals, was equipped with a regular PMT. The other side, intended for the detection of scintillation, was equipped with a red-extended PMT (PMTL). The filter on this side was changed in order to optimize the sensitivity to the different components of the scintillation spectrum, indicated in Fig 3.11b. Two different sampling frequencies of the digital oscilloscope were used for these measurements: 0.4 ns/point, intended to study the Cherenkov component, and 4 ns/point, for the scintillation component of the light produced in these crystals.

3.7.1 The time structure of the signal

The time structure of the signals generated by 50 GeV electrons in the PMTs detecting the filtered light is shown in Figure 3.16.
The crystal was oriented at $\theta = 30°$, such as to maximize the signal from the production of Cherenkov light. The signals read from the blue side and from the yellow one are shown in Fig 3.16(a) and (b) respectively. Surprisingly, the yellow signal also has a dominant prompt component, which was instead expected only on the other side, due to Cherenkov radiation. In order to investigate the nature of this signal component, we studied its angular dependence, moving the rotating platform, with respect to the beam, of an angle θ from -35^o to 35^o, in steps of 5^o. The signal amplitude was sampled at a rate of 0.4 ns/point.
Figure 3.16 (bottom) shows the time structures of the blue (c) and yellow (d) signals, measured at angles $\theta = 30^o$ (the solid red histograms) and -30^o (the dashed, blue histograms), respectively. These results clearly indicate that the prompt component observed in the yellow signals is caused by Cherenkov radiation. Additional evidence for this conclusion was obtained by studying the different angular characteristics of the "prompt" and "delayed" components of the signals. These components were defined by integrating the signals over an interval of 7 ns around the peak (prompt) and from t = 70 − 112 ns (delayed), respectively. Apparently, the light transmitted by the yellow filter thus contains a very significant Cherenkov component. Part of the reason why this component is so prominently present in the time structure of the signal is the fact that the scintillation contribution to the signals is dominated by very slow components. This becomes evident when we compare the time structures

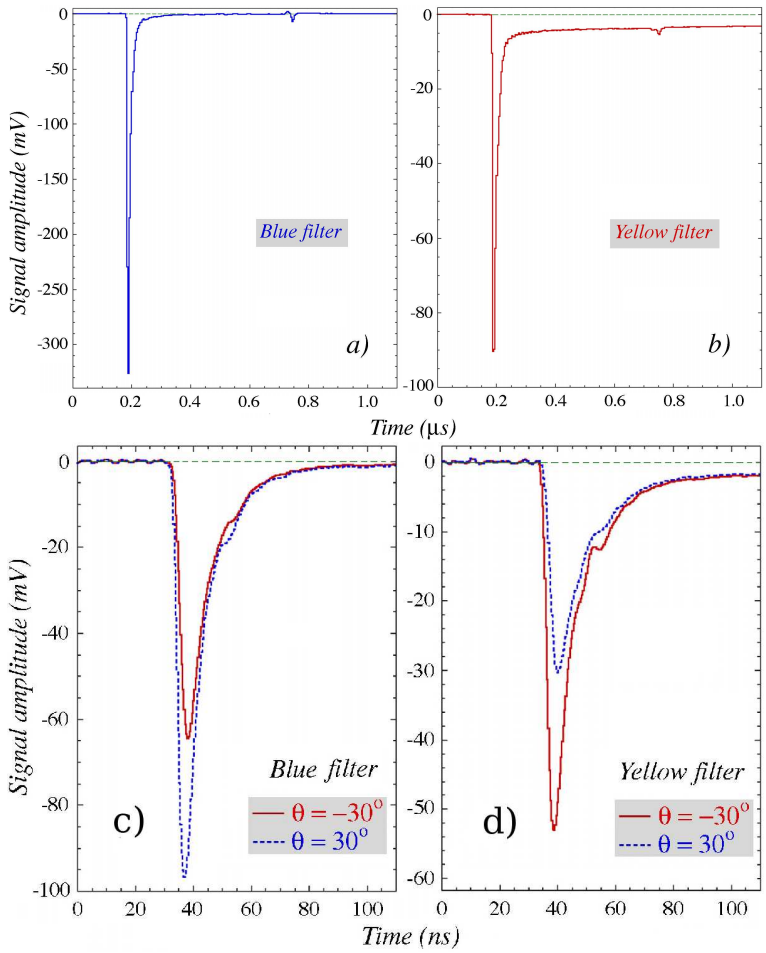

Figure 3.16: *Time structure of the signals in* 0.5% *Pr-doped* $PbWO_4$ *crystal, measured with light traversing the blue filter, in PMTR (a,c), and the yellow filter (b,d), in PMTL. The crystal was oriented at an angle* θ *of 30°, and the signal amplitude was sampled at a rate of 4 ns/point (top figure). (Bottom) The crystal was oriented at an angle* θ *of 30 or* $-30°$*, and the signal amplitude was sampled at a rate of 0.4 ns/point.*

measured with the 4 ns/point sampling frequency (fig 3.16)(top). Whereas the blue signal reaches the baseline shortly after the prompt peak, the yellow signal exhibits a long tail which has barely diminished when the sampling of the signal amplitude ends, 1100 ns after the trigger that started the time base of the oscilloscope.

3.7.2 Cherenkov/Scintillation ratio

The Cherenkov over scintillation ratio is shown in Figure 3.17, as the ratio of the prompt and delayed signal components of the time structure. The prompt component contained light detected during a time interval of 7 ns after the start of the signal, the delayed component was obtained by integrating from

t=70-112 ns. This ratio reaches a maximum at $\theta = 30°$ for the blue light, just as in the comparable setup for the Mo-doped crystals. The fact that the prompt/delayed ratio reaches a maximum at $\theta = -30°$for the yellow light confirms again the Cherenkov nature of the prompt component in this signal. We

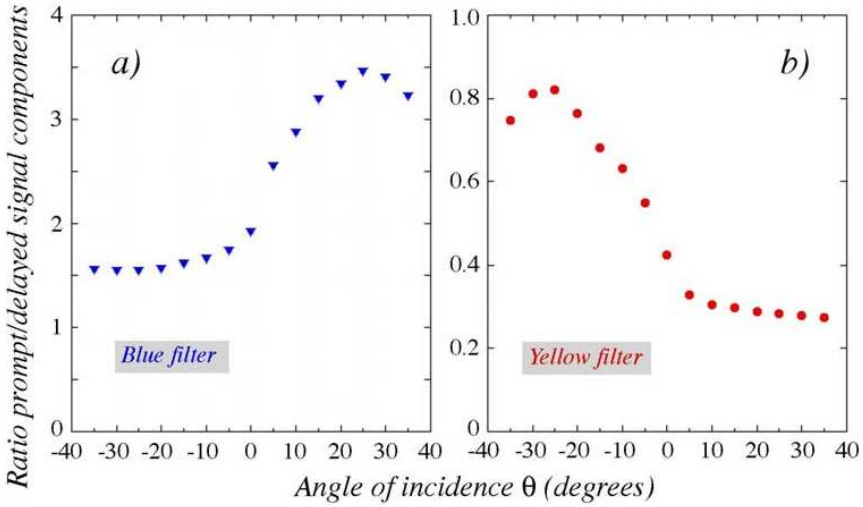

Figure 3.17: *Ratio of the prompt and delayed components of the signals from the light transmitted by the blue (a) or the yellow (b) filter, as a function of the angle of incidence of the beam particles.*

have tried three different filters on the scintillation side (yellow, orange and red). In Figure 3.18(a) the slow tail of the scintillation component for the three cases is shown. One clear effect of increasing the cut-off wavelength of the filter is a change in the decay constant of this component. The exponential curves, show that the decay time increases from ~ 2 μs to ~ 5 μs when the cut-off wavelength is increased from 495 nm to 610 nm. This trend is consistent with observations made in radioluminescence measurements [45]. In fact M. Nikl *et al.*reported lifetimes of $2 - 50$ μs for the various components of the Pr emission peak. In our setup, we are not able to measure the properties of these individual resonances separately, but we integrate over the wavelength band transmitted by the filter and convoluted with the quantum efficiency curve of the PMT.

At the same time, the relative contribution of Cherenkov light to the signals from this filtered light was observed to decrease. This is illustrated in Table 3.6, which shows that the ratio of the signals integrated over the prompt peak and over the long tail decreased by about a factor of two when the cut-off wavelength of the light was increased from 495 nm to 610 nm. Since the intensity of the Cherenkov radiation is proportional to λ^{-2} while most of the scintillation light is concentrated in the wavelength region from $610 - 650$ nm,

Filter	*Decay Constant* μs	*S/C ratio* $\theta = -30°$
OG495 "Yellow"	2.1 ± 0.1	1.38
OG570 "Orange"	2.9 ± 0.2	2.06
RG610 "Red"	5.1 ± 0.5	2.81

Table 3.6: *Effects of the light filters on the decay characteristics and the relative abundance of scintillation light in the filtered signals from the $PbWO_4$ crystal doped with* 0.5% *praseodymium. This abundance is defined as the ratio of the signals integrated from $t = 400 - 1100$ ns and $t = 184 - 204$ ns in Fig 3.16 (a) and its equivalent for the other filters, for the angle $\theta = -30°$, at which detection of the Cherenkov component in the filtered light is maximized.*

this observation is what we would espect.

3.7.3 Changing the doping concentration

Beside the 0.5% of doping, we also studied $PbWO_4$ crystals doped with 1% or 1.5% praseodymium. In principle, one might expect three types of changes as a result of changing the doping concentration:

- change in *light attenuation* as a result of increased self-absorption,
- change in the *intensity of the scintillation light*, and/or
- change in the *decay constants* of the scintillation process.

The first issue is discussed on the next section.
The total intensity of the scintillation light did increase with the concentration of praseodymium. Systematic studies which allowed us to quantify this statement were only carried out with the red filter. At the anti-Cherenkov angle, the total signal was observed to increase from a normalized value of 1.0 for the 0.5% crystal to 1.27 for the 1.0% crystal and 1.63 for the 1.5% crystal, as we can see from Figure 3.18(b).
We also observed that the decay of the scintillation process became faster as the Pr-concentration was increased. As illustrated in Figure 3.18(b), the tail of the time structure beyond the reflection of the prompt peak was well described by a single exponential.
The time constant was observed to decrease from 4.9 μs for the 0.5%-Pr crystal to 3.9 μs for 1.0%-Pr crystal and 3.1 μs for the 1.5%-Pr crystal[14]. It may be that the increased signal strength was primarily a consequence of the faster decay. While the integrated signal was found to increase by 63%, the decay

[14]We have to keep this in mind when interpreting the change in the intensity of the "red" signal mentioned above, since our measurements only concerned a period of about 1 μs after the start of the signal.

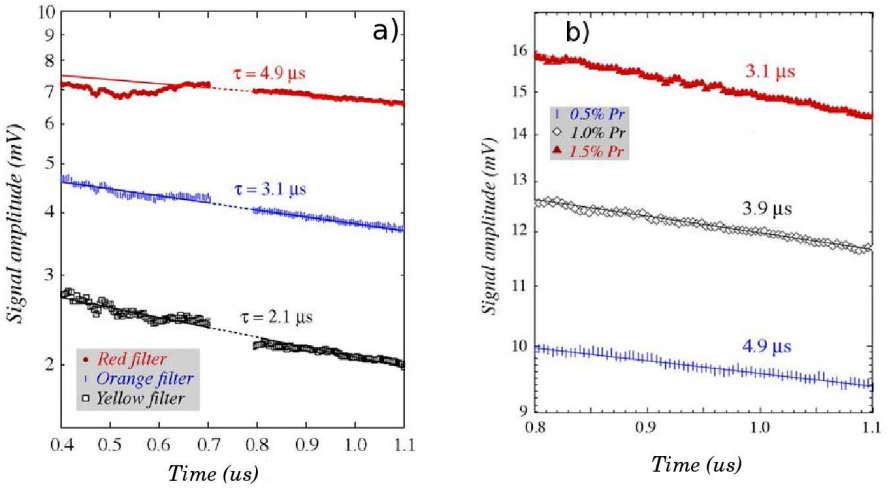

Figure 3.18: *Time structure of the tail of the signals observed in the $PbWO_4$ crystal doped with* 0.5% *praseodymium, measured with different filters (a). The tail of the signals measured with orange filter, but with different doping concentrations is plotted in (b). The region where the reflection of the Cherenkov pulse was detected has been deleted for sake of clarity.*

constant increased by 60% when the Pr-concentration was increased from 0.5% to 1.5%. Therefore, it seems that the main consequence of an increase in the Pr-concentration is a shortening of the time interval in which the scintillation light is released. This conclusion is commensurate with the findings of Nikl *et al.*[45].

3.8 Comparison of Mo- and Pr-doping for calorimeter purposes

3.8.1 Effects of light attenuation

The short-wavelength Cherenkov light was considerably attenuated on its way from the production centre to the light detector. This might give rise to systematic effects in dual-readout calorimetry.

We studied therefore the effects of light attenuation on the Cherenkov and scintillation components of the signal, both in Mo-doped and Pr-doped crystals, by moving the crystal along the x axis (see Figure 3.3) in steps of 1 cm[15]. In this way the response of the two PMTs was measured over the full length

[15]In the Case of Mo-doped crystal, it was equipped with yellow and UV filters, and it was tilted of an angle θ of 20°in order to generate Cherenkov signals with a reasonable amplitude. The Pr-doped crystal was equipped only with blue filter, and was perpendicular to the beam.

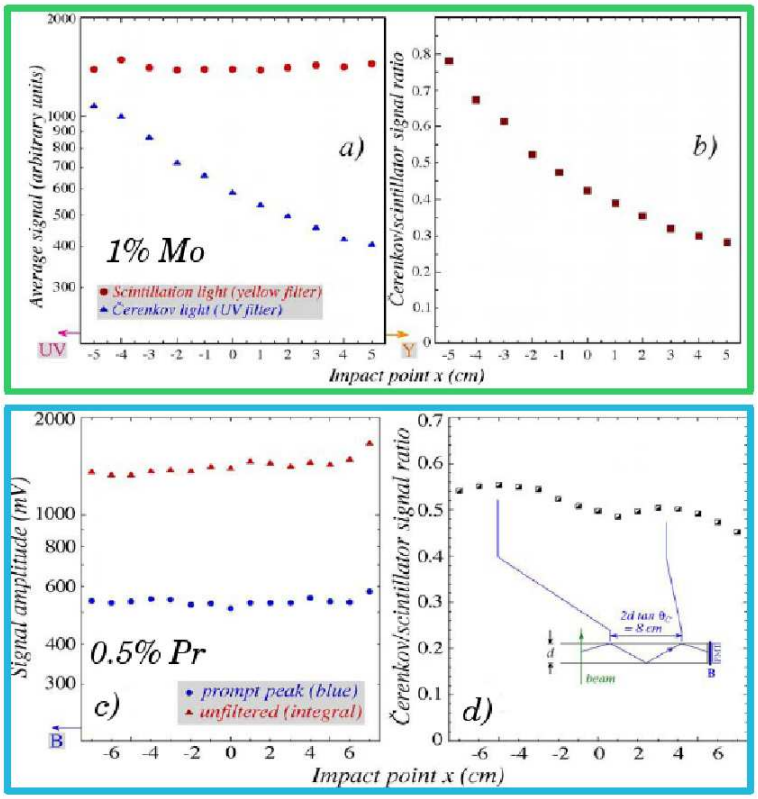

Figure 3.19: *Average signal from 50 GeV electrons in the $PbWO_4$ crystal doped with 1% Mo, (top figure), and 0.5 % Pr (bottom) as a function of the impact point of the particles. The signals generated by the light passing the UV and yellow filter for Mo-doping (a), the BLUE and no filter for Pr-doping (c) and and their ratio (b and d) are shown. The positions of these filters (UV, Y) are indicated.*

of the crystal.
The results are shown in Figure 3.19, where the average signals[16] observed in the PMTs on the two sides of the crystal are plotted as a function of the impact point of the 50 GeV beam electrons both for 1% Mo-doping (top figure) and 0.5% Pr-doping (bottom figure).
In the case of Mo-doping crystal, the light transmitted by the yellow filter, was almost independent of the impact point, while the signals on the UV-filter side decreased strongly as the distance to the point where the light was produced increased. Since these two PMTs measured almost pure scintillation and Cherenkov light, respectively, we conclude that the Cherenkov light was strongly attenuated in the crystal, (the attenuation length amounted to $\sim$ 10 cm) whereas the scintillation light was not. Figure 3.19b shows that, as a result of this difference, the Cherenkov/scintillation ratio varied by as much

[16]Calculated from the time structure, as described in previous sections.

as a factor of three over a distance of only 10 cm.
In the case of Pr-doping instead, the signals do not depend significantly on the distance the light had to travel to the PMT. In Figure 3.19c, the circles represent the prompt component of the light that passed the blue filter, the triangles the integrated, unfiltered light measured on the other side of the crystal. In Figure 3.19d, the ratio of both signals is plotted as a function of the impact point of the beam particles, for the 1% Pr-doped crystal. Interestingly, this result seems to exhibit an oscillating pattern. Similar patterns were observed in the position scan of a BGO crystal [42]. We attribute this effect to a position dependence of the PMT that read out the blue light. The Cherenkov light generated by the beam particles represents a narrow cone which propagates through the crystal and illuminates the PMT in a non-uniform way. Non-uniformities in the quantum efficiency of the photocathode (which are very common near the edge) and/or in the optical contact between cookies, filter and PMT will thus translate into a position-dependent response to the Cherenkov signal. Any pattern in the Cherenkov response should repeat itself over a distance of $2d\ tan\ \theta_C \sim 8$ cm, where d is the thickness of the crystal and θ_C the Cherenkov angle (63°), as illustrated in the insert of Figure 3.19d. Indeed, the response pattern exhibits this characteristic.

3.8.2 Cherenkov Light Yield

As we have seen on section 1.2, a limiting factor in the hadronic energy resolutions that can be obtained with dual-readout calorimeters is the Cherenkov light yield (8 photoelectrons per GeV on the DREAM fibre calorimeter). In order to determine the Cherenkov light yield for doped crystals, we have measured event to event fluctuations in the Cherenkov signal, as a function of the size of the scintillations signal. We have subdivided the horizontal scale of the ADC distribution of the PMTL into 30 equal bins of equal width, and obtained the distribution of the Cherenkov signals for each of these bins, using the integral over the time structure measured with the oscilloscope.
The relationship between the ADC counts and the deposited energy was established with a GEANT-4 Monte Carlo simulation of the development of 50 GeV electron showers in a 2.0 cm thick $PbWO_4$ crystal oriented at an angle $\theta = 30°$. This simulation showed that, on average, 0.578 GeV was deposited in this process.
The Figure 3.20 shows the distributions of Cherenkov signals measured in the two types of crystals, for 50 GeV electrons that deposited the same amount of energy, ~ 0.65 GeV, as measured by ADC that converted the (red) scintillation light detected by the PMT at the opposite side of the crystal. In the case of the Mo-doped crystal, the Cherenkov signal was obtained from the light traversing the UV filter, which contained almost no contamination of scintillation light. In the case of the Pr-doped crystal, the blue filter was used to obtain the Cherenkov signals. In order to eliminate contaminating contributions from scintillation light, we only used the signal contained in the prompt peak for

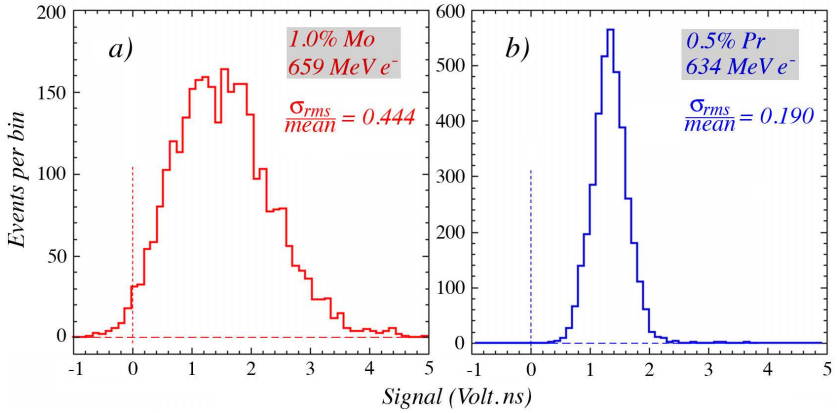

Figure 3.20: *Distributions of the C signals from 50 GeV electrons traversing the $PbWO_4$ crystals doped with 1% Mo (a) or 0.5% Pr (b), when the beam particles deposited ∼ 0.65 GeV in these crystals, as measured by ADCs that converted the red (scintillation) light generated in this process. The Cherenkov light was obtained with the UV filter in the case of the Mo-doped crystal, and with the blue filter in the Pr-doped one. The crystals were oriented at $\theta = 30^o$.*

this study.
The light yield follows directly from the relative width (σ_{rms}/mean) of these distributions. In the case of the Mo-doped crystal, this width is 0.444, which corresponds to 5.1 photoelectrons, or 7.7 photoelectrons per GeV. In the Pr-doped crystal, the relative width amounts to 0.190, which represents the statistical fluctuations in 28 photoelectrons, or 44 photoelectrons per GeV deposited energy.
The fractional width ($\sigma_{rms}/mean$) of the Cherenkov distribution is shown as a function of the total signal in Figure 3.21 for the 1% Mo-doped crystal. This signal (which was found to be approximately proportional to the deposited energy as derived from the yellow ADC signal) is plotted on a scale linear in its inverse square root, so that scaling with $E^{-1/2}$ implies the data points to be located on a straight line through the bottom right hand corner. The experimental data are indeed well described by such a straight line, any energy-independent deviations ("constant term") are statistically insignificant.

From the fit shown in Figure 3.21 we find that for an energy deposit of 1 GeV, the relative width (sigma/mean) is 37%:

$$\frac{\sigma_{rms}}{\langle C \rangle} = \frac{0.37}{\sqrt{E}} \tag{3.6}$$

with the energy E given in GeV. And we can conclude from this that the number of Cherenkov photoelectrons per GeV deposited energy was about 8 ($\pm$ 1).
In the case of Pr-doped, the equation 3.6 becames:

$$\frac{\sigma_{rms}}{\langle C \rangle} = \frac{0.15}{\sqrt{E}} \tag{3.7}$$

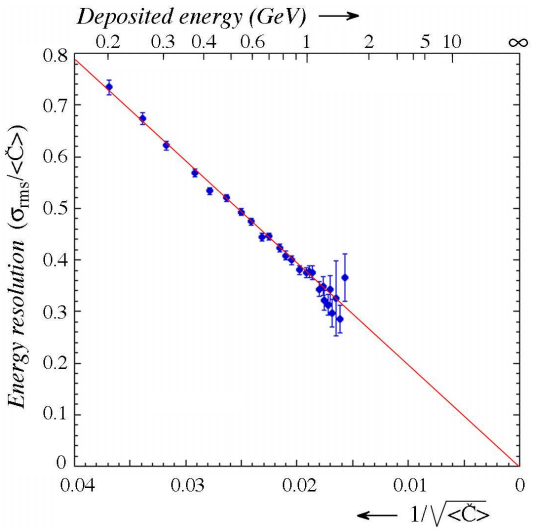

Figure 3.21: *Fractional width of the distribution of the C signals for Mo-doped crystal, as a function of the total scintillation (yellow) signal measured with the ADC. The corresponding energy loss is indicated on the top axis. The crystal was oriented at* $\theta = 30°$

giving a smaller statistical term.

This large difference can be ascribed to two factors:

- **The self-absorption** As explained previsiously, the light transmitted through the UV filter in the Mo-doped crystal was attenuated by a factor of 2.5 in the 10 cm separating the production origin of the light and the PMT. No such effect played a role in the case of the Pr-doped crystal.

- **The filters**. The UV filter, used for Mo-doped crystals, only transmitted light with $\lambda < 400$ nm, whereas the cutoff wavelength was 500 nm for the blue filter, used for Pr-doped. Since the quantum efficiency of the PMT quickly decreased for $\lambda < 350$ nm, the detection window of the blue filter was significantly larger than that of the UV filter.

Figure 3.22 shows the implications of these effects quantitatively; in the case of Mo-doped crystal is in fact suddendly clear the little gap, with respect to the one of the Pr-doped one, between the trasmission windows of the UV filter and the absorption cut-off of the crystal.

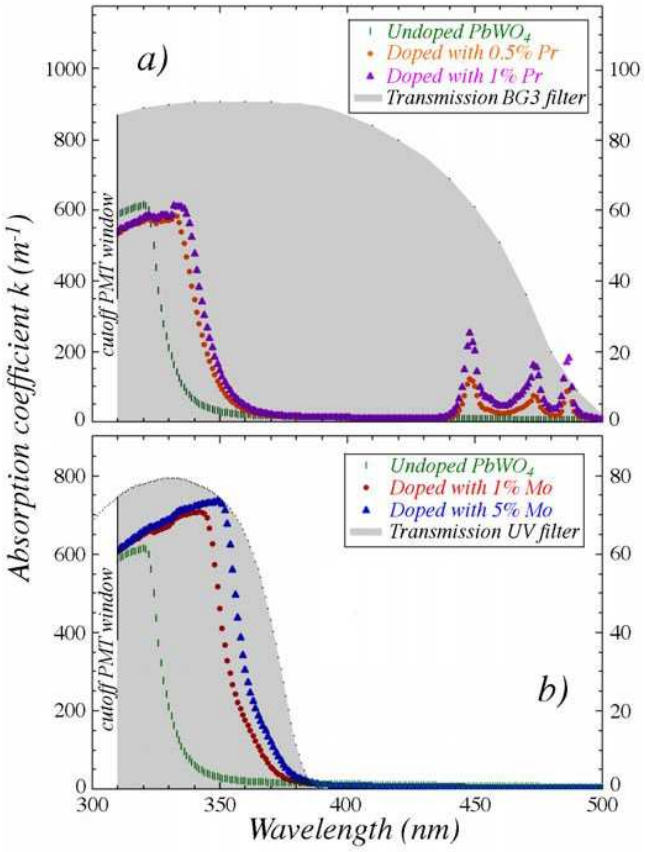

Figure 3.22: *The absorption coefficient as a function of wavelength, for Pr (a) and Mo-doping (b). The shaded areas represent the bandwidths of the light transmitted through the optical filters with which the measurements were performed.*

3.8.3 Conclusions from Pr and Mo doping tested during 2008

From the results seen in the previsious sections, we can draw some conclusions about the suitability of these doped crystals for the dual readout calorimetry. In evaluating the results, four aspects are important (summarized in table 3.7):

1. **Spectral separability of Cherenkov and Scintillation signal components**
   Both Mo- and Pr-doped crystals show a clear improvement with respect to the undoped $PbWO_4$ crystal. In fact, both dopings produce a shift of the scintillation wavelength, allowing the use of filters to separate the Cherenkov to the scintillation light. In undoped $PbWO_4$ crystals, instead, it is very hard to obtain a reasonable separation because the scintillation emission is higher in the blue region, where there is also the main production of Cherenkov light.

Dual Readout requests	*Mo* 1%	*Pr* 0.5%
Separability of C and S components	OK	OK
Time characteristics of S	OK	not OK
C Self-absorption	not OK	OK
C Light Yield	not OK	OK

Table 3.7: *Resume of the reliability of the tested crystals for Dual Readout Calorimetry*

2. **Time characteristics of Scintillation light**
   Here we see a big difference between the two kinds of dopings. In Mo-doped crystals,we can see components with decay time of 26 and 59 ns (Fig 3.12). This time scale is ideal for calorimetric applications, and makes it much easier to separate the Cherenkov prompt peak from the scintillation exponential decay signal than on undoped crystals (in which the S decay time is 10 ns, depending on the temperature [43]).
   On the other hand, the μs time scale of scintillation signals in the Pr-doped crystals is clarly too long for most of the high energy physics applications.

3. **Cherenkov light self absorption**
   Unfortunately, in this respect, the characteristics of the Mo-doped crystals tested in this study (read with UV filter) make them impractical for calorimetric applications. Typically, hadronic showers fluctuate on a distance scale of 1 nuclear interaction length, which corresponds to ~ 20 cm in these crystals. A light attenuation lengths of the order of 10 cm, as observed in Figure 3.19, are thus completely unacceptable in this respect.
   It is of course possible that the characteristics of the Mo-doped crystals could be improved for this application. The (effects of) attenuation of the Cherenkov light could be reduced by reducing the molybdenum concentration, which would shift the absorption cut-off to shorter wavelengths[17]. Extending through higher wavelengths the transmission region of the band pass filter used for Cherenkov light, could also be beneficial in that sense.
   On the other hand, self-absorption of Cherenkov light does not seem to be an important problem in the Pr-doped crystals, read out with a blue filter.

4. **Cherenkov light Yield**
   The Cherenkov signals derived from the crystals tested in this study correspond to an effective light yield of ~ 8 photoelectrons per GeV in the case of the (1%) Mo-doped crystal and ~ 44 photoelectrons per

[17]In fact we are now testing some Mo-doped crystals with lower doping concentrations.

GeV in the case of the (0.5%) Pr-doped one. The latter number would translate into a contribution of $0.15 \cdot E^{-1/2}$ to the hadronic resolution, which would be non-dominant in practical devices. The light yield of Mo-doped crystal is too low, and needs some improvement, for example by using an optimized filter, or a fotocathode with quantum efficiency highter for low wavelengths, or lowering the doping concentration. The light yield of 8 p.e. per GeV, in fact, is comparable to the one found for the original DREAM fibre calorimeter, that was a limiting factor for hadronic energy resolution, and one of the main reasons why we started looking into crystals as an alternative.

In summary, the tested crystals represent most definitely a considerable improvement with respect to undoped $PbWO_4$. However, in order to make them realistic candidates for application in practical calorimeters, further improvements would be needed.

3.9 2009 test beam and preliminary results

The results shown above are extremely encouraging. Nonetheless, an increase of the wavelength gap between crystal absorption edge and filters cutoff is needed in order to avoid light attenuation and increase the C light yield, still maintaining a good separation in both time structure and spectral properties. To do that, we have chose new possibilities for the 2009 testbeam:

- **Lower concentration of Mo-doping crystals**.
- **Higher PMT QE and different UV filters**.
- **Bismut Silicate (BSO) crystal**.

Data from the 2009 test beam have still to be fully analyzed offline, however in the following are reported some preliminary results. The testbeam setup was almost the same as the one described in Section 3.2.1.

Lower concentration of Mo-doping crystals It has been shown that a lower Molybdenum doping concentration allows to maintain the shift of the scintillation emission spectrum to higher λ with respect to undoped $PbWO_4$, but reduces the shift of the absorption cut-off to higher wavelength with respect to higher Mo concentrations[50, 53]. We have then tested Mo-doped $PbWO_4$ crystals with 0.1%, 0.2%, 0.3% of Mo-doping concentrations. For each doping concentration, we have asked to to produce these crystals to two different factories that use different techniques for crystal growth; the companies have an important role since the production technique can influence the quality of

the crystal (*e.g.,* presence of light absorbing "colour centres" which can absorb light with a characteristic wavelength). The two companies chosen are the Russian RI&NC which has produces for the DREAM collaboration also the 2008 test beam crystals, and the Chinese SIC. The RI&NC adopts the Czochralski method to make crystals (a seed crystal is rotated in the melt and progressively pulled up), the SIC uses the adopts the Bridgman method: the container with the melt is moved through a temperature gradient, and progressively cooled down to form the crystal starting from the tip (seed crystal). We searched in the existing data to find an indication for the dopants and the concentration levels. Studies for PWO_4 doping were carried on in the past to increase rad hardness and scintillation LY[50, 53]. After reviewing the various dopants with crystal experts, we concluded that Mo at small concentrations seems to be the best candidate for our application.
In Figure 3.23 the characteristics of different Mo-doping concentrations, both for radioluminescence (left) and for absorption(right)[53] are shown. From these plots is possible to see that lowering the concentration of Mo-doping at least down to a concentration of 0.1%, there is suppression of blue emission with decrease of absorption with respect to the 1% doping.

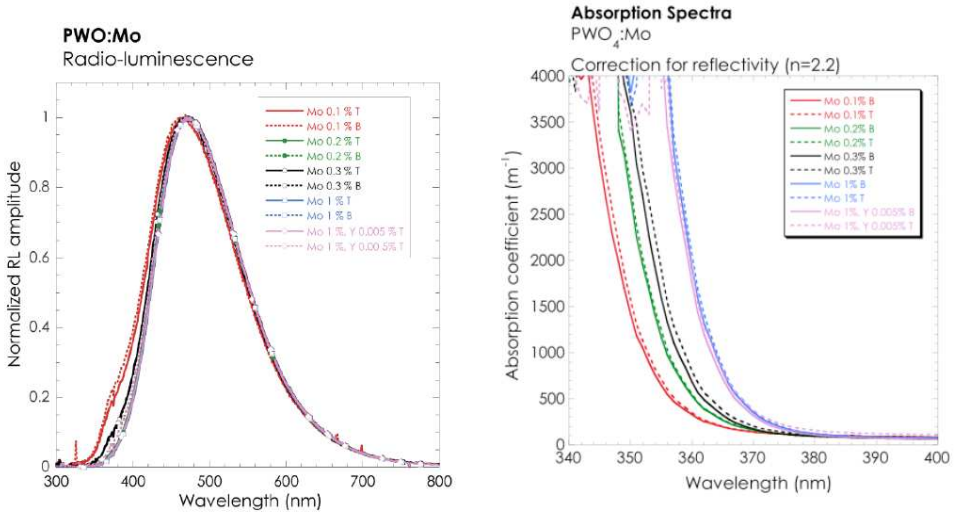

Figure 3.23: *Comparison between radioluminescenze (left) and absorption (right) spectra of $PbWO_4$ doped with different concentrations of Molybdenum.*

In Figure 3.24 the radiolumiunescence measurements of crystals from the two production companies are shown. It is possible to see that the Russian crystals are much more transparent.

Higher PMT QE and different UV filters. In order to reduce the problems of self-absorption and low Cherenkov light yield, we have replaced, on the Cherenkov side, the standard PMT (bialkali) with a PMT with higher quantum efficiency, called ultra-bialkali. In this way, the quantum efficiency goes

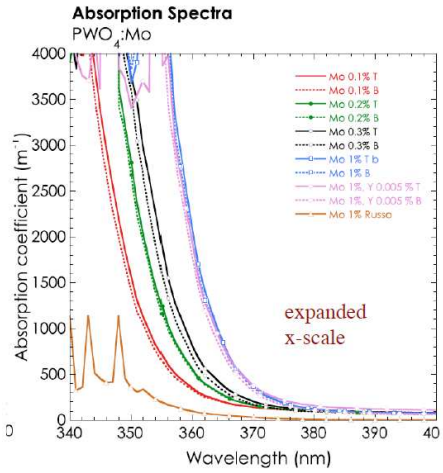

Figure 3.24: *Comparison between radioluminescenze spectra of crystals produced from the two companies.*

from 0.25 to 0.45 for wavelengths of 350 nm (Figure 3.26 left).
We also tested each crystal with three different UV filters on the Cherenkov side, that are characterized by a transmission region extended through higher wavelengths.
In Figure 3.26 right the curves of the effective transmission (PMT quantum efficiency multiplied by the filter transmission) for the three UV filters considered for the Cherenkov light are shown. Is also shown the curve of standard bialkali PMT and UG11 filter as used for the 2008 test beam.

The UV filters used are :

- UG11: This filter is the one used for the 2008 test beam. Its transmission window has a sharp cut-off at λ= 400 nm.
- U330: The transmission window of this filter has a cutoff at about 420 nm.
- UG5: The transmission window of this filter is broader than the one of the other two filters; it goes to about 440 nm, with a shoulder to about 500 nm.

On the scintillation side the Yellow filter was used for each crystal.

Bismut Silicate (BSO) crystal. Since we proved BGO to be a fairly good candidate for DREAM technique, we found that the BSO crystal (it has almost the same chemical composition as BGO, but with Silicon atoms instead of

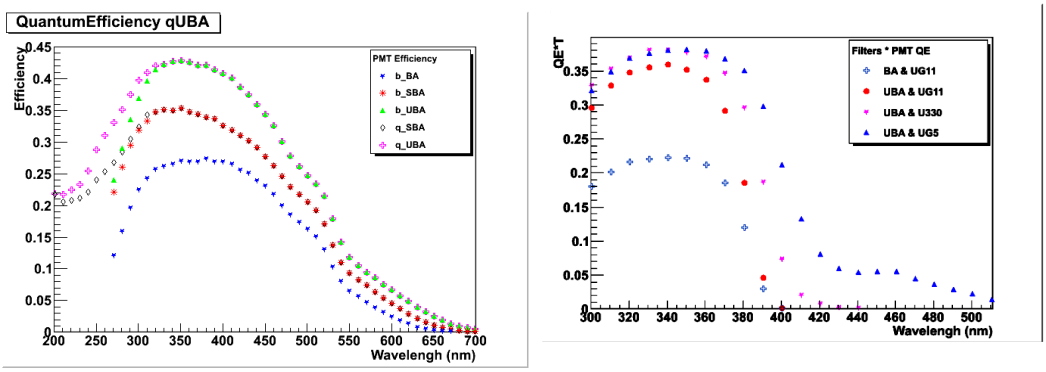

Figure 3.25: *Left: quantum efficiency curves for different PMTs; in particular the bialkali (BA) and ultrabialkali (UBA) are shown. Right: effective transmission for three UV filters (UG11, U330, UG5) and UBA PMT window (UBA). The standard bialkali PMT (BA) with the UG11 filter, used for 2008 test beam is also shown.*

Germanium ones: $Bi_4Ge_3O_{12}$) shows even more suitable characteristics for dual readout, in particular a lower-wavelength absorption cut-off.

In Table 3.8 there is a comparison between the characteristics of BSO and BGO crystals. The main differences are a smaller LY (20% of BGO), a shorter decay time of scintillating light (dominating 100 ns), and slightly better transparency to Cherenkov light (absorption cutoff below 300 nm). More details can be found here [54, 55, 56, 57]

Property	**BSO**	**BGO**
Density (g/cm^3)	6.80	7.13
Peak emission (nm)	480	480
Relative LY	20	100
d(LY)/dT (%K)	-2	-1.5
	2.4 (6%)	5.2 (2%)
Decay constants (ns)	26 (12%)	45 (9%)
	99 (82%)	279 (98%)

Table 3.8: *Comparison between characteristics of BSO and BGO crystals.*

3.9.1 Preliminary results

Table 3.9 shows the summary of the preliminary analysis results of the separation power (C/S), the percentage of absorbance per cm of Cherenkov light, and the Cherenkov light yield (as a number of photoelectrons per GeV) for all the combinations of crystals and filters measured during the test-beam[18]. The

[18]Results of the BSO crystals have been obtained with the online analysis.

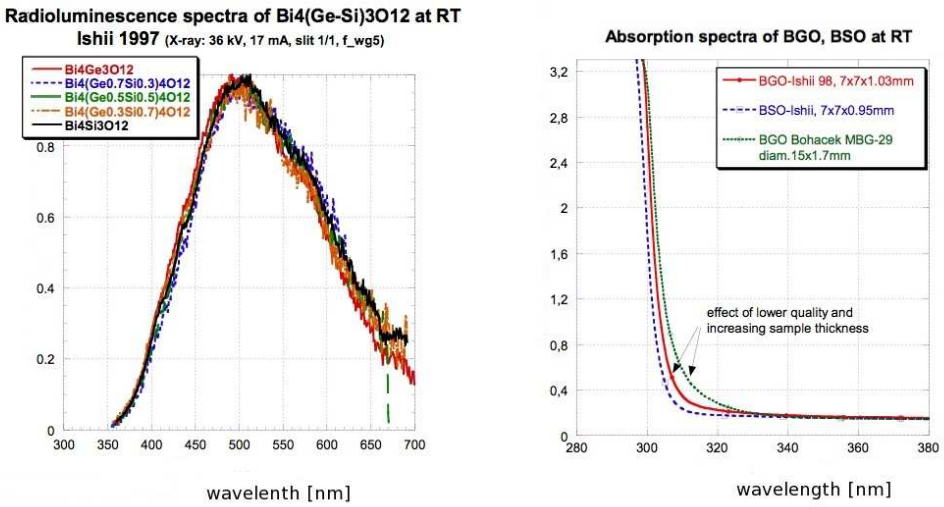

Figure 3.26: *Comparison between radioluminescenze (left) and absorption (right) spectra of BSO and BGO crystals.*

Cherenkov and scintillations signals are calculated as the integral of the time structure, event by event, after the subtraction of the baseline. The crystal results reported in the table are about the three $PbWO_4$ low Mo-doping concentrations (0.1%, 0.21% and 0.3%) produced by the Russian factory, as the ones of the 2008 test beam. We have also tested the 1% and 5% Mo-doping concentrations, but with the new U330 filter. In the table the results of the 0.1% Mo-doped crystal produced by the Chinese factory are also reported. In Figures 3.27 and 3.28 some plots are shown, from the absorbance as a function of x position for C and S lights, to the C/S ratio as a function of the rotating angle, and the energy resolution as a function of the scintillation light.

Crystal	Filter	C/S	Abs C (%/cm)	C l.y. p.e./GeV
Mo-0.1%	UG5	2.1	1.12	77.6
Mo-0.1%	U330	2.3	1.34	55.1
Mo-0.1%	UG11	4.7	5.55	8.2
Mo-0.1% SIC	UG11	2.2	9.3	1.9
Mo-0.2%	U330	1.7	1.51	57.3
Mo-0.3%	U330	1.5	1.0	64.2
Mo-0.3%	UG11	1.8	4.52	7.0
Mo-1%	U330	1.7	0.81	57.0
Mo-5%	U330	0.3	2.34	39.6
BSO	UG11	2.3	1.9	–

Table 3.9: *Separation power (C/S), percentage of absorbance per cm for Cherenkov light (Abs), and Cherenkov light yield as a number of photoelectrons per GeV (C l.y.) for all the combinations of crystals and filters tested.*

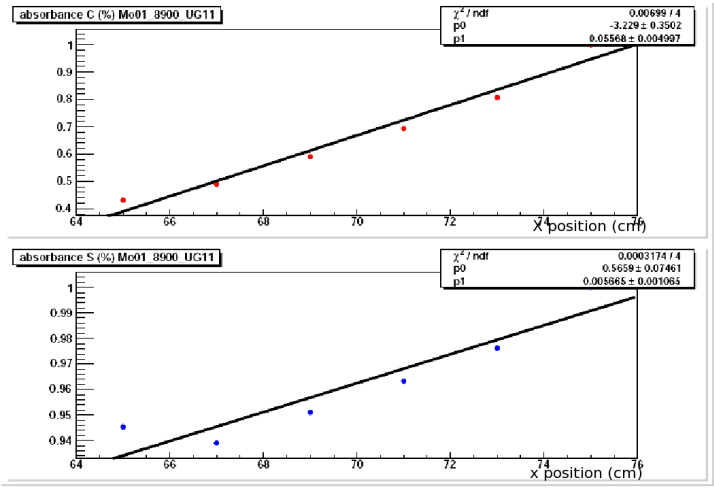

Figure 3.27: *Cherenkov (top) and scintillation (medium) integral of the signal as a function of the position, normalized to one of the crystal end for 0.1% Mo-doped $PbWO_4$ crystal with UG11 filter. From the parameters of the fit (the slope) is possible to see the absorbance per cm that is reported in Table 3.9.*

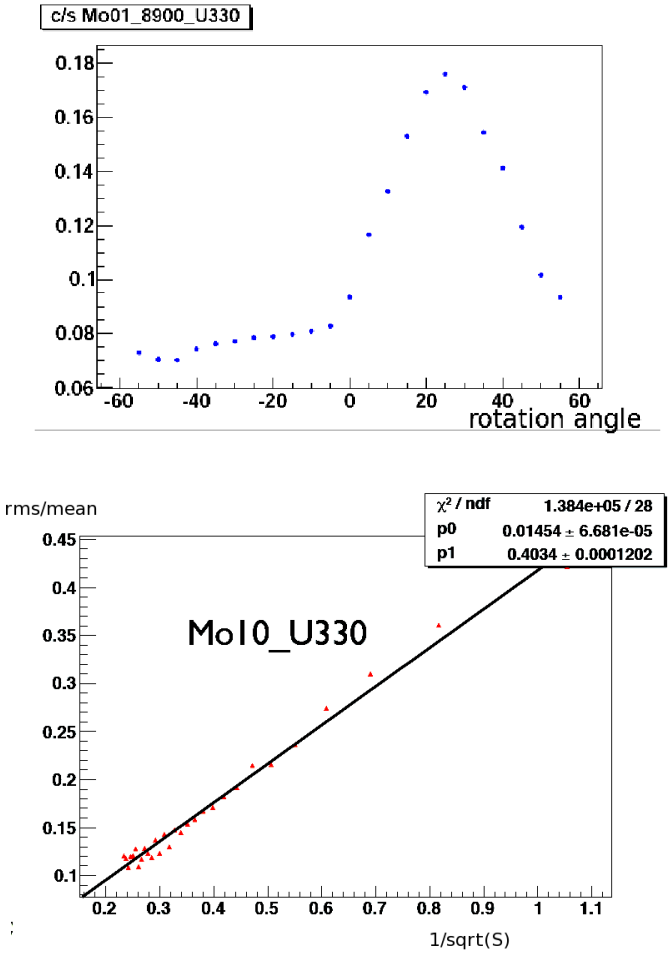

Figure 3.28: *Left: C/S ratios a function of the rotation angle θ for 0.1% Mo-doped $PbWO_4$ Russian crystal with filter U330 on the Cherenkov side. Right: example of fractional width of the distribution of C signals as a function of the total scintillation signal for the mo-doped 1% crystal read with the U330 filter.*

Chapter 4

The ATLAS physics programme

The high luminosity (10^{34} cm^{2}s^{-1}) that will be provided by LHC will lead to large production rates for many relevant processes; LHC can therefore be considered as a factory of many different particles, like W and Z bosons, t and b quarks and possibly also Higgs boson(s) and supersymmetric particles. Even if the search for the Higgs boson has been the first benchmark for the detector optimization, the design of the ATLAS experiment is adapted to cover a large spectrum of possible physics signatures, accessible at high luminosity and centre of mass energy of LHC. More details about the ATLAS performances and analysis strategies for each physics channel can be found here [69].
It is possible to divide in four main topics the physics studies that are in the programme of the ATLAS experiment:

- Higgs boson search;
- physics of top and bottom quarks;
- new physics beyond the Standard Model;
- precision measurements of the Standard Model.

4.1 Search for the Higgs boson

Despite the success of the Standard Model (its predictions have been verified at the level of 0.1% by LEP, SLC and Tevatron experiments), some aspects of the theory are still to be understood. In particular the origin of the particle masses and the motivation for the mass hierarchy of leptons, quarks and gauge bosons are not known. The Standard Model (SM) is a quantum field theory which describe the interaction of spin 1/2 point-like fermions with interactions that are mediated by spin-1 gauge bosons. The bosons are a consequence of local gauge invariance applied to the fermion fields and are a manifestation of the symmetry group of the theory, *i.e.,* SU(3) $\times$ SU(2) $\times$ U(1).

The SU(2) × U(1) symmetry group, which describes the electroweak interaction, is spontaneously broken by the existence of a postulated Higgs field with non-zero vacuum expectation value. When the electroweak symmetry breaking occurs, one physical degree of freedom remains in the Higgs sector and should manifest itself as a neutral scalar boson H. The Higgs field leads to massive vector bosons, W and Z, which mediate the weak interaction, while photons remain massless. This Higgs mechanism generates fermion mass terms by self-interaction; the strenght of this interaction (G_f) is proportional to the fermion masses m_f:

$$G_f \propto \frac{\sqrt{2}m_f}{v} \qquad m_H = \sqrt{2\lambda}v \tag{4.1}$$

where v is provided by the theory and is called "vacuum expectation value" ($v = 246$ GeV) and λ is a free parameter of the theory. The mass of the Higgs boson is not predicted by the model, but should not exceed about 1 TeV, in order to preserve unitarity of the theory at high energy.

Indirect experimental bounds for the Higgs mass are obtained from fits to precision measurements of electroweak observables and to the measured top and $W^{\pm}$ masses. In fact, the Higgs boson mass is included in the radiative corrections of the electroweak interactions with logarithmic terms. Figure 4.1 bottom resumes the results of the fit of the electroweak observables, using as unique free parameter the Higgs boson mass. It shows the $\Delta\chi^2 = \chi^2 - \chi^2_{min}$ curve derived from high-Q^2 precision electroweak measurements, performed by the LEP experiments and by SLD, CDF, and D0 experiments, as a function of the Higgs-boson mass, assuming the Standard Model to be the correct theory of nature. The preferred value for its mass, corresponding to the minimum of the curve, is[1]:

$$m_H = 84^{+34}_{-26} GeV \text{ at } 68\%\ CL.$$

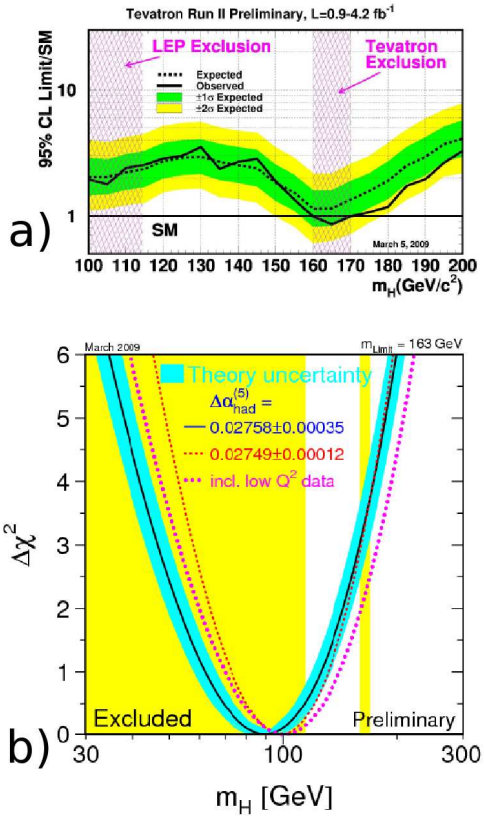

Figure 4.1: *Tevatron results as in March 2009: (a) exclusion plot; (b) $\Delta\chi^2$ as a function of m_H for the fit of electroweak observables.*

The experimental uncertainty derived from $\Delta\chi^2 = 1$ for the black line, thus

[1] $m_H < 163$ GeV at 95% CL and $m_H < 191$ GeV including LEP results.

not taking into account the theoretical uncertainty shown as the blue band. Experimentally the lower limit of the Higgs boson mass is derived from the LEP-2 experiments[3] and is m_H>114.4 GeV[2]; and recently Tevatron has excluded at 95% CL the value of 160 GeV < m_H < 170 GeV (Figure 4.1 top). At LHC the main Higgs production mechanism of the Higgs boson are illustrated in Figure 4.2; the dominated one is the gluon fusion, followed by vector boson fusion WW(ZZ) which is enhanced for very high Higgs mass ($m_H \sim 1$ TeV).

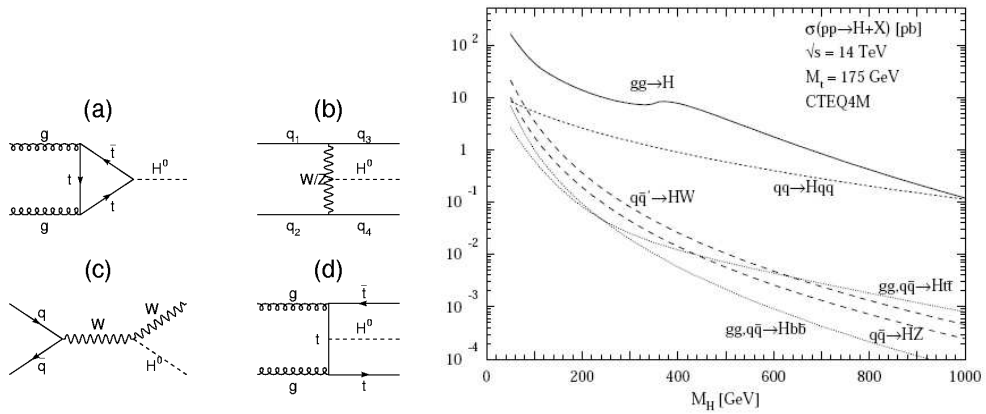

Figure 4.2: *Left: main Higgs production mechanisms (a) gg → H gluon fusion, (b) qq → W^+W^-(ZZ) → qqH vector boson fusion, (c) qq̄→ Z(W)H Higgs-strahlung from W boson, (d) gg → tt̄H, tt̄ associate production. Right: BR of the Higgs production as a function of m_H.*

From equation 4.1, it is clear that H predominantly couples to the heaviest particles of the SM, *i.e.,* W and Z gauge bosons, *t* and *b* quarks. The decay into these particles will be dominant, if they are kinematically allowed. The branching ratios of the Higgs as a function of its mass is shown in Figure 4.3. For m_H < 120 GeV the $b\bar{b}$ decay mode dominates, since b-quarks are the most massive fermions kinematically accessible in this region. For $m_H \sim 2m_Z$ also the vector gauge bosons become kinematically accessible and consequently the H → WW$^{(*)}$ and H → ZZ$^{(*)}$ decays dominate the high m_H region.

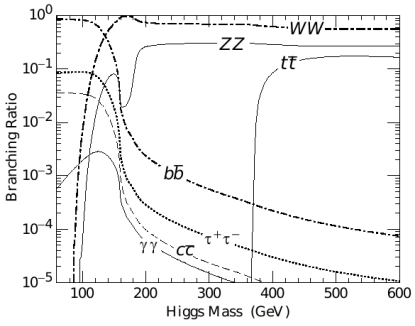

Figure 4.3: *The branching ratio of the Higgs boson as a function of the Higgs mass.*

[2]At the end of 2000, the ALEPH collaboration at LEP claimed an excess of events beyond the background expectations consistent with the production of an Higgs boson with m_H=$115^{+1.3}_{-0.9}$ GeV ([3], [4]); but the observed statistical significance of the effect was 3σ.

The SM Higgs boson will be searched for in various decay channels, whose choice is given by the signal rates and the signal to background ratios in the various mass regions.

Low mass regime $m_H <$ 130GeV. In this region the search is based on the challenging channels $H \to \gamma\gamma$ and $H \to b\bar{b}$.
The $H \to \gamma\gamma$ channel has a branching ratio at the level of 10^{-3} and therefore a small cross section[3] ($\sim$ 20 fb). The signal signature is simple, but the background is very hard to fight. The $\gamma\gamma$ production, for the continuum irreducible background, has a cross section 60 times larger than the signal one. The reducible background is due to γj and jj production, where one or both jets fake a photon. The jet rejection factor (of 10^3-10^4 depending from used cuts) is achieved by the electromagnetic calorimeter and its excellent energy and angular resolution.
The $H \to b\bar{b}$ has a branching ratio close to 100% in most of this mass region (Figure 4.3), and therefore inclusive Higgs production followed by $b\bar{b}$ pairs decay has a relatively large cross section ($\sim$ 20 pb). However, since the signal to background ratio for the inclusive production is smaller than 10^{-5}, it will be impossible to observe this channel above the QCD background and even to select it at the trigger level. The associated production $t\bar{t}H$, WH, ZH, with $H \to b\bar{b}$ and with an additional lepton coming from the decay of the accompanying particles, have much smaller cross sections ($\sim$ pb) but give rise to signatures which can be much more easily extracted from the background. The discovery of this decay mode depends considerably on the impact parameter measurement performance and on the b-tagging capabilities of the inner detector.

Intermediate mass region: 130 GeV $< m_H <$ 2 m_Z. The most promising channels for the experimental search are H $\to$ ZZ$^{(*)}$ $\to 4l$ and H $\to$ WW$^{(*)}$ $\to l\nu l\nu$. They both give rise to very distinctive signatures, consisting of leptons in the final states (electron or muons, since taus do not allow a clean reconstruction of the Higgs mass peak and are also contaminated by large QCD background).

High mass region: $m_H >$ 2m_Z. This is the best region where to discover a Higgs boson signal at the LHC, since the H $\to$ ZZ $\to 4l$ gives rise to a gold-plated signature, almost background free. A very massive Higgs boson ($m_H >$ 600 GeV) can be instead discovered in the channels H $\to$ ZZ $\to ll\nu\nu$ and H $\to$ WW $\to l\nu jj$ which offer branching ratios respectively 6 times and 150 times larger than that of the gold-plated Higgs decay in four leptons.

A SM Higgs boson can be discovered by the ATLAS experiment over the

[3]The H$\gamma\gamma$ coupling is forbidden at the tree level so that this decay can only occur at higher order through a W loop.

full mass range from the LEP2 lower limit up to the TeV scale with a high significance. A 5σ-discovery can already be achieved over the full mass range after a few years of running at low luminosity. Over a large fraction of the mass range, the discovery of a Standard Model Higgs boson will be possible in two or more independent channels. Also important SM Higgs parameters like the mass and the width as well as production rates can be measured with a reasonable precision.
In the MSSM, the Minimal Supersymmetric Extension of the Standard Model with R-parity conservation (see Section 4.3.1), two isospin Higgs doublets have to be introduced in order to preserve supersymmetry. After the electroweak symmetry breaking mechanism, three of the eight degrees of freedom become the longitudianl modes of the Z and W massive bosons. The remaining five Higgs mass eigenstates manifest themselves as the five Higgs scalar particles of MSSM: two CP-even neutral (scalar) particles h, H, one CP-odd neutral (pseudoscalar) particle A, and two charged particles $H^{\pm}$. In addition for the channel discussed for the Standard Model case, the MSSM Higgs search relies heavily on the H/A/$h \rightarrow \tau\tau \rightarrow l^{+}l^{-}4\nu$, H/A/$h \rightarrow \mu^{+}\mu^{-}$ channels, and $H \rightarrow hh \rightarrow bb\gamma\gamma$.

4.2 Standard Model physics and precision measurements

LHC will be not only a machine dedicated to the discovery of new physics, but it will carry out precision measurements in many different sectors: *e.g.,* vector gauge bosons, heavy quarks physics, triple-gauge couplings. As a consequence of high statistics, significant improvements on the Tevatron and LEP results are expected even after only few years of operation. Indeed the statistical error, which scale as $1/\sqrt{N}$ (where N is the number of selected events), will be negligible in most measurements. The uncertainty will instead be dominated by systematic errors. Moreover large statistics will allow hard cuts to be applied in order to select clean and well understood events. Further more high statistics samples will be available to study the detector response in great details. The main sources of uncertainty which will affect precision measurements will be the lepton and momentum scale, related to calibration and intercalibration of the different sub-detectors, the jet energy scale and the knowledge of the absolute luminosity, which will contribute to the uncertainty on all cross section measurements.

4.2.1 Minimum bias physics

The study of low-p_T events, produced by soft interactions (minimum bias events) can be interesting expecially at the beginning of the LHC data taking. The total pp cross-section can be divided into elastic (σ_{elast}) and inelastic

components, and the inelastic component can be further divided into: non-diffractive (σ_{nd}), single diffractive (σ_{sd}) and double diffractive (σ_{dd}) components. The total cross-section (σ_{tot}) can then be written as:

$$\sigma_{tot} = \sigma_{elast} + \sigma_{nd} + \sigma_{sd} + \sigma_{dd}$$

Historically, the minimum bias triggering used in hadron collider experiments often used triggers based on forward-backward coincidences that favoured the detection of non-single diffractive inelastic events (NSD), *i.e.*,

$$\sigma_{nsd} = \sigma_{tot} - \sigma_{elast} - \sigma_{sd}$$

Thus, NSD events have often been classified as "minimum bias events".
The aim of the minimum bias physics it to measure the central pseudorapidity and transverse momentum distributions of charged particles produced in inelastic proton-proton collisions during early running at the LHC at low luminosity. The minimum bias events allow the soft-part of the underlying event in high-p_T collisions to be characterised. Studies of inclusive particle distributions in minimum bias events in pp collisions are important to provide the baseline for measurements in heavy-ion collisions, such as allowing differences in the number of particles to be attributed to QCD effects rather than the simple scaling of the number of nucleons. Finally these interactions will be a major background during low luminosity running (10^{33} cm^{-2}s^{-1}) and high luminosity running (10^{34} cm^{-2}s^{-1}), where the average number of such interactions per beam crossing is ~ 2.3 and ~ 23, respectively.

Minimum bias interactions have previously been studied at a range of different energies at the CERN's ISR and S$p\bar{p}$S, at the Tevatron and RHIC colliders. Based on these results, Monte Carlo models have been tuned to generate predictions for LHC multiplicities [66]. Figure 4.4 shows a comparison of model predictions for the central charged particle density in NSD inelastic $p\bar{p}$ events for a wide range of centre-of-mass energies. The data points shown are from UA5 and CDF $p\bar{p}$ data, and are corrected for detector and trigger effects and efficiencies back to the particle level. It is clear from this figure that there is a large uncertainty in the predicted central particle density of non-single diffractive interactions at the LHC energy, even though the models have been tuned to agree with data at lower energies. This uncertainty arises because the

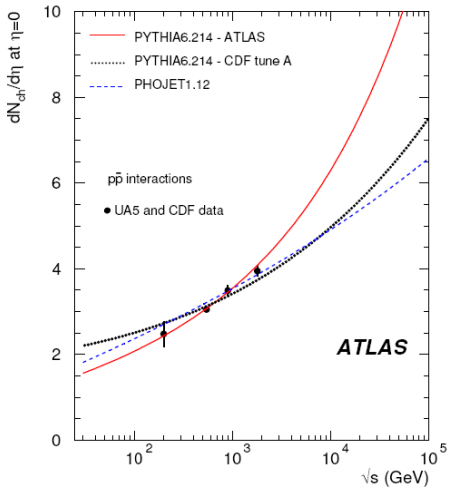

Figure 4.4: *Central charged particle density for NSD events as a function* $\sqrt{s}$.

energy dependence in a variety of different models for low-p_T non perturbative hadronic processes is not well understood. Measuring the central particle density at the LHC will thus be crucial to determining the energy dependence of the central particle density and to constrain models of inelastic events.

4.2.2 Electroweak bosons studies

The study of the production of W and Z events at the LHC is fundamental in several respects. First, the calculation of higher order corrections to these simple, colour singlet final states is very advanced, with a residual theoretical uncertainty at a level of few percent [58]. Such precision makes W and Z production a stringent test of QCD, and any difference between the measurements and predictions can be a hint to find new physics. For example, the total width of the W boson can also get contributions from processes beyond the SM. For example, in supersymmetry, the decay $W^+ \rightarrow \chi^+\chi^0$ may be possible if the charginos and neutralinos are light, and so a precise measurement of $\Gamma(W)$ can constrain the properties of these particles. Secondly, more specifically for Z production, the clean and fully reconstructed leptonic final states will allow a precise measurement of the transverse momentum and rapidity distributions, respectively $d\sigma/dp_T$ and $d\sigma/dy$. The transverse momentum distribution will provide more constraints on QCD, most significantly on non-perturbative aspects related to the resummation of initial parton emissions, while the rapidity distribution is a direct probe of the parton density functions (PDFs) of the proton. The high expected counting rates will bring significant improvement on these aspects, and this improvement translates to virtually all physics at the LHC, where strong interaction and PDF uncertainties are a common factor.
From the experimental point of view, the precisely measured properties of the W/Z boson provide strong constraints on the detector performance. Their mass, width and leptonic decays can be exploited to measure the detector energy and momentum scale, its resolution, and lepton identification efficiency very precisely.
A detailed description of the W cross section measurement technique is explained in Chapter 5.
A number of fundamental electroweak parameters can be accessed through W and Z final states (m_W, through the W boson decay distributions; $\sin^2\theta_W$, via the Z forward-backward asymmetry; lepton universality, by comparing electron and muon cross-sections). These measurements are long term applications where the understanding of the hadronic environment at the LHC is crucial, and to which the above-mentioned measurements are necessary inputs.
The measurement of the W mass is very important because, being

$$m_W = \sqrt{\left(\frac{\pi\alpha}{G_F\sqrt{2}}\right) \cdot \frac{1}{sin\theta_W\sqrt{1-\Delta R}}} \tag{4.2}$$

where α is the fine structure constant, G_F the Fermi constant, θ_W the Weinberg angle, and ΔR the radiative correction that receives contributions from the square of the top mass and the logarithm of the Higgs mass, precise measurements of the W mass, together with m_t, will provide stringent test of the consistency on the mass of the Higgs boson. The mass of the W boson is currently measured to be $m_W = 80.420 \pm 0.031$ GeV from recent (August 2009) results [59]. With the early ATLAS data ($\int L\ dt \sim$ 10-20 pb^{-1}), it is foreseen to have a statistical precision of about 100 MeVon W mass measurement. In this context, the main sources of systematic uncertainty are of experimental origin (energy and momentum scales, resolution, efficiency). The principal method adopted for measuring the W mass at the LHC employs the leptonic decay channels. Selection is performed searching for a single isolated charged lepton inside the region devoted for precision physics ($|\eta| < 2.5$), significant missing transverse energy and minimal hadronic activity. While the Z decay can be fully reconstructed, and its mass calculated from the invariant mass of the decay leptons, this is not the case for W decays, where the neutrino goes undetected. From the momentum imbalance one can infer the missing energy, but with limited precision and only in the transverse direction. This means that the invariant mass can not be determined, and one is forced to consider other variables sensitive to the W mass. The W mass is then obtained from the distribution of the transverse mass, m_T^W, that is the invariant mass of the decay products evaluated in the plane transverse to the beam and is given by:

$$m_T^W = \sqrt{2 p_T^l p_T^\nu (1 - cos\Delta\phi)} \tag{4.3}$$

where $\Delta\phi$ is the azimuthal angle between the charged lepton and the system X which recoils against the W. The transverse momentum of the missing neutrino has to be reconstructed from that of the lepton and the recoil. The transverse mass distribution, and in particular the falling edge of the Jacobian peak, is sensitive to the value of the W mass, though this sensitivity is reduced by the smearing effect due to the detector resolution (Fig 5.3). Mass measurement is done by fitting the experimental distribution to Monte Carlo spectra obtained for different values of m_W, and then deducing the mass value which is preferred by the data. At the LHC the accuracy on the measurement of m_W is expected to be 15 MeV.

The forward-backward asymmetry, A_{FB}, measurement is one of the important precision measurements that can be done at the LHC. The Z boson events in pp collisions originate from the annihilation of valence quarks with sea antiquarks or from the annihilation of sea quarks with sea antiquarks. Since the valence quarks carry on average a larger momentum fraction than the sea quarks, the boost direction of the dilepton system can indicate the quark direction. However, dilepton events which originate from the annihilation of sea quarks with sea antiquarks do not contribute to the observed asymmetry. A_{FB} measurements with quarks and leptons at the Z peak provide a precise determination of the weak mixing angle $sin^2\theta_{eff}^{lept}$. The weak mixing angle is an important

parameter in the electroweak theory that describes the mixing between weak and electromagnetic interactions. In the global fit of the Standard Model, the weak mixing angle constrains indirectly the Higgs mass. In order to improve the measurement precision, it will be necessary to detect leptons in the very forward pseudorapidity region, which favors electrons over muons at ATLAS, due to the major coverage in η of the calorimeters.
The analysis of diboson production at the LHC (W^+W^-, $W^\pm Z$, ZZ, $W^\pm Z$, Zg) using lepton and photon final states provides an important test of the high energy behavior of electroweak interactions. Any theory predicting physics beyond the Standard Model, while maintaining the Standard Model as a low-energy limit, may introduce deviations in the gauge couplings at some high energy scale. Precise measurements of the couplings will not only provide stringent tests of the Standard Model, but will also probe for new physics in the bosonic sector. These tests will provide complementary information to other direct searches for new physics at the LHC. The signature for such anomalous couplings is enhanced diboson production cross-sections, particularly at high transverse momentum of the bosons. Experimental limits on non-Standard Model anomalous triple gauge boson couplings can be obtained by comparing the shape of the measured p_T or mass distributions (or transverse mass, for final states involving W) with predictions, provided that the signal is not overwhelmed by background.

4.2.3 Bottom physics

Even if at LHC a dedicated experiment for B-physics studies (LHCb) has been built, also the general purpose experiments ATLAS and CMS will cover this topic, expecially during the low luminosity phase of the collider, when b quark identification is not hindered by pile-up in the detectors.

From Figure 4.5 one can see that the ATLAS and LHCb detectors cover different regions the phase space, both in pseudorapidity and transverse momentum of B-hadrons detected, and hence they can do complementary studies.
The ATLAS B-physics programme covers many aspects of beauty flavour physics. First, by measuring production cross-sections of beauty and charm hadrons and of the heavy-flavour quarkonia, J/ψ and Υ, ATLAS will provide sensitive tests of QCD predictions of production in proton-proton collisions at the LHC. Secondly, ATLAS will study the properties of the entire family of B mesons (B_d^0, B^+, B_s^0, B_c and their charge-conjugate states) and B baryons, thereby broadening our knowledge of both the spectroscopic and dynamical aspects of B-physics. However, the main

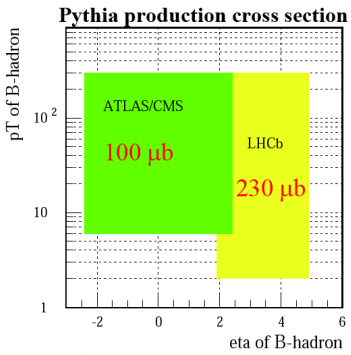

Figure 4.5: *Acceptances in η and p_T of the ATLAS and LHCb detectors.*

emphasis will be on precise measurements of weak B hadron decays. In the Standard Model, all flavour phenomena of weak hadronic decays are described in terms of quark masses and the four independent parameters in the Cabibbo-Kobayashi-Maskawa (CKM) matrix. Enormous quantities of data collected in the past decade by the experiments BaBar, Belle, CDF and D0 allowed very precise measurements of flavour and CP-violating phenomena. Whilst the analysis of the remaining data of these experiments may still push the boundaries, no evidence of physics beyond the Standard Model, nor any evidence for CP violation other than that originating from the CKM mechanism, has yet been found. At the LHC, thanks to the large beauty production cross-section and the high luminosity of the machine, the sensitivity of B decay measurements is expected to substantially improve. Whilst direct detection of new particles in ATLAS will be the main avenue to establish the presence of new physics, indirect constraints from B decays will provide complementary information. In particular, precise measurements and computations in B-physics are expected to play a key role in constraining the unknown parameters of any new physics model emerging from direct searches at the LHC.
At the beginning of the data taking, after an integrated luminosity of order of 10-100 pb^{-1}, B-physics and heavy flavour quarkonia signatures will serve in helping to understand detector properties and the muon trigger, as well as measuring production cross-sections. The physics analyses in that phase will deal with prompt J/ψ and Υ events, along with inclusive B hadron decays to muon pairs via J/ψ. Further on, the exclusive decays of $B^+ \to J/\psi K^+$, $B_d^0 \to J/\psi K^{0*}$ and $B_s^0 \to J/\psi\phi$ will be studied.
During the next period, from about 200 pb^{-1} to 1 fb^{-1} of integrated luminosity, ATLAS is expected to collect the same or higher statistics as are currently available at the Tevatron. During this period it will be possible to improve current measurements of B hadron properties and set new decay rate limits or possibly give evidence for rates above Standard Model predictions for rare decays (*e.g.,* in the channel $B_s^0 \to \mu^+\mu^-$).
In the most important period for B-physics ATLAS is expected to achieve about 10 - 30 fb^{-1} and many studies about a large variety of B-physics topics, covering both the production and decay properties of B hadrons are planned. It will be studied, for example, the oscillation of the $B_s^0 - \bar{B}_s^0$ system, and it is expected to achieve sensitivities allowing the confirmation of possible contributions of physics beyond the Standard Model.

4.2.4 Top physics

The top quark, discovered at Fermilab in 1995 [67], completed the three generation structure of the Standard Model and opened up the new field of top quark physics. Produced predominantly, in hadron-hadron collisions, through strong interactions (at the LHC the gluon scattering process as shown in Figure 4.6 dominates at $\sim 90\%$ of the cases, while at the Tevatron, production

of top quark pairs is kinematically restricted to the quark dominated region), the top quark decays rapidly without forming hadrons, and almost exclusively through the single mode $t \rightarrow Wb$. The W-boson can then decay leptonically or hadronically. The relevant CKM coupling is already determined by the (three-generation) unitarity of the CKM matrix.

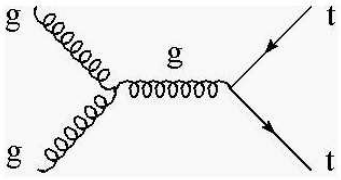

Figure 4.6: *Main top production processes at the LHC: gluon-gluon scattering diagram.*

The top has an unique property to have a large mass, about 35 times larger than the mass of the next heavy quark, and close to the electroweak symmetry breaking scale, and this raises a number of interesting questions. Therefore precision measurements in the top sector are important to get more clues on the origin of the fermion mass hierarchy and to test the electroweak symmetry breaking mechanism. Furthermore, because of the large value of m_t, it plays a special role in the radiative corrections; in fact the top quark mass is present in the ΔR term of Equation 4.2 as terms proportional to m^2_{top}/m^2_Z, while the Higgs boson mass is present only in terms proportional to $log(m_H/m_Z)$. Therefore, the dependence on the Higgs boson mass is much weaker than the dependence on the top quark mass. An accurate measurement of the top quark mass can therefore help to constrain the mass of the SM Higgs boson. The current value of the top mass is $m_{top} = 173.1 \pm 0.6$ (stat) $\pm$ 1.1 (syst) GeV [5], and we expect to reach an accuracy of 1 GeV at the LHC. Non Standard Model physics could first manifest itself in non-standard couplings of the top quark which show up as anomalies in top quark production and decays, therefore a detailed study of the top quark properties may provide a hint of new physics.
As the top quark decays before it can form hadronic bound states, a consequence of its high mass, the spin information of the top quark is propagated to its decay products. This unique behaviour among quarks allows direct top quark spin studies, as spin properties are not washed out by hadronization. Through the measurement of the angular distributions of the decay products, the information of the top quark spin can be reconstructed. Top quark spin polarization and correlations in $t\bar{t}$ events produced at the LHC are precisely predicted by the Standard Model and are sensitive to the fundamental interactions involved in the top quark production and decay.
The LHC will be a top quark factory, producing millions of $t\bar{t}$ pairs in a sample of 10 fb^{-1}. With the first few fb^{-1} of integrated luminosity, a top quark signal can be clearly separated from the background even with an imperfectly calibrated detector and the top quark pair production cross-section can be extracted at better than 20% accuracy and with negligible statistical error. The first measurement of the top quark mass will provide feedback on the detector performance (the understanding of the experimental signatures for top quark events involves most parts of the ATLAS detector) and top quark events can be

used to understand and calibrate the light jet energy scale and the b-tagging. A good understanding of top quark physics is also essential as $t\bar{t}$ production is expected to be the main background to many physics processes.
The top mass will be measured by the analysis of the semi-leptonic decay of the $t\bar{t}$ sample, by finding the peak in the invariant mass distribution of the top quark's decay products,where one W boson decays leptonically while the other one decays into two jets. The high p_T (>10 GeV) lepton and the large E_T^{miss} produced by the first top decay will be used to tag the event, while m_t will be determined from the hadronic decay of the second top ($m_t \sim m_{jjb}$). An important tool for selecting clean top quark samples, particularly in the single lepton plus jets mode, is the ability to identify b quarks.

4.3 Physics beyond the Standard Model

There are several reasons to believe that the Standard Model is not the ultimate theory of particle interactions. The Higgs mechanism has in any case little physical justification thus leading to divergent radiative corrections to the Higgs boson mass at large mass scale, unless fine-tuned cancellations occur. Furthermore, there are hints that the coupling costants of the electromagnetic, weak and strong interactions, which run with energy over the presently accessible energy range, could unify into a single value α_G at a very high energy scale ($\sim 10^{16}$ GeV). This possibility, which is predicted by Grand Unified Theories (GUT), is very actractive, because beyound the unification scale physics becomes simple: only one force with α_G strength exists. In the Standard Model, the coupling costants, as extrapolated from the experimentally measured values up to very high energy, fail to meet at a single point. On the other end, unification succeeds in more general theories, like Supersimmetry.

4.3.1 Supersymmetry

SUperSYmmetry (SUSY) is one of the theoretically favoured candidates for physics beyond the Standard Model. The main motivation is to protect the Higgs boson mass from quadratically diverging radiative corrections, in a theory where the Standard Model is valid only up to a high scale λ.
The SUSY postulates the invariance of the theory under a symmetry which transforms fermions into bosons and vice-versa. The basic prediction of SUSY is thus the existence, for each Standard Model particle degree of freedom, of a corresponding supersymmetric particle, called "sparticle", with spin different by half a unit. With unbroken SUSY, the partner particles would have the same quantum numbers and masses as the Standard Model particles. Since no superpartner has been observed up to date, SUSY must be broken. A common approach to the phenomenological study of SUSY is to assume the minimal

possible particle content, and to parametrise the SUSY-breaking lagrangian as the sum of all the terms which do not reintroduce quadratic divergences into the theory. The model thus obtained is called Minimal Supersymmetric Standard Model (MSSM) and is characterised by a large number of parameters (∼100). In order to warrant the conservation of baryonic and leptonic quantum numbers, a new multiplicative quantum number, R-parity, is introduced, which is 1 for particles and -1 for the SUSY partners. The consequences of R-parity conservation are that sparticles must be produced in pairs, and that each of them will decay at the end into to the Lightest Susy Particle (LSP), or neutralino, which must be stable. Cosmological arguments suggest that stable LSPs should be weakly interacting (LSP can be seen as candidate for "cold dark matter") and so would escape direct detection at ATLAS, resulting in the characteristic feature expected for SUSY events: an imbalance of the transverse energy measured in the detector (E_T^{miss}). Other decay products have usually large p_T since they originate from heavy particles. Such spectacular signatures are therefore quite easy to extract from the Standard Model background. If SUSY will be discovered, many precise measurements of the SUSY particle masses should be possible at ATLAS experiment.

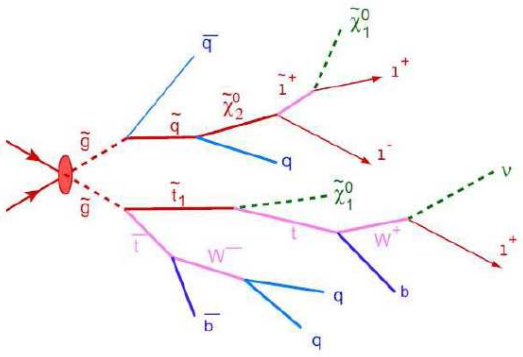

Figure 4.7: *Typical event with production and decay of many SUSY particles.*

In Figure 4.7 a typical SUSY event is displayed; the signature is a great amount of missing transverse energy (from neutralinos) and many high energy jets and leptons.

4.3.2 Other physics beyond the Standard Model

Other than SUSY there are many other physics models beyond the Standard Model, like grand unified theories, technicolor, little Higgs models, and models including extra dimensions [60, 61, 62, 63].
Many of these models predict new heavy states forming a narrow resonance decaying into dileptons. Several models predict the existence of additional

new gauge bosons (W', Z'). In particular, grand unified theories, as well as "little Higgs" models, predict their existence as a manifestation of an extended symmetry group. Generically, there are no predictions for the mass of these particles. In Figure 4.8 an example of the signal of a Z' resonance decaying in the electron channel is shown.

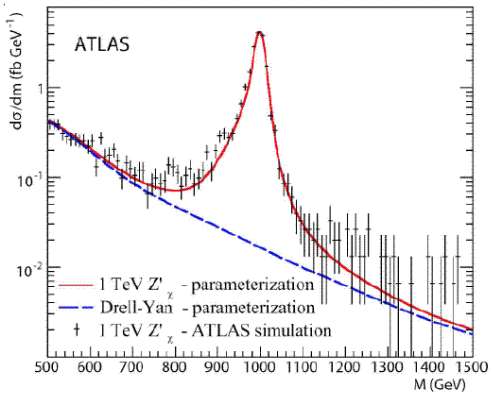

Figure 4.8: *Signal of Z' with mass of 1TeV, decaying in e^+e^- over background. The dashed line corresponds to the simulation of Drell-Yan background. [69]*

The technicolor theory provides a dynamcal means of breaking electroweak symmetry, and predicts the existence of many new technifermions which are bound together by a QCD-like force. Technicolor studies in ATLAS will be focused on searches of techni-resonances, like $\rho_T \rightarrow \mu^+\mu^-$, or $\omega_T \rightarrow \mu^+\mu^-$ Furthermore the experimentally observed symmetry between leptons and quarks has motivated the search for leptoquarks, hypothetical bosons carrying both quark and lepton quantum numbers, as well as fractional electric charge [64]. Models with extra space dimensions, in which our universe exists on a 4-dimensional brane embedded in a higher dimensional bulk space-time, offer a new way to address outstanding problems in and beyond the Standard Model. In such models the Planck scale in the bulk can be of the order of the electroweak symmetry breaking scale. This allows the coupling strength of gravity to increase to a size similar to the other interactions, opening the way to the unification of gravity and the gauge interactions. The increased strength of gravity in the bulk space-time means that quantum gravity effects would be observable in the TeV energy range reachable by the LHC. The most spectacular phenomenon would be the production of black holes [65], which would decay semi-classically by Hawking radiation emitting high energy particles.
In summary, the ATLAS detector should be able to test various theoretical scenarios, and it will have the potential to discover:

- excited quarks in the photon plus jet channel, up to masses of 6 TeV;

- couples of leptoquarks that decay in charged leptons and quarks, up to mass scale of about 1.5 TeV;

- new vector boson (W' and Z') with masses lower than 4-5 TeV, through their decay in di-leptons;

- technicolour resonances in their decay to a pair of gauge bosons or to a tecni-pion and a gauge boson (the mass limit is about 1 TeV);

- possible signature foreseen by extra-dimensions models, characterized by jets plus missing transverse energy signatures, due to the weak interaction of graviton with the detector;

- evidence for new heavy particles predicted by "Little Higgs" model, with production cross section of the order of a few fb (this means several years of LCH running will be necessary to draw conclusions on this model).

4.4 LHC early physics

As already said, the LHC operation is about to start, and during the last five years, all the elements of the ATLAS detector have been progressively installed in the cavern. Overall the detector is ready and well functioning with full solid angle coverage and only a very small fraction of dead channels. Many dedicated combined commissioning runs recording cosmic ray events have taken place in the last two years, helping in pre-calibrating the detector and having the full chain ready for data taking. With first collisions the most urgent task will be to understand and calibrate the detector in-situ using well known physics samples "standard candles" which are known theoretically to a few percent. In parallel, first measurements of Standard Model processes having large production cross sections, like minimum-bias events, QCD jets, W/Z and top pair production, will also be performed. These measurements will test the Standard Model in a much extended kinematic region and provide important first constraints on the MC generators.
It is possible to summarize in three steps the goals that the ATLAS detector intends to achieve, depending from the integrated luminosity that will be acquired:

- **few pb^{-1}** Understand and commission the detector and reconstruction algorithms beyond the current understanding based on simulations, test beam, and cosmic data. To this end will be used well known physics samples, like $Z \rightarrow ee, \mu\mu$ for tracker, ECAL and muon spectrometer calibration and alignment, and $t\bar{t} \rightarrow bl\nu bjj$ to calibrate the jet energy scale, b-tag performance, etc.

- $\sim$ **10 pb**$^{-1}$ Establish how pp collisions at the LHC really look like in each distribution and "rediscover" the Standard Model (W, Z $t\bar{t}$, QCD jets) in a new window of centre of mass energy.

- $\sim$ **100 pb**$^{-1}$ Search for new physics (W'/Z', SUSY, ...), determine what new model can actually describe the data, precision measurements of Standard Model processes.

After the incident on September 19, 2008 the LHC schedule has been revised and the initial centre of mass energy is not any more planned to be 14 TeV. At the moment, the LHC schedule plans to have few days of collisions at 900 GeV, starting from November 2009, then few months at 7 TeV and other few months at 10 TeV. An integraded luminosity of up to 200 pb^{-1} could hopefully be reached in the first year of operation. Then there will be a long shut-down and in 2012 collisions at 14 TeV will be delivered with the designed high luminosity.
Depending on each process, production cross sections at 10 TeV are reduced of about 30% (50%) for quark (gluon) induced processes compared to the 14 TeV collision and are much more reduced with 7 TeV. In Figure 4.9 the ratio of parton cross sections at 10 and 7 TeV versus the 14 TeV LHC nominal centre of mass energy, for processes induced both by gluons and quarks scattering is shown. It is very clear that lowering the energy the probability of creating high mass objects is lower.

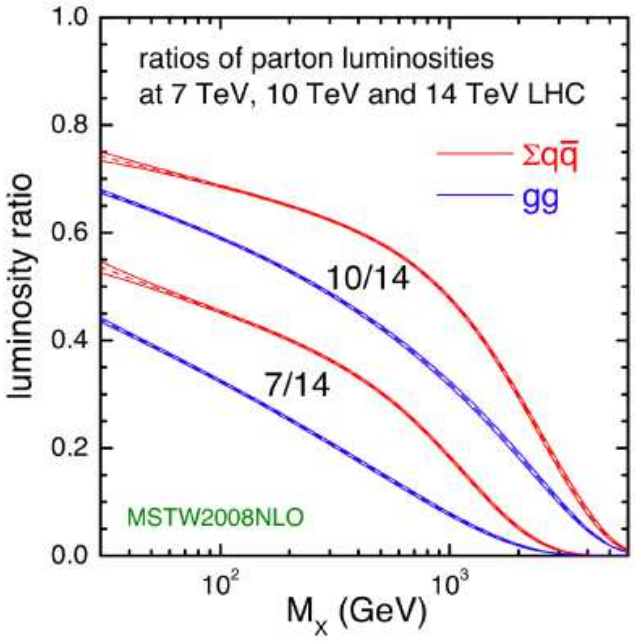

Figure 4.9: *Ratio of parton luminosities at 7, 10 and 14 TeV centre of mass energy at LHC.*

In Figure 4.10 and in Table 4.1 the processes that will be studied at the begin-

ning of LHC running and the respective number of events that are expected, after selection cuts, for the firsts 100 pb^{-1} of integrated luminosity are summarized .

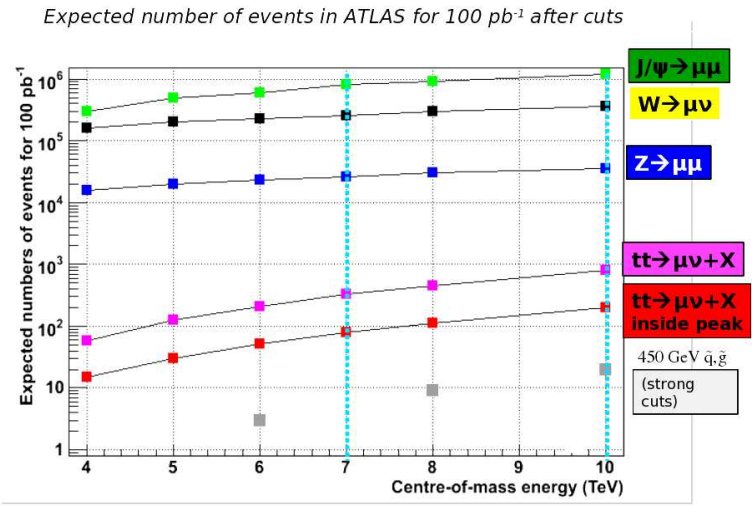

Figure 4.10: *Expected events in ATLAS, after selection cuts, for 100 pb^{-1} of integrated luminosity for different processes as a function of $\sqrt{s}$.*

Process	**expected events in 100 pb^{-1} at 10 TeV (after cuts)**
$J/\Psi \rightarrow ll$	$\sim$ 10^6
$\Psi \rightarrow ll$	$\sim$ $5{\cdot}10^4$
$W \rightarrow l\nu$	$\sim$ $3{\cdot}10^5$
$Z \rightarrow ll$	$\sim$ $3{\cdot}10^4$
$t\bar{t} \rightarrow WbWb \rightarrow l\nu + X$	$\sim$ 350
Jet $p_T > 1$ TeV	$\sim$ 500
Gluinos, squarks m$\sim$ 1 TeV	$\sim$ 5

Table 4.1: *Expected events in ATLAS, after selection cuts, for 100 pb^{-1} of integrated luminosity at 10 TeV, for different processes.*

In Table 4.2 the expected performances of each ATLAS sub system at start-up and those that will be ultimately reached are shown . The physics processes used and the physics goals are also shown.

Due to the clean signals and high cross section, the Z and W bosons will be very important at the beginning of the data taking for the detector calibration. In particular the Z mass will be one of the firsts peaks seen by ATLAS, observable in the firsts pb^{-1} of data. As seen from Table 4.2 the Z events will be

Subdetector calibration	**Performance at start-up**	**nominal**	**Physics goals**	**Physics signals tools**
EM energy uniformity	$\sim 2.5\%$	0.7%	$H \to \gamma\gamma$	isolated e, $Z \to ee$
EM energy scale	$\sim 2\%$	0.02%	W mass	$J\Psi$,$Z \to ee$
Jet energy scale	5-10%	1%	t, SUSY	$W \to jj$, QCD jets
ID alignment	50-200 μm	<10 μm	b-tagging	$Z \to \mu\mu$, isolated μ
MS alignment	<200 μm	<30 μm	Z', H	$Z \to \mu\mu$, straight μ
MS momentum scale	$\sim 1\%$	0.02%	W mass	$Z \to \mu\mu$

Table 4.2: *Expected ATLAS performances at the start-up and at the nominal regime and physics signals used as standard candles.*

used for the alignment both of the muon spectrometer and of the inner detector traker and will allow the calibration of the lepton energy scale and resolution, using the Z mass contraint. The Z events will also be used to study the trigger and recontruction efficiencies. With about 100 pb^{-1} of data it should also be possible to measure the Z and W cross sections with a precision around 10%, dominated by the uncertainty on the luminosity measurements. A complete analysis of W boson cross section in the muon channel decay at 10 TeV of centre of mass energy is presented in Chapter 5.

4.5 The ATLAS analysis software

The complexity of the physics events that will be analyzed at the LHC and the diversity of the detectors that constitute the ATLAS experiment demand for a detailed description of the event generation and simulation of the detector response, in order to evaluate in detail detector and physics performances.
The ATLAS simulation program can be divided into three separate modules (in yellow in the Figure 4.11):

- **event generation** to reproduce as closely as possible the outcome at particle levels of the physics interactions between fundamental constituents;
- **detector simulation** to include the effects of the interaction of particles with the detector and infrastructure components;
- **digitization** where the physical information registered within the simulation step is re-processed in order to simulate the detector output in a form similar to the one which might be expected from readout electronics in the actual experiment.

Figure 4.11 shows a simplified view of the processing stages in the simulation dataflow. Algorithms and applications to be run are placed in square-cornered

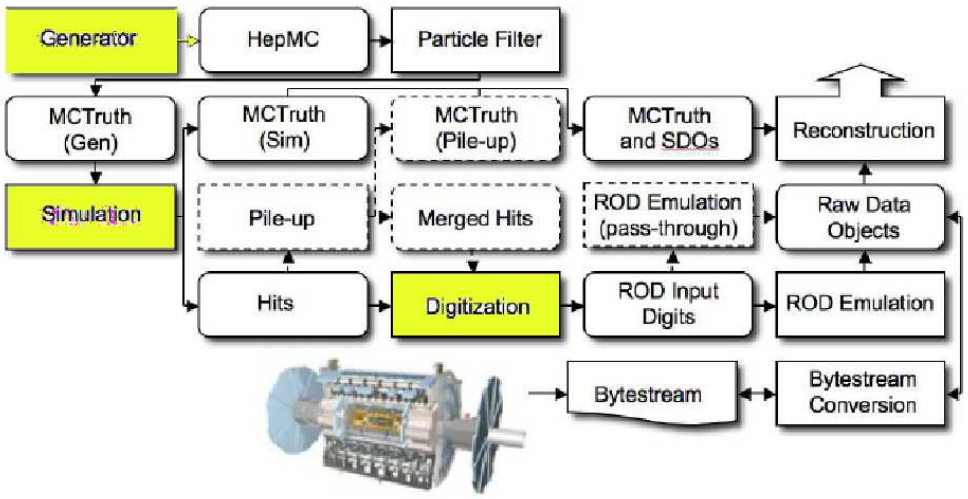

Figure 4.11: *The flow of the ATLAS simulation software, from event generators (top left) through reconstruction (top right). Algorithms are placed in boxes and persistent data objects are placed in rounded boxes. The optional pile-up portion of the chain, used only when events are overlaid, is dashed. Generators are used to produce data in HepMC format. Monte Carlo truth is saved in addition to energy depositions in the detector (hits). This truth is merged into Simulated Data Objects (SDOs) during the digitization. Also, during the digitization stage, Read Out Driver (ROD) electronics are simulated.*

boxes, and persistent data objects are placed in round-cornered boxes.
Input for the simulation comes from event generators after a particle filtering stage (where defined selections are performed on the phase space of the particles produced, *e.g.,* only events with muons with p_T>5 GeV and $|\eta|$< 2.8 are selected). The generator is responsible for any prompt decays (*e.g.,* Z or W boson) but stores any "stable" particle[4] expected to propagate through a part of the detector. Because it only considers immediate decays, there is no need to consider detector geometry during the generation step, except in controlling what particles are considered stable.
These generated events are then read into the simulation. Each particle is propagated through the ATLAS detector by the simulation program (see Section 4.5.2). The ATLAS detector geometry used in the simuation is as much as possible matched to the as built detector conditions.
The energies deposited in the sensitive portions of the detector are recorded as "hits" containing the total energy deposition, position, and time, and are written to a simulation output file, called a **hit file**. In both event generation

[4]Particles with a proper lifetime $c\tau$ >10 mm are considered stable by the event generator. They can propagate far enough to interact with detector material before decaying. Their decays are handled by the simulation. Any particles with $c\tau$ < 10 mm are decayed by the event generator, and their interactions with material or curving in the magnetic field of ATLAS are ignored.

and detector simulation, information called "truth" is recorded for each event. In the generation jobs, the truth is a history of the interactions from the generator, including incoming and outgoing particles. A record is kept for every particle, whether the particle is to be passed through the detector simulation or not. In the simulation jobs, truth tracks and decays for certain particles are stored. This truth contains, for example, the locations of the conversions of photons within the inner detector and the subsequent electron and positron tracks. The truth information is further processed in the reconstruction jobs and can be used during the analysis of simulated data to quantify the success of the reconstruction software.
Hits produced by the simulation can be directly processed by the digitization algorithm and transformed into Raw Data Objects (RDOs). The ROD functionality is then emulated, and the output is a **Raw Data Object (RDO) file**. Alternatively they can be sent first to the pile-up algorithm and then passed to the digitization stages.
The ATLAS high level trigger (HLT) and reconstruction run on these RDO files. The reconstruction is identical for the simulation and the data, with the exception that truth information can be treated and is available in simulated data.
The different stages in the simulation process, the reconstruction and the analysis tools used for the analysis are briefly described in the following sections, giving references for a more detailed description.
The ATLAS software framework, Athena, uses `PYTHON` as an object-oriented scripting and interpreter language to configure and load `C++` algorithms and objects. Rather than develop an entirely new high-energy physics data processing infrastructure, ATLAS adopted the Gaudi framework, originally developed for LHCb and written in `C++` . Gaudi was created as a flexible framework to support a variety of applications through base classes and basic functionality. As much as possible, the infrastructure relies on the CLHEP common libraries, which include utility classes particularly designed for use in high-energy physics software (*e.g.,* vectors and rotations).
Large-scale production is then done on the **World-wide LHC Computing Grid ("WLCG" or "Grid")** [71]. A single task on the Grid is separated into many jobs depending on the content and complexity of the task. A job can be completed by a single CPU within the maximum allowed time for a job on the Grid (typically 2-3 days). The output, including log files, of every Grid job is registered with the ATLAS Distributed Data Management system (DDM). The DDM uses DQ2 for dataset bookkeeping, and allows users to search for datasets and retrieve them from the Grid. Separate Grid software controls the distribution of jobs to the various Grid sites.

4.5.1 Event generation

Event generators are indispensable tools for modelling of complex physics processes that lead to the production of hundreds of particles per event at LHC

energies.
To first approximation all processes have a simple structure at the level of interactions between fundamental objects of nature: quarks, leptons and gauge bosons. The leading order process of a general event occurring at LHC can be written as $q\bar{q}(g) \rightarrow l\bar{l}(q\bar{q})$. Corrections to this picture can be subdivided into three main classes.
Firstly there are bremsstrahlung-type modifications: the emission of additional initial and final state particles by branching such as $l \rightarrow l\gamma$ or $q \rightarrow qg$, generally called **Initial and Final State Radiation (ISR, FSR)** processes. Because of the largeness of the strong coupling constant α_S and of the triple gluon vertex, QCD emission of quarks and gluons is especially prolific. Also photon emission by QED bremsstrahlung may give sizeable effects in processes with leptonic final state (*e.g.*, $W \rightarrow \mu\nu$). The bulk of the bremsstrahlung corrections is universal: it does not depend on the details of the process studied, but only on few key numbers, such as the momentum transfer scale of the process considered. Such universal corrections may be included to arbitrary high order levels, using a probabilistic language (Parton Shower (PS) methods). The fundamental property of both QED and QCD Parton Shower solution is the fact that it follows step by step the evolution of the photons or gluon emission respectively, extracting the virtualities and the energy fractions at each branching as it occurs: these quantities can be used to give an approximate kinematics reconstruction of the emitted particles, allowing an exclusive generation of the event.
Secondly there are **high-order corrections** that can be exactly calculated order by order in perturbation theory. They involve a combination of loop and bremsstrahlung graphs in a way to cancel some divergences. The necessary perturbative calculations are usually very difficult and only rarely have results that include more that one correction. In a complete description it is therefore not possible to consider bremsstrahlung separately, but an accurate matching of the emission generated by the PS approach and by NLO calculations have to be performed in order to avoid double-counting effects. Thirdly, quarks and gluons are confined. In the two points above a perturbative picture has been adopted to describe the short-distance interactions of quarks, lepton and gauge bosons. For leptons and EW gauge bosons this description is sufficient. However, for quarks and gluons it must be complemented with the structure of incoming hadrons and a picture for the **hadronization process**, wherein the coloured partons are transformed into jets of colourless hadrons, photons and leptons. The hadronization can be further subdivided into fragmentation and decays, where the former describes the way the creation of new quark-antiquark pairs can break up a high mass system into lower mass ones, ultimately hadrons. This process is still not yet understood from first principles, but has to be based on models. The simple structure of the leading order approximation has now become considerably more complex, instead of two final state particles there are hundred particles produced (a sketch of a

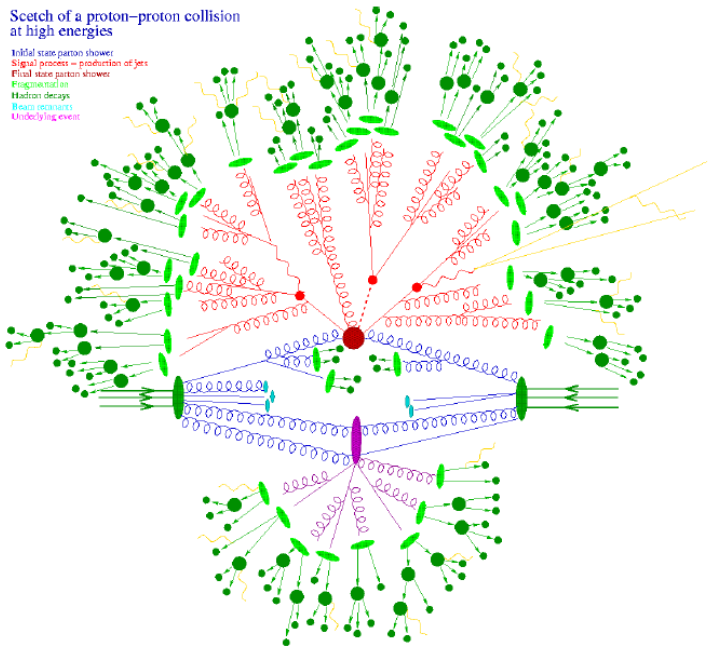

Figure 4.12: *Sketch of a proton-proton collision at high energies.*

proton-proton collision at high energies is illustrated in Figure 4.12). It is there that event generators come to the rescue. In an event generator, the objective striven for is to use computers to generate events as detailed as could be observed by a perfect detector.
The complexity, the modularity and the number of simulation programs for hadron colliders has increased considerably with the requirements of the LHC physics and that availability of the Tevatron Run II results. The best accurate description of hadron collider data is often obtained combining components of different simulation programs: for example simulation of minimum bias from one generator, a signal process from another and yet other programs for background generation. Further on, specific programs are used to generate the hard processes, to evolve the event through parton shower algorithms, or to hadronize the coloured products of the shower.
In ATLAS the individual generators are executed outside the Athena framework and their output is converted into a common format by mapping into HepMC; events can also be stored as POOL files for later use as input of the ATLAS simulation.
`PYTHIA` [72] and `HERWIG` [73] are the benchmark event generators in ATLAS (the first one is used as default). These programs, referred to as showering and hadronization generators, are general purpose tools, able to simulate a wide variety of initial and final states. They begin with a leading order hard subprocess and higher order effects are added by "evolving" the event adding additional QCD and QED radiation in a shower approximation (parton shower) which

is most accurate when the radiation is emitted at small angle. This allows partons to split into pairs of other partons. The resulting partons are then grouped together and hadronized into colour-singlet hadrons and resonances are decayed. In addition, PYTHIA uses a model for hard and soft scattering processes in a single event in order to simulate underlying activity.
These general purpose generators have many parameters, some of them are related to fundamental parameters such as the QCD coupling constant and electroweak parameters, and others describing the models used to parametrize long distance QCD, soft QCD, and electroweak processes. These generators are used both standalone or with specialized generators that improve the description of certain final states (like the generators PHOTOS [74] and HORACE [75] that are used for the events that have been analyzed in these thesis and are described in Chapter 5).
Another aspect of the event generation that has to be considered is the description of the internal structure of the incoming hadrons. The distributions of the momentum fraction x of the partons (gluons and quarks) in the hadrons, the so called **Parton Distribution Functions (PDFs)**, can not be calculated perturbatively but rather are determinate by global fits to data from deep inelastic scattering, Drell-Yan and jet production at current energy ranges. The PDFs are used by all event generators as external inputs. Two major groups, CTEQ [76] and MRST [77], provide semiregular updates to the parton distribution functions when new data and/or new theoretical developments become available.

4.5.2 Detector simulation

Depending on the speed and the precision with which the user wants to simulate data through ATLAS, there are different levels of simulation of the detector. In fact, large computing resources are required to accurately model the complex detector geometry and physics descriptions in the standard ATLAS simulation, called "full simulation". This has lead to the development of several varieties of "fast simulations". The different simulation package developed in ATLAS are briefly desribed in the following; more details can be found in [70].

Full simulation

The standard ATLAS detector simulation is based on the GEANT4 toolkit, that provides both a framework and the necessary functionalities for running detector simulation in particle physics and other fields. The functionalities provided include optimized solutions for geometry description, the propagation of particles through detectors, the description of materials, the modelling of physics processes, visualization, and many more. GEANT4 is part of the LCG application software project and it is developed with a world-wide effort, coordinated by a strong development team by CERN. The use of GEANT4 functionalities within ATLAS specific setup is embedded in the TLAS program, integrated in

the Athena framework, where tailored packages for handling geometry, kinematics, materials, physics, fields, sensitive detectors, etc., have been added by means of plug-in modules.

Simulated detector geometry The ATLAS detector geometry used in the simuation is as much as possible matched to the as built detector conditions. In addition to the standard detector layouts, several commissioning layouts have been made available to the user for simulation of cosmic ray data taking. An example is shown in Figure 4.13, that represents the `GEANT4` detector geometry, where the calorimeter end-caps were shifted out of position while the inner detector was being accessed and were missing large portions of the beam pipe that had not yet been installed.

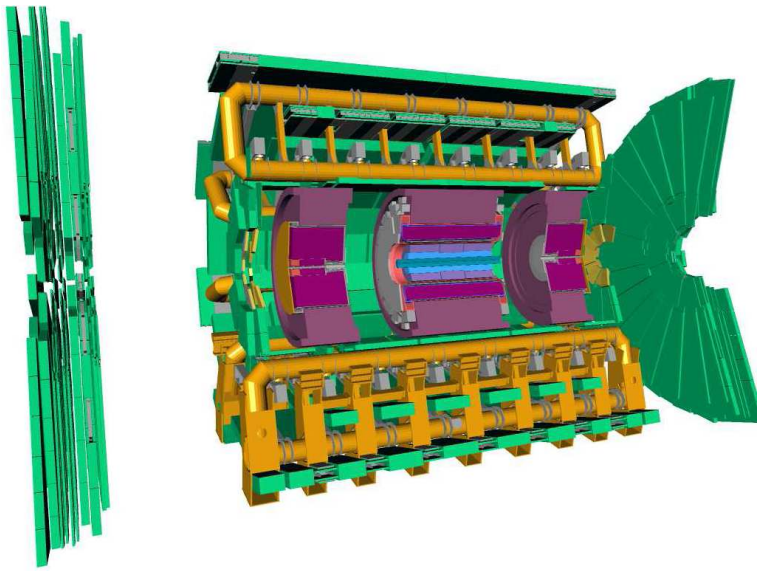

Figure 4.13: *Commissioning layout of the detector used for cosmic ray data taking during beginning of 2008. The endcap toroidal magnets and beampipe were not yet installed. The calorimeter end-caps (purple) were shifted by 3.1 m and the muon end-caps (green) were shifted to provide access to the inner detector during installation. The barrel toroid magnets are shown in yellow, and the inner detector is shown in blue [70].*

In order to study the cosmic rays and cavern backgrounds, the ATLAS cavern surrounding the detector was simulated, as well as the bedrock surrounding the two shafts leading down from the surface. Some approximations were necessary for describing dead materials, for example bundles of cables and cooling pipes in the service areas of the detector. Several different magnetic field configurations, both for toroid and solenoid, has been also made available for some of the full detector layouts. Field maps have also been constructed that reflect the as-built misalignments of the magnet system. Many misalignments were also introduced for the inner detector, in order to simulate the early data con-

figuration and to speed the process of global detector alignment and improve early physics searches. The configuration of the detector can be set at run time by the user.

Fast simulation

Because of the complicated detector geometry and detailed physics description used by the ATLAS GEANT4 simulation, it is impossible to achieve the required simulated statistics for many physics studies without faster simulation. To that end, several varieties of fast simulation programs have been developed to complement the GEANT4 simulation. In particular are now used three of these programs: Fast G4 Simulation, ATLFAST-I and ATLFAST-II. All of them have the goal to speed up the calorimeter simulation, that is the slowest part of the full simulation; in fact almost 80% of the full simulation time is spent simulating particles traversing the calorimetry, in particular electromagnetic showers.

- **Fast G4 Simulation**: the approach taken is to remove low energy electromagnetic particles from the calorimeter and replace them with pre-simulated showers stored in memory. Using this approach, computing time is reduced by a factor of three in hard scattering events with little physics penalty. This simulation can be applied to study all processes that do not require extremely accurate modeling of calorimeter response or electromagnetic physics.

- ATLFAST-**I**: truth objects are smeared by detector resolutions to provide physics objects similar to those of the reconstruction. Object four-vectors are output, without any detailed simulation of efficiencies and fakes. A factor of 1000 speed increase over full simulation is achieved with sufficient detail for many general studies. ATLFAST-I is the least detailed simulation method. In fact there is neither a realistic detector description, nor any simulation of reconstruction efficiency or misidentification rates, so studies of detector-based quantities, such as calorimeter sampling energies and track hit positions, are not possible.

- ATLFAST-**II** makes use of the simplified detector description used for reconstruction. It is a fast simulation meant to provide large statistics to supplement full simulation studies. The aim is to try to simulate events as fast as possible while still being able to run the standard ATLAS reconstruction, in fact, ATLFAST-II directly simulates the input to the standard Athena reconstruction algorithms to mimic the full simulation. Unlike ATLFAST-I, which provides only momenta for the reconstructed objects, reconstructed ATLFAST-II output includes all the properties associated with a reconstructed object.
  ATLFAST-II is made up from two components: the *Fast ATLAS Tracking*

Simulation (Fatras) for the inner detector and muon system simulation and the *Fast Calorimeter Simulation (FastCaloSim)* for the calorimeter simulation. Optionally, any subdetector can be simulated with `GEANT4` to provide the higher level of accuracy without the same computing time consumption as full simulation of the entire detector.
By default, `ATLFAST`-II uses full simulation for the inner detector and muon system and FastCaloSim in the calorimetry. When the Fatras package is also added, `ATLFAST`-II is called `ATLFAST`-**IIF**.
The Fatras package uses as input, the HepMC format, performs a smearing of the primary vertex position to represent the luminous region within ATLAS, and records truth information in a way similar to the full simulation. The simulation process is significantly speed up by the use of a simplified reconstruction geometry. It re-uses to a large extent modules and resources of the offline track reconstruction, while only few dedicated components replace standard offline algorithms and tools. The integration of material effects for particles that traverse detector material is mainly implemented in a stochastic way.
The FastCaloSim package uses the truth information of all interacting particles exiting from the inner detector as input to the calorimeter simulation. Instead of simulating the particle interactions with the detector material, the energy of single particle showers is deposited by FastCaloSim directly using parametrizations of the longitudinal and lateral energy profile. The distribution of active and inactive material in the calorimeter needs to be respected by the parametrization, so a fine binning of the parametrization in the particle energy and pseudorapidity is needed. The parametrizations are based on a 30 million event sample of fully-simulated single photons and charged pions in an energy range between 200 MeV and 500 GeV. All electron and photon showers are approximated by the photon parametrization and all hadronic showers are approximated by the charged pion parametrization.
An improvement over full simulation time of a factor of 10 is achieved with full `GEANT4` inner detector and muon simulation and FastCaloSim, and a factor of 100 is achieved enabling Fatras and FastCaloSim.

In Table 4.3 there are some examples of simulation times in kSI2K seconds[5] for various types of events in the full and fast simulations, and in Figure 4.14 left there is a comparison between full and fasts simulation of the the reconstructed muon transverse momentum resolution for $Z \rightarrow \mu\mu$ events. In the cases of `ATLFAST`-II and the Fast `G4` simulation, the muon spectrometer simulation is done by `GEANT4` and should, therefore, be identical to full simulation. In the right figure is shown the missing transverse energy along the x-axis for the full and fast simulations in di-jet events. Also in this case, `ATLFAST`-II and the Fast `G4` Simulation agree quite well with full simulation in missing transverse

[5]SI2K (SpecINT2000) is a standard CPU speed normalization between machines connected in the Grid system.

energy spectrum, even in the tails of the distribution. ATLFAST-I does not sufficiently populate the tails of the missing transverse energy distribution, and ATLFAST-IIF has too wide a distribution.

Sample	G4	F	AF-II	AF-IIF	AF-I	Digit	Reco
Min Bias	551	246	31	2	0.03	20	8
$t\bar{t}$	1990	757	101	7	0.1	29	47
Jets	2640	832	94	8	0.1	29	78
γs and Jets	2850	639	71	6	0.06	25	45
$W^{\pm} \rightarrow e^{\pm}\nu_e$	1150	447	57	4	0.05	23	8
$W^{\pm} \rightarrow \mu^{\pm}\nu_{\mu}$	1030	438	55	4	0.05	23	14
Heavy ions	56000	21700	3050	203	5	267	470

Table 4.3: *Comparison of simulation time per event, in kSI2K seconds, between different simulation algorithms. G4 stands for ATLAS- the full simulation, FG4 is FastG4 and AF stands for ATLFAST. For each process is also shown the average digitization and reconstruction time. Simulation, digitization, and reconstruction times are averaged over 250 events, except simulation of heavy ion events, which were averaged over 50 events. Reconstruction time can vary dramatically depending on the algorithms run and the trigger configuration. These times should be taken as indicative of the order of magnitude, rather than as a precise measurement. [70]*

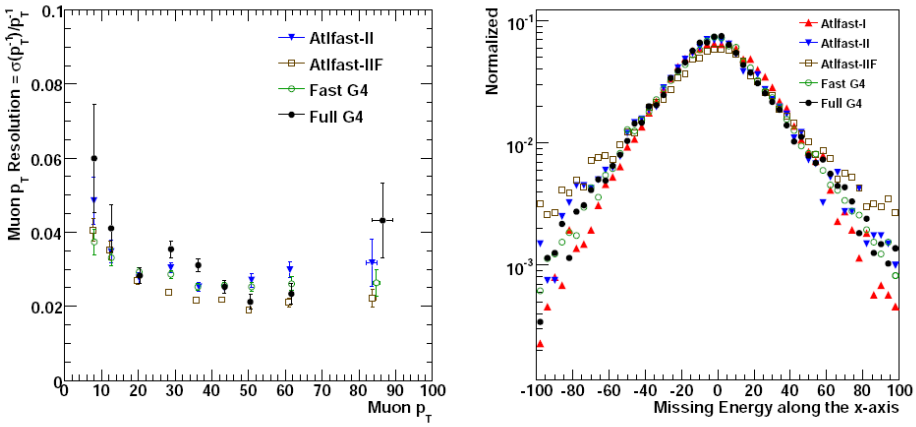

Figure 4.14: *Left: fast and full simulations comparison of reconstructed muon p_T resolution as a function of muon p_T for central ($|\eta| < 1.2$) muons in $Z \rightarrow \mu\mu$ events, using the Reconstruction with the Muon Spectrometer in stand-alone; right of missing transverse energy along the x-axis in di-jet events with a leading parton p_T between 560 and 1120 GeV. [70]*

It is generally left to the physics groups to evaluate the fast simulations with

their analysis and to determine which is acceptable. Having evaluated both the time performances of all the fast simulation algorithms, and the muon and the missing transverse energy reconstruction performances, in the analysis described on Chapter 5 was decided to use ATLFAST-II in the default mode.

4.5.3 Digitization

The hits produced either directly by the simulation step, or from the merging of pile-up events, need to be converted in the output format really produced by the readout electronic elements of the ATLAS detector: "digits". Typically, a digit is produced when the voltage or current on a particular readout channel rises above a pre-configured threshold within a particular time-window. Some subdetector's digit formats include the signal shape in detail over this time, while others simply record that the threshold has been exceeded within the relevant time window. The propagation of charges (as in the tracking detectors and in the liquid argon calorimeter) or light (as in the case of the tile calorimeter) into the active media has to be considered as well as the response of the readout electronics. The peculiarities of each subdetector's charge collection, including cross-talk, electronic noise and channel-dependent variations in detector response are modelled in subdetector-specific digitization software. The properties of the digitization algorithms were tuned to reproduce the detector response seen in lab tests, test beam data, and cosmic ray running, like dead channels and noise rates.
The final output of the digitization step are the RDOs, that are the input of the event reconstruction chain. The ATLAS detector electronics produce data in bytestream format. The RDO format can be thought of as a POOL -compatible version of the bytestream. The file size on disk is typically around 2.5MB per event for hard scattering events and increases in the presence of pile-up.

4.5.4 Event reconstruction and analysis

As already said, after the digitization step, real and simulated events are treated at the same manner, a part the truth objects that are only in the simulated data. During the LHC running, the ATLAS detector will produce about 3 PByte of raw data per year, a huge amount of information which prohibits the simple distribution to world-wide collaborations. To enable physics to analyze the data on remote sites, several different types of datasets, corresponding to different stage of the reconstruction chain, are produced. Thus the following dataset has been adopted:

- **Bytestream data**: is a representation of the event data provided by the detector and flowing from the TDAQ system.
- **Raw Data Object data (RDO)**: is a C++ object representation of the bytestream information; its size is approximately 2 MB/event.

- **Event Summary Data (ESD)**: contains detailed output of reconstruction process from RAW data. Its content is intended to make access to RDO data unnecessary for most of physics applications, other than for some calibrations or reconstructions. ESD has an object oriented representation, and is stored in `POOL` files. Typical objects that are contained in the ESD are tracks (and their hits), calo clusters, calo cells, combined reconstruction objects etc. The typical size for the ESD is 1 MB/event initially, but it will be decreased as the understanding of the detector will improve. ESD will be fully available at T1 grid centres and partially (30/80 per cloud) available at T2.

- **Analysis Object Data (AOD)**: which is a summary of the reconstructed event with "physics" objects, like electrons, muons, jets etc. It contains sufficient information for common analysis. The AOD can be produced from the ESD and a back navigation mechanism is possible in order to recover additional information from them. The typical size of the AOD is 100 kByte per event. AOD will be fully available at T1 and multiple copies (between 5-10) copies will be available among T2 sites among each cloud.

- **Derived Physics Data (DPD)**: it is a more compact format tahn AOD. The aim is to provide sufficient compression and flexibility that a small set of event formats can satisfy the physics community, thus easing the burden of maintenance and encouraging cross-group analysis. There are three levels of DPD:

  - Primary DPD (D1PD): is more specific to certain type of analysis and it is foreseen that of the order of 10 types of D1PD will be defined. It consist of the subset information from AOD and ESD after skimming (removal of irrelevant events), thinning (removal of irrelevant object) and slimming (removal of irrelevant pieces of information from objects) to reduce its size. Typical size of D1PD is between 10-30kB per event and its primary purpose is to optimize data access pattern. The availability of D1PD on the grid facilities is the same as that of AOD.
  - Secondary DPD (D2PD): provides further refinement of contents for even more specific analysis than the generality of D1PD. They are `POOL` files created from AODs or D1PDs in Athena. These files must be read in Athena and can contains in addition to the standard reconstruction containers any sort of analysis-specific information. Typical size of D2PD is around 10kB though it varies depending on its purposes.
  - Tertiary DPD (D3PD): provides the same level of contents as D1PD and D2PD with difference that it is in flat ntuple format. Typically D3PD size is less than 10kB.

- **Event tag**: summarizes some general features of the event, allowing rapid selection of and access to a subset of events. The size for tha tags is 1 kByte per event.

Physics Analysis Tools

The scope of the Physics Analysis Tools (PAT) it is to cover the gap between the combined reconstruction output and the n-tuple based analysis level. They are organized as an analysis framework, integrated in the Athena environment, that provide useful tools to select and combine the reconstructed objects. They include, for example, combination, permutation with or without selection criteria, back navigation mechanism to/from the AOD to the ESD level.
The analysis shown in the next chapter is performed using the analysis framework called EWPA, that is integrated in the Athena official ATLAS package, and has been developed by the Pavia ATLAS analysis group.

EWPA (EveryWhere Physics Analysis) is a simple and light framework upon which is possible to create multiple plugin tools for users's specific physics analysis. The user can run its analysis reading ESD or AOD datasets and creating D2PD in Athena, or creating D3PD and then working without Athena installed. The schema of the EWPA[81] framework is illustrated in Figure 4.15.

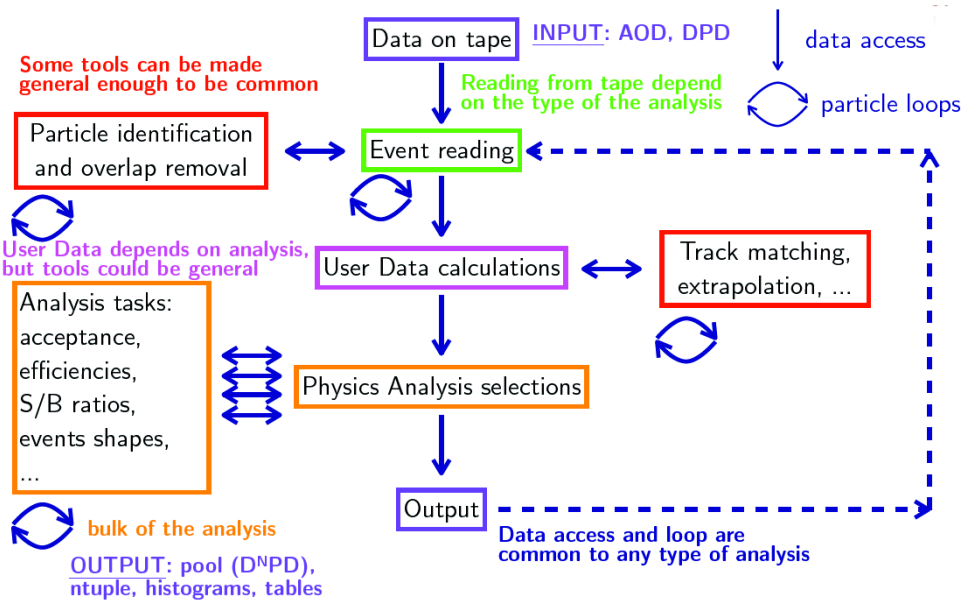

Figure 4.15: *Schema of the EWPA analysis framework.*

Chapter 5

W boson cross section measurement

5.1 Introduction

The gauge bosons $W^{\pm}$ and Z^0, together with the massless photon (γ), compose the bosonic fields of the unified electroweak (EW) theory proposed by Weinberg, Salam, and Glashow. The W and Z bosons were discovered at CERN in 1983 and 1984[82, 83, 84, 85] using the UA1 and UA2 detectors which were designed and built for this very purpose. Albeit a long time has passed since then, the production of electroweak gauge bosons in hadronic collisions is still a topic of deep interest in modern particle physics. Actually, single W and Z boson production is used at the Fermilab Tevatron collider to derive precision measurements of the W boson mass and width, to extract the electroweak mixing angle from the forward-backward asymmetry in the neutral current (NC) channel and to strongly constrain the Parton Distribution Functions (PDF) through the measurement of the W charge asymmetry. These processes are also used for detector calibration and the measurement of their total production cross section can be compared with the corresponding Quantum ChromoDynamics (QCD) prediction, in order to test the convergence of the strong coupling expansion in perturbative QCD calculations.
At the Large Hadron Collider, the production of W and Z bosons will continue to be a relevant process because of their large cross section and very clean signature, given by one isolated charged lepton with missing transverse energy (for W production) and by two isolated charged leptons with opposite charges (for Z production). While the parameters of the Z boson have been well studied at LEP, the properties of the charged current carriers, the W bosons, are known with less precision.
As briefly described in Chapter 4, thanks to the very large statistics, a measurement of the W mass with an uncertainty of about 15 MeV should be feasible at the LHC. These processes are also good candidates to understand the detec-

tors performances in the early stage of data analysis at the LHC, to monitor the collider luminosity with per cent precision and constitute a background, in the high p_T tails, to new physics searches, like the new heavy gauge bosons Z' and W', whose discovery is an important goal of the LHC.
It is important to realize that the many facets of the W/Z physics programme at hadron colliders require, for obvious reasons, the measurement of different observables, depending on the physics goal of interest. Correspondingly, a number of these observables must be precisely predicted and simulated, to avoid theoretical bias in data analysis. For example, for precise W mass measurements, relevant observables are the W transverse mass and the lepton transverse momentum, while luminosity studies require a deep understanding of the total cross section and lepton pseudorapidity. On the other hand, the lepton pair invariant mass produced in Z production and the W transverse mass in their high tails are the observables to be focused on when searching for new physics signals.
The high luminosity at the LHC implies that systematic errors, including theoretical ones, will play a dominant role in determining the accuracy of the cross sections since statistical errors will be reduced quickly. This needs calculations of W and Z production cross sections including higher-order corrections originating from the EW and QCD sector of the Standard Model. Furthermore, the implementation of such calculations in Monte Carlo (MC) generators is mandatory, in order to perform realistic studies of the impact of higher-order corrections on the observables and to compare theory with data.
In this chapter a brief introduction to the W boson production and decay processes (Section 5.2) is first given; in Sections 5.3 and 5.4 QCD and EW corrections to the Born process respectively, and Monte Carlo tools that implement these correction are then described. The second part of the chapter is focused on the inclusive cross section measurement strategy (Section 5.5), together with possible sources of systematical uncertainties, and on electroweak corrections implemented into the `HORACE` event generator and the study of the effects of the ATLAS detector simulation to these corrections.

5.2 W boson production and decay

In hadron-hadron collisions the W and Z are predominantly produced via the processes illustrated in Figure 5.1, in which the first diagram represents the Born leading order process, and in the others next-to-leading order ones are displayed. The dominant production mechanism is the Drell-Yan process, in which a quark and an antiquark annihilate to form a vector boson.
Present experimental measurements of electroweak parameters, including vector boson masses and decay widths, are precise enough to provide tests of QCD and the electroweak part of the Standard Model beyond leading order. These precise measurements not only test the electroweak theory but also provide possible windows to sectors of the theory at mass scales higher than those di-

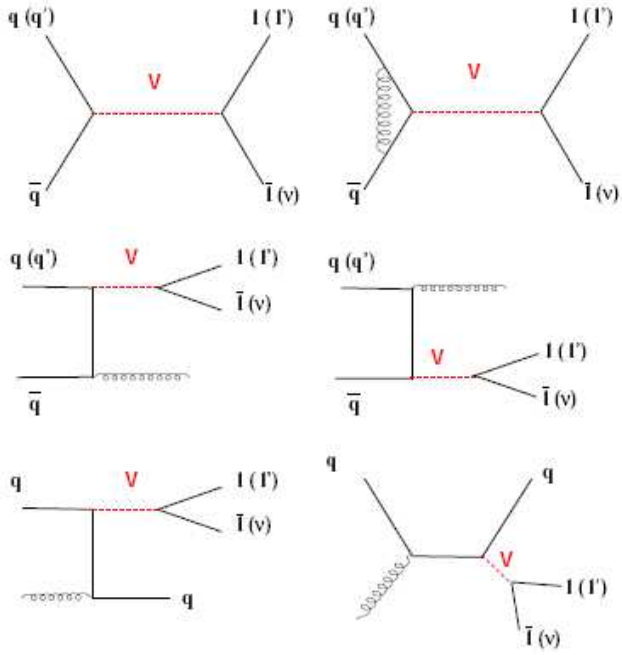

Figure 5.1: *Diagrams for production and leptonic decay of a vector boson $V = W, Z$ at leading (upper left) and next-to-leading order (others).*

rectly observable at current accelerator energies. These sectors enter into the electroweak observables through radiative corrections.
Calculations of the total production cross sections for W boson incorporate parton cross sections, parton distribution functions, higher-order QCD effects. In the case of parton-parton scattering ($pp \rightarrow W + X$) the theoretical cross section can be schematically written as follows:

$$\sigma_W^{th}(p, p') = \sum_{ab} \int_0^1 dx dx' F_a(x) F_b(x') \times \hat{\sigma}_W^{ab}(xp, x'p') \tag{5.1}$$

where $F_i(x)$ is the PDF of each parton (quark or gluon) involved, and the $\hat{\sigma}_W^{ab}$ is the parton level cross section of the process $ab \rightarrow W + X$ and is theoretically computable. Moreover, the majority of the theoretical work on W production has the scope of improving the accuracy with which $\hat{\sigma}_W^{ab}$ is known. Since the final state may include additional partons which form a shower, the output from the hard QCD process must be fed to a shower generator to create a realistic final $p - p$ collision state seen as in a detector.
The decay modes of the W boson are $W \rightarrow l\nu$, $(l = e, \mu, \tau)$ and $q\bar{q}'$, where the main modes $u\bar{d}$, $u\bar{s}$, $c\bar{s}$ and $c\bar{d}$ have branching ratios proportional to their corresponding CKM matrix elements. The measured value for the branching fraction of the three combined leptonic modes is 32.0 $\pm$ 0.4%, where the remaining fraction is assigned to the hadronic decay modes.

The partial width into fermion pairs is calculated at lowest order to be:

$$\Gamma_0(W \to f\bar{f}') = |V_{f\bar{f}'}|^2 N_C G_F m_W^3/(6\sqrt{2}\pi) \tag{5.2}$$

where $V_{f\bar{f}'}$ is the corresponding CKM matrix element for quark pairs or one for leptons; m_W is the W boson mass and G_F is the Fermi coupling constant. N_C is the corresponding color factor which is three for quarks and one for leptons. The expression for the partial decay widths into quark pairs also has an additional QCD correction due to vertex graphs involving gluon exchange and electroweak corrections due to next-to-leading order graphs which alter the effective coupling at the W fermion vertex for all fermions. Within the context of the Standard Model, there are also vertex and bremsstrahlung corrections that depend on the top quark and Higgs boson masses.

5.2.1 PDFs uncertainty

A precise knowledge of the partonic structure of the proton will be an essential ingredient for the physics potentials of the LHC, both for what concerns discovery and precision physics. At present, there is a great deal of interest in understanding how the uncertainties on the determination of the Parton Distribution Functions (PDF), both of experimental and theoretical origin, translate into uncertainties for those observables that will be measured at the LHC.
As of today, the PDFs cannot be computed in QCD and are extracted from experimental observables in lepton-hadron scattering (DIS processes from fixed target, like HERA experiments), Drell-Yan lepton pair production processes and jet data at hadron colliders. These results are obtained at different Q^2 with respect to the scale of LHC centre of mass energy and hence have to be evoluted through the Dokshitzer-Gribov-Lipatov-Altarelli-Parisi (DGLAP) equations [86, 87, 88] to the relevant scale of the studied process. PDFs are nowadays available up to the next-to-next-to leading order (NNLO) in perturbative QCD for most processes and in recent years they have been also providing uncertainties which take into account experimental systematic errors and the correlations between data points that enter the global fits. Despite the great improvement on PDFs in recent years, their uncertainty still dominate many cross section calculations for the LHC. In fact the LHC will probe kinematic regions never explored before, as shown in Figure 5.2 such as the very high-Q^2 and the very low-x regions. In this regime the current theoretical formalism (DGLAP) is at the edge of its supposed applicability and the uncertainties are therefore very large. At the electroweak scale (*i.e.,* for Z and W boson production) the participating partons have small momentum fractions at central rapidity. In fact, at leading order in perturbation theory, the momentum fractions of the interacting partons are given by:

$$x_{1,2} = \frac{M}{\sqrt{s}} e^{\pm y} \tag{5.3}$$

where M is the mass scale of the process ($M_{W,Z}$), $\sqrt{s}$ is the centre of mass energy of the reaction and y is the parton rapidity. As shown in the LHC kinematical plane, illustrated in Figure 5.2, at central rapidity the participating partons have small momentum fractions, $x \sim 0.005$. Moving away from central rapidity one parton goes to lower x value and one to higher x, however over the measurable y interval ($y \leq 2.5$) x values are contained in the range $10^{-4} \leq x \leq 0.1$. Thus, at the electroweak scale the theoretical predictions for the LHC cross sections are dominated by low-x PDF uncertainty. Thus, in contrast to the Tevatron interaction dynamic, the scattering is happening mainly between sea quarks. Thus the precision of our knowledge of hadronic W and Z cross sections at the LHC is highly dependent on the uncertainty in the momentum distribution of the gluon.

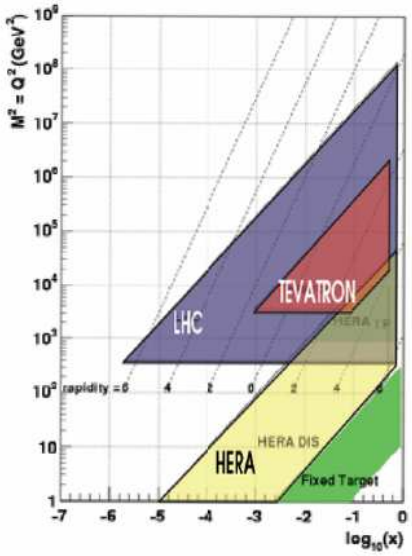

Figure 5.2: *Kinematic plane (x, Q^2) showing the interested region for different colliders and for different value of the process energy scale (M) and rapidity (y).*

Recent determinations of the W and Z cross sections dependencies on the PDFs uncertainties have been performed by CTEQ [76] and MRST [77] groups. Generally these analysis have been performed at the next-to-leading order (NLO) approximation of perturbation theory (1-loop hard cross section and 2-loop evolution kernels). In QCD the order of magnitude of the neglected terms of the perturbative expansion is $\sim \alpha_S^2$ with respect to the leading order terms. Thus the theoretical uncertainty of the predicted cross sections at the energy scales of Tevatron and LHC colliders is expected to be of the order of a few percent. Recently next-to-next-to-leading order (NNLO) analysis have been done either on DIS alone or in a global analysis context. The difference with respect to the corresponding NLO analysis were indeed of the expected or-

der of magnitude. Furthermore NNLO results should have an higher accuracy ($\sim 3\%$).

5.2.2 W boson observables

Tranverse momentum and mass

Main observables that are used for the W analysis are the muon transverse momentum (p_T^μ), and the W transverse mass (M_T^W), defined as:

$$M_T^W = \sqrt{2p_T^\mu p_T^\nu (1 - cos\phi^{\mu\nu})} \tag{5.4}$$

where $\phi^{\mu\nu}$ is the azimuthal angle between the two decay production. Both the p_T^μ and the M_T^W distributions have a jacobian peak at $M_W/2$ and M_W respectively. The width of the jacobian peak is due to the finite experimental resolution ("smearing") and to the initial transverse momentum of the W boson given, for example, by initial state radiation processes.
In Figure 5.3 the p_T^μ and the M_T^W distributions are shown. The p_T distribution is strongly affected by the intrinsic W transverse momentum, while the effect of the detector smearing is marginal. On the opposite, in the case of the M_T^W distribution the main effect is due to the experimental resolution with which the p_T is measured. Due to the difference in the behaviour of these two distributions, both of them are usually used for the study of the W boson.

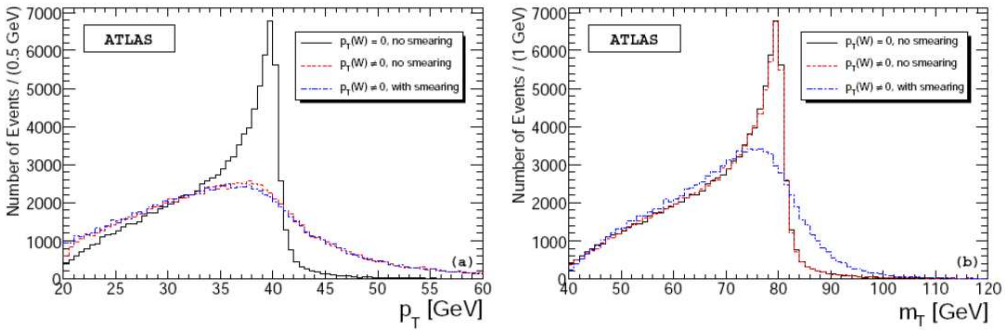

Figure 5.3: *Muon transverse momentum and W transverse mass distributions, showing the effects of detector smearing and of W intrinsic p_T.*

Pseudorapidity

At the LHC the cross section for the production of the W^+ is larger than the one for the production of W^- bosons. The contribution from $c\bar{s}$ quarks (and $s\bar{c}$) initial states amounts to 10% at LHC energies (about 2% for the

Tevatron). The latter processes mainly contribute to the central production of W^- bosons, and that are a direct consequence of parton distribution functions; whereas forward W^+ production is mostly due to $u\bar{d}$ ($d\bar{u}$) states. Hence, at LHC, the shape of the rapidity distributions is different for the two charged bosons. The difference in the shape of the rapidity distribution should survive in the detectable decay lepton.
In Figure 5.4 the expected shape of the rapidity distribution for W^+ and W^- production is shown. The cross-section times leptonic branching ratio has been obtained from `PYTHIA` using the CTEQ2L parton distributions, without applying cuts on the decay lepton. In both figures the different shapes of the W^+ and the W^- are visible; the W^+ goes further out in rapidity and has a maximum at $|\eta| \sim 3$. The central region ($|\eta| = 0$) corresponds to a symmetric configuration of the parton momenta ($x_{1,2} \sim 0.005$), whereas at $|\eta| = 2.5$ an asymmetric configuration can be found ($x_1 \sim 0.1$, $x_2 \sim 0.0007$). The precise measurement of these rapidity distributions can be used to constrain the u and $\bar{d}$ (resp. d and $\bar{u}$) distributions.

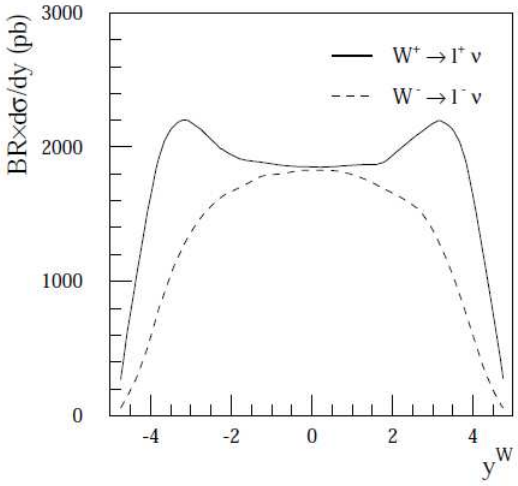

Figure 5.4: *Differential cross-section for W^+ and W^- production as a function of the vector boson rapidity y^W from a leading order calculation (14 TeV). [8]*

5.3 QCD corrections and Monte Carlo tools

QCD simulations typically used in high-energy collider experiments are "general purpose" parton shower Monte Carlo, such as, for example, `HERWIG` [73] or `PYTHIA` [72] or MC programs based on a fixed-order perturbative calculation of a given process. However, the new challenges of the Tevatron Run II and the LHC have required improvements on the approaches to QCD MCs and calculations, including the matching of exact leading-order matrix elements for multiparticle production with parton shower, the matching of NLO corrections with parton shower, improvements in the techniques for NNLO calculations, as well as improvements in the parton shower algorithms. An example is the MC event generator *MC@NLO* [89], that allows to incorporate NLO QCD matrix elements consistently into a parton shower framework.
The matrix element (ME) approach allows a systematic expansion in powers of α_S, and thereby offers a controlled approach towards higher precision. Calculations can be done with several (up to ~ 8) partons in the final state, as long as only Born-level results are asked for, and it is possible to require the phase-space cuts for these partons accordingly to the experimental needs. Loop calculations are much more difficult, on the other hand, and the mathematically correct cancellation between real- and virtual-emission graphs in the soft/collinear regions is not physically sensible. Therefore ME cannot be used to explore the internal structure of a jet, and are difficult to match to hadronization models, which are supposed to take over in the very soft/collinear region.
The Parton Shower (PS) approach, on the other end, clearly is an approximation and does not have any topology of events with well separated jets. It is not possible steer the probabilistic evolution of a shower too far, and therefore the efficiency for events in a specific region of phase space can be quite low. On the other hand, PS is universal, so for any new model only the basic hard process is required and then PS will turn that into reasonably realistic multiparton topologies. The use of Sudakov factors[1] ensures a physically sensible behaviour in the soft/collinear regions, and it is also here that the PS formalism is supposed to be most reliable. It is therefore possible to obtain a good picture of the internal structure of jets, and to provide a good match to hadronization models.
Figure 5.5 shows the rapidity distribution of an on-shell W^- boson (left) and W^+ boson (right) at the LHC (at 14 TeV) for LO, NLO and NNLO QCD predictions with PDF set MRST. Distributions are symmetric in y. The bands indicate the common variation of the renormalization and factorization scales in the range $\mathrm{M}_W/2 \leq \mu \leq 2M_W$.
QCD high order effects, as one can see from Figure 5.5 give a big contribution on the cross section value predictions, up to a level of 20%. They also have a consequence on the p_T distributions of muons, giving them a longer tail:

[1] In the parton shower development the Sudakov factors gives the probability that a parton starting with virtuality t will not have branched by the lower cut-off scale t_0 by emitting a gluon.

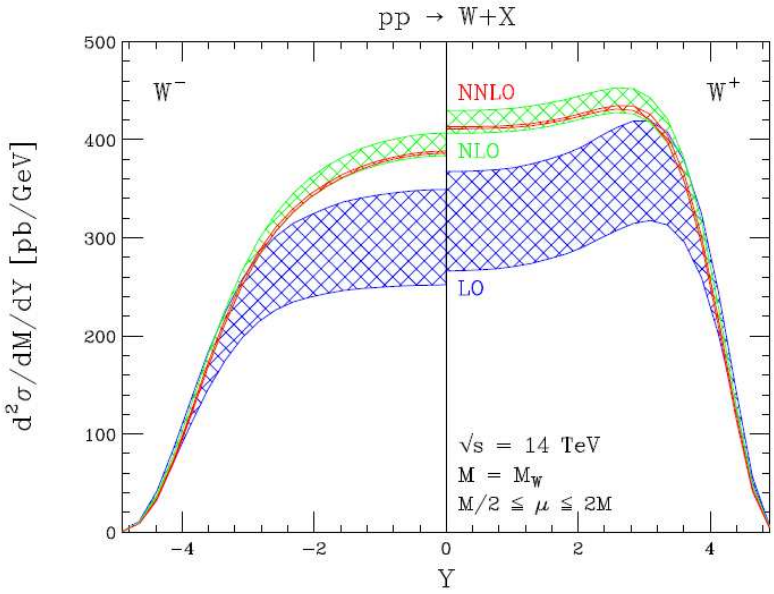

Figure 5.5: *Rapidity distribution of an on-shell W^- boson (left) and W^+ boson (right) at the LHC for LO, NLO and NNLO QCD predictions with PDF set MRST (14 TeV).*

hence they cannot be neglected when comparing with data at these energies.

5.4 Radiative EW corrections

Although QED bremsstrahlung in particle decays is one of the most elementary effects in quantum mechanics, it is not usually considered explicitly; in fact, it is only the case of a few specific decay channels, where exact fixed-order ($\mathcal{O}(\alpha^2)$) fully-differential formulae, with spin amplitudes or matrix elements squared, are available in analytical, semi-analytical or Monte-Carlo form. Nonetheless, in the analysis of the experimental data, radiative corrections are usually treated together with the detector effects (*e.g.,* conversion, detector efficiency) to form the "QED-subtracted" data. This problem does not seem to be so evident for "discovery" experiments; usually the effects of radiative corrections do not exceed a few per cent. However, for high-precision measurements, good control of the radiative corrections becomes vital not only for the assessment of the overall experimental error of the respective cross-sections or branching ratios, but also for the shapes of the distributions. The effects of radiative corrections gradually became an important topic in the context of such measurements as high-precision determination of W-boson properties or B, D, K meson decays for measurements of CKM-matrix coefficients in B-physics. With increasing statistics of available experimental data, QED radiative corrections

have become a significant element in the systematic error of the measured quantities.
The omission of EW radiative corrections in the comparison of predictions with data could fake signals of non-standard physics. For example, effects of non-standard weak gauge boson self-coupling can be similar in size and shape to the effects of the EW corrections, and, thus, non including the latter could be mistaken as signals of new physics. Consequently, in recent years, a lot of theoretical effort has gone into improving the predictions for the gauge bosons production processes in order to match (or better exceed) the experimental accuracy. A realistic phenomenological study and data analysis require then the inclusion of the relevant radiative corrections and their implementations into Monte Carlo event generators, through the QED parton shower, for example, in order to simulate all experimental cuts and to allow, for instance, an accurate determination of detector acceptance (Section 5.5).
The importance of fully understand and control EW radiative corrections to precise measurements of W and Z boson observables at hadron collider is illustrated in Table 5.1 on the example of W mass and width measurements. It demonstrates how theoretical progress is driven by improvements in the experimental precision.

Theory includes:	**Effects on osservable**	**Experimental precision**
final-state QED (approx)	shift in M_W -65 ± 20 MeV ($W \to e\nu$) -168 ± 20 MeV ($W \to \mu\nu$)	Tevatron Run I: $\delta M_W^{exp} = 59$ MeV $\delta\Gamma_W^{exp} = 87$ MeV
full EW $\mathcal{O}(\alpha)$ corrections to resonant W production (pole approx)	shift in M_W (0.1%)	Tevatron Run II: $\delta M_W^{exp} = 27$ MeV
full EW $\mathcal{O}(\alpha)$ corrections	affects distrib. high Q^2, direct Γ_W measurement shift in $\Gamma_W \sim 7$ MeV	Tevatron Run II: $\delta\Gamma_W^{exp} = 25 - 30$ MeV
multiple final-state photon radiation	shift in M_W 2(10)MeV in $e(\mu)$ case	LHC: $\delta M_W^{exp} = 15$ MeV

Table 5.1: *Impact of EW radiative corrections on W boson observables, in particular M_W and Γ_W extracted from the $M_T(W)$ distribution, compared with present and anticipated experimental accuracies.*

Hence, W and Z boson observables are strongly affected by EW corrections, and their main characteristics can be summarized as follows:

- Photon radiation off the final state charged lepton can considerably distort kinematic distributions and usually makes up the bulk of the effects

of EW corrections. For istance, W and Z boson masses extracted respectively from the tranverse masses and invariant mass ditributions of the final-state lepton pair are shifted by $\mathcal{O}(100)$ MeV due to the final-state photon radiation. This is due to the occurence of mass singular logarithms (Sudakov logarithms) of the form $\alpha\ log(Q^2/m_l^2)$ (Q is a typical energy of the scattering process) that arise when a soft photon is emitted collinear to the charged lepton. Because of their numerical importance at one-loop, the higher-order effects of multiple final-state photon radiation have to be under good theoretical control as well. These logarithms give rise to a large negative corrections in exclusive cross sections.

- At high energies, *i.e.,* in the tails of kinematic distributions, $M_T(l\nu) \gg M_W$, Sudakov-like contributions of the term $\alpha\ log^2(Q^2/M_V^2)$ ($M_V = M_{W,Z}$) are important. Their relevance grows for large invariant mass of the final state lepton pair, while they are almost negligible at the W resonance, hence these effects will become strongly visible in the tails of the distributions.

The $\mathcal{O}(\alpha)$ corrections include the contribution of real and virtual corrections, and they are shown in Figure 5.8. The virtual amplitude includes two contributions, namely the one-loop renormalization of the tree-level amplitude and the virtual one-loop diagrams. The real radiative corrections to the charged Drell-Yan process, are given by all the Feynman diagrams (Figure 5.8, bottom) with the emission of one extra photon, from all the electrically charged legs of the Born diagram, including the internal W boson. The $\mathcal{O}(\alpha)$ EW radiative corrections to the resonant single-W production and decay can be divided in a gauge-invariant way into the Initial-State Radiation corrections (ISR), and the Final-State Radiation corrections (FSR). The leading ISR (mass-singular) QED corrections can be absorbed in the parton distribution functions, in a way similar to the leading QCD corrections. In general, the EW-ISR corrections have a rather minor effect on the single-W observables at hadron colliders. The non-factorizable corrections are negligible in resonant W-boson production. On the contrary, the FSR corrections affect various W observables considerably as it will be shown later.

`HORACE` (Higher Order RAdiative CorrEctions) [75] is a Monte Carlo generator for precision simulations of charged-current and neutral-current Drell-Yan processes $pp \to W \to l\nu$ and $pp \to Z \to ll$ ($l = e, \mu$) at hadron colliders. In its original version `HORACE` is based on a pure QED parton shower approach to account for final-state-like QED corrections, both at $\mathcal{O}(\alpha)$ and at higher orders in leading logarihms approximation. Recently `HORACE` has been improved and, in its present version (3.1) it includes the exact $\mathcal{O}(\alpha)$ electroweak corrections to the charged current process and higher order QED contributions in the parton shower approach (initial and final state corrections). In order to avoid double counting of leading logarithmic contributions, already included in

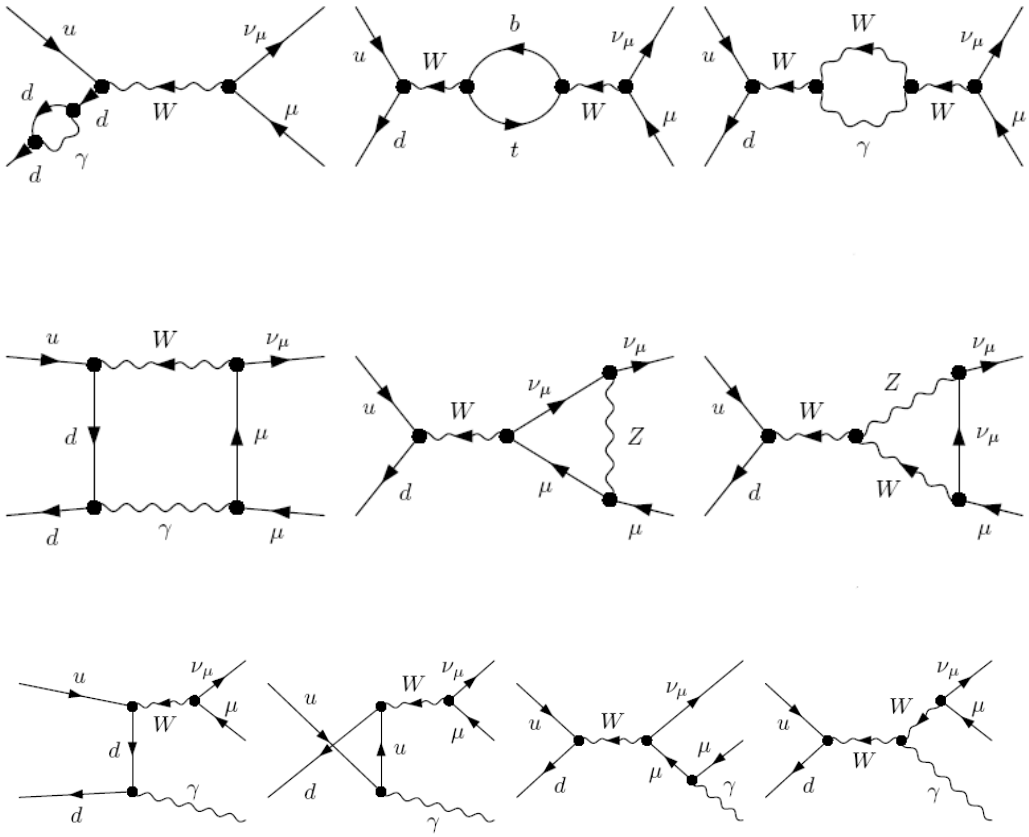

Figure 5.6: *Feyman diagrams of vitual one-loop corrections (electroweak Sudakov logs) (top), and real bremsstrahlung corrections (collinear singularities) (last line).*

the parton shower, a matching procedure between fixed order and resummed calculation has been developed. Hence in HORACE , the exact one-loop EW corrections to the charged current Drell-Yan (CC DY) process are consistently matched with higher-order leading logarithms due to multiple photon emission, that have been shown to be not irrelevant for the precision target of W mass measurements at hadron colliders. HORACE does not include itself any effect due initial-state QCD parton shower, but the events generated with it can be interfaced with standard shower MC programs, like HERWIG or PYTHIA .
Figure 5.7 shows the transverse mass distribution of the W boson as simulated by the HORACE event generator with and without EW corrections; a difference in shape of a few percent is visible, especially in the region of the peak, as is better shown in the right part of the figure for the muon and electron channel. PHOTOS [74] event generator is a specialized final state radiation program which generates, with internal calculated probability, bremsstrahlung photon(s), which are later added to the particles record. Kinematic configurations are appropriately modified, assuring energy-momentum conservation. This

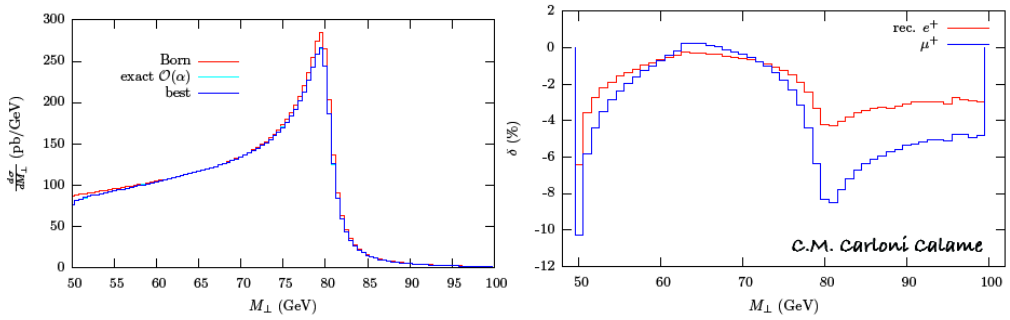

Figure 5.7: *HORACE results of transverse mass distribution for the CC DY process in Born, $\mathcal{O}(\alpha)$ and best approximations (left); relative corrections with respect to the Born cross section due to the exact $\mathcal{O}(\alpha)$ corrections for muons and recombined electrons final states (right). (For more detail see [80].)*

event generator has to be added to the general parton shower ones, like HERWIG or PYTHIA .

5.5 Cross section measurement

In a collider experiment, the total cross section σ_W^{exp} can be measured as:

$$\sigma_W^{exp} \cdot B_r(W \to l\nu) = \frac{N_W^{obs} - N_W^{bkg}}{\int Ldt \cdot A_W \cdot \epsilon_W} \tag{5.5}$$

where N_W^{obs} is the numbers of $W \to l\nu$ candidates observed in the data; N_W^{bkg} is the numbers of expected background events in the W boson candidate samples; A_W is the acceptances of the W decays, defined as the fraction of these decays satisfying the geometrical constraints of the detector and the kinematic constraints of the selection criteria; ϵ_W is the reconstruction efficiency of the signal within the fiducial acceptance and $\int Ldt$ is the integrated luminosity of the data samples. The rescaling of $(N_W^{obs} - N_W^{bkg})$ by $1/(A_W \cdot \epsilon_W)$ allows one to relate the measured quantity (the number of W events) to the relevant W cross section; acceptance and efficiency corrections, in fact, depend from detector characteristics and performances, and provide an estimate of the number of undetected events. While the efficiency can be determined with measurements based on data (with the tag and probe technique as explained later), the value of the acceptance must be determined from Monte Carlo generators. Hence, the theoretical model used by the MC generator has to be as much accurate as possible.
From Eq. 5.5, one can see that the overall measurement uncertainty gets contributions from the different terms as below:

$$\frac{\delta\sigma}{\sigma} = \frac{\delta N \oplus \delta B}{N - B} \oplus \frac{\delta L}{L} \oplus \frac{\delta A}{A} \oplus \frac{\delta \epsilon}{\epsilon} \tag{5.6}$$

Above, $\delta N \sim \sqrt{N}$ is of purely statistical origin, and the relative uncertainty decreases with increasing luminosity following $\delta N/N \sim 1/\sqrt{L}$. The terms δB, δA and $\delta\epsilon$ are of both theoretical and experimental origin. They are considered as systematic uncertainties in the cross-section measurements, but can be constrained via auxiliary measurements. We thus expect these terms to improve over time, provided the auxiliary measurements have statistically dominated uncertainties.

Luminosity

The machine luminosity L will be measured with various methods[2]. The uncertainty on this parameter, δL, is expected to decrease through improved understanding of the LHC beam parameters and of the ATLAS luminosity detector response. Alternatively to the σ_W measurement, the W yield can be used as a standard candle for a luminosity monitor at LHC if one can calculate the theoretical cross section 5.1 and solves:

$$\sigma_W^{th} = \sigma_W^{exp} \tag{5.7}$$

as a function of $\int Ldt$. Of course, this method can be used only if all the others parameters of Eq. 5.5 (background estimation, efficiency and acceptance) are well understood.

Background and event selection

The signature of W$\rightarrow \mu\nu$ events may be hidden by other physics processes. Some processes, in fact, have similar final state event topologies to those of the signal samples and others can fake similar topologies when a non-lepton object within the event is misidentified as a muon. The main background channels for the muonic decay of the W boson can be summarized as:

- Z $\rightarrow \mu\mu$: where one of the muons goes out of detector acceptance and hence mimics missing energy. This process is well understood (in particular with respect to W$\rightarrow \mu\nu$ signal), and can be safely estimated based on simulation.

- QCD background: the main source of energetic muons (p_T>10 GeV) are the decays of *b*-quarks. Muons originating from QCD events appear highly non-isolated in the detector, as they are produced along with many other particles. Hence, this kind of background can be reduced by requiring the isolation of the muon; this isolation can be described by the

[2]At the LHC there are several dedicated experiments for the measurement of instantaneous luminosity, like the ATLAS forward detectors ALPHA and LUCID (Chapter 1).

number of tracks ($\sum N^{ID}$) and the p_T-sum ($\sum p_T^{ID}$) of these tracks within a cone in the η-ϕ plane ($\Delta R = \sqrt{\Delta\eta^2 + \Delta^2}$). For the signal selection is then required to have required a low number of reconstructed tracks within a cone of the candidate muon. In some cases it is also required that the p_T sum of these tracks to be less than a threshold value, usually of 5 GeV.

- Z $\rightarrow \tau\tau$ events in which one of the τ lepton subsequently decays into a muon (or both of them and one is not detected).

- top quark background: the semi-leptonic decay of a top quark pair in the muon channel leads to a W bosons ($t\bar{t}\rightarrow WbWb\rightarrow\mu\nu + j_b + j_W + j_W + j_b$), which decays further into one muon and one neutrino, and four further jets in the final state.

- W $\rightarrow \tau\nu$ events in which τ lepton subsequently decays into a muon.

The last two backgrounds are irreducible because both of them produce W bosons, and have to be estimated by simulated data.
Monte Carlo event simulation, however, can differ substantially from data, especially in the tails of distributions. In order to estimate reliably the remaining backgrounds, a number of data-driven methods has developed and will be used when enough integrated luminosity will be acquired.
The W signal selection criteria are chosen by each analysis group, however, differences on selections are very minor.
In the following, W events are selected as summarized in Table 5.8. The events should contain exactly one muon track candidate, passing the μ20 trigger item (p_T^{μ} >20 GeV) and satisfying $|\eta| < 2.5$. The energy deposited in the calorimeter around the muon track, within a cone of radius ΔR = 0.4, is required to be lower than 5 GeV. The event missing transverse energy should satisfy E_T^{miss}> 25 GeV.

Cut	**Value**
Acceptance	p_T>15 GeV, $\|\eta$<2.5$\|$
Kinematics	p_T>20 GeV, $\|\eta$<2.5$\|$
Isolation	ID cone (0.4), $\sum p_T^{ID}$<5 GeV, $\sum N^{ID}$<6
Trigger	μ20
MET	E_T^{miss}>25 GeV

Table 5.2: *Selection cuts applied in order to select $W \rightarrow \mu\nu$ events over the background.*

The samples used for the analysis (in the AOD format) are the official Atlas Monte Carlo production called "mc08" and generated with `PYTHIA` event generator at centre of mass energy of 10 TeV, with the misaligned detector geometry

that is foreseen for the first data taking period. The number of events processed corresponds to an integrated luminosity of 50 pb^{-1}. The analysis has been performed in the EWPA analysis framework.
Cut flow results for a $W \to \mu\nu$ sample plus background are shown in Figures 5.9 and 5.10. In the first one the number of events passing each applied cut is shown; one can see that at the end of the selection, the signal selection efficiency is 44.8% and that the QCD background is reduced to a level of 1.2%.

Cuts (%)	$W \to \mu\nu$	$Z \to \mu\mu$	$Z \to \tau\tau$	$W \to \tau\nu$	$t\bar{t}$	$BB\mu\mu$
Events	517600	54900	56400	209200	10300	1372868
MCAcc	64.26 ± 0.07	100.000 ± 0.000	100.000 ± 0.000	100.000 ± 0.000	100.000 ± 0.000	100.000 ± 0.000
Comb	61.12 ± 0.07	90.348 ± 0.126	19.667 ± 0.167	32.065 ± 0.102	55.398 ± 0.490	98.945 ± 0.009
Kine	60.74 ± 0.07	77.645 ± 0.178	5.188 ± 0.093	7.946 ± 0.059	34.243 ± 0.468	96.869 ± 0.015
Iso	60.15 ± 0.07	77.293 ± 0.179	5.126 ± 0.093	7.882 ± 0.059	27.990 ± 0.442	15.853 ± 0.031
Trigger	48.63 ± 0.07	68.561 ± 0.198	4.005 ± 0.083	6.123 ± 0.052	22.845 ± 0.414	13.570 ± 0.029
MET	44.83 ± 0.07	17.738 ± 0.163	1.280 ± 0.047	4.627 ± 0.046	20.883 ± 0.401	1.213 ± 0.009

Figure 5.8: *Cut flow analysis results with a sample of W boson plus backgrounds for 50 pb^{-1} of integrated luminosity.*

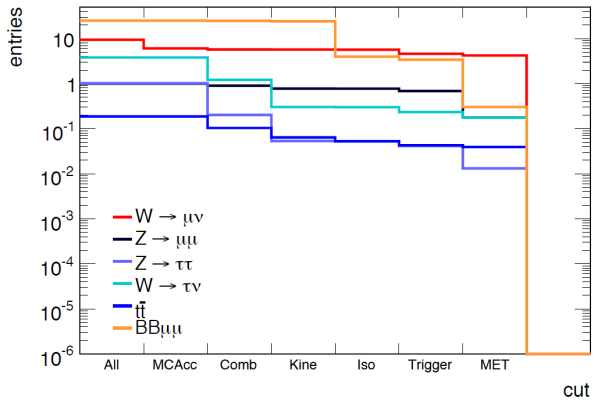

Figure 5.9: *$W \to \mu\nu$ cut flow results for 50 pb^{-1} of W data: background suppression as a function of applied cuts.*

It is worth noticing that the selection cut based on the missing energy will not be used at the beginning of data taking because the calorimeters have still to be calibrated and dead material in front of them can easily mimic missing energy.
In Figure 5.10 the transverse mass distribution of a $W \to \mu\nu$ simulated sample before (left) and after (right) selection cuts it is shown: after the cuts the W signal is well visible over the background.

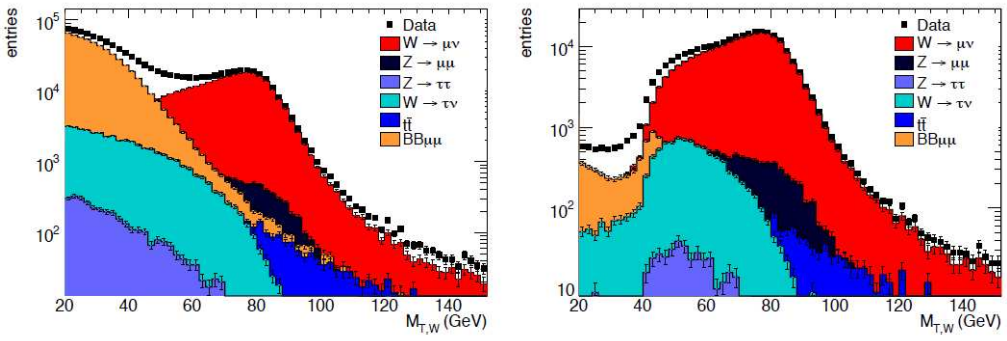

Figure 5.10: *$W \to \mu\nu$ cut flow results for 50 pb^{-1} of W data: M_T distribution for W and main backgrounds, before (left) and after all selection cuts (right).*

Efficiency

In order to determine the muon spectrometer reconstruction efficiencies directly from data, the so-called "tag-and-probe" method can be used, using the $Z \to \mu\mu$ channel. Muons from Z decays will be detected by the inner tracking detector and the muon spectrometer in the common acceptance range of $|\eta|$<2.5. The measurements of the inner detector and the muon spectrometer are independent, though not necessarily uncorrelated. Requirements are: two reconstructed tracks in the inner detector, at least one associated track in the muon spectrometer, and the invariant mass of the two inner-detector tracks to be close to the mass of the Z boson. The last request ensures that the reconstructed tracks are the tracks of the decay muons of the Z boson. Moreover, the two inner tracks have to be isolated to reject possible QCD background. The inner track which could be associated to the track in the muon spectrometer is therefore a muon and is called the tag muon. It is also required that the tag muon fired the 20 GeV single-muon trigger in order to ensure that the event is recorded. The second inner track must then be a muon, too, which is called the probe muon (see Figure 5.11)[3].
The efficiency of a given trigger item is defined as the fraction of the selected events where the second reconstructed muon passed this trigger item. The offline reconstruction efficiency can be calculated in a similar way.
This procedure depends obviously on the Inner Detector reconstruction efficiency, which is however very close to 100%. It has also the advantage to allow for η, ϕ differential analysis of the efficiencies with high precision (Fig. 5.11 right), which can be very useful to spot possible located problems in the trigger and reconstruction system.

[3]The tag-and-probe technique is not restricted to the measurement of the stand-alone reconstruction efficiency. It can, for instance, be used to measure the muon reconstruction efficiency of the inner detector or the trigger efficiency.

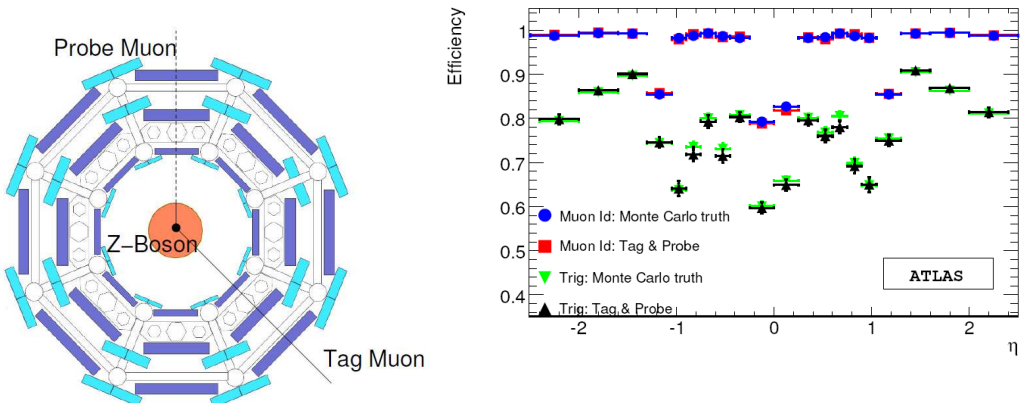

Figure 5.11: *Schematic illustration of the tag and probe method (left); muon detection efficiency vs. η, as estimated from the tag-and-probe method with reconstructed Monte Carlo data and compared to the truth (generated Monte Carlo samples), for 50 pb^{-1} (right). The mu20 trigger efficiency, and the combined muon reconstruction efficiency are also represented, convoluted with the corresponding geometrical acceptance. [69]*

Acceptance

As already seen above, the geometrical and kinematic acceptance has to be calculated from Monte Carlo, by imposing the same cuts on pseudorapidity and transverse momentum (η^0, p_T^0) that are used to select the signal in the analysis. The acceptance is then the ratio between the events that have passed this selection, and the inclusive set of events:

$$A_W = \frac{N_W^{p_T > p_T^0, |\eta| < \eta^0}}{N_W^{inclusive}} \tag{5.8}$$

where N is the number of events from the Monte Carlo generator. In this way the acceptance is strongly dependent on the phase-space distribution of the sample and its decay products, and hence it strongly depends from the theoretical model that has been used to generate the sample. The theoretical predictions for the acceptance, in fact, are based on different models, describing different aspects of the theoretical understanding of the proton-proton collisions and the subsequent production and decay of vector boson. Not only the acceptance itself, but also its corresponding theoretical uncertainty depends on the chosen cuts.
The various theoretical models differ for:

- knowledge of the parton density functions (PDFs) of the proton;
- description of the inizial and final state radiation (ISR, FSR);
- uncertainties due to higher order radiation;

- description of the intrinsic k_T in the colliding protons;
- QCD matrix element corrections to the Born-level process;
- QED and electroweak corrections;
- modelling of hadronization;
- modelling of multiple interactions.

Total cross-section measurements are hence dominated by the systematic uncertainty even for modest integrated luminosity. The main cross-section uncertainty is related to the acceptance one, which in turn comes from our limited knowledge of the underlying physics (notably non-perturbative mechanisms and PDFs). It is therefore important to measure the W boson observable distributions, which will help to constrain these uncertainties.
In the following the effect on muon observables, and hence on the acceptance calculation, of the electroweak corrections will be analyzed in detail.

5.6 EW effects to W boson observables

Conventions and notations

Event generations have been performed inside the Athena framework by means of dedicated interfaces to Monte Carlo algorithms, which are part of the official ATLAS software. All numerical results are obtained using the values for input parameters reported in Table 5.3.

Par.	Value	Par.	Value	Par.	Value
α	1/128	G_μ	$1.16637 \times 10^{-5}\text{GeV}^{-2}$	$sin^2\theta_W$	$1 - m_W^2/m_Z^2$
Λ_{QCD}	0.18 GeV	m_Z	91.19 GeV	m_W	80.425 GeV
Γ_Z	2.495 GeV	Γ_W	2.141 GeV	m_H	115 GeV
m_e	510.99892 KeV	m_μ	105.658369 MeV	m_τ	1.77699 GeV
m_u	320 MeV	m_c	1.55 GeV	m_t	174.3 GeV
m_d	320 MeV	m_s	500 MeV	m_b	4.95 MeV
V_{ud}^2	0.9512	V_{us}^2	0.0493	V_{ub}^2	0
V_{cd}^2	0.0488	V_{cs}^2	0.951	V_{cb}^2	0
V_{td}^2	0	V_{ts}^2	0	V_{tb}^2	1

Table 5.3: *Input parameters used in analysis.*

The particular choice of the SM model input parameters has an impact on the predicted physics observables. This schema dependence is induced by the truncation of the perturbative expansion, which is formally of higher order, but which can be numerically relevant, while it would be absent only if the calculation is ideally resummed up to all orders. Two different schemes are adopted to calculate the EW corrections: the $\alpha(0)$, which has a proper coupling α for the emission of real photons and parameterize the charged current coupling $g = \sqrt{4\pi\alpha}/sin\theta_W$; and the G_μ-scheme, *i.e.,* parameterizing the cross section by the Fermi constant G_μ instead of the fine-structure constant α:

$$\alpha = \frac{e^2}{4\pi} \rightarrow \alpha_{G\mu} = \frac{\sqrt{2}G_\mu m_W^2 sin^2\theta_W}{\pi} \tag{5.9}$$

In this case the weak coupling g is related to the Fermi constant and to the W boson mass by the relation:

$$\frac{G_\mu}{\sqrt{2}} = \frac{g^2}{8m_W^2}(1 + \Delta r) \tag{5.10}$$

where Δr represents all the radiative corrections to the muon decay amplitude. In the analysis performed the G_μ schema it is used. The $\alpha(0)$ one is used only to compare the cross section predictions between the two approaches.
The events have first been generated with `HORACE` (version 3.1) in stand-alone; then they were given as input to `HERWIG` (version 6.510) for the QCD parton

shower in the ATLAS Athena framework[4]. After this step events were passed through the ATLAS simulation chain: simulation with ATLFAST-II (see Chapter 4), digitization and reconstruction and the output was produced in the AOD data format. As reconstructed muons, the muon combined ones have been analyzed. In order to perform these steps the official ATLAS jobs transform has been used[5]. AOD pool files are then processed by the EWPA analysis framework which creates lighter D3PD objects that are analyzed by ROOT macros. All these described steps required large amount of CPU time, which is only available via Grid computing. The jobs were then run on the LHC Computing Grid, and the tasks were submitted and managed by the Ganga [97] toolkit.
In order to evaluate the EW corrections introduced by HORACE, two sets of data are compared: the Born data (HORACE Born) and NLO(α) (HORACE at the higher order of EW corrections).
The relative difference (δ_j) of two compared osservables (j), or their differential cross sections ($d\sigma/dj$), is useful to quantify the amount of EW correction:

$$\delta_j = \frac{d\sigma/dj(NLO(\alpha)) - d\sigma/dj(Born)}{d\sigma/dj(Born)} \tag{5.11}$$

In Table 5.4 main HORACE parameters that have been used, and their meaning, are reported.

Value	**Meaning**
new	exact $\mathcal{O}(\alpha)$ EW corrections matched with higher orders QED
Born(exp)	order of radiative corrections
2212	initial state hadrons: 2212 protons
2	PDF set in HORACE (CTEQ6L1)
10000	centre of mass energy (GeV)
W+andW-	boson Drell-Yan production
1 (0)	EW input scheme (G_μ, α)
muon	final state lepton
10	maximum lepton rapidity
0.1	minimum lepton p_T(GeV)
0.1	minimum missing p_T (GeV)

Table 5.4: *Main HORACE parameters used for the event generation.*

[4]In order to do this step the ATLAS official python script *jobOptions.Herwig.AtlasHorace.py* has been used [98].

[5]The used job transform is the*: csc_simul_reco_trf.py* that can perform all the simulation chain in one step, the ATLAS release used is the 14.2.85. The detector geometry that has been used (ATLAS-GEO-02-01-00) is more realistic as possible, and takes in account also possible inefficiencies of the detector as in the beginning of data taking.

Born-level tuning

In order to compute reliable comparisons between theoretical calculations characterized by corrections of different order and type, the first step consists in a fine tuning of the generators input parameter. The common starting point is represented by the Born approximation: here calculations are simple, if compared with higher orders, and thus predictions from different Monte Carlos can be easily checked. The level of accuracy to be reached is dictated by the precision needed in the overall analysis. The observation of NLO EW effects at the percent level therefore implies an agreement <1% for the Born cross section prediction. The Born level tuning has been performed between HERWIG [6] and HORACE stand-alone (with the G_μ EW schema) and the best tuned resulting cross sections are reported in Table 5.5. σ^W_{incl} reperesents the inclusive cross section with no selectrion cuts, and σ^W_{lf}, where "lf" stands for "lepton filter", with selection cuts of $|\eta|$<2.8 and p_T>5 GeV. The agreement observed is at the level of per mille[7].

Event generator	σ^W_{incl} (pb)	σ^W_{lf} (pb)
HERWIG (ISR, softme, hardme) ≡ false	11894 ± 12	8774 ± 10
HORACE (Born, G_μ schema)	11896 ± 11	8702 ± 8

Table 5.5: *The best cross section obtained after the tuning of the HORACE (stand-alone) and HERWIG (in the Athena framework) at the Born level. Values were obtained averaging 5·10^5 events.*

In Figure 5.12 the comparison between transverse momentum, transverse mass and pseudorapidity of muons emitted by the Drell-Yan process at the Born level are shown. In black are distributions of HERWIG , and in green the ones of HORACE with HERWIG parton shower. The shape of every distributions is well tuned between the two event generators.
In order to reach the goal to have better than 1% of difference between the cross sections (both inclusive and with lepton filter), many parameters of HERWIG have been investigated, in particular the effect of the ISR radiation, and the matrix elements[8].
Adding PHOTOS event generator to HERWIG does not change the cross sections, in fact, this generator it is added after the event is already created by others parton shower generators.
From the comparison of cross section values, both inclusive and with selection

[6] In order to have the leading-order QCD parton shower, the QCD initial state radiation, together with matrix elements have been kept off.

[7] In HORACE the value of the electromagnetic coupling constant α has been tuned (improved Born approximation) to properly take into account the running of the coupling costant implemented in HERWIG .

[8] One of the features of HERWIG 6 is the matching of first-order matrix elements with parton showers through the two parameters "soft-me" and "hard-me".

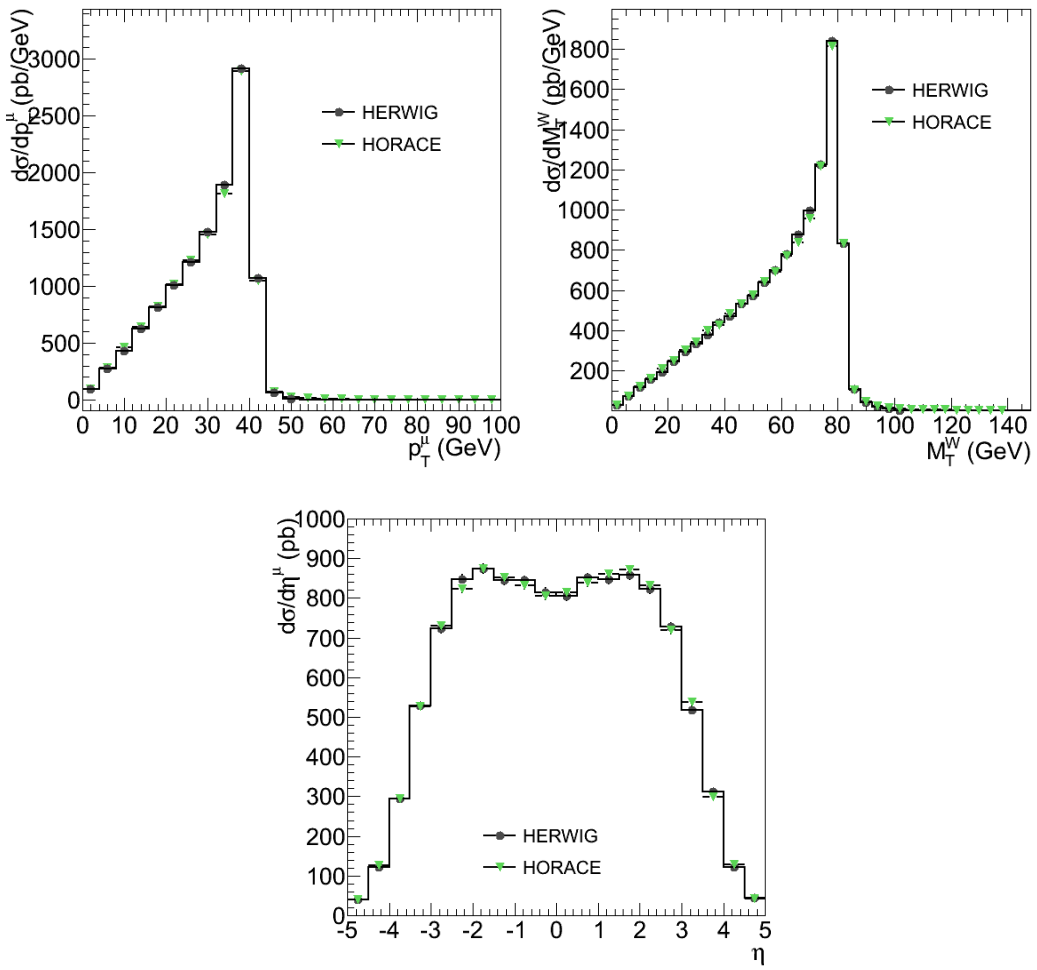

Figure 5.12: *Comparison between transverse momentum, transverse mass and pseudorapidity of muons emitted by the Drell-Yan process at the Born level with* **HERWIG** *(black) and* **HORACE** *with* **HERWIG** *parton shower.*

ISR	**hard-me**	**soft-me**	σ^W_{incl} (pb)	σ^W_{lf} (pb)
TRUE	FALSE	FALSE	11933 ± 11	8847 ± 8
FALSE	FALSE	FALSE	11894 ± 12	8774 ± 8
TRUE	TRUE	FALSE	11787 ± 10	8699 ± 7
TRUE	FALSE	TRUE	11801 ± 12	8307 ± 9

Table 5.6: *Comparison of inclusive (inc) and with lepton filter (lf) cross sections of $W^\pm \to \mu\nu$ enabling different* **HERWIG** *parameters: ISR (parameter "nospac"), hard-martix-element ("hardme") and soft-matrix-element ("softme").*

cuts, obtained with HORACE stand-alone (Tab 5.5) and with HERWIG stand-alone (Tab 5.6), the best agreement is obtained with ISR, and matrix elements off.

However, a more realistic description of the process is described with the Initial State Radiation included (first line of Tab. 5.6). Hence, we have evaluated the effects of it on muons and photons observables.

Evaluation of the effects of QCD ISR on photon observables

The effect of the QCD Initial State Radiation introduced by `HERWIG` has been studied on the photon observables. Two samples of events generated with `HORACE` with EW corrections and convoluted with `HERWIG`, both enabling or disabling the ISR effect, have been compared.
In Figure 5.13 the effects of the ISR is displayed on the differential cross section $d\sigma/dp_T$ of the photons. Even if the distributions of all emitted photons are quite different, selecting only photons coming from the EW process (as described in Section 5.7.4), the p_T distributions are very similar (Figure 5.13 right).

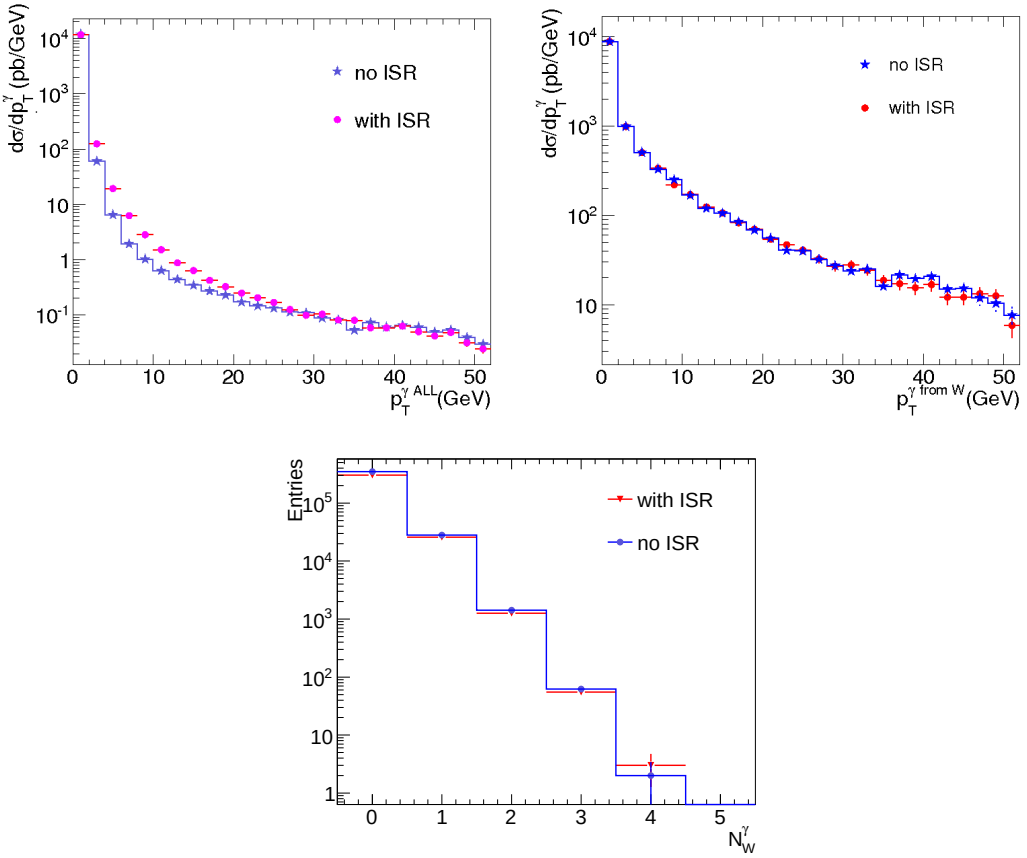

Figure 5.13: *Transverse momentum of total generated photons (left) with and without QCD ISR enabled in* ***HERWIG*** *, and selecting photons created after the W decay (right). Bottom plot: number of photons created after the W decay with, and without ISR enabled.*

Initial state radiation doesn't affect also the distributions of the number of

photons emitted after the W decay, as is shown in Figure 5.13 bottom.

Evaluation of the effects of QCD ISR on muon observables

The evaluation of the effects of the QCD ISR has been studied also on the muon observables. In Figure 5.14 the difference in azimuthal angle ($\Delta\phi$) between the muon and the neutrino produced by the W decay is shown. In the case of disabled ISR the two final leptons are back to back in ϕ, in fact the $\Delta\phi$ distribution has a peak at $\Delta\phi{=}\pi$. Enabling the initial state radiation the effect is that the two colliding partons gain transverse momentum, and hence the $\Delta\phi$ distribution is broader. This effect can also be seen in the p_T distribution (Figure 5.15), while the W transverse mass seems not to be too much affected by this effect (as explained in Section 5.2.2).

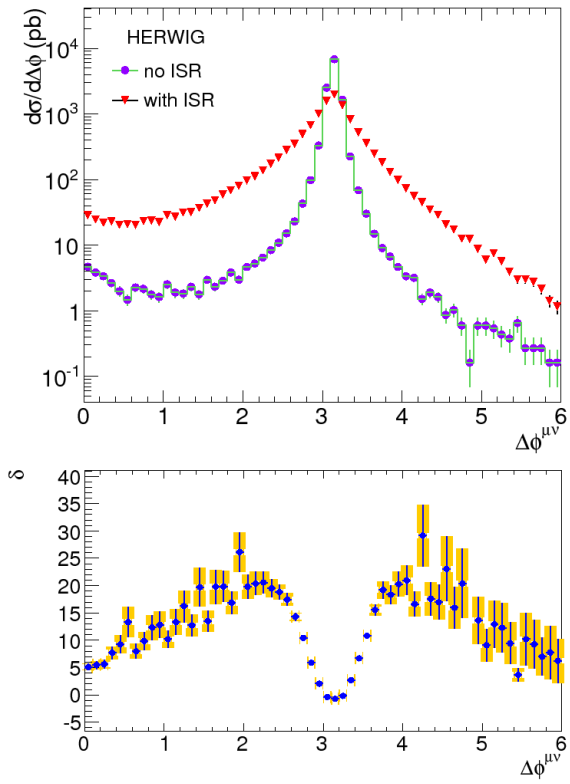

Figure 5.14: *Difference in azimuthal angle ϕ between μ and ν from $W^{\pm}$ decay; events have been simulated with (red triangles) and without (violet dots) QCD ISR enabled in* ***HERWIG****.*

Given the little difference, in particular on the photons distributions, and due to the fact that including ISR effects gives a more realistic description of *p-p* collisions, for the following analysis we have decided to use the `HERWIG` generator with ISR effects included.

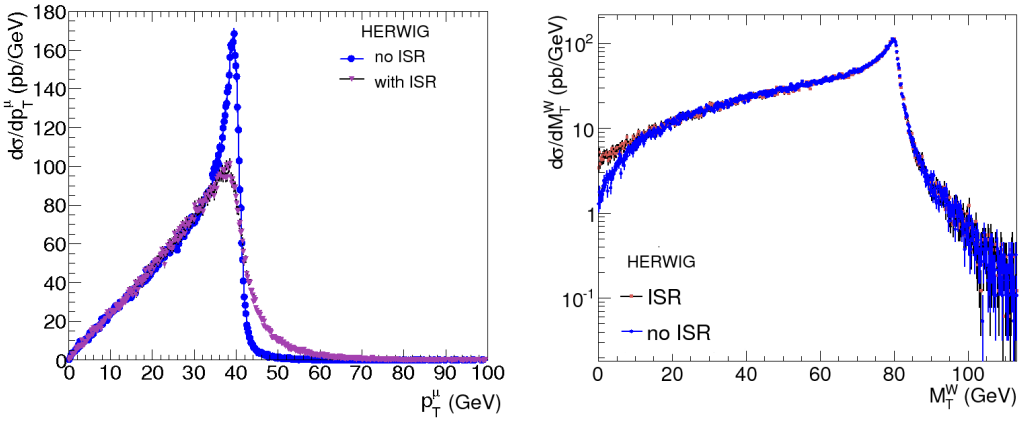

Figure 5.15: *Effects of the QCD ISR (enabled in* ***HERWIG*** *) on the muon transverse momentum (left) and the W transverse mass (right).*

5.7 Evaluation of EW effects

5.7.1 Generated events

The inclusive cross section values obtained generating events with HORACE stand-alone in the Born approximation and including complete NLO correction matched with the QED PS are summarized in Table 5.7. Two schemas for calculation of EW corrections: $\alpha(0)$ and G_μ have been used for the HORACE generator.

Schema	EW Correction	$\sigma_{inc}^W(pb)$
$\alpha(0)$	BORN	12709 $\pm$30
$\alpha(0)$	NLO(α)	13788 $\pm$40
G_μ	BORN	11882 $\pm$28
G_μ	NLO(α)	12290 $\pm$35

Table 5.7: *Inclusive cross sections of* $W^\pm \to \mu\nu$ *using the two different schemas.*

All the following analysis on the evaluation of EW effects has been done with a sample of $3\cdot 10^5$ events, that corresponds about to 25 pb^{-1} of integrated luminosity. Accordingly to the present schedule of LHC, this statistics, at centre of mass of 10 TeV, should be reached before the long LHC shut-down. From the Table 5.7 it can be seen that, between the cross sections calculated at the Born level and using the best approximation of the EW effects (NLO(α)), there is an effect at a level of 8.4% for the $\alpha(0)$ schema and of 3.4% for the G_μ one. This cross section growth is clearly visible in the pseudorapidity differential distributions of muon generated with these theoretical calculations (Figure 5.18).

The results reported above are calculated in HORACE stand-alone; when this

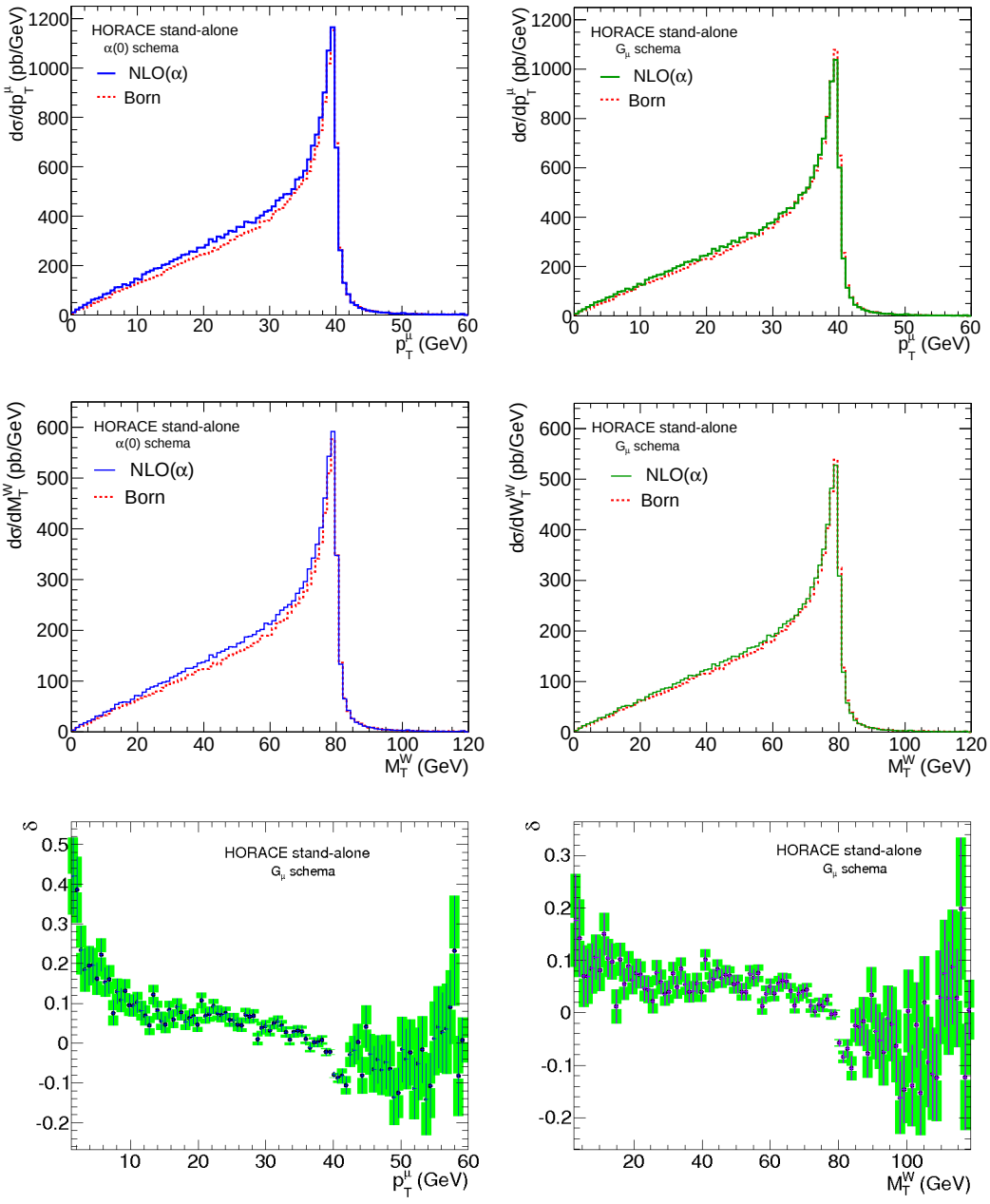

Figure 5.16: *Comparison between transverse momentum and transverse mass distributions of the muons coming from the $W^{\pm}\to\mu\nu$ decay using* ***HORACE*** *in stand-alone at Born level and with EW corrections in the $\alpha(0)$ schema (left) and the G_μ one (right). Bottom plots: Relative difference for p_T distributions and M_T between the Born and EW corrected (G_μ schema) process in* ***HORACE*** *stand-alone.*

events are also convoluted with the QCD parton shower of HERWIG this difference is less evident, but it is still visible. In Figure 5.17 the differential cross section as a function of the muon p_T and of the W transverse mass are shown with and without the EW effects. In the figures on the left, results with the $\alpha(0)$ schema are shown, while at the right the same distributions, but with the G_μ schema, are reported.

In Figure 5.17 (bottom plots) the relative difference, as defined by Equation 5.6, of the differential cross sections between the Born process and including EW effects with the G_μ schema are shown. It is possible to notice that the average value of this difference is at 3% level, as it is on the cross section, but it is not uniformly distributed on the phase space.

In Figure 5.18 the differential cross section as a function of the muon pseudorapidity is shown for both the EW input schema.

As it is shown in Table 5.7, the Born cross section using the $\alpha(0)$ schema is far away from the one obtained from HERWIG (11894 pb). Hence, as also suggested by the authors of HORACE, it was decided to use the G_μ for the following analysis.

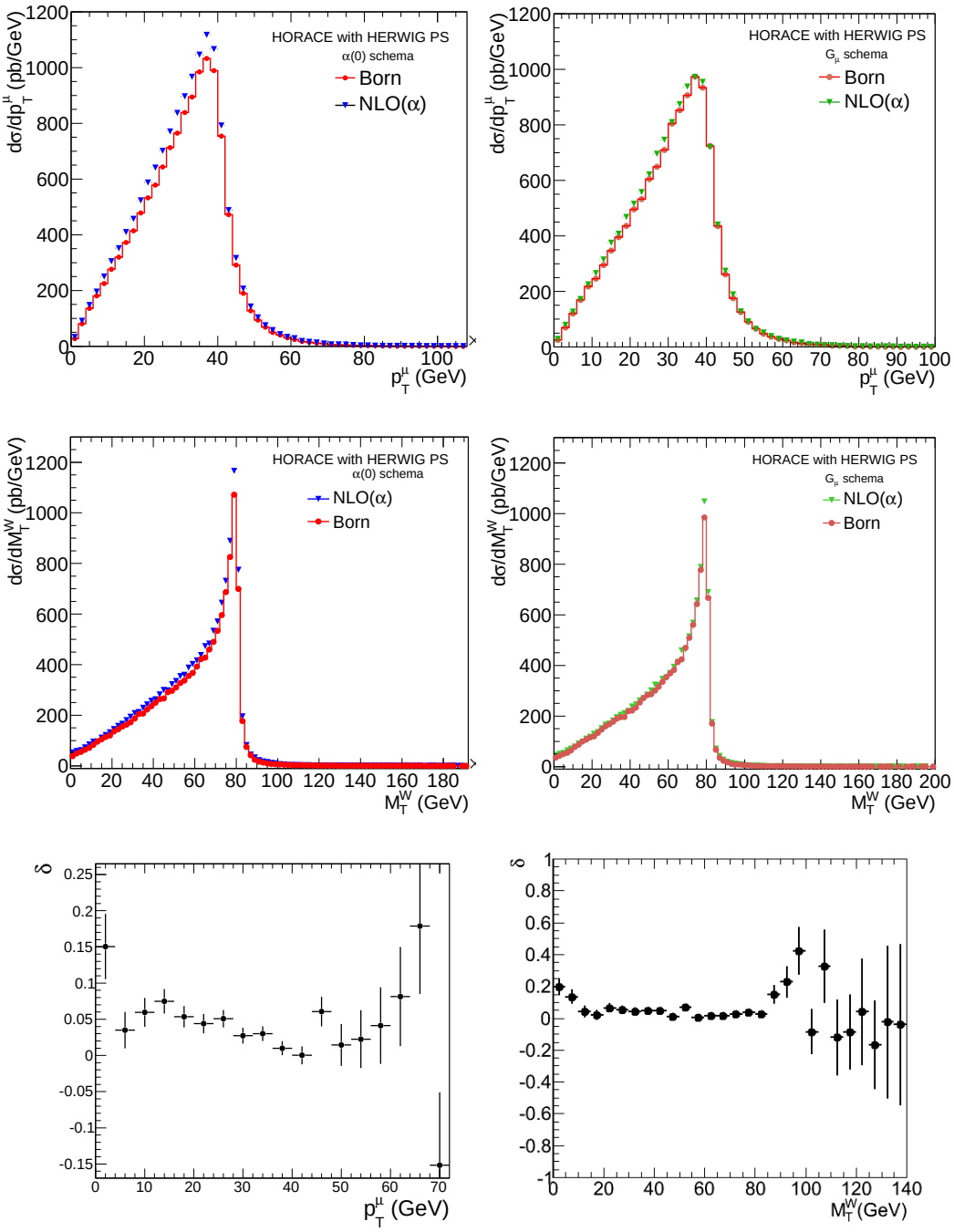

Figure 5.17: *Transverse momentum of the muon from the decay of $W^{\pm}$ (left) and transverse mass of $W^{\pm}$ at the Born level and with EW correction in the $\alpha(0)$ (left) and G_{μ} (right) schema of* ***HORACE*** *with the* ***HERWIG*** *parton shower. Bottom plots: relative difference for p_T distributions (left) and M_T ones (right).*

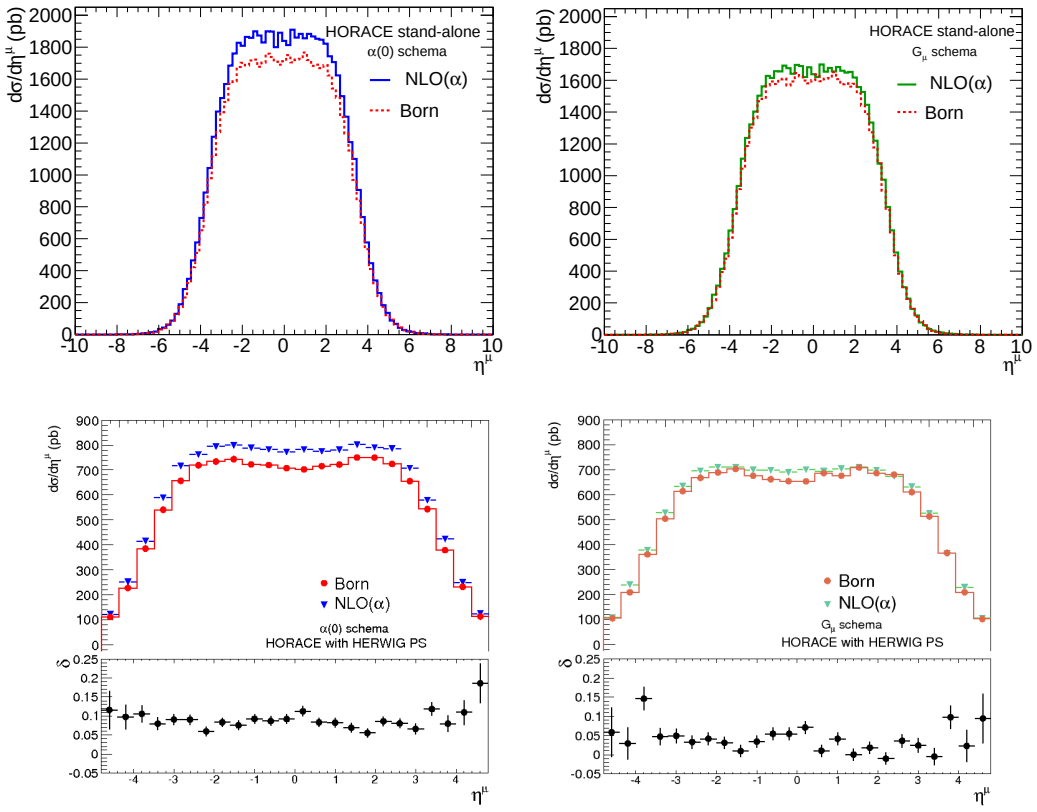

Figure 5.18: *Pseudorapidity distribution of muons from $W^{\pm}$ decay at the Born level and with EW correction in the $\alpha(0)$ schema (left) and the G_{μ} one (right) in* ***HORACE*** *stand-alone (top) and in* ***HORACE*** *with* ***HERWIG*** *parton shower (bottom).*

5.7.2 Reconstructed data

In order to evaluate the effects of electroweak corrections on the calculation of the geometrical and kinematic acceptances, the effects of limited detector coverage and the ones introduced by the detector resolution on the reconstruction of the W observable distributions have been investigated. The samples described above have been simulated in ATLAS with the `ATLFAST-II` simulation (see. Chapter 4). Events have been afterwards reconstructed through the offline reconstruction chain.
In Figure 5.19 the differential distribution as a function of the pseudorapidity of reconstructed muons is shown for both the Born and the EW corrected data. In the bottom figure the relative difference is also shown. From the figure it is evident the effect of the geometrical acceptance of the detector, which reconstructs muons only for $|\eta|<2.7$ and has some inefficient regions like the one at $\eta=0$ between A and C side of the spectrometer, and the one at $|\eta| \sim 1.3$ that is the transition region between the barrel and the end-caps. However, it is also possible to see that the EW effects are still visible after the reconstruction.

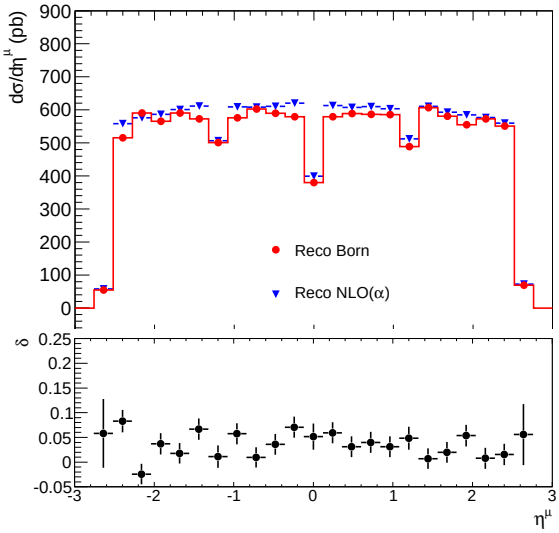

Figure 5.19: *Differential cross section as a function of pseudorapidity of reconstructed muons, at the Born level (red dots) and with EW corrections (blue triangles).*

In Figure 5.20 the reconstructed p_T and M_T distributions for the Born and the EW effects corrections are shown. The difference between generated (Fig. 5.17) and reconstructed distributions is that the jacobian peak is smeared by the intrinsic detector resolution.

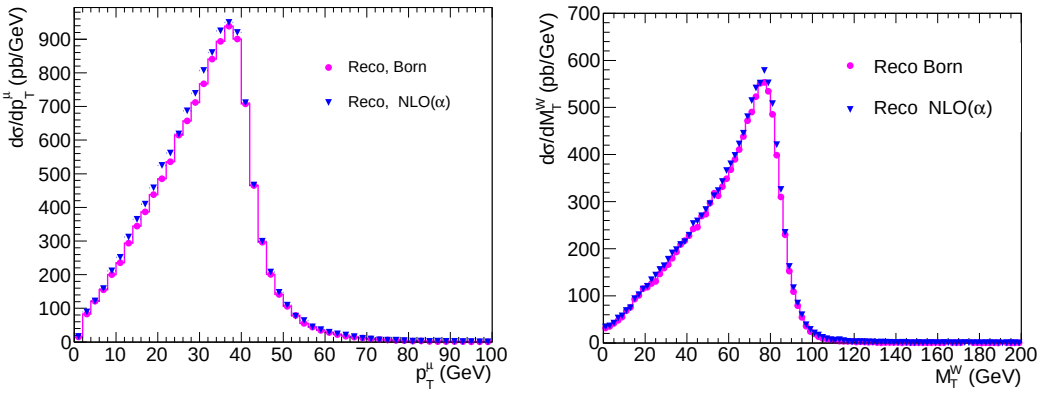

Figure 5.20: *p_T (left) and M_T (right) reconstructed distributions with and without EW effects.*

The relative difference (Fig. 5.21) shows that the effects of electroweak corrections are not hidden by the experimental resolution, and that the trend is almost the same for generated and reconstructed events.

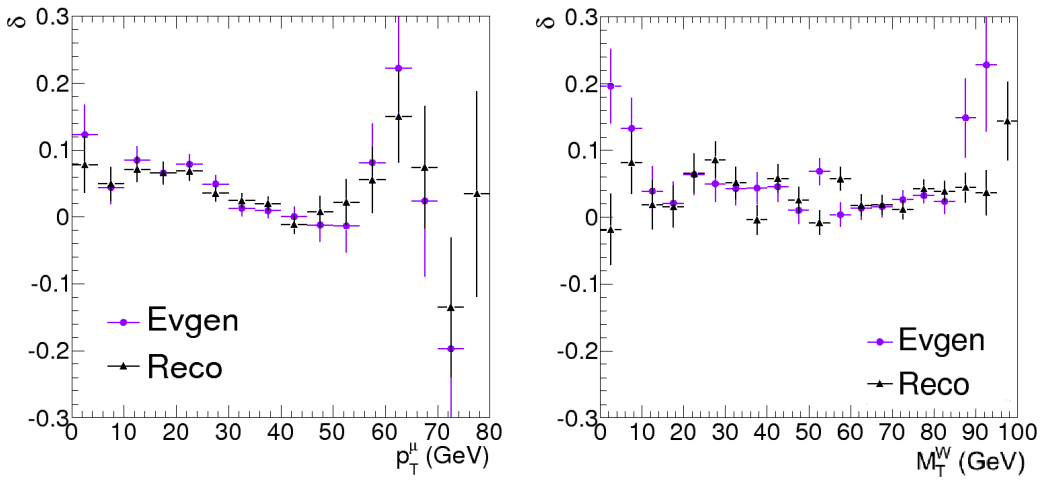

Figure 5.21: *Comparison between relative difference of differential cross sections for generated events (violet dots) and reconstructed ones (black triangles).*

5.7.3 Analysis of EW corrections on acceptances

The acceptance for the W boson (A_W) as a function of the minimum muon momentum ($p_T^\mu(min)$) and the maximum pseudorapidity $\eta^\mu(max)$ reachable with the detector are defined as:

$$A_W(p_T^\mu(min)) = \frac{1}{\sigma_{tot}} \int_{p_T^\mu(min)}^{\sqrt{s}/2} dp_T^\mu \frac{d\sigma}{dp_T^\mu} \tag{5.12}$$

$$A_W(\eta_W(max)) = \frac{1}{\sigma_{tot}} \int_0^{\eta^\mu(max)} d|\eta^\mu| \frac{d\sigma}{d|\eta^\mu|} \tag{5.13}$$

where no cut is applied on $d\sigma/dp_T$, $d\sigma/d|\eta|$ and σ_{tot} is the total cross section evaluated with the event generator.
The acceptances on muon transverse momentum and pseudorapidity have been firstly calculated without any cuts (Figure 5.22).
The same distributions have been studied applying some selection cuts, summarized in Table 5.8.

Selection cuts
$\eta^\mu < 2.7$
$p_T{}^\mu > 20$ GeV
$E_T^{miss} > 20$ GeV

Table 5.8: *Selection cuts used for acceptance estimation.*

In Figure 5.23 the acceptances with selection cuts are shown. On the plots the relative difference is superposed, to show the effect of EW correction.

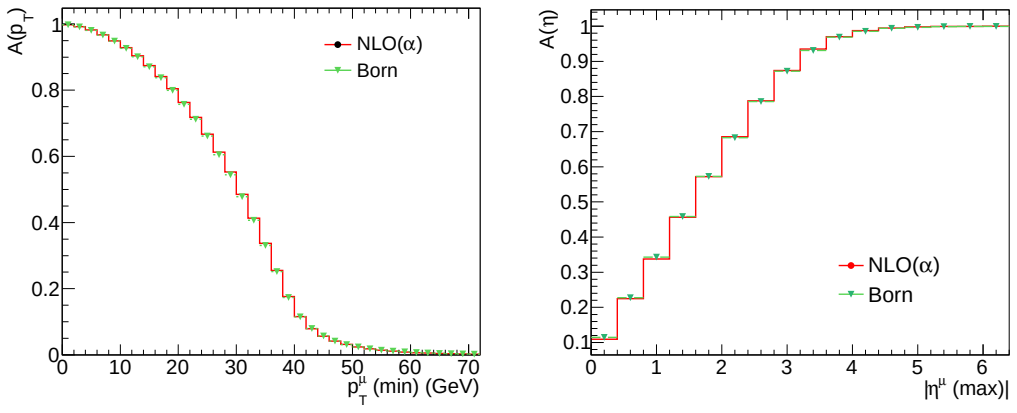

Figure 5.22: *Acceptance as a function of p_T(min) (left) and η(max)(right).*

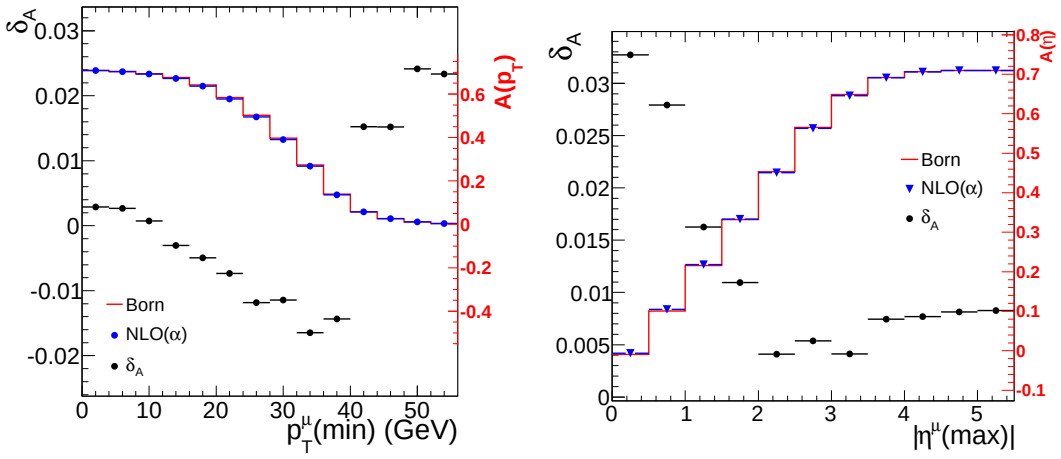

Figure 5.23: *Acceptances (right scale) as a function of p_T (left plot) and η (right plot) calculated with selection cuts. The relative difference between the Born and EW corrections it is also shown (black dots and left scale).*

In Figure 5.24 the comparison of the relative differences on acceptances (including or not the EW corrections) of generated (pink) and reconstructed muons (black) is illustrated. From these plots one can see that the intrinsic detector resolution does not hinder the difference on acceptance; especially on the relative difference of acceptance as a function of p_T it is possible to see a well defined structure that is reproduced by both generated and reconstructed events.
By definition, these quantities are normalized to the cross section and thus they are sensitive only to the difference in shapes of the differential cross sections. In order to be sensitive also to the absolute cross section, the quantity

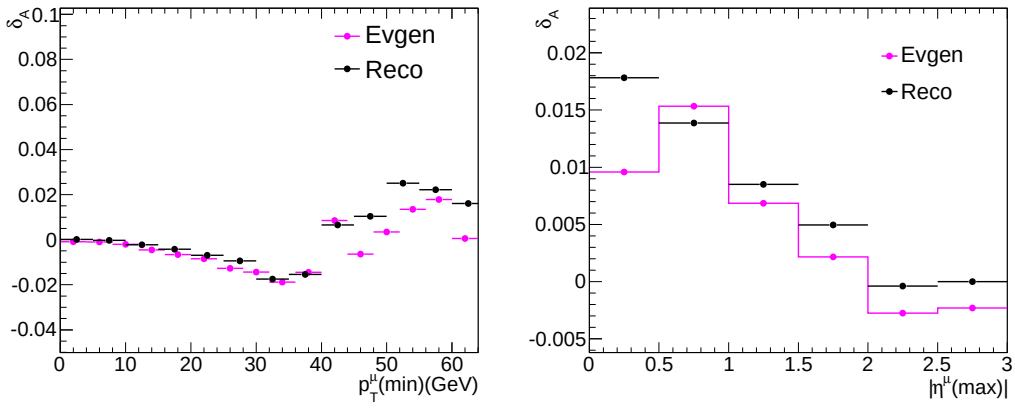

Figure 5.24: *Relative difference between the Born and EW corrections on acceptances for generated events (pink) and reconstructed ones (black).*

Σ_W has been introduced for a generic observable j:

$$\Sigma_W(j_1, j_2) = A_W(j_1, j_2) \times \sigma_{tot} = \int_{j_1}^{j_2} dj \frac{d\sigma}{dj}(cuts) \tag{5.14}$$

where j_1 and j_2 are the limits for each variable imposed by the analysis selection cuts. Σ_W represents the cumulative distribution of the differential cross sections. Comparing the predicted Σ_W it is possible to extract differences related to the cross section or, from a detector point of view, the number of events experimentally seen.

In Figures 5.25 and 5.26 the Σ_W distributions for Born processes and EW

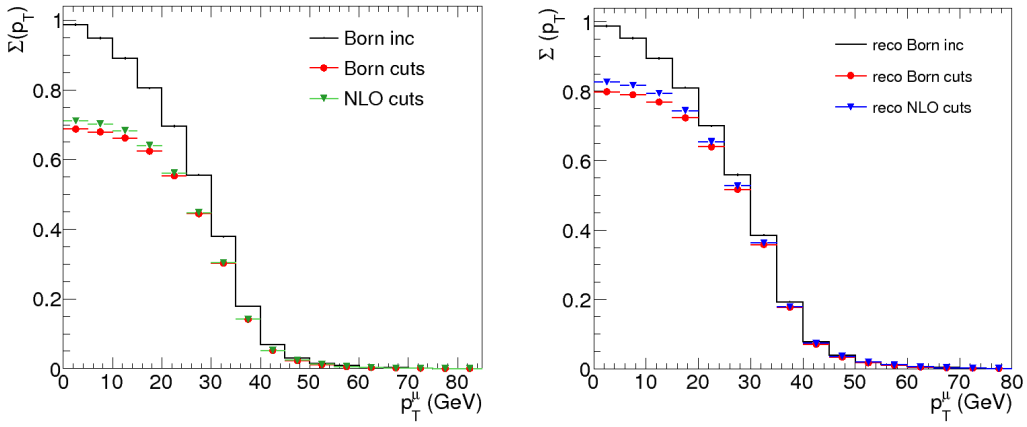

Figure 5.25: *Distribution of the cumulative cross section (Σ_W) with selection cuts, as a function of p_T for generated events (left) and reconstructed ones (right) weighted with the cross sections of the Born level and the EW-corrected processes. The black histograms corresponds to the acceptance with no cuts.*

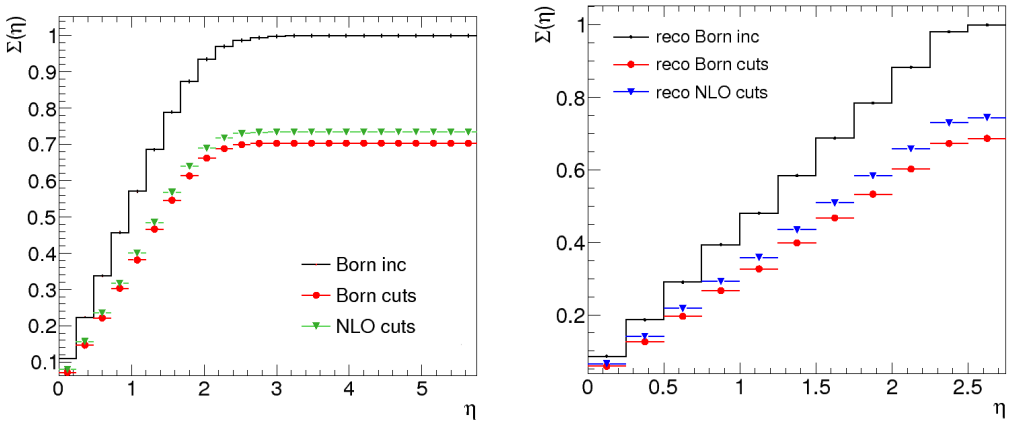

Figure 5.26: *Distribution of the cumulative cross section (Σ_W) with selection cuts, as a function of η for generated events (left) and reconstructed ones (right) weighted with the cross sections of the Born level and the EW-corrected processes. The black histograms corresponds to the acceptance with no cuts.*

corrected ones are compared, both for the generated events (left) and for the reconstructed ones (right). On each plot the value of the calculated acceptance with no cuts is superimposed.

5.7.4 Analysis of EW corrections on photons observables

In order to evaluate the effects of the electroweak corrections, the radiative emission of photons has also been studied. In the HORACE generator multiple photon emissions are taken into account by means of all orders leading-log approximation with the Parton Shower approach.
In Figure 5.27 the distributions of photons in the datasets with the Born process and the one with EW corrections are compared, both at generator level (left) and after the detector simulation and reconstruction (right). Up to $p_T \sim 10$ GeV the two distributions look very similar, while at higher p_T the EW processes dominate. From this figure one can see that photons with transverse momentum higher than 50 GeV should come only from EW radiative effects, and this effect is well visible even after the reconstruction.

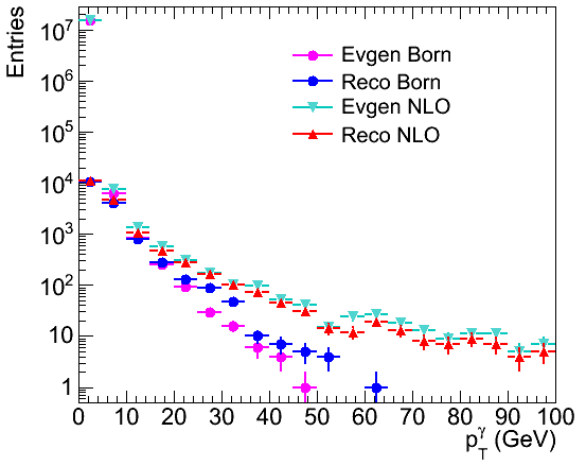

Figure 5.27: *Transverse momentum of photons emitted during the pp collision in evgen and reconstructed data. The spectrum of the process with EW corrections is harder than the Born process where there is only the effect of the underlying event. Even after the reconstruction this effect is well visibe.*

In order to understand the source of such photons (Born Drell-Yan process does not have any photon) the PdgId[9] of particles who generate them, both for the Born process and the one with EW corrections, has been studied. In Figure 5.28 on the left, the overview of the PdgId of particles who generate photons is shown "photons mothers"; the main source of them is from π^0, η^0, ρ^0 coming from the hard process. On the left a zoom is shown, both for the Born sample (top) and for the NLO-EW one (bottom). It is possible to see that in the EW process there are two more entries, corresponding to |PdgId|=24, that is the $W^\pm$ boson[10]. Hence, in order to select only photons produced by

[9]It is a Monte Carlo particle numbering scheme that identify particles with numbers. [99]
[10]Photons, of course, are not created by the W boson itself, by the muons after its decay.

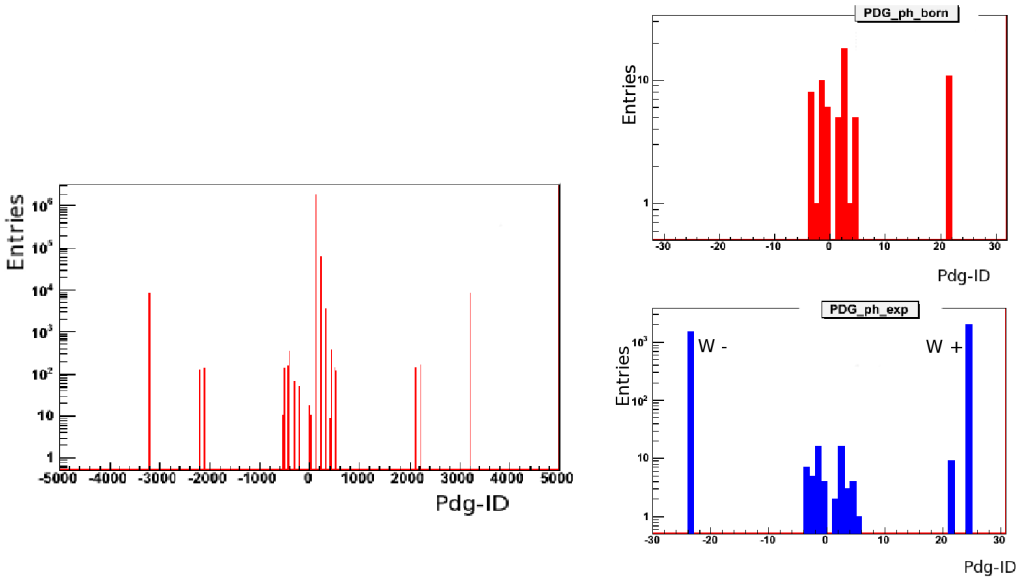

Figure 5.28: *PdgId of particles that create photons in their decay. In the right figures there is a zoom for both Born process (top) and EW process (bottom). PdgId* $= \pm 24$ *corresponds to* $W^{\pm}$ *and this process there is only in the EW corrected sample.*

electroweak corrections, a selection cut on the photon mother has been done.

HORACE versus PHOTOS effects

Relevant observables have been compared between HORACE (with HERWIG) in exponentiated mode and HERWIG plus PHOTOS predictions. Differential cross section distributions of the relevant observables have been investigated, in particular the N-photon emission cross sections ($d\sigma/dN_\gamma$) related to the NLO EW corrections and the p_T of the photons emitted in the process.
In Figure 5.29 (top) the differential cross section as a function pf p_T of emitted photons is shown, in the middle plots the same spectrum is displayed, but separating photon coming from EW corrections (left) and all the others (right). From both these figures one can see a quite good agreement, but the effects introduced by the two generators on the photon distributions are not exactly the same; in particular, HORACE seems to give to the photons from W a tail at higher p_T (even if the statistic here is limited). This effect, given the region of transverse momentum, can be connected to a slightly different infrared cut-off value to regularize γ emissions. Another reason for the difference on the two distributions is that HORACE takes in account also electroweak effects, while PHOTOS has only QED correction.
In Figure 5.29 bottom, the N-photons emission cross section inclusive (left) and

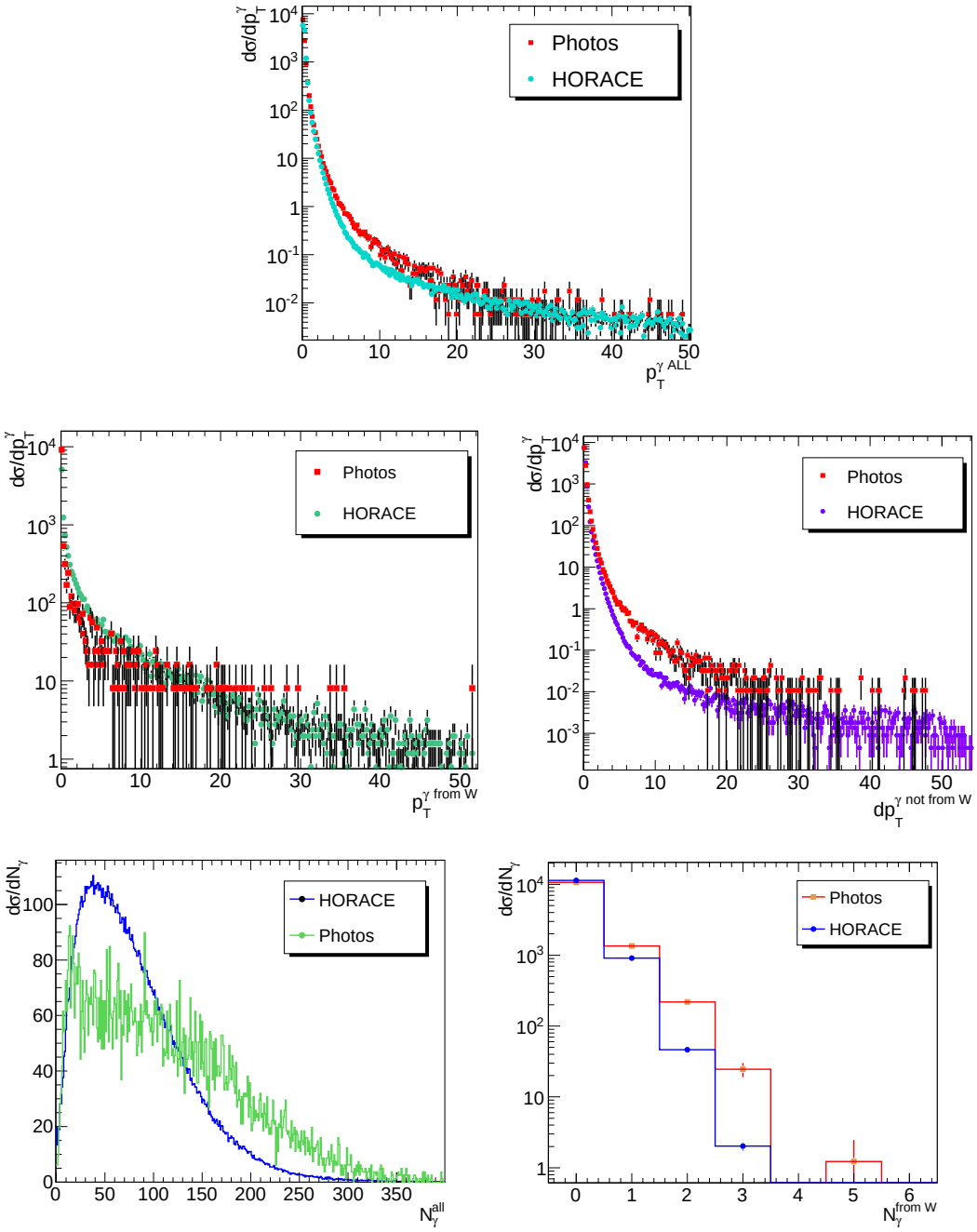

Figure 5.29: *Transverse momentum distribution of inclusive photon distribution (top), of the one emitted by radiative effects of $W \to \mu\nu$ (middle right) and from other processes (middle left) generated both with* **HORACE** *and Photos. Bottom: distribution of the number of photons emitted by radiative effects of $W \to \mu\nu$ (right) and from other processes (left) generated both with* **HORACE** *and Photos.*

selecting events from W (right) is shown for both the generators. For what concerns the N-photons from W prediction, it is possible to see that PHOTOS predicts an higher number of photons emitted per event.

5.7.5 Tails of kinematic distributions

In order to have the best understanding of W boson kinematic distributions, that constitute a background for new physics processes, the high tails of p_T and M_T distributions have been studied, including EW processes introduced by HORACE.
In Figure 5.30 the comparison of p_T distributions at the Born level and with EW processes is displayed; the simulation has been performed using two different cuts on the lepton transverse momentum: 200 GeV (left) and 600 GeV (right). The cross section values obtained by HORACE, with both the cuts, are shown in Table 5.9.

p_T cut (GeV)	σ_{sec}^{BORN} (fb)	$\sigma_{sec}^{NLO(\alpha)}$ (fb)	δ (%)
200	155.56 ± 0.58	140.00 ±0.51	-6.3
600	1.215 ± 0.003	0.952 ±0.003	-21

Table 5.9: *Inclusive cross sections of $W^{\pm}\rightarrow\mu\nu$ of events in the high tails of p_T distributions.*

From these figures, and from Table 5.9 one can see that the cross section at these high p_T values is very low (p_T = 1 TeV the differential cross section $d\sigma/dp_T \ll$ fb). Hence these distributions will not be studied until the LHC will provide enough integrated luminosity ($\sim$ 100 fb^{-1}). However, as is possible to see from the relative differences[11], EW effects are very high in these kinematic regions, and they have not to be ignored in the theoretical model. As better explained here [96], in the high p_T tails EW effects contribute with large and negative Sudakov logarithms that compensate large and positive QCD NLO effects. Therefore, a precise normalization of the SM background to new physics searched and for precision studies as the luminosity monitoring or the measurement of W mass, necessarily requires the simultaneous control of QCD and EW corrections. Remarkably, in the region of the high transverse mass tail above 1 TeV, important for the search for new gauge bosons, these cancellation occurs almost completely between huge positive QCD corrections and very large negative contributions due to EW Sudakov logarithms. This emphasizes the need for a careful combination of strong and EW contributions

[11]In Fig. 5.30 on teh right the error bars are higher because the p_T cut is lower on the generator, and hence there are fewer events on the tail of the distribution.

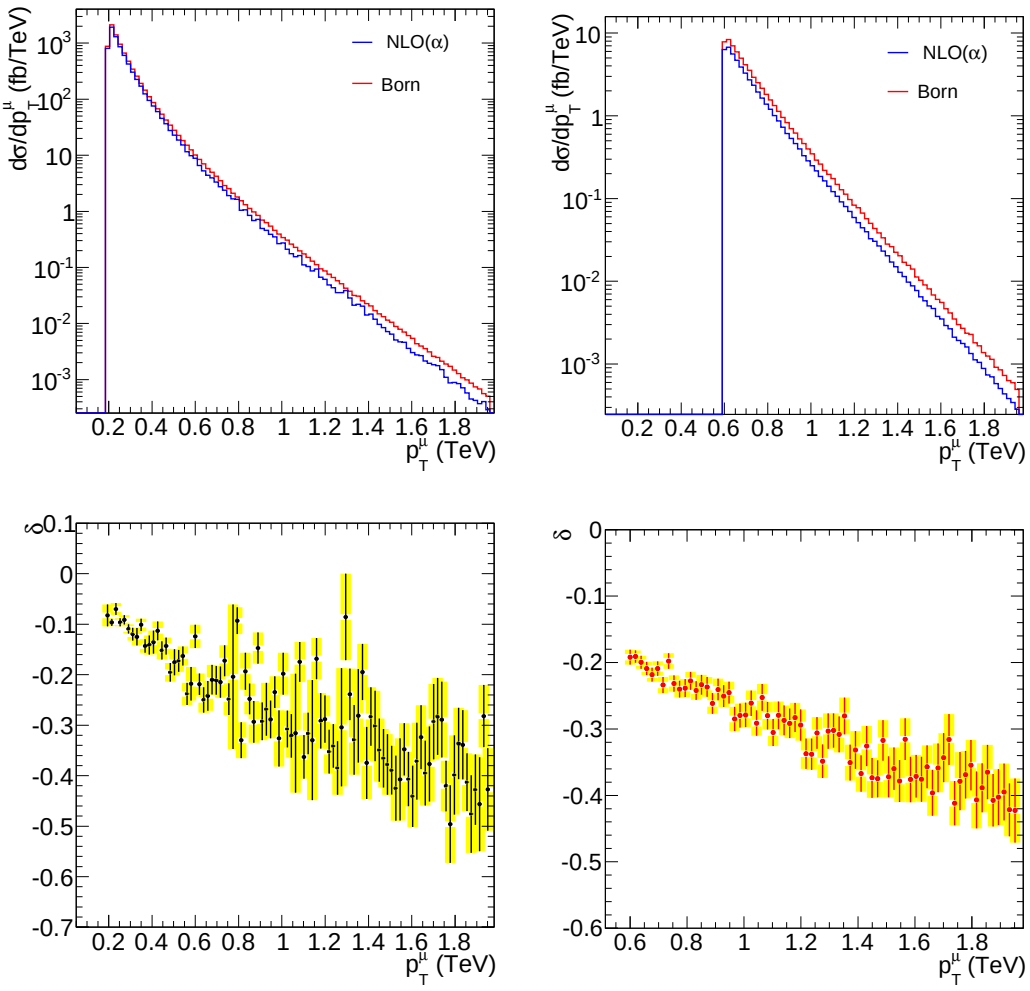

Figure 5.30: *Comparison of the tails of Born and EW corrected p_T distributions (**HORACE** stand-alone), and relative differences. Right and left distributions are produced with differents p_T cuts on the genaration of events (200 GeV and 600 GeV). The statistic is 2·10^4 events.*

in present and future analysis of the charged current DY process. The convolution of the EW effects with QCD shower evolution is definitely relevant for a correct simulation of the distributions, since the relative size and shape of EW contributions is considerably modified when compared with the same features in the absence of the combination with a QCD PS. This can be understood in terms of the modifications introduced by QCD PS on the kinematics of the final-state leptons w.r.t. a pure EW calculation.

Reconstructed data

In Figure 5.31 the comparison between the Born-level and the EW-corrected one of the muon transverse momentum distributions and the W transverse

mass are shown. In the figures on the top, events have been generated with HORACE and then the HERWIG QCD parton shower has been added. In the figures on the middle, the same events have also been reconstructed through the ATLAS detector with the ATLFAST-II package. The statistic is $9{\cdot}10^3$ events, generated with a p_T cut of 600 GeV.

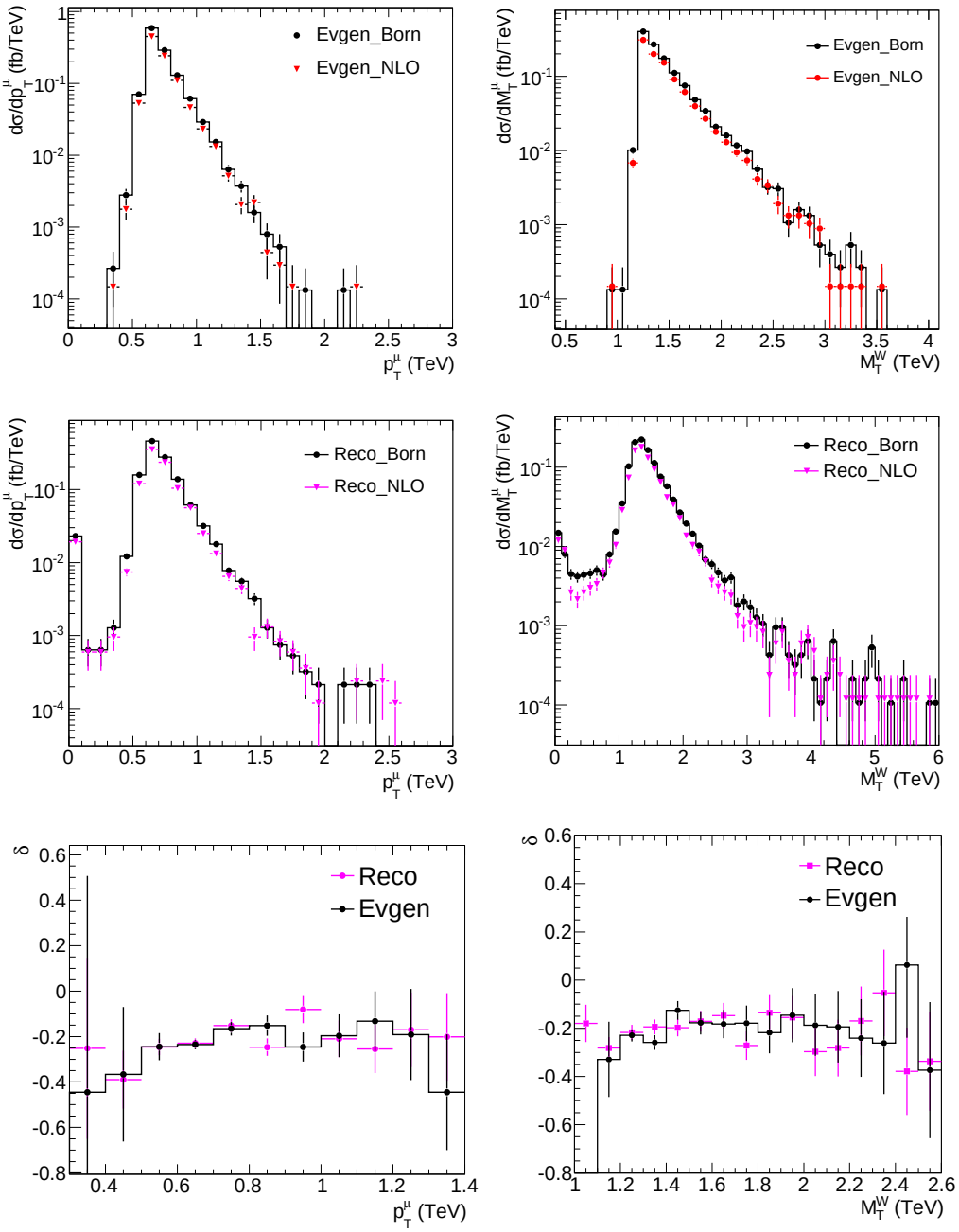

Figure 5.31: *Comparison between of the tails of Born and EW corrected p_T and M_T distributions and relative differences. Top: HORACE with HERWIG parton shower event generator, middle: reconstructed events.*

From the figures on can see that the detector resolution does not hinder the effects of EW corrections, and these are very important, at a level of 30% both with only the generated events, and with the reconstructed ones.
As already said before, EW effects on the W decay have to been taken in account, especially on the tails of the distributions, where W production decays are background to any new physics searches.

Conclusions

The research activity presented in this PhD thesis has been performed in the field of high energy physics at hadron colliders within the Pavia ATLAS group. ATLAS is one of the two general purpose experiments at the LHC proton-proton collider. The performance and the physics research potentialities that will be provided by the LHC entail significant challenges for the design, installation and commissioning of such a great number of different detectors that compose this experiment.
The relevance of muonic signatures for the physics goals of ATLAS has driven the choice of a high resolution Muon Spectrometer whose precision measurement is performed by Monitored Drift Tube (MDT) chambers that cover an area of 5500 m^2. The performance requirements and the complexity of the system, have required a three year period of commissioning in situ, starting with the installation of the first chambers. The commissioning procedures, both of MDT in stand-alone and within the integrated ATLAS system through the acquisition of cosmic rays and the first LHC splash and collision events, have been presented. Most of this commissioning work has been performed at CERN, in the ATLAS experimental cavern and in the control room.
The complexity of modern detectors used for high energy physics leads to many years of design and test on prototypes, before being really built at a full scale. In the second part of this thesis, a new calorimetric technique (DREAM: Dual REadout Method), whose goal is to improve hadronic calorimetry performances by comparing the scintillation and Cerenkov signals produced by particles, have been described in details. In particular, results of test beams applying this technique to homogeneous media are described. This work has been in part accomplished in the framework of *"International Certificate of Doctoral Studies"*, between the Universities of Pavia and Texas Tech.
The ultimate goal of this thesis has been the study of electroweak (EW) effects on the W boson production cross section and decay in the muon channel. EW effects become crucial for an high precision measurement of the W boson properties like the cross section or the mass, in fact they can give effects up to 5% on the cross section value. They can also affect the shape of the W observable distributions, hence giving fake signals of non-standard physics. The

EW correction effects have been evaluated both at generator level, using the HORACE event generator, and at a level of reconstructed events, using the ATLFAST-II ATLAS detector simulation. A detailed study on the feasibility of detect electroweak effects with the ATLAS detector has been presented. In particular, the effect of detector simulation and event reconstruction on the acceptances shapes has been studied.
Lastly, the EW NLO effects in the high tail of muon transverse momentum distributions of W boson have been evaluated. These corrections (up to 30 %) are negative and are compensated by positive NLO QCD effects. Therefore, their interplay is unavoidable both for a precise W boson mass extraction, yielding an overall correction up to 10%, and for new-physics searches at LHC. All these effects are found to be experimentally accessible and measurable.

Appendix A

Acronyms and abbreviations

ADC: *Analog to Digital Converter*
AOD: *Analysis Object Data*
ASD: *Amplifier Shaper Discriminator*
ALICE: *A Large Ion Collider Experiment*
ALFA: *Absolute Luminosity For ATLAS*
ATLAS: *A Toroidal Lhc Apparatus*
BC: *Bunch Crossing*
BIL(S): *Barrel Inner Large (Small)*
BML(S): *Barrel Medium Large (Small)*
BOL(S): *Barrel Outer Large (Small)*
BPTX: *Beam Timing Pickup*
CCC: *Chamber to Chamber Connection*
CCD: *Charge Coupled Device*
CMS: *Compact Muon Solenoid*
C/S: *Cherenkov/Scintillation signal*
CSC: *Cathode Strip Chamber*
CSM: *Chamber service Module*
CTP: *Central Trigger Processor*
DAQ: *DAta AcQuisition*
DCS: *Detector Control System*
DPD: *Derived Physics Data*
DQMF: *Data Quality Monitoring Framework*
DREAM: *Dual REadout Method*
DY: *Drell Yan process*
EB: *Event Builder*
EF: *Event Filter*
EIL(S): *End-cap Inner Large (Small)*
ELMB: *Embedded Local Monitor Board*
EML(S): *End-cap Medium Large (Small)*
EMEC: *ElectroMagnetic End-cap Calorimeter*

EOL(S): *End-cap Outer Large (Small)*
ESD: *Event Summary Data*
EW: *Electro Weak*
EWPA: *EveryWhere Physics Analysis*
FCal: *Forward Calorimeter*
f_{em}: *Electromagnetic fraction*
FSR: *Final State Radiation*
GUT: *Grand Unified Theories*
HEC: *Hadronic End-cap Calorimeter*
HLT: *High Level Trigger*
JTAG: *Joint Test Action Group*
ID: *Inner Detector*
ISR: *Initial State Radiation*
GNAM: *GNAM is not AtlMon*
LAr: *Liquid Argon calorimeter*
LEP: *Large Electron Positron*
LHC: *Large Hadron Collider*
LHC-b: *LHC-beauty*
LSP: *Lightest Supersymmetric Particle*
LUCID: *Luminosity measurement using Cherenkov Integrating Detector*
LVL1: *First LeVeL trigger*
LVL2: *Second LeVeL trigger*
MBTS: *Minimum Bias Trigger Scintillators*
MC: *Monte Carlo*
MDM: *MDT DCS Module*
MDT: *Monitored Drift Tube*
MSSM: *Minimal Supersymmetric Standard Model*
MROD: *MDT Read Out Driver*
MUCTPI: *Muon To Central Trigger Processor Interface*
MS: *Muon Spectrometer*
NLO: *Next to Leading Order*
NNLO: *Next to Next to Leading Order*
OHP: *Online Histogram Presenter*
PDF *Parton Distribution Functions*
PS: *Parton Shower*
QCD: *Quantum ChromoDynamics*
QED: *Quantum Electro-Dynamics*
RDO: *Row Data Object data*
RO: *Read Out*
ROB: *Read Out Buffer*
ROD: *Read Out Driver*
RoI: *Rgion-of-Interest*
RPC: *Resistive Plate Chamber*
SCT: *Semi-Conductor Tracker*

SM: *Standard Model*
SUSY: *SUper SYmmetry*
TDC: *Time to Digital Converter*
TGC: *Thin Gap Chamber*
TRT: *Transition Radiation Tracker*
TTC: *Timing Trigger Control*
WLCG: *World LHC Computing Grid*
ZDC: *Zero Degree Calorimeter*

Bibliography

[1] D.Boussard *et al.The Large Hadron Collider Conceptual Design*, CERN/AC/95-05 (1995).

[2] The LEP Electroweak Working Group, hep-ex/0212036.

[3] ALEPH, DELPHI, L3, OPAL Collaborations and The LEP Working Group for Higgs Boson Searches, *Search for the Standard Model Higgs boson at LEP*, Phys. Lett. B565:61-75, (2003).

[4] The ALEPH Collaboration, *Observation of an Excess in the Search for the Standard Model Higgs Boson at ALEPH*, CERN-EP/2000-138 (2000).

[5] The Tevatron Electroweak Working Group, *Combination of CDF and D0 Results on the Mass of the Top Quark* FERMILAB-TM-2427-E TEVEWWG/top 2009/03, arXiv:0903.2503v1 (2009).

[6] The CDF collaboartion, *Measurement of the Bs-Bsbar Oscillation Frequency*, arXiv:hep-ex/0606027 (2006).

[7] The ATLAS Collaboration, *The ATLAS Experiment at the CERN Large Hadron Collider*, JINST 3 (2008) S08003.

[8] The ATLAS collaboration, *ATLAS Detector and Physics Performance Technical Design Report*, CERN/LHCC/ATLAS TDR 1999.

[9] CMS Collaboration, *CMS Technical Design Report*, Vol. 1 and Vol. 2, CERN/LHCC/2006-001 (2006).

[10] LHCb Collaboration, *LHCb Technical Design Report*, CERN-LHCC-2003-030 (2003).

[11] ALICE Collaboration, *ALICE Technical Design Report*, CERN/LHCC 2001-021 (2001).

[12] R.Schmidt and J.P.Tock *Summary of the session III, repair of 34* Proceedings of Chamonix 2009 workshop on LHC Performance.

[13] A. Negri *et al.*,*ATLAS TDAQ System Integration and Commissioning*, Preprint submitted to TIPP09 Proceedings in Nucl. Instr. and Meth. .

[14] CERN courtesy.

[15] F. Sauli *Principles and operation of multiwire proportional and drift chambers*, CERN 77-09 (1977).

[16] Y. Aray *et al.*, *ATLAS Muon Drift Tube Electronics* 2008 JINST 3 P09001.

[17] M. Bellomo *et al.*, *The barrel-inner-large tracking chambers for the ATLAS muon spectrometer: Ready for installation* Nucl. Instr. and Meth. A573 (2007) 340.

[18] The ATLAS Muon Run Analysis Task Force, *Results from the Commissioning of the ATLAS Muon Spectrometer with Cosmic Rays*, ATLAS note, to be submitted to Nucl. Instr. and Meth. (2009).

[19] S. Kircher *et al.*, *Parameter of MDT Ageing and Reanimation*, ATL-MUON-2001-012 (2001).

[20] M. Aleksa *et al.*, *non-linear MDT Drift gases like Ar-CO_2*, ATL-MUON-98-261 (1999).

[21] J.E.Huth, *et al.*, *Development of an octal CMOS ASD for the ATLAS Muon detector*, Proceedings of the 5th Conference on Electronics for LHC Experiments, Snowmass, CO, September 1999, p.436.

[22] C.Posch, E.Hazen, and J.Oliver, MDT-ASD: ATL-MUON-2002-003.

[23] *http://weblib.cern.ch/Home/ATLAS_Collection/ATLAS_Notes/Muon/*

[24] http://garfield.web.cern.ch/garfield/

[25] S. Hassini *et al.*, Nucl. Instr. and Meth. A572 (2007) 77.

[26] Th. Lagouri *et al.*, IEEE Trans.Nucl. Sci. 51 (2004).

[27] D. Adams *et al.*, ATL-SOFT-2003-007 (2003).

[28] S. Tarem *et al.*, Nuclear Science Simposium Conference Record, 2007 IEEE (2007).

[29] A. Belloni *et al.*, *Muon Segment Studies: calibration and resolution* ATLAS NOTE 2009.

[30] F. Felici, *Verifica delle funzionalitá delle camere MDT al CERN prima dell'installazione*, Degree thesis, Universitá Degli Studi di Roma 3.

[31] D.Salvatore, *Intensive irradiation studies, monitoring and commissioning data analysis on the ATLAS MDT chambers*, Ph.D. thesis, Universitá degli studi della Calabria.

[32] P. Adragna *et al.*, *GNAM and OHP: Monitoring Tools for ATLAS experiment at LHC.* IEEE Trans. Nucl. Sci. 2006.

[33] D. Salvatore *et al.*, *The GNAM system in the ATLAS online monitoring framework.* Nucl. Instr. and Meth. B (Proc. Suppl.) 172 (2007).

[34] M.J.Costa, *Commissioning of the ATLAS detector with cosmic rays and first LHC beams.* Atlas note: ATL-COM-GEN-2009-005.

[35] http://atlas.web.cern.ch/Atlas/index.html

[36] R. Wigmans, Calorimetry - Energy Measurement in Particle Physics, International Series of Monographs on Physics, vol. 107, Oxford University Press, Oxford, 2000.

[37] N.Akchurin *et al.*, Nucl. Instr. and Meth. **A536** (2005) 29.

[38] N.Akchurin *et al.*, Nucl. Instr. and Meth. **A537** (2005) 537.

[39] N.Akchurin *et al.*, Nucl. Instr. and Meth. **A399** (1997) 202.

[40] R.Wigmans, New Journal of Physics **10** (2008) 025003.

[41] N.Akchurin *et al.*, Nucl. Instr. and Meth. **A582** (2007) 474.

[42] N.Akchurin *et al.*, Nucl. Instr. and Meth. **A595** (2008) 359.

[43] N.Akchurin *et al.*, Nucl. Instr. and Meth. **A593** (2008) 530.

[44] M.V.Korzhik *et al.*, Proc. IEEE Nucl. Sci. Symp., Dresden (2008).

[45] M.Nikl *et al.*, Journal of Applied Physics **104** (2008) 1.

[46] N.Akchurin *et al.*, Nucl. Instr. and Meth. **A604** (2009) 512.

[47] S. Franchino on behalf of the DREAM collaboration, *New crystals for the DREAM project* Proceedings of the conference TIPP09, submitted to: TIPP09 Proceedings in Nucl. Instr. and Meth. (2009).

[48] N.Akchurin *et al.*, Nucl. Instr. and Meth. **A581** (2007) 643.

[49] N.Akchurin *et al.*, Nucl. Instr. and Meth. **A598** (2009) 422.

[50] M.Nikl *et al.*, Journal of Applied Physics **91** (2002) 2791.

[51] N.Akchurin *et al.*, Nucl. Instr. and Meth. **A584** (2008) 273.

[52] N.Akchurin *et al.*, *Dual-Readout Calorimetry with Crystal Calorimeters*, Nucl. Instr. and Meth. **A**(2008), doi:10.1016/j.nima.2008.10.010.

[53] M.Nikl *et al.*Nim A 540 (2005) 381-394.

[54] Ishii *et al.*, Optical Materials 19, (2002) 2001.

[55] Harada *et al.*, Journal of Applied Physics. Vol.40 (2001) 1360.

[56] Kobayashi *et al.*, Nucl. Instr. and Meth. 205 (1983) 113.

[57] H. Shimizua *et al.*, Nucl. Instr. and Meth. 550 (2005) 258.

[58] K. Melnikov, F. Petriello, *Electroweak gauge boson production at hadron colliders through* $\mathcal{O}(\alpha_S^2)$.

[59] The Tevatron Electroweak Working Group, *Updated Combination of CDF and D0 Results for the Mass of the W Boson* TEVEWWG/WZ 2009/01 FERMILAB-TM-2439-E (August 2009).

[60] H. Georgi and S. L. Glashow, Phys. Rev. Lett. 32 (1974) 438-441.

[61] K. D. Lane and E. Eichten, Phys. Lett. B222 (1989) 274.

[62] N. Arkani-Hamed, A. G. Cohen, and H. Georgi, Phys. Lett. B513 (2001) 232-240.

[63] L. Randall and R. Sundrum, Phys. Rev. Lett. 83 (1999) 3370-3373.

[64] J. C. Pati and A. Salam, Phys. Rev. D10 (1974) 275-289.

[65] S. Hossenfelder, arXiv:hep-ph/0412265.

[66] Moraes, A., Buttar, C. and Dawson, I., Eur. Phys. J. C 50 (2007) 435.

[67] CDF Coll., Phys. Rev. D 50 (1994) 2966; Phys. Rev. Lett. 74 (1995) 2626; Phys. Rev. Lett. 73 (1994) 225.
D0 Coll., Phys. Rev. Lett. 74 (1995) 2632.

[68] D.Adams *et al.The ATLAS computing model* ATL-SOFT-2004-007, CERN-LHCC-2004-037/G-085 V1.2.

[69] ATLAS Collaboration, *Expected Performance of the ATLAS Experiment, Detector, Trigger and Physics*, CERN-OPEN-2008-020, Geneva, 2008.

[70] k.Assamagan *et al.The ATLAS simulation project*, Atlas note 2009.

[71] I.Bird *et al.*, CERN-LHCC-2005-024 (2005).

[72] T. Sjostrand, P. Eden, C.Friberg, L. Lonnblad, G. Miu, S. Mrenna and E. Norrbin, Comput. Phys. Commun. 135 (2001) [arXiv:hep-ph/0010017].

[73] G. Corcella et al., JHEP 0101 (2001) 010 [arXiv:hep-ph/0011363].

[74] E. Barberio and Z. Was, Comput. Phys. Commun. 79, (1994) 291.
E. Barberio, B. van Eijk and Z. Was. Comput. Phys. Commun. 66, (1991) 115.

[75] - C. M. Carloni Calame, G. Montagna, O. Nicrosini, and M. Treccani, Phys. Rev. D69 (2004) 037301, [hep-ph/0303102].
- HORACE Home Page http://www.pv.infn.it/hepcomplex/horace.html
- C. M. Carloni Calame, G. Montagna, O. Nicrosini, and M. Treccani, JHEP 05 (2005) 019, [hep-ph/0502218].

[76] http://www.phys.psu.edu/ cteq/

[77] R. S. Thorne, A.D. Martin andW.J. Stirling,*MRST Parton Distributions - Status 2006* , [arXiv:hep-ph/0606244] 2006.

[78] http://wwwasdoc.web.cern.ch/wwwasdoc/geant html3/geantall.html.

[79] The Geant4 Collaboration, *Geant4 - A Simulation Toolkit*, Nucl. Instr. and Meth. , A 506 (2003), 250.
Geant4, http://wwwasd.web.cern.ch/wwwasd/geant4/geant4.html.

[80] C.M.Carloni Calame *et al.Precision electroweak calculation of the charged current Drell-Yan process* FNT/T 2006/08 IFUM-874/FT [hep-ph/0609170] (2006).

[81] https://twiki.cern.ch/twiki/bin/view/AtlasProtected/EWPAMainPage

[82] The UA1 Collaboration: *Experimental observation of events with large missing transverse energy accompanied by a jet or a photons(s) in $p\bar{p}$ collisions at $\sqrt{s}$ = 540 GeV.* Physics letters (1983).

[83] The UA2 Collaboration: *Observation of single isolated electrons of high transverse momentum in events with missing transverse energy at the CERN $p\bar{p}$ collider* Physics letters (1983).

[84] The UA1 Collaboration: *Observation of muonic Z^0 decay at the anti-pp collider*, Physics letters (1984).

[85] The UA2 Collaboration: *A study of high transverse momentum electrons produced in p collisions at 540 GeV* Zeitschrift fur Physik C24 (1984).

[86] V.N. Gribov, L,N. Lipatov. Sov.J.Nucl.Phys. 15:438 (1972).

[87] G. Altarelli and G. Parisi. Nucl. Phys. B126:298 (1977).

[88] Yu. L. Dokshitzer. Sov.Phys. JETP, 46:641 (1977).

[89] S. Frixione and B.R. Webber, *Matching NLO QCD computations and parton shower simulations*, JHEP 0206 (2002) 029 [hep-ph/0204244].
E. Barberio, B. van Eijk and Z. Was. Comput. Phys. Commun. 66, (1991) 115.

[90] V.V. Sudakov, Zh.E.T.F. 30 (1956) 87 Sov. Phys. J.E.T.P. 30 (1956).

[91] A. Abulencia *et al.Measurement of Inclusive W and Z Cross Sections in* $p\bar{p}$ *Collisions at* $\sqrt{s}$ *= 1.96 TeV.* arXiv:hep-ex/0508029v3 (2007).

[92] The ATLAS collaboration *Electroweak boson cross-section measurements with ATLAS* ATLAS NOTE (2008).

[93] M.Scott *Theoretical uncertainties on the W- and Z- boson acceptance in the first phase of LHC.* ATLAS NOTE (2009).

[94] M.Scott, E. Dobson, T. Peterson *Feasibility study on the measurement of the W and Z leptonic cross section ratio in the muoin decay channel with early data.* ATLAS NOTE (2009).

[95] M. Bellomo, *ATLAS muon trigger performance and luminosity measurements with Z and W bosons at LHC*, Ph.D. thesis, Universitá Degli Studi di Pavia (2006).

[96] G. Balossini *et al.Combination of electroweak and QCD corrections to single W production at the Fermilab Tevatron and the CERN LHC* FNT/T 2009/02 IFUM-942/FT [hep-ph/09070276v1] (2009).

[97] J.T. Moscickif *et al.Ganga: A tool for computational-task management and easy access to Grid resources* Computer Physics Communications, 180 (2009).

[98] https://twiki.cern.ch/twiki/bin/view/AtlasProtected/HoraceForAtlas

[99] http://pdg.lbl.gov/2005/reviews/montecarlorpp.pdf

Acknowledgments

At this point I feel obliged to thank most of those who have accompanied me on my many activities in physics during the last three years and contributed to making my PhD adventure very special and unforgettable.

First I would like to thank my supervisor Michele, for having undertaken my supervision (even if it was not very easy!) and for having supported (almost always) my choices and allowing me to escape from Pavia to work in others foreign institutes. I would also like to thank him for having created a friendly ambience in our ATLAS-Pavia working group.

I would also like to thank "my personal corrector" Valerio, for having supervised my analysis, for his constant guidance and support during my analysis activities, (he always keeps after me!!!), for his many useful suggestions and for his (unfortunately, not so few) last minute corrections.

A special thank you to my favorite "capetta" Gabri. What would I have done without her valuable advice, her kindness, friendship, helpfulness and support throughout my PhD, since I was taking (literary) my firsts steps in ATLAS. I was also happy to share an office with her (when she didn't try to kill me by throwing napkin packages!!!), we have spent a great time together!

Another special thank you is for "the conku" and "personal on-line helper" Negri. He made work easier by giving quick and efficient assistance, especially in computing problems and he was always available to give advice (that, however, I usually didn't listen to)....Only one remark: why do you always have to trigger Marco when you come into my office in Pavia :-) ??

I would also like to thank many people from the ATLAS Pavia group, professors, researchers and technicians with whom I have worked at some point during my PhD experience, for their professional support and the friendly atmosphere they created. In particular Agostino (for his complete availability, his useful suggestions and... his endless talking!), Max and "La Rebu" for their

help, especially on Monte Carlo tools, Claudio Conta (with his original neckties), Diana, Domenico, Marco (and his poems), Bob, and many others.

At this point I would also like to thank all the people with whom I have worked closely together during the period I spent at CERN. In particular the "MDT bosses" Fabio, Ludo and Sotiris. Since the earliest days of my commissioning work, I have worked together with them; they supervised me when I had first arrived at CERN without any idea how to work in experimental particle physics. I (hopefully) learned a lot from them. Especially with Sotiris, who never remembers that I'm always right! :-), I spent a lot of good times during the commissioning phase, climbing in the ATLAS Muon Spectrometer, and fearing yellow men. That was hard, but, being an unusual work, it was also amusing.
I also thank all my MDT-commissioning colleagues and friends, in particular Bernhard, Charilaos, Eleni, Emily, Giovanni, Jorghino, Jorg, Mauretto, Steffen, Verena and many others. With them I shared some tough times but also a lot of fun, which made me look forward to every stay at CERN. A special thanks to Daniel Ventura for his almost complete availability for last minute help, mostly about the ATLAS software and many English language corrections. About the English corrections, thanks also to Sander, who didn't like the "*MDT calibration in loco..* :-)" sentence in my thesis.

Another special thanks to Richard Wigmans who offered me the possibility to work with him at Texas Tech University and to learn a lot, especially about "the art of calorimetry". Also thanks to all my DREAM colleagues, in particular John Hauptman for his kindness and availability.

At the end I thank many colleagues from Pavia University. Thanks to the phenomenologists, in particular to Giovanni for his help with the `HORACE` code, his kindness, availability and friendship.
And thanks to all my friends, especially to the three "cmssini" Claudio, Paolo and Davide, to Fede and Paolino, and to Trotti, for their friendship shown both in Pavia and elsewhere all over the world.

A big thank you to my family who gave me the opportunity to study physics and hence to obtain the PhD.